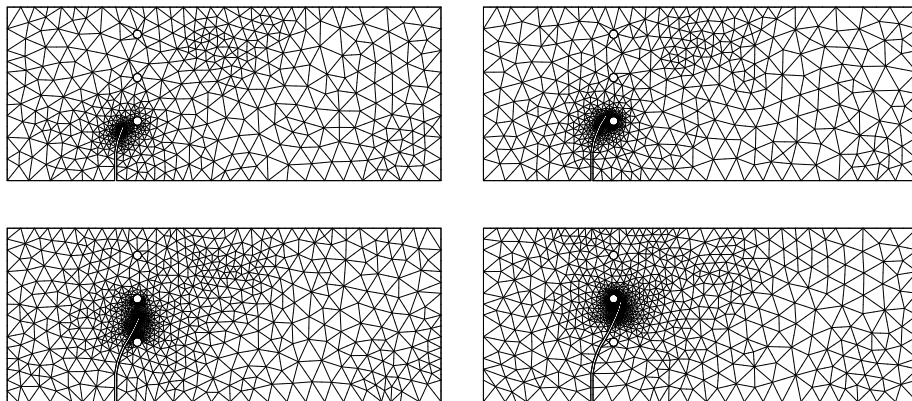


# Material Forces in Finite Inelasticity and Structural Dynamics: Topology Optimization, Mesh Refinement and Fracture

Dominik Zimmermann



$$\text{Div}\Sigma + \bar{\Gamma}_0 = \mathbf{0} \quad \Rightarrow \quad \mathbf{F}_I + \mathbf{P}_I = \mathbf{A} \left\{ \int_{\mathcal{B}^e} -\mathbf{B}_I^T \Sigma + \mathbf{N}_I^T \bar{\Gamma}_0 \, dV \right\} = \mathbf{0}$$

Bericht Nr.: I-21 (2008)  
Institut für Mechanik (Bauwesen), Lehrstuhl I  
Professor Dr.-Ing. C. Miehe  
Stuttgart 2008









# Material Forces in Finite Inelasticity and Structural Dynamics: Topology Optimization, Mesh Refinement and Fracture

Von der Fakultät Bau- und Umweltingenieurwissenschaften  
der Universität Stuttgart zur Erlangung der Würde  
eines Doktor-Ingenieurs (Dr.-Ing.)  
genehmigte Abhandlung

vorgelegt von

**Dominik Zimmermann**

aus Koblenz

Hauptberichter: Prof. Dr.-Ing. Christian Miede

Mitberichter: Prof. Dr.-Ing. Paul Steinmann

Tag der mündlichen Prüfung: 21. Januar 2008

Institut für Mechanik (Bauwesen) der Universität Stuttgart  
Januar 2008

**Herausgeber:**

Prof. Dr.-Ing. habil. C. Miehe

**Organisation und Verwaltung:**

Institut für Mechanik (Bauwesen)

Lehrstuhl I

Universität Stuttgart

Pfaffenwaldring 7

D-70550 Stuttgart

Tel.: ++49-(0)711/685-66378

Fax : ++49-(0)711/685-66347

© Dominik Zimmermann

Institut für Mechanik (Bauwesen)

Lehrstuhl I

Universität Stuttgart

Pfaffenwaldring 7

D-70550 Stuttgart

Alle Rechte, insbesondere das der Übersetzung in fremde Sprachen, vorbehalten. Ohne Genehmigung des Autors ist es nicht gestattet, dieses Heft ganz oder teilweise auf fotomechanischem Wege (Fotokopie, Mikrokopie) zu vervielfältigen.

ISBN 3-937859-09-8 (D 93 Stuttgart)

## Abstract

The present work serves two major purposes. On the one hand, theoretical approaches to configurational mechanics are elaborated. For inelastic problems, the spatial and material equilibrium conditions are derived by means of a global dissipation analysis. In the dynamical framework, a variational formulation based on Hamilton's principle is established inducing the balances of physical momentum, material pseudomomentum and kinetic energy. On the other hand, configurational-force-based computational algorithms are developed. At first, configurational forces are exploited in the context of topology optimization. The theoretical basis is provided by a dual variational formulation of finite elastostatics. This scenario is applied to the  $r$ -adaptive optimization of finite element meshes and the optimization of truss structures. In the second step, a configurational-force-based strategy for  $h$ -adaptivity is presented. The discrete version of the material balance equation is exploited to formulate global and local refinement criteria controlling the overall decision on mesh refinement and the local refinement procedure. The method is specified for problems of finite elasticity and plasticity including thermal and dynamical effects as well. Finally, a configurational-force-driven procedure for the simulation of crack propagation in brittle materials is introduced. The algorithm bases on the separation of the geometry model and the finite element mesh. The process of crack propagation is carried out by a structural update of the underlying geometry model. The generation of the new triangulation incorporates a configurational-force-based adaptive refinement criterion. The capabilities of the derived algorithms are demonstrated by means of a variety of numerical examples including the comparison with benchmark analyses and experimental observations.

## Zusammenfassung

Die vorliegende Arbeit verfolgt zwei Hauptziele. Einerseits werden theoretische Ansätze der Konfigurationsmechanik erarbeitet. Für inelastische Probleme werden die räumlichen und materiellen Gleichgewichtsbedingungen aus einer globalen Dissipationsanalyse hergeleitet. Im dynamischen Fall wird eine Variationsformulierung basierend auf dem Hamiltonschen Prinzip betrachtet. Dieses Vorgehen induziert die lokalen Bilanzen des räumlichen Impulses, des materiellen Pseudoimpulses und der kinetischen Energie. Andererseits werden konfigurationskraft-basierte numerische Algorithmen entwickelt. Zunächst werden materielle Kräfte im Rahmen der Topologieoptimierung genutzt. Die Basis bildet eine duale Variationsformulierung der finiten Elastostatik, die hinsichtlich der  $r$ -adaptiven Optimierung von Finite-Elemente-Netzen und der Strukturoptimierung von Fachwerken spezifiziert wird. Im zweiten Schritt wird eine konfigurationskraft-basierte  $h$ -adaptive Strategie vorgestellt. Ausgehend von der diskreten Form der materiellen Bilanzgleichung werden globale und lokale Kriterien entwickelt, die die Verfeinerungsprozedur steuern. Das Konzept wird auf Probleme der finiten Elastizität und Plastizität angewandt, wobei thermische und dynamische Effekte ebenfalls berücksichtigt werden. Schließlich wird ein konfigurationskraft-getriebenes Verfahren zur Simulation von Rißfortschritt in spröden Materialien eingeführt. Der Algorithmus basiert auf der Trennung von Geometriemodell und Triangulierung. Das Rißwachstum wird durch Aufdatierung des zugrundeliegenden Geometriemodells abgebildet. Die Neuvernetzung schließt ein konfigurationskraft-basiertes Verfeinerungskriterium ein. Die Leistungsfähigkeit der entwickelten Algorithmen wird mittels einer Vielzahl numerischer Beispiele, die auch die Vergleiche mit Benchmark-Untersuchungen und experimentellen Beobachtungen beinhalten, bewiesen.



## Acknowledgements

The work presented in this thesis was elaborated in the years between 2003 and 2008 while I was a co-worker at the Institute of Applied Mechanics (Civil Engineering) at the University of Stuttgart.

I want to thank my academic teacher Professor Christian Miehe. During my studies, he enforced my application for the scholarship of the Studienstiftung des deutschen Volkes and finally gave me the opportunity to work as an assistant lecturer in his research group. I would like to express my gratitude for his support and his guidance.

In addition, I offer my thanks to Professor Paul Steinmann for being interested in my work and for acting as the second referee of this thesis.

Next, I want to thank all my colleagues at the Institute of Applied Mechanics. In particular, I would like to thank Dr. Nikolas Apel and Dr. Martin Becker for all the fruitful discussions we had and for their close friendship and support in many scientific and personal questions. Furthermore, I want to thank Ayhan Acartürk and Manuel Birkle for their friendship and good collaboration.

I am very grateful to Tuncay Yalcinkaya, Fabian Welschinger, Ingrid Bruss, Fabian Fürle, Martina Hofacker and Ilona Frankenreiter who provided me significant support through their master and diploma theses. The supervision of these theses was a true pleasure and without their work this thesis would not have been possible.

Finally, I thank my brother Benedikt and my parents Rita and Joachim for their everlasting support and backing.

Stuttgart, January 2008

Dominik Zimmermann



## Contents

<b>1. Introduction</b> . . . . .	<b>1</b>
1.1. Motivation and State of the Art . . . . .	1
1.2. Overview and Outline . . . . .	4
<b>2. Fundamentals of Continuum Mechanics</b> . . . . .	<b>7</b>
2.1. Finite Kinematics . . . . .	7
2.1.1. Motion of a Material Body . . . . .	7
2.1.2. Dual Bases and Metric Tensors . . . . .	8
2.1.3. The Deformation Gradient . . . . .	9
2.1.4. Strain Tensors . . . . .	11
2.1.5. Time Derivatives of Material and Spatial Objects . . . . .	12
2.1.6. Velocity Gradients and Lie-Derivative . . . . .	14
2.2. Concept of Stresses and Heat Flux . . . . .	14
2.2.1. Traction Vector. Stress Tensors . . . . .	15
2.2.2. Heat Flux. Heat Flux Vector . . . . .	16
2.2.3. Stress Power and Material Work of Deformation . . . . .	16
2.3. Physical Balance Principles . . . . .	17
2.3.1. Balance of Mass . . . . .	17
2.3.2. Balance of Linear Momentum . . . . .	18
2.3.3. Balance of Angular Momentum . . . . .	19
2.3.4. Balance of Energy. First Axiom of Thermodynamics . . . . .	19
2.3.5. Balance of Entropy. Second Axiom of Thermodynamics . . . . .	20
<b>3. Configurational Setting of Thermo-Inelasticity</b> . . . . .	<b>23</b>
3.1. Introductory Remarks . . . . .	23
3.2. Formulation and Exploitation of a Global Dissipation Postulate . . . . .	24
3.2.1. Basic Geometry of a Solid with Structural Changes . . . . .	24
3.2.2. Global Constitutive Response of an Inelastic Solid . . . . .	27
3.3. Discrete Finite Element Formulation . . . . .	34
3.3.1. Spatial Discretization of the Inelastic Solid . . . . .	34
3.3.2. Global Response of the Spatially Discretized Inelastic Solid . . . . .	35
3.4. Summary of Governing Equations and Numerical Solution Procedure . . . . .	38
3.5. Evaluation of Discrete Configurational Nodal Forces . . . . .	40
3.5.1. Global Formulation: Introduction of Additional Nodal Degrees . . . . .	41
3.5.2. Local Formulation. Application of Smoothing Algorithms . . . . .	43
3.6. Specification and Numerical Example . . . . .	46

---

3.6.1. Model Problem: Thermo-Crystal-Plasticity . . . . .	46
3.6.2. Numerical Example: Cook's Membrane Problem . . . . .	49
<b>4. Configurational Solid Dynamics . . . . .</b>	<b>53</b>
4.1. Preliminary Aspects . . . . .	53
4.2. Variational Formulation of Configurational Solid Dynamics . . . . .	54
4.2.1. Hamilton's Principle . . . . .	56
4.2.2. Variation with respect to Spatial Coordinate . . . . .	57
4.2.3. Variation with respect to Material Coordinate . . . . .	59
4.2.4. Variation with respect to Time . . . . .	62
4.2.5. Additional Remarks. Noether's Theorem . . . . .	63
4.3. Global Material and Spatial Balance Equations . . . . .	65
4.4. Numerical Treatment: Discretization in Space and Time . . . . .	66
4.4.1. General Aspects and Numerical Solution Procedure . . . . .	66
4.4.2. Solution of Equation of Spatial Motion . . . . .	67
4.4.3. Treatment of Equation of Material Motion . . . . .	71
4.5. Specification and Numerical Example . . . . .	72
4.5.1. Material Model and Constitutive Relations . . . . .	72
4.5.2. Numerical Example: Oscillation of a Strip . . . . .	72
<b>5. Material-Force-Based Optimization Strategies . . . . .</b>	<b>77</b>
5.1. General Remarks . . . . .	77
5.2. Dual Variational Formulation of Finite Elastostatics . . . . .	78
5.2.1. Variational Formulation . . . . .	79
5.2.2. Exploitation of Global Dissipation Postulate . . . . .	80
5.2.3. Dual Euler-Lagrange Equations of the Variational Formulation . . . . .	81
5.3. Discussion of Numerical Solution Procedures . . . . .	81
5.3.1. Polak-Ribière Non-Linear Conjugate Gradient Method . . . . .	82
5.3.2. Newton-Raphson Iteration Scheme . . . . .	84
5.3.3. Viscous-Type Relaxation of Configurational Forces . . . . .	85
5.4. Topology Optimization of Finite Element Meshes . . . . .	86
5.4.1. $r$ -Adaptive Mesh Optimization . . . . .	86
5.4.2. Numerical Example: Plane Sheet in Tension . . . . .	88
5.4.3. Numerical Example: Homogeneous Block in Tension . . . . .	90
5.5. Topology Optimization of Truss Structures . . . . .	91
5.5.1. Structural Optimization of Truss Systems . . . . .	91
5.5.2. Numerical Example: Optimization of a Truss Structure . . . . .	93



---

<b>6. Material-Force-Based <math>h</math>-Adaptive Refinement Procedures</b> . . . . .	<b>97</b>
6.1. General Aspects . . . . .	97
6.2. Refinement Criterion Based on Discrete Material Nodal Forces . . . . .	98
6.3. Algorithms and Numerical Implementation . . . . .	102
6.3.1. Mesh Generation . . . . .	102
6.3.2. Mapping of Solution Variables . . . . .	104
6.4. Application to Finite Elasticity . . . . .	105
6.4.1. Material-Force-Based Refinement Indicator in Finite Elasticity . . . . .	105
6.4.2. A Short Review of Recovery-Based Error Estimation . . . . .	106
6.4.3. Numerical Example: Plate with a Circular Hole . . . . .	108
6.4.4. Numerical Example: Buckling of a Circular Bar . . . . .	110
6.5. Application to Finite $J_2$ -type Thermo-Plasticity . . . . .	115
6.5.1. General Remarks . . . . .	115
6.5.2. Numerical Example: Plate with a Circular Hole . . . . .	116
6.5.3. Numerical Example: Necking of an Axisymmetric Bar . . . . .	121
6.5.4. Numerical Example: Necking of a Metallic Rod . . . . .	126
6.6. Application to Finite Elastodynamics . . . . .	134
6.6.1. Remarks on Particular Numerical Treatment . . . . .	134
6.6.2. Numerical Example: Oscillation of a Two-dimensional Strip . . . . .	135
<b>7. Material-Force-Based Simulation of Crack Propagation</b> . . . . .	<b>139</b>
7.1. Introductory Aspects . . . . .	139
7.2. Variational Setting of Brittle Fracture . . . . .	140
7.2.1. Basic Geometry of a Cracked Solid . . . . .	140
7.2.2. Global Response of a Cracked Solid . . . . .	142
7.3. Space-Time-Discrete Setting of Brittle Fracture . . . . .	144
7.3.1. Global Response of the Spatially Discretized Cracked Solid . . . . .	144
7.3.2. Time Discretization of Crack Evolution Problem . . . . .	145
7.4. Solution Procedure for Adaptive Fracture Simulation . . . . .	146
7.4.1. Material-Force-Based Geometry Update . . . . .	146
7.4.2. Material-Force-Based Adaptive Refinement Procedure . . . . .	148
7.4.3. Staggered Solution Algorithm . . . . .	149
7.5. Numerical Examples . . . . .	151
7.5.1. Tension Test of a Notched Specimen . . . . .	151
7.5.2. Three Point Bending Test . . . . .	152
7.5.3. Tension Test of Planar Sheet with Two Holes . . . . .	156
<b>8. Conclusion</b> . . . . .	<b>159</b>

A. A Reminder of Eshelby's Reasoning . . . . .	161
B. Time Derivatives of Fundamental Kinematic Objects . . . . .	165
C. Enhanced Strain Formulation . . . . .	167
D. Noether's Theorem . . . . .	173
E. Dual Variational Formulation of Truss Structures . . . . .	177
References . . . . .	179

## 1. Introduction

The objective of the present work is the investigation of some specific aspects of *configurational mechanics*. On the one hand, attention is focused on the presentation of two conceptual approaches towards the *theoretical description* of the configurational setting of finite thermo-inelasticity and structural dynamics. On the other hand, the work is devoted to the development of *numerical algorithms and their application* to particular problems of computational mechanics.

### 1.1. Motivation and State of the Art

In recent years, configurational mechanics, often also denoted mechanics in material space, has become a generic term with regard to the study of inhomogeneities. This concept is naturally linked to the notion of material or configurational forces. The fundamental ideas date back to the pioneering works of ESHELBY [42, 43, 44], who in fact never used this expression. To set the stage, the basic features of Eshelby's concept of a force acting on a singularity or an inhomogeneity are briefly recapitulated in Appendix A.

Configurational mechanics or, in other words, the theory of configurational forces has proven to be appropriate to handle all kinds of inhomogeneities or defect situations with the most prominent application being in fracture mechanics. In general, an inhomogeneity is defined as a defect in the translational invariance of material properties with respect to the material manifold. Consider for instance an elastic body with defects in the form of e.g. dislocations, voids, inclusions or cracks. The inhomogeneity is characterized by an explicit dependence of either the mass density  $\rho_0$  or the energy density  $\psi$  on the material position  $\mathbf{X}$  of the material particle. Vice versa,  $\partial_{\mathbf{X}}\rho_0 = \mathbf{0}$  and  $\partial_{\mathbf{X}}\psi^{expl} = \mathbf{0}$  state the conditions for the homogeneity of the material. Besides these true material inhomogeneities so-called quasi-inhomogeneities exist, cf. MAUGIN [104], such as field singularities in the sense of singular lines in fracture mechanics or singular surfaces associated with phase transitions, and also thermal effects, evolving inelastic deformation or the evolution of micro-structures. Most remarkably, even the discretization, e.g. the triangulation via a finite element mesh, of an in other respects homogeneous body induces an artificial inhomogeneity. This is reflected by the occurrence of discrete configurational nodal forces indicating the inaccuracy of the respective finite element mesh.

A change in the material position of the defect, i.e. a structural change within the material setting of a body, can be described by means of the material configurational map. It represents a time-dependent parameterization of the reference configuration  $\mathcal{B}$  irrespective of the question whether the material body as a whole moves with respect to its spatial setting. This movement of the defect with respect to the ambient material comes along with a change in the energetic state of the system. Configurational forces are the energetically dual objects to these configurational changes in the sense that in common thinking the change of energy with respect to the change of position defines a force. In particular, configurational forces define an *energy release* associated with the translation of the defect in the material space. Since material forces are related to a variation of the point in the material space at fixed position in the physical space, they are the dual objects to the usual physical forces generated by changes in the actual physical placement keeping the material framework fixed. It is a remarkable circumstance that in contrast to the spatial viewpoint, where a physical force causes a spatial displacement, in the material setting the reasoning is just opposite, namely a material displacement corresponding to a change

in energy implies a change in the configurational force acting on the defect.

Inspired by the seminal works of Eshelby, the investigation of the configurational setting of continuum mechanics gave rise to lively research activities. Thereby, the dependence on the material coordinate necessitates the formulation of balance equations in the material space. The fundamental material balance law is the *equation of material motion* with its ingredients being the material pseudomomentum, the configurational volume force and the energy-momentum tensor. This purely material second order tensor is nowadays, to the honor of Eshelby, often denoted the *Eshelby (stress) tensor*. It was originally introduced by Eshelby himself, who used at first, ESHELBY [42], the notation *Maxwell tensor of elasticity* and later on, ESHELBY [43, 44], the term *energy-momentum tensor*, see also CHADWICK [30] and HILL [69] for additional aspects and applications.

Several approaches towards the theoretical description of configurational mechanics have been developed in the literature. The references quoted below display just a few selected publications among lots of interesting and expedient contributions available on this broad topic. Therefore it is worth mentioning that further literature will be referred to in the respective paragraphs of this work.

The notion of an *inverse motion* has been exploited by MAUGIN, e.g. [99, 103]. It relies on the parameterization of the reference coordinates in terms of their spatial counterparts and the time. The material balance appears as a projection of the usual equation of spatial motion onto the material manifold by means of premultiplication with the transpose of the deformation gradient.

Moreover, STEINMANN, e.g. [171, 172, 174], emphasized the duality between the *direct* and the *inverse motion problem*, cf. SHIELD [159], OGDEN [140] and ERICKSEN [41], and developed a sound formalism for the transition between the spatial and material settings. A *variational approach* is presented e.g. in KIENZLER & HERRMANN [76], whose considerations base on the application of Noether's theorem, NOETHER [139], cf. GUPTA [58] and LI & GUPTA [93] for further informations. The material field equations represent the Euler-Lagrange equations of a variational principle upon variation with respect to the reference coordinates. To be specific, Noether's reasoning implies the existence of conservation laws in terms of certain invariants conditions, see also the contributions of KNOWLES & STERNBERG [78], FLETCHER [46], GOLEBIEWSKA HERRMANN [52], OLVER [143, 144], LI [94] and BUGGISCH, GROSS & KRÜGER [25]. In fact, the treatments of the latter work base on the translational invariance of the energy equation and can be seen as the global counterpart of Eshelby's local procedure.

The probably most controversially discussed approach is due to GURTIN, e.g. [60, 61], who introduced the material balance equations as *independent balance laws*. This is in contrast to the afore-mentioned strategies which rely on a rearrangement of known spatial expressions. The crucial difference arises from the fact that the material balance is obtained based on invariance properties without invocation of a constitutive relation.

Irrespective of the conceptual approach, the configurational description does not pose a new physical problem at least in the continuous framework but induces an additional set of equations dual to those of the spatial setting and hence allows for a much deeper understanding of continuum mechanics.

The idea of forces in the material space resulting in the notion of configurational forces in the sense of driving forces acting on inhomogeneities and defects within the material setting has been elaborated e.g. by ROGULA [153], BATRA [12], MAUGIN & TRIMARCO [110], MAUGIN [99], DASCALU & MAUGIN [33], GURTIN [60] and STEINMANN [171].

A typical example is the Peach-Koehler force, i.e. the force on the singularity of an elastic distortion in crystals. The study of the movement of dislocations in crystals is related to the idea of local structural rearrangements, cf. EPSTEIN & MAUGIN [37, 38, 40, 39], EPSTEIN [36] and STEINMANN [173]. The thermodynamical dual of the structural changes is the Eshelby stress tensor while the translation of the dislocation associated with change in the energetic state of the system causes a material force acting on the singularity.

The concept of material forces is naturally linked to the investigation of path integrals and energy release rates in the context of fracture mechanics as discussed by GÜNTER [57], RICE [152], BUDIANSKY & RICE [24], GURTIN [59], GOLEBIEWSKA HERRMANN [53] and later on by MAUGIN & TRIMARCO [110] and GURTIN & PODIO-GUIDUGLI [62, 63].

The description of thermo-elastic effects is provided by EPSTEIN & MAUGIN [38], DASCALU & MAUGIN [34] and, using Gurtin's viewpoint, KALPAKIDES & DASCALU [74]. An extension to thermo-inelasticity is due to MAUGIN & BEREZOVSKI [108] including the fully dynamical framework and CLEJA-TIGOIU & MAUGIN [32]. In view of problems of (elasto-)plasticity MAUGIN [105, 106, 101] discussed the influence of the energy-momentum tensor and reported on the application to ductile fracture mechanics. A view on the configurational description of multiplicative elasto-plasticity is given in the recent contribution of MENZEL & STEINMANN [116] as well.

Further developments with regard to dynamical problems can be found in the works of MAUGIN [99, 100] or STEINMANN [172, 174] while MAUGIN [102] and GURTIN & SHVARTSMAN [64] study the application of configurational forces in dynamical fracture mechanics. In addition, KUHL & STEINMANN [85] worked out a variational arbitrary Lagrangian Eulerian (V-ALE) formulation of hyperelastodynamics.

Turning next to the impact of configurational forces in computational mechanics, the main areas of application are numerical fracture mechanics, structural optimization and adaptivity including both mesh optimization and refinement techniques.

The numerical treatment dates back to the seminal work of BRAUN [21] showing material forces induced by a finite element discretization. Later on, STEINMANN, ACKERMANN & BARTH [175], MÜLLER, KOLLING & GROSS [133] and MÜLLER & MAUGIN [134] developed various aspects of the algorithmic setting and the numerical implementation by means of the finite element method. Numerical examples are concerned with fracture mechanics, namely the numerical evaluation of the  $J$ -integral, mesh improvement in the sense of  $r$ -adaptivity and inclusion-matrix problems, see also GROSS, KOLLING, MÜLLER & SCHMIDT [56] and STEINMANN & MAUGIN [176] for a spectrum of applications.

Basically, the numerical approaches can be classified in two groups. The first one are variational ALE formulations. They base on the simultaneous variation of both the spatial and material coordinates and result in a simultaneous equilibration of Newtonian and Eshelbian forces. These method is mainly applied in the context of  $r$ -adaptive mesh improvement, e.g. KUHL, ASKES & STEINMANN [83], ASKES, KUHL & STEINMANN [8], THOUTIREDDY & ORTIZ [182] and MOSLER & ORTIZ [130, 131], with the latter one taking into account inelastic effects as well. The extension to structural optimization of truss structures is due to ASKES, BARGMANN, KUHL & STEINMANN [7] whereas ZIELONKA [191] suggests a variational ALE approach incorporating the application of variational time integrators in view of the simulation of dynamical problems.

The second concept exploits the discrete version of the material balance equation as a postprocessing procedure subsequent to a standard spatial computation. This attempt has actually been used within the afore-mentioned quotations. Based on this method-

ology, the thermo-elastic framework has been investigated by KUHL, DENZER, BARTH & STEINMANN [84] while the inelastic setting is studied e.g. by LIEBE, DENZER & STEINMANN [88], MENZEL, DENZER & STEINMANN [115] and NGUYEN, GOVINDJEE, KLEIN & GAO [138]. Material-force-based  $h$ -adaptive finite element strategies have been proposed by MÜLLER, GROSS & MAUGIN [132] in finite elasticity and MIEHE & ZIMMERMANN [127] in view of problems of finite deformation elasticity and inelasticity. Material-force-driven algorithms for the simulation of crack propagation can be found e.g. in the contributions of LARSSON & FAGERSTROEM [87], FAGERSTROEM & LARSSON [45] and HEINTZ [67] as well as in MIEHE & GÜRSES [123], MIEHE, GÜRSES & BIRKLE [124] and MIEHE & ZIMMERMANN [128] in combination with  $r$ - or  $h$ -adaptive strategies.

## 1.2. Overview and Outline

The first part of the thesis is mainly concerned with the theoretical formulation of configurational mechanics. One goal is the analysis of the configurational setting of solids that include dissipative effects, primarily the framework of thermo-inelasticity but also, as it will be shown later on in this work, crack propagation in elastic bodies. The second objective is the investigation of configurational solid dynamics. To be specific, two fundamental approaches are presented. While the second one turns out to be a true variational formulation, the first one proves to be close to a variational setting.

The investigations of **Chapter 3** are devoted to the configurational setting of non-isothermal inelasticity. The analyses focus on a general inelastic response of the solid and are based on energetic arguments. The key aspect is the formulation of the global dissipation postulate. Using this dissipation postulate, the spatial and material field equations are derived in the sense of a Coleman-type exploitation method. The remaining reduced dissipation inequality serves as the point of departure for the derivation of an evolution equation for the internal variable governing the inelastic response of the material. For the thermo-mechanically coupled problem under consideration, an evolution equation for the temperature field is developed starting from the balance of internal energy. Subsequent to the continuous framework, the discrete setting is elaborated. A staggered solution strategy is proposed with the material balance equation being used as a postprocessing tool. In view of the algorithmic treatment, particular emphasis is laid on the evaluation of discrete configurational nodal forces. Finally, the fundamental equations are specified with regard to the model problem of thermo-crystal-plasticity and a representative boundary value problem is solved in order to discuss the essential properties of the current formulation.

In **Chapter 4** the configurational framework of structural solid dynamics is outlined. The theoretical basis is provided by well-known Hamilton's principle. The necessary condition of this principle demands a vanishing first variation of the action functional. The variation is carried out with respect to the three primary variables, namely the spatial and material coordinates as well as the time. The Euler-Lagrange equations of the variational formulation represent the local formats of the balances of spatial linear momentum, material pseudomomentum and kinetic energy. The conceptual procedure used for the derivation of the local balance equations is shown to be close to the application of Noether's theorem, NOETHER [139]. The discrete setting once more incorporates the material balance law as a postprocessing procedure. The important effects are highlighted by means of the analysis of a descriptive boundary value problem.

Both procedures are characterized by the fact that they are governed by just one scalar



equation and thus, subjected to the condition that they are used in the sense of a principle, allow for a compact description of a broad class of mechanical problems.

In the second part of this work, three particular fields of the application of configurational mechanics or rather configurational forces are investigated in detail.

**Chapter 5** covers the use of configurational forces in the context of topology optimization. Attention is restricted to the framework of isothermal elasticity. The fundamental equations are obtained by a dual spatial-material variational formulation based on the principle of minimum potential energy. Both the continuous as well as the discrete setting are elaborated by means of the two theoretical approaches introduced in the previous chapters. Rather than using the material branch of the variational setting as a postprocessing tool, the dual problem is solved simultaneously for the unknown variables, namely the spatial and material coordinates. For the solution of this coupled problem, different solution strategies are presented. At first, the procedure is specified with regard to the optimization of finite element meshes corresponding to a  $r$ -adaptive refinement strategy. Secondly, the optimization of truss structures is analyzed. In this scenario, the optimization process appears as a methodology of structural optimization. Numerical examples are presented to demonstrate the capability of the optimization procedure.

**Chapter 6** sets up a configurational-force-based  $h$ -adaptive strategy. While in the continuous setting the dual spatial and material balance equations are entirely equivalent, i.e. in case the spatial balance is satisfied, the material balance is automatically fulfilled as well, in the discrete setting this equivalence is broken. This characteristic motivates the use of these out of balance equations, or rather out of balance nodal forces, as an indicator for the accuracy of the underlying discretization, in the present context the triangulation by means of a finite element mesh. A global criterion and a local refinement indicator are introduced with the first one governing the global decision on mesh refinement and the latter one controlling the local refinement process. The adaptive strategy is recast into a staggered solution scheme. In the first step the spatial problem is solved. Then, in a material postprocessing, the accuracy of the triangulation is estimated and, if necessary, the refinement process including the process of mesh generation and the mapping of the solution data is executed. The whole procedure is adjusted to the particular cases of finite elasticity and thermo-inelasticity and applied to representative boundary value problems in both two and three dimensions. Finally, the procedure is specified with regard to dynamical problems.

**Chapter 7** discusses a configurational-force-based procedure for the simulation of crack propagation in brittle materials. The theoretical framework bases on the global dissipation analysis adjusted to the framework of elastic fracture mechanics. Upon application of the Coleman-type exploitation method, the dissipation principle degenerates to the reduced dissipation inequality. Using the principle of maximum dissipation locally at the crack tip, the procedure results in a crack propagation law. Once again a staggered solution strategy is proposed. The material postprocessing bases on the separation of the geometry model and the finite element mesh. The configurational-force-driven crack propagation process is performed on the geometry model in the sense of a structural update. This scenario is accompanied by  $h$ -adaptive remeshing of the geometry ensuring an appropriate resolution of the crack tip zone. The capability of the method to capture arbitrary crack paths and even multiple cracks is demonstrated by means of a variety of numerical examples.





## 2. Fundamentals of Continuum Mechanics

Before starting with the main developments of this contribution, in this chapter a short survey of fundamental aspects of continuum mechanics is given. Furthermore the notation used throughout the thesis is introduced. Without claim of completeness, the author refers to the monographs of MALVERN [95], TRUESDELL & NOLL [185] and MARSDEN & HUGHES [98] for a detailed discussion of the topic. More recent publications on this issue are e.g. HOLZAPFEL [71], HAUPT [66] and BAŞAR & WEICHERT [11], among others. Subsequent to the description of the kinematics of a material body at finite deformations, the concept of stresses and heat flux is presented. Finally, some essential balance laws are considered being of major interest within the forthcoming sections.

### 2.1. Finite Kinematics

Kinematics deals with the purely geometrical description of the motion and the deformation of material bodies. To be specific, the kinematics of a body undergoing finite deformations is analyzed. The investigations conceptually rely on the terminology of modern differential geometry.

**2.1.1. Motion of a Material Body.** A material body  $B$  is a physical object consisting of specific physical properties such as texture, stiffness, etc. defining its material behavior.  $B$  is considered to be an open set of infinitely many material points  $P \in B$  which are in a one-to-one relationship to a subset of the Euclidean space  $\mathbb{E}^3$ . The placement of the material body within the  $\mathbb{E}^3$  is characterized by the map

$$\chi : \begin{cases} B \times \mathbb{R} \rightarrow \mathbb{E}^3 \\ (B, t) \mapsto \chi(B, t). \end{cases} \quad (2.1)$$

At frozen time  $t$  the map  $\chi_t$  uniquely maps a material point  $P$  onto a coordinate triple  $\mathbf{x} \in \mathbb{E}^3$  with respect to a global Cartesian frame  $\{\mathbf{E}_i\}_{i=1,2,3}$ . The images  $\mathbf{x} = \chi_t(B)$  of all material points  $P$  of the material body  $B$  define the actual configuration  $\mathcal{S}$  of  $B$  referred to as the current, spatial or Eulerian configuration. As visualized in Figure 2.1, the motion of

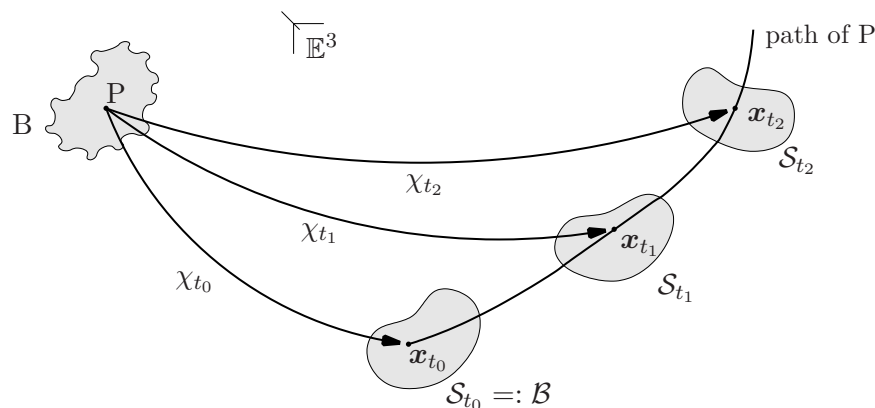


**Figure 2.1:** The placement of the material body  $B$  within the Euclidean space  $\mathbb{E}^3$  is governed by the map  $\chi$  defining the current configuration  $\mathcal{S}$ . The motion of the material body is described by a sequence of configurations. Typically, the motion is related to the reference configuration  $\mathcal{B}$  obtained from  $\chi_{t_0}$  at time  $t_0$ .

the material body is described by a sequence of configurations, while a particular material point  $P$  moves along a path of current placements  $\mathbf{x} = \chi_P(t)$  within the Euclidean space.

It is convenient to relate the motion of the material body to a specific configuration  $\mathcal{B}$  referred to as the reference, material or Lagrangian configuration. Following traditional continuum mechanics, the reference configuration is associated with the initial state at time  $t_0$

$$\chi_{t_0} : \begin{cases} \mathcal{B} \rightarrow \mathcal{B} \subset \mathbb{E}^3 \\ \mathcal{P} \mapsto \mathbf{X} = \chi_{t_0}(\mathcal{P}). \end{cases} \quad (2.2)$$

The reference configuration assumes the material body in a natural state without strains or stresses in the absence of physical forces. The placement of the material point  $\mathcal{P}$  is given by the Lagrangian coordinates  $\mathbf{X} \in \mathcal{B} \subset \mathbb{E}^3$  with respect to the global Cartesian frame  $\{\mathbf{E}_i\}_{i=1,2,3}$ . Based on the introduction of a reference configuration, a relative motion of material points is described by the non-linear point or deformation map

$$\varphi_t : \begin{cases} \mathcal{B} \rightarrow \mathcal{S} \\ \mathbf{X} \mapsto \mathbf{x} = \chi_t \circ \chi_{t_0}^{-1} = \varphi_t(\mathbf{X}). \end{cases} \quad (2.3)$$

In general,  $\varphi$  is parameterized in the Lagrangian space-time, i.e. the four-dimensional manifold of space-time events  $(\mathbf{X}, t)$ ,  $\varphi(\mathbf{X}, t)$ . The short cut  $\varphi_t(\mathbf{X})$  characterizes the representation of the general map  $\varphi(\mathbf{X}, t)$  for a specific time  $t$ .

**Remark 2.1:** Observe that in the present section the restriction to a fixed reference configuration  $\mathcal{B}$  with time-independent material coordinates  $\mathbf{X} = \text{const.}$  holds. This leads to a purely spatial description of the motion and deformation of the material body. Starting with the following section, this limitation is omitted and all the considerations are extended to a non-constant, time-dependent evolving reference configuration corresponding to a dual material or configurational description of the motion and deformation of the material body.

**2.1.2. Dual Bases and Metric Tensors.** In addition to the global Cartesian frame  $\{\mathbf{E}_i\}_{i=1,2,3}$  an arbitrary three-dimensional Eulerian basis  $\{\mathbf{g}_i\}_{i=1,2,3}$  is introduced. The vectors  $\mathbf{g}_i$  are linearly independent and in general not necessarily of unit length. Furthermore, a dual basis  $\{\mathbf{g}^i\}_{i=1,2,3}$  is defined. Both bases are linked via the property  $\mathbf{g}_i \cdot \mathbf{g}^j = \delta_i^j$ . Representing the Eulerian position  $\mathbf{x}$  in terms of curvilinear coordinates  $\theta^i$  which are oriented along material lines deforming with the body in the spatial configuration,  $\mathbf{x} = x^i(\theta^1, \theta^2, \theta^3)\mathbf{E}_i$ , the dual bases are obtained by

$$\mathbf{g}_i := \partial_{\theta^i} \mathbf{x} = \partial_{\theta^i} x^j(\theta^1, \theta^2, \theta^3)\mathbf{E}_j \quad \text{and} \quad \mathbf{g}^i := \partial_{\mathbf{x}} \theta^i = \partial_{x^j} \theta^i(x^1, x^2, x^3)\mathbf{E}^j. \quad (2.4)$$

The same ideas yield to dual Lagrangian bases  $\{\mathbf{G}_i\}_{i=1,2,3}$  and  $\{\mathbf{G}^i\}_{i=1,2,3}$ . A relation between the co- and contravariant bases is given by the metric coefficients. For instance, the covariant Eulerian metric coefficients  $g_{ij}$  decompose the covariant basis  $\{\mathbf{g}_i\}$  in the direction of the contravariant basis  $\{\mathbf{g}^i\}$  and vice versa

$$\mathbf{g}_i = g_{ij}\mathbf{g}^j \quad \text{and} \quad \mathbf{g}^i = g^{ij}\mathbf{g}_j. \quad (2.5)$$

The inner products of the co-/contravariant basis vectors yield the identities

$$\mathbf{g}_i \cdot \mathbf{g}_j = g_{ik}\mathbf{g}^k \cdot \mathbf{g}_j = g_{ik}\delta_j^k = g_{ij} \quad \text{and} \quad \mathbf{g}^i \cdot \mathbf{g}^j = g^{ik}\mathbf{g}_k \cdot \mathbf{g}^j = g^{ik}\delta_k^j = g^{ij}. \quad (2.6)$$

The associated metric tensors  $\mathbf{G} = G_{ij}\mathbf{G}^i \otimes \mathbf{G}^j$  and  $\mathbf{g} = g_{ij}\mathbf{g}^i \otimes \mathbf{g}^j$  of the Lagrangian and Eulerian configuration describe the mapping between the dual frames  $\{\mathbf{G}_i\}$ ,  $\{\mathbf{G}^i\}$

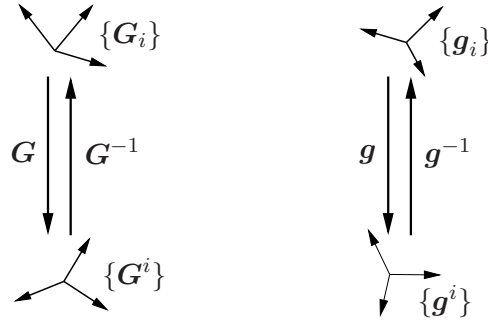


**Figure 2.2:** The Lagrangian metric  $\mathbf{G}$  governs the mapping between the covariant and the contravariant Lagrangian bases  $\mathbf{G}_i$  and  $\mathbf{G}^i$ , respectively. In the spatial configuration the map between co- and contravariant bases  $\mathbf{g}_i$  and  $\mathbf{g}^i$  is described by the Eulerian metric  $\mathbf{g}$ .

and  $\{\mathbf{g}_i\}$ ,  $\{\mathbf{g}^i\}$ , respectively, see Figure 2.2 for a visualization. The links between the Lagrangian covariant basis  $\{\mathbf{G}_i\}$  and its Eulerian counterpart  $\{\mathbf{g}_i\}$  and, in analogy, between the contravariant frames are given by

$$\mathbf{g}_i = \mathbf{F}\mathbf{G}_i \quad \text{and} \quad \mathbf{g}^i = \mathbf{F}^{-T}\mathbf{G}^i \quad (2.7)$$

in terms of the two-field tensor  $\mathbf{F}$ . This transformation tensor consists of the sum of dyadic products of corresponding basis vectors

$$\mathbf{F} = \mathbf{g}_i \otimes \mathbf{G}^i \quad \text{and} \quad \mathbf{F}^{-T} = \mathbf{g}^i \otimes \mathbf{G}_i. \quad (2.8)$$

Figure 2.3 deals with a sketch of the mapping property of the transformation tensor  $\mathbf{F}$ .

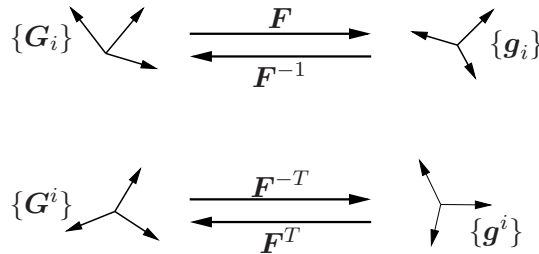


**Figure 2.3:** The transformation tensor  $\mathbf{F}$ , later on identified as the deformation gradient, maps the covariant Lagrangian basis vectors  $\mathbf{G}_i$  onto their Eulerian counterparts  $\mathbf{g}_i$ , whereas the transposed inverse of  $\mathbf{F}$  governs the mapping between the contravariant basis vectors.

**2.1.3. The Deformation Gradient.** The fundamental quantity in the kinematics of finite deformation is the deformation gradient  $\mathbf{F}$ . Recalling definition (2.3) of the non-linear point map  $\varphi_t$ , the deformation gradient is defined by the Fréchet derivative of  $\varphi_t$  with respect to the material coordinate  $\mathbf{X}$

$$\mathbf{F}(\mathbf{X}) := \nabla_{\mathbf{X}}\varphi_t(\mathbf{X}). \quad (2.9)$$

As it has been pointed out above,  $\varphi$  is in general a function of the Lagrangian space-time  $(\mathbf{X}, t)$ . Hence, definition (2.9) is to be understood as the partial derivative of the motion with respect to the *space*  $\mathbf{X}$ , i.e.  $\mathbf{F} = \partial\varphi(\mathbf{X}, t)/\partial\mathbf{X}$ . The deformation gradient  $\mathbf{F}$  is considered as a linear mapping of vectors, it maps tangent vectors  $\mathbf{T} \in \mathcal{B}$  to material curves onto tangent vectors  $\mathbf{t} \in \mathcal{S}$  to deformed spatial curves. Using the dual bases introduced

in the previous section, the covariant bases  $\{\mathbf{G}_i\}, \{\mathbf{g}_i\}$  span the tangent spaces  $T_X\mathcal{B}$  and  $T_x\mathcal{S}$  of the Lagrangian and Eulerian configuration. These three-dimensional vector spaces contain locally at one material point all tangent vectors to every material or spatial curve. Thus  $\mathbf{F}$  governs the following mapping procedure

$$\mathbf{F} : \begin{cases} T_X\mathcal{B} \rightarrow T_x\mathcal{S} \\ \mathbf{T} \mapsto \mathbf{t} = \mathbf{F}\mathbf{T}. \end{cases} \quad (2.10)$$

In this sense, definition (2.9) of the deformation gradient coincides with its definition (2.8) based on its property as the link between the covariant bases within the Lagrangian and Eulerian configuration. Note that in this representation the deformation gradient is written purely in terms of the basis vectors. Hence, the information about the deformation of the material body is exclusively carried within these basis vectors.

In the next step, a material area element is considered. It is defined by the vector product of two infinitesimal material line elements, i.e.  $d\mathbf{A} = d\mathbf{X} \times d\tilde{\mathbf{X}} = dA \mathbf{N}$  in terms of the Lagrangian normal or co-vector  $\mathbf{N}$ . Its Eulerian counterpart is obtained by Nanson's formula  $d\mathbf{a} = da \mathbf{n} = \text{cof}[\mathbf{F}] dA$  in terms of the cofactor  $\text{cof}[\mathbf{F}] := \det[\mathbf{F}]\mathbf{F}^{-T}$  of the deformation gradient. Neglecting the scalar quantities of the area map,  $\mathbf{F}^{-T}$  maps normals to material area elements onto normals to deformed spatial area elements. Recalling again the introduction of general bases, the contravariant bases  $\{\mathbf{G}^i\}, \{\mathbf{g}^i\}$  span the cotangent spaces  $T_X^*\mathcal{B}$  and  $T_x^*\mathcal{S}$  of the Lagrangian and Eulerian configuration. These cotangent spaces are three-dimensional vector spaces containing locally at one material point all normal vectors to every material or spatial area. In analogy to (2.10) the normal map can be written in the following manner

$$\mathbf{F}^{-T} : \begin{cases} T_X^*\mathcal{B} \rightarrow T_x^*\mathcal{S} \\ \mathbf{N} \mapsto \mathbf{n} = \mathbf{F}^{-T}\mathbf{N}. \end{cases} \quad (2.11)$$

Note that in the sense of the ideas outlined before, the tangent and cotangent spaces within one configuration (Lagrangian or Eulerian) are related by the respective metric tensor in the sense of a change of basis.

Finally, an infinitesimal material parallelepiped is spanned by three infinitesimal material line elements. The scalar material volume is given by  $dV = (d\mathbf{X} \times d\tilde{\mathbf{X}}) \cdot d\tilde{\tilde{\mathbf{X}}}$ . The Eulerian counterpart is obtained by multiplication with the Jacobian  $J$ , i.e. the determinant of the deformation gradient

$$J := \det[\mathbf{F}] : \begin{cases} \mathbb{R} \rightarrow \mathbb{R} \\ dV \mapsto dv = J dV. \end{cases} \quad (2.12)$$

The Jacobian  $J$  poses restrictions to the deformation gradient. To guarantee a one-to-one bijective relation between material and spatial position  $\mathbf{X}$  and  $\mathbf{x}$ ,  $J$  needs to be non-equal to zero. To preclude penetration of material,  $J$  has to be greater than zero.

The deformation gradient is the key ingredient for the kinematics of finite deformations as it describes the deformation state locally at every material point of the material body. In Figure 2.4 the key mappings between the covariant tangent spaces and the contravariant cotangent spaces at a material point in its reference position  $\mathbf{X}$  and its deformed spatial position  $\mathbf{x}$  are visualized.

The kinematics of finite deformation discussed so far is carried out in terms of general curvilinear coordinates. An alternative approach, used throughout this thesis, is

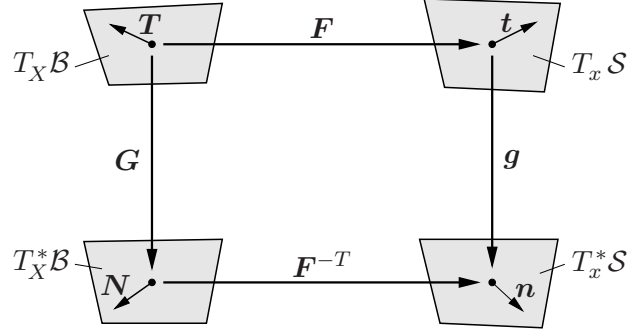


**Figure 2.4:** Fundamental mappings between the different vector spaces. The deformation gradient  $\mathbf{F}$  maps elements of the tangent spaces whereas the transposed inverse  $\mathbf{F}^{-T}$  acts between the cotangent spaces. The mapping between the tangent and cotangent spaces of one single configuration is described by the metric tensors.

to formulate the whole setting with respect to just one global Cartesian frame, i.e.  $\{\mathbf{G}_i\} = \{\mathbf{g}_i\} = \{\mathbf{E}_i\}$ . In order to avoid confusion, the differentiation between the Lagrangian and Eulerian tangent and cotangent spaces is retained. To do so, the different vector spaces are assumed to be spanned by the Cartesian frames  $\{\mathbf{E}_i\}$ ,  $\{\mathbf{E}^i\}$ ,  $\{\mathbf{e}_i\}$  and  $\{\mathbf{e}^i\}$  which coincide but are differentiated for the sake of clarity. The metric tensors boil down to the identity maps

$$\begin{aligned} \mathbf{G} &= \delta_{AB} \mathbf{E}^A \otimes \mathbf{E}^B & \text{and} & & \mathbf{g} &= \delta_{ab} \mathbf{e}^a \otimes \mathbf{e}^b \\ \mathbf{G}^{-1} &= \delta^{AB} \mathbf{E}_A \otimes \mathbf{E}_B & \text{and} & & \mathbf{G}^{-1} &= \delta^{ab} \mathbf{e}_a \otimes \mathbf{e}_b \end{aligned} \quad (2.13)$$

and thus do no longer contain any information about the current deformation state but are used as mappings between tangent and cotangent spaces. They can be interpreted as index lowering or raising procedures of co- and contravariant objects. The definition (2.9) of the deformation gradient still holds but its representation changes to

$$\mathbf{F} = F^a_A \mathbf{e}_a \otimes \mathbf{E}^A. \quad (2.14)$$

Again, the basis does no longer contain any information about the deformation but all these informations are stored in the mixed-variant coordinates  $F^a_A$ .

**2.1.4. Strain Tensors.** Consider a material direction  $\mathbf{T}$  with basepoint  $\mathbf{X}$  and property  $|\mathbf{T}|_{\mathbf{G}} = (\mathbf{T}\mathbf{G}\mathbf{T})^{\frac{1}{2}} = 1$ . The stretch vector  $\boldsymbol{\lambda}$  with respect to  $\mathbf{T}$  is defined by the directional derivative of the non-linear point map  $\varphi_t$ , i.e. the change of deformation in the direction  $\mathbf{T}$ , yielding the relation  $\boldsymbol{\lambda} = \mathbf{F}\mathbf{T}$ . Since  $\boldsymbol{\lambda}$  is an Eulerian object, its length is measured with respect to the current metric  $\mathbf{g}$ . The stretch itself is obtained by

$$\lambda = |\boldsymbol{\lambda}|_{\mathbf{g}} = (\boldsymbol{\lambda}\mathbf{g}\boldsymbol{\lambda})^{\frac{1}{2}} = (\mathbf{T}\mathbf{F}^T \mathbf{g} \mathbf{F}\mathbf{T})^{\frac{1}{2}} = (\mathbf{T}\mathbf{C}\mathbf{T})^{\frac{1}{2}} = |\mathbf{T}|_{\mathbf{C}}. \quad (2.15)$$

Here, the second order tensor  $\mathbf{C}$  denotes the right Cauchy Green tensor representing the Lagrangian representation of the Eulerian metric  $\mathbf{g}$ . Formally,  $\mathbf{C}$  is written as

$$\mathbf{C} = \varphi^*(\mathbf{g}) = \mathbf{F}^T \mathbf{g} \mathbf{F} \quad (2.16)$$

where  $\varphi^*(\bullet)$  represents the pull-back of the Eulerian object  $(\bullet)$ . In strict duality a push-forward operation  $\varphi_*[\bullet]$  is defined that characterizes the Eulerian representation of a Lagrangian object  $[\bullet]$ . In analogy to (2.16) the left Cauchy Green tensor is established

$$\mathbf{c} = \varphi_*(\mathbf{G}) = \mathbf{F}^{-T} \mathbf{g} \mathbf{F}^{-1} \quad (2.17)$$

being the Eulerian representation of the Lagrangian metric  $\mathbf{G}$ . Its inverse is referred to as the Finger tensor  $\mathbf{b} := \mathbf{c}^{-1} = \mathbf{F}\mathbf{G}^{-1}\mathbf{F}^T$ .

With the objective of measuring strains locally at a material point, the length of an infinitesimal line element is compared in both its reference as well as its current state

$$\delta := \frac{1}{2} [ |d\mathbf{x}|_g^2 - |d\mathbf{X}|_G^2 ] = d\mathbf{X}\mathbf{E} \cdot d\mathbf{X} = d\mathbf{x}\mathbf{e} \cdot d\mathbf{x}. \quad (2.18)$$

Apparently, this comparison can be carried out either in the Lagrangian or in the Eulerian setting. On the one hand the Lagrangian Green strain tensor  $\mathbf{E} = \frac{1}{2}[\mathbf{C} - \mathbf{G}]$  and on the other hand the Eulerian Almansi strain tensor  $\mathbf{e} = \frac{1}{2}[\mathbf{g} - \mathbf{c}]$  are obtained. In general, a strain tensor compares the reference and current metric tensors within one specific setting. This allows for the generalization of the just-mentioned strain tensors to a family of generalized strain measures, cf. TRUESDELL & TOUPIN [186],

$$\begin{aligned} \mathbf{E}_m &= \frac{1}{m} [\mathbf{C}^{\frac{m}{2}} - \mathbf{G}] & \text{and} & & \mathbf{e}_m &= \frac{1}{m} [\mathbf{g} - \mathbf{c}^{\frac{m}{2}}] & \text{for} & & m &\neq 0 \\ \mathbf{E}_0 &= \ln[\mathbf{C}] & \text{and} & & \mathbf{e}_0 &= \ln[\mathbf{c}] & \text{for} & & m &= 0. \end{aligned} \quad (2.19)$$

The Green and Almansi strain tensors are obtained for  $m = 2$  and the logarithmic strains  $m = 0$  are denoted Hencky strains. In general, strain tensors do not include any information about the rotational part of the deformation but only about stretches and changes of angles. This can be verified by considering the polar decomposition  $\mathbf{F} = \mathbf{R}\mathbf{U} = \mathbf{v}\mathbf{R}$  of the deformation gradient into a rotation tensor  $\mathbf{R}$  and a positive definite symmetric stretch tensor, i.e.  $\mathbf{U}$  referred to as the Lagrangian right stretch tensor or  $\mathbf{v}$  representing the Eulerian left stretch tensor. Inserting this decomposition into the right and left Cauchy Green tensors, one ends up with the relations  $\mathbf{C} = \mathbf{U}^{\frac{1}{2}}$  and  $\mathbf{c} = \mathbf{v}^{\frac{1}{2}}$ . By substitution of these results into definition (2.19) it is rather obvious that strain tensors do not include any information about rotation.

**2.1.5. Time Derivatives of Material and Spatial Objects.** Remember definition (2.3) of the non-linear deformation map. It was said to be in general a function of the Lagrangian space-time  $(\mathbf{X}, t)$ . The material velocity  $\mathbf{V}(\mathbf{X}, t)$  is the partial derivative of the motion with respect to the *time*  $t$  at fixed material positions.  $\mathbf{V}$  is the dual object to the deformation gradient  $\mathbf{F}$  representing the partial derivative of the motion with respect to the *space*  $\mathbf{X}$ , cf. (2.9). Observe that  $\mathbf{V}$  refers to the current configuration  $\mathcal{S}$  as it characterizes the temporal change of the motion of a material body but is parameterized in the Lagrangian space-time  $(\mathbf{X}, t)$ . By contraction with the inverse  $\varphi_t^{-1}$  of the non-linear point map, the velocity is re-parameterized by the current coordinates  $\mathbf{x}$  yielding the spatial velocity field  $\mathbf{v}(\mathbf{x}, t)$

$$\mathbf{V}(\mathbf{X}, t) = \frac{\partial}{\partial t} \varphi(\mathbf{X}, t) \quad \text{and} \quad \mathbf{v}(\mathbf{x}, t) = \frac{\partial}{\partial t} \varphi(\mathbf{X}, t) \circ \varphi_t^{-1}(\mathbf{x}). \quad (2.20)$$

In analogy to the Lagrangian space-time  $(\mathbf{X}, t)$ , the manifold of events  $(\mathbf{x}, t)$  is referred to as the Eulerian space-time. It is emphasized that the velocity fields  $\mathbf{V}$  and  $\mathbf{v}$  represent the same vectorial quantity and thus exhibit the same physical meaning as they both display the velocity of a material point in the current configuration. They are Eulerian spatial objects and just differ by their parameterization. With this argument at hand, it is supposed to be appropriate to apply solely the denotation  $\mathbf{v}$  for this spatial quantity irrespective of its parameterization.

The distinction between a time-independent reference configuration, assumed for the time being, and a non-constant time-dependent material configuration, to be adopted within the investigations to follow, demands a concise notation with regard to the time derivatives. The temporal change of an object  $(\bullet)$  at an arbitrary but fixed material position is given by its material or total time derivative  $d/dt(\bullet)$ . The total time derivative of a spatial field  $f(\mathbf{x}, t)$  parameterized by the Eulerian space-time consists of a local part  $\partial f/\partial t$  and, due to its dependence on the time-dependent spatial coordinate  $\mathbf{x}$ , a convective part  $\nabla_x f \cdot \mathbf{v}$  described by Leibniz' formula

$$\frac{d}{dt}f = \frac{\partial}{\partial t}f + \nabla_x f \cdot \mathbf{v} \quad (2.21)$$

In contrast, assuming a time-independent reference configuration  $\mathbf{X} = const.$ , the total time derivative of a material quantity  $F(\mathbf{X}, t)$  parameterized by the Lagrangian space-time equals its partial time derivative,  $dF/dt = \partial F/\partial t$ . However, focusing on non-constant material positions  $\mathbf{X} \neq const.$ , this equivalence does not hold anymore, i.e.  $dF/dt \neq \partial F/\partial t$  in general. Then, the total time derivative of a material object has to be evaluated by application of Leibniz' formula (2.21)

$$\mathbf{X} = const. : \frac{d}{dt}F = \frac{\partial}{\partial t}f \quad \text{but} \quad \mathbf{X} \neq const. : \frac{d}{dt}F = \frac{\partial}{\partial t}F + \nabla_x F \cdot \frac{\partial}{\partial t}\mathbf{X}. \quad (2.22)$$

Herein, the very last factor can be replaced by the total time derivative  $\partial \mathbf{X}/\partial t = d\mathbf{X}/dt$  as the material coordinates  $\mathbf{X}$  are a function of the time  $t$  at most. It is convenient to introduce the alternative notation  $\partial F/\partial t = dF/dt|_{X \text{ fixed}}$  for the partial time derivative indicating that the material coordinates are assumed to be time-independent.

The same reasoning applies in the context of time differentiation of integral expressions. To this end, consider the time derivative of an integral of an Eulerian object integrated over the time-dependent current configuration  $\mathcal{S}$ , or a part  $\mathcal{P}_S$  of  $\mathcal{S}$ . As the integration limit is time-dependent, differentiation and integration do not commute but product rule has to be employed

$$\frac{d}{dt} \int_{\mathcal{P}_S} f(\mathbf{x}, t) dv = \int_{\mathcal{P}_S} \frac{d}{dt}f dv + \int_{\mathcal{P}_S} f \frac{d}{dt}dv = \int_{\mathcal{P}_S} \frac{\partial}{\partial t}f + f \operatorname{div} \mathbf{v} dv. \quad (2.23)$$

Observe that the time derivative of  $dv$  has been evaluated according to  $d(dv)/dt = dJ/dt dV = \operatorname{div} \mathbf{v} J dV = \operatorname{div} \mathbf{v} dv = (\mathbf{1} : \nabla_x \mathbf{v})dv$ . For the total time derivative of  $f$  Leibniz' formula (2.21) is adopted. Then, by application of integration by parts (2.23) can be transformed to the essential relation, often denoted Reynolds' transport theorem

$$\frac{d}{dt} \int_{\mathcal{P}_S} f(\mathbf{x}, t) dv = \int_{\mathcal{P}_S} \frac{\partial}{\partial t}f + \operatorname{div} [f\mathbf{v}] dv = \int_{\mathcal{P}_S} \frac{\partial}{\partial t}f dv + \int_{\partial \mathcal{P}_S} f \mathbf{v} \cdot \mathbf{n} da. \quad (2.24)$$

Assuming a time-independent reference configuration, time differentiation and integration do commute. Since the analyses of the upcoming chapters into account changes of the reference configuration, (2.23) has to be used for the time derivative of an integral over the reference configuration  $\mathcal{B}$  as well. Observe that all the relationships provided in this subsection also apply to vector- and tensor-valued quantities  $\mathbf{F}(\mathbf{X}, t)$  and  $\mathbf{f}(\mathbf{x}, t)$ .

**Remark 2.2:** For the sake of abbreviation the notation  $(\dot{\bullet}) = d(\bullet)/dt$  is employed for the total time derivative of an object  $(\bullet)$ . Currently, this does not pose any inconveniences



as no differentiation between total and partial time derivative of a time-independent Lagrangian object is necessary. With regard to the formulations to follow a strict distinction will be crucial. To avoid confusion later on, in some essential equations of this paragraph the exact representation of the time derivative is displayed.

**2.1.6. Velocity Gradients and Lie-Derivative.** Consider the spatial stretch vector  $\boldsymbol{\lambda} = \mathbf{F}\mathbf{T}$  introduced above. Its material time derivative reads  $\dot{\boldsymbol{\lambda}} = \dot{\mathbf{F}}\mathbf{T}$  governed by the material velocity gradient

$$\mathbf{L} := \dot{\mathbf{F}} = \left. \frac{d}{dt} \right|_{X \text{ fixed}} \nabla_X \varphi(\mathbf{X}, t), \quad (2.25)$$

reflecting the total time derivative of the deformation gradient for a time-independent reference configuration  $\mathbf{X} = \text{const.}$  On the other hand, the temporal change of  $\boldsymbol{\lambda}$  in terms of the current direction  $\boldsymbol{\lambda}$  itself reads  $\dot{\boldsymbol{\lambda}} = (\dot{\mathbf{F}}\mathbf{F}^{-1})\boldsymbol{\lambda} =: \mathbf{l}\boldsymbol{\lambda}$ . The spatial velocity gradient

$$\mathbf{l} := \dot{\mathbf{F}}\mathbf{F}^{-1} = \nabla_x \mathbf{v}(\mathbf{x}, t) \quad (2.26)$$

characterizes a relative time derivative in the sense that  $\mathbf{l}$  describes the relative change of a spatial object with respect to its current state in the Eulerian configuration.

The Lie-derivative is the relative time derivative of a spatial object. It describes the temporal change of the spatial object keeping the basis vectors fixed. In other words, the Lie-derivative is associated with that part of the total time derivative observed by an observer sitting in the moving frame of the current configuration. Considering a spatial object  $(\bullet)$ , the Lie-derivative is defined by

$$\mathcal{L}_v(\bullet) := \varphi_* \left[ \left. \frac{d}{dt} \right|_{X \text{ fixed}} \{ \varphi^*(\bullet) \} \right] \quad (2.27)$$

and thus evaluated in three steps. First, the Eulerian object is pulled back to the time-independent reference configuration. The material time derivative of the Lagrangian object is computed whereupon the resulting quantity is pushed forward to the spatial configuration. In particular, the Lie-derivative  $\mathcal{L}_v \mathbf{g}$  of the current metric  $\mathbf{g}$  coincides with the spatial rate of deformation tensor  $\mathbf{d}$ , i.e. the symmetric part of the spatial velocity gradient,

$$\mathcal{L}_v \mathbf{g} = \mathbf{l}^T \mathbf{g} + \mathbf{g} \mathbf{l} = 2 \text{sym}[\mathbf{g} \mathbf{l}] = 2\mathbf{d}. \quad (2.28)$$

Recalling the duality between the current metric  $\mathbf{g}$  and its material representation  $\mathbf{C}$ , i.e. the right Cauchy Green tensor, the material rate of deformation tensor  $\mathbf{D} := \frac{1}{2} \dot{\mathbf{C}}$  corresponds to the Lie-derivative of  $\mathbf{g}$  in the sense of dual Lagrangian-Eulerian objects linked via pull-back and push-forward transformations.

## 2.2. Concept of Stresses and Heat Flux

Consider a material body in its deformed configuration  $\mathcal{S}$ . With the objective of introducing the notion of stresses and heat flux an arbitrary part  $\mathcal{P}_{\mathcal{S}}$  is cut out of the material body, see Figure 2.5. Following the methodology of Euler's cut principle, the effects of the cut-off part onto  $\mathcal{P}_{\mathcal{S}}$  are replaced by phenomenological quantities, namely the surface traction  $\mathbf{t}$  and the heat flux  $\bar{q}_n$  governing mechanical and thermal effects, respectively.



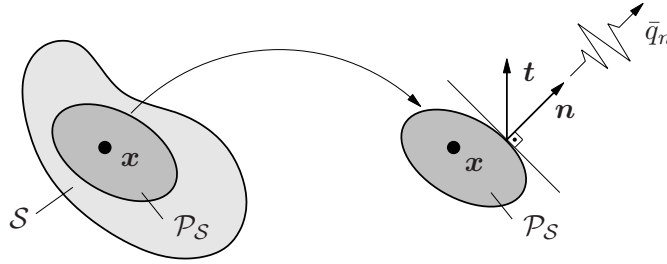


**Figure 2.5:** Application of Euler's cut principle. An arbitrary part  $\mathcal{P}_S$  is cut out of the deformed material body. The effects of the cut-off part are replaced by the surface tractions  $\mathbf{t}$  and the heat flux  $\bar{q}_n$ .

**2.2.1. Traction Vector. Stress Tensors.** The surface traction  $\mathbf{t}$  is obtained by taking the limit of the ratio of the resultant force  $d\mathbf{f}$  acting on an infinitesimal area element  $da$  of the cut-surface and the area element itself. According to Cauchy's theorem, the surface traction  $\mathbf{t}$  at a point  $\mathbf{x}$  of the cut-surface is a linear function of the normal  $\mathbf{n}$  characterizing the orientation of the cut-surface at that point

$$\mathbf{t}(\mathbf{x}, t, \mathbf{n}) = \boldsymbol{\sigma}(\mathbf{x}, t)\mathbf{n}. \quad (2.29)$$

The Cauchy stress tensor  $\boldsymbol{\sigma}$  relates the actual force acting on the cut-surface to the deformed area element. For this reason the Cauchy stresses are also denoted true stresses. Following the viewpoint of differential geometry, the surface traction  $\mathbf{t}$  is an element of the tangent space  $T_x\mathcal{S}$  of the current configuration whereas the normal  $\mathbf{n}$  is an element of the respective cotangent space  $T_x^*\mathcal{S}$ . Hence, the Cauchy stress tensor is a covariant Eulerian object and describes a mapping between the two vector spaces via

$$\boldsymbol{\sigma} : \begin{cases} T_x^*\mathcal{S} \rightarrow T_x\mathcal{S} \\ \mathbf{n} \mapsto \mathbf{t} = \boldsymbol{\sigma}\mathbf{n}. \end{cases} \quad (2.30)$$

Multiplication of the Cauchy stresses  $\boldsymbol{\sigma}$  with the determinant  $J$  of the deformation gradient defines the weighted Cauchy or Kirchhoff stress tensor  $\boldsymbol{\tau} = J\boldsymbol{\sigma}$ .

Relating now the resultant force  $d\mathbf{f}$  acting on the cut-surface to an area element of the undeformed Lagrangian surface, the limit results in the so-called nominal surface traction vector  $\tilde{\mathbf{t}}$  being still an element of the Eulerian tangent space  $T_x\mathcal{S}$ . In analogy to (2.29) a linear relation between the nominal traction and the Lagrangian normal  $\mathbf{N}$  is assumed via the Cauchy-type relation

$$\tilde{\mathbf{t}} = \mathbf{P}\mathbf{N}. \quad (2.31)$$

The nominal or first Piola-Kirchhoff stress tensor  $\mathbf{P}$  is a mixedvariant two-field tensor and is interpreted as a mapping between the cotangent space  $T_X^*\mathcal{B}$  of the reference configuration and the tangent space  $T_x\mathcal{S}$  of the current configuration

$$\mathbf{P} : \begin{cases} T_X^*\mathcal{B} \rightarrow T_x\mathcal{S} \\ \mathbf{N} \mapsto \tilde{\mathbf{t}} = \mathbf{P}\mathbf{N}. \end{cases} \quad (2.32)$$

The resultant force acting on the cut-surface can be written in terms of the undeformed or the deformed area element yielding the identity  $d\mathbf{f} = \mathbf{t}da = \tilde{\mathbf{t}}dA$ . Recalling Nanson's formula introduced in the context of the deformation of area elements, i.e.  $da\mathbf{n} = \text{cof}[\mathbf{F}]dA\mathbf{N}$ , the link between the true and nominal stresses is given by

$$\mathbf{P} = J\boldsymbol{\sigma}\mathbf{F}^{-T} = \boldsymbol{\tau}\mathbf{F}^{-T}. \quad (2.33)$$

Finally, the second Piola-Kirchhoff stresses  $\mathbf{S}$  are introduced.  $\mathbf{S}$  is the purely Lagrangian covariant counterpart of the Eulerian Kirchhoff stresses  $\boldsymbol{\tau}$ . It can be seen as a mapping between the cotangent space  $T_X^*\mathcal{B}$  and the tangent space  $T_X\mathcal{B}$  of the reference configuration and is defined by the pull-back operation

$$\mathbf{S} := \mathbf{F}^{-1}\boldsymbol{\tau}\mathbf{F}^{-T}. \quad (2.34)$$

Figure 2.6 summarizes the mapping properties of the alternative stress measures. Note

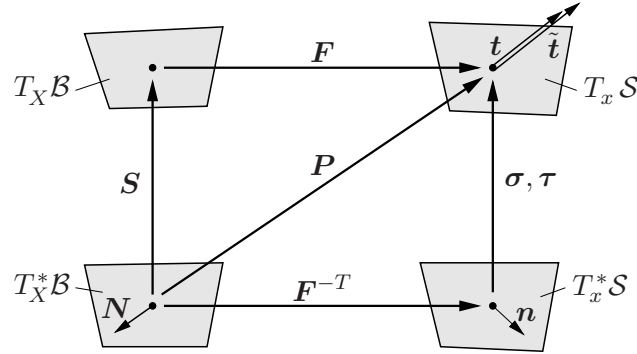


**Figure 2.6:** The alternative stress measures are interpreted as mappings between the respective vector spaces. The second Piola-Kirchhoff stresses  $\mathbf{S}$  and the Kirchhoff stresses  $\boldsymbol{\tau}$  are purely contravariant Lagrangian and Eulerian objects, respectively. The first Piola-Kirchhoff stress tensor  $\mathbf{P}$  is a mixedvariant two-field tensor.

that the Lagrangian stress tensor is a purely geometric object and not equipped with any physical meaning. In particular, no Cauchy type theorem in the sense of (2.29) and (2.31) exists in the Lagrangian setting because the reference configuration is assumed to be stress-free and no Lagrangian surface traction does exist a priori whereas the surface tractions  $\mathbf{t}$  and  $\tilde{\mathbf{t}}$  are Eulerian objects.

**2.2.2. Heat Flux. Heat Flux Vector.** The thermal effects of the cut-off part onto the remaining part  $\mathcal{P}_S$  are described by the scalar heat flux  $\bar{q}_n$ . This field characterizes the heat flux through the cut-surface in the direction of the outer normal  $\mathbf{n}$ , see Figure 2.5. It is a function of the normal vector  $\mathbf{n}$ , the current position  $\mathbf{x}$  and time  $t$ . In analogy to Cauchy's theorem (2.29) for the stresses, a linear dependence of the heat flux on the normal is assumed via Stoke's heat flux theorem

$$\bar{q}_n(\mathbf{x}, t, \mathbf{n}) = \mathbf{q}(\mathbf{x}, t) \cdot \mathbf{n} \quad (2.35)$$

where  $\mathbf{q}$  denotes the true or Cauchy heat flux vector defined per unit deformed area. Based on the demand  $\mathbf{q} \cdot \mathbf{n} da = \mathbf{Q} \cdot \mathbf{N} dA$ , i.e. relating the heat flux vector to the undeformed area, the Lagrangian counterpart of  $\mathbf{q}$  is introduced. Application of Nanson's formula for the relation between undeformed and deformed area elements results in the identity

$$\mathbf{Q} = J\mathbf{F}^{-1}\mathbf{q}. \quad (2.36)$$

The material object  $\mathbf{Q}$  is referred to as the Lagrangian or nominal heat flux vector.

**2.2.3. Stress Power and Material Work of Deformation.** Based on the kinematic objects and the stress measures defined in the previous sections, the stress power  $\hat{\mathcal{P}}$  with

respect to unit volume of the undeformed configuration can be expressed in three different alternative representations

$$\hat{\mathcal{P}} := \tilde{\mathbf{P}} : \dot{\mathbf{F}} = \mathbf{S} : \frac{1}{2} \dot{\mathbf{C}} = \boldsymbol{\tau} : \frac{1}{2} \mathcal{L}_v \mathbf{g}, \quad (2.37)$$

i.e. the two-field, the Lagrangian, and the Eulerian formulation in terms of the dual kinematic/kinetic objects  $(\mathbf{F}, \tilde{\mathbf{P}})$ ,  $(\mathbf{C}, \mathbf{S})$ , and  $(\mathbf{g}, \boldsymbol{\tau})$ . Based on this definition, the total work  $W$  needed for the deformation of an (in)elastic continuum can be computed for applied essential boundary conditions via

$$W = \int_{\mathcal{B}} w \, dV \quad \text{with} \quad w = \int_0^t \mathcal{P} \, d\tau \quad (2.38)$$

where  $w$  is denoted the specific work at every point  $\mathbf{X} \in \mathcal{B}$  of the reference configuration.

**Remark 2.3:** According to (2.32), the first Piola-Kirchhoff stress tensor  $\mathbf{P} = P^{aA}$  is a contravariant two-field tensor mapping normals  $\mathbf{N}$ , i.e. Lagrangian covariant objects  $N_A$ , onto tractions  $\tilde{\mathbf{t}}$ , i.e. Eulerian contravariant vectors  $\tilde{t}^a$ . For the stress power an alternative mixedvariant representation  $\tilde{\mathbf{P}} = \tilde{P}_a^A$  of the nominal stresses is used dual to the deformation gradient  $\mathbf{F} = F^a_A$ . Both versions are linked via the current metric,  $\tilde{\mathbf{P}} = \mathbf{g}\mathbf{P}$  or  $\tilde{P}_a^A = g_{ab}P^{bA}$ . Within this thesis, the description is related to one single Cartesian frame and the metric tensors coincide with the identity maps, cf. (2.13). Consequently, it appears to be appropriate to renounce the distinction between both representations.

### 2.3. Physical Balance Principles

In this section the classical balance principles of continuum mechanics are discussed. These balance laws describe the change of a particular physical quantity, such as mass, momentum and energy, with respect to thermo-mechanical loading of the material body. The principles are valid in all branches of continuum mechanics. They are applicable to any material and must be satisfied for all times. At first, the integral representations valid for any arbitrary part  $\mathcal{P}_S$  cut out of the material body are formulated. Upon application of Gauss integration theorem and the localization theorem, these global statements are transformed into local counterparts valid at every single point  $\mathbf{x} \in \mathcal{P}_S$  of the cut-out part.

**2.3.1. Balance of Mass.** The subsequent considerations are restricted to closed systems without mass transport through the boundary and without mass production inside the material body. Assuming this, the mass of a cut-out part is defined in terms of the material density  $\rho_0 = dm/dV$  and the spatial density  $\rho = dm/dv$ . The balance of mass states that the mass  $m_{\mathcal{P}_S}$  of an arbitrarily cut-out part of the body remains constant

$$\frac{d}{dt} m_{\mathcal{P}_S} = 0 \quad \Rightarrow \quad m_{\mathcal{P}_S} = \int_{\mathcal{P}_S} \rho \, dv = \int_{\mathcal{P}_B} \rho_0 \, dV = M_{\mathcal{P}_B}. \quad (2.39)$$

Starting from this global format, its local counterparts can be derived by application of the localization theorem and substitution of the rate expression  $dJ/dt = J \operatorname{div} \mathbf{v}$

$$\rho_0 - J\rho = 0 \quad \text{and} \quad \frac{d}{dt} \rho + \rho \operatorname{div} \mathbf{v} = 0. \quad (2.40)$$

The first statement is the Lagrangian version, valid for all material positions  $\mathbf{X} \in \mathcal{P}_B$ , and the second one refers to the Eulerian configuration and thus holds for all spatial

positions  $\mathbf{x} \in \mathcal{P}_B$ . Obviously, the current density depends on the Eulerian space-time,  $\rho(\mathbf{x}, t)$ , whereas the reference density  $\rho_0(\mathbf{X})$  is a function of the material coordinates  $\mathbf{X}$  at most. That is why the partial derivatives of the material density with respect to the Lagrangian space-time event  $(\mathbf{X}, t)$  read

$$\frac{\partial}{\partial t}\rho_0 = \frac{d}{dt}\Big|_{X \text{ fixed}}\rho_0 = 0 \quad \text{but} \quad \frac{\partial}{\partial \mathbf{X}}\rho_0 = \nabla_X \rho_0 \neq \mathbf{0}. \quad (2.41)$$

The second equation accounts for possible inhomogeneities inside the material body. For homogeneous material bodies it becomes  $\nabla_X \rho_0 = \mathbf{0}$ . Note that in case the partial time derivative of the reference density does not vanish but  $\rho_0$  evolves in time by addition or subtraction of matter, the theory captures the phenomena of growth or resorption.

With relationship (2.40)<sub>2</sub> for the Eulerian density at hand, an enhanced version of a vectorial representation of Reynolds' transport theorem (2.24) can be written as

$$\frac{d}{dt} \int_{\mathcal{P}_S} \rho(\mathbf{x}, t) \mathbf{f}(\mathbf{x}, t) dv = \int_{\mathcal{P}_S} \rho \frac{d}{dt} \mathbf{f} dv. \quad (2.42)$$

**2.3.2. Balance of Linear Momentum.** The linear momentum of a part  $\mathcal{P}_S$  of the material body is defined by

$$\mathbf{I}_{\mathcal{P}_S} = \int_{\mathcal{P}_S} \mathbf{v} dm = \int_{\mathcal{P}_S} \rho \mathbf{v} dv = \int_{\mathcal{P}_S} \mathbf{i} dv \quad (2.43)$$

based on the physical linear momentum  $\mathbf{i}(\mathbf{x}, t) = \rho \mathbf{v}$  per unit volume of the current configuration. Obviously, the linear momentum can alternatively be formulated in the reference setting simply by insertion of the volume map (2.12) and the local Lagrangian version of the balance of mass (2.40)<sub>1</sub>. This induces the definition of the material representation of the physical linear momentum  $\mathbf{I} = \rho_0 \mathbf{v}$  per unit volume of the reference configuration. The balance of linear momentum states that the temporal change of the linear momentum of a cut-out part  $\mathcal{P}_S$  of the body equals the resultant forces acting on this part

$$\frac{d}{dt} \mathbf{I}_{\mathcal{P}_S} = \mathbf{F}_{\mathcal{P}_S} = \int_{\mathcal{P}_S} \bar{\boldsymbol{\gamma}} dv + \int_{\partial \mathcal{P}_{S_t}} \bar{\mathbf{t}} da. \quad (2.44)$$

The resultant physical forces consist of a surface part in terms of the surface traction  $\bar{\mathbf{t}}$  and a volume contribution governed by the spatial volume force  $\bar{\boldsymbol{\gamma}}$  defined by the product of the Eulerian density and a spatial acceleration field,  $\bar{\boldsymbol{\gamma}} = \rho \mathbf{b}$ . On account of (2.42) and by application of Cauchy's theorem (2.29) as well as Gauss integration theorem this global form can be transferred into the local expressions

$$\text{Div} \mathbf{P} + \bar{\boldsymbol{\gamma}}_0 = \rho_0 \frac{\partial}{\partial t} \mathbf{v} \quad \text{and} \quad \text{div} \boldsymbol{\sigma} + \bar{\boldsymbol{\gamma}} = \rho \frac{d}{dt} \mathbf{v}. \quad (2.45)$$

These local balance equations have to be satisfied at every single point of the cut-out part of the body and again are alternatively formulated with respect to the Lagrangian and Eulerian configuration. For the Lagrangian statement, the physical volume force with respect to unit volume of the reference configuration,  $\bar{\boldsymbol{\gamma}}_0 = \rho_0 \mathbf{b}$ , has been introduced.

**Remark 2.4:** Recalling the arguments provided in Section 2.1.5, the two-point formulation (2.45)<sub>1</sub> appears in the alternative format  $\text{Div} \mathbf{P} + \bar{\boldsymbol{\gamma}}_0 = \rho_0 d\mathbf{v}/dt|_{X \text{ fixed}}$  indicating that the time derivative of  $\mathbf{v}$  has to be evaluated at fixed material positions. The use of  $\mathbf{V}$  instead of  $\mathbf{v}$  would signify its parameterization by the Lagrangian space-time.

**2.3.3. Balance of Angular Momentum.** The angular momentum of a part  $\mathcal{P}_S$  of the material body with respect to the origin  $o$  of the basis is defined by

$$\mathbf{D}_{\mathcal{P}_S}^o = \int_{\mathcal{P}_S} \mathbf{x} \times \mathbf{v} \, dm = \int_{\mathcal{P}_S} \mathbf{x} \times \rho \mathbf{v} \, dv = \int_{\mathcal{P}_S} \mathbf{x} \times \mathbf{i} \, dv. \quad (2.46)$$

The balance of angular momentum states that the temporal change of the angular momentum of a cut-out part of the body equals the resultant moment acting on this part

$$\frac{d}{dt} \mathbf{D}_{\mathcal{P}_S}^o = \mathbf{M}_{\mathcal{P}_S} = \int_{\mathcal{P}_S} \mathbf{x} \times \bar{\boldsymbol{\gamma}} \, dv + \int_{\partial \mathcal{P}_{S_t}} \mathbf{x} \times \bar{\mathbf{t}} \, da. \quad (2.47)$$

The resultant physical momentum  $\mathbf{M}_{\mathcal{P}_S}$  adopted in this equation does not introduce any new physical quantities as an intrinsic spin or externally applied torques but just uses the same entities compared to the linear momentum, i.e. the physical forces consisting of volume and surface contributions  $\bar{\boldsymbol{\gamma}}$  and  $\bar{\mathbf{t}}$ . Based on the global statement (2.47) material and spatial local formats can be developed demanding the symmetry of the purely Lagrangian and Eulerian stress tensors

$$\mathbf{S} = \mathbf{S}^T \quad \text{and} \quad \boldsymbol{\sigma} = \boldsymbol{\sigma}^T. \quad (2.48)$$

The latter identity also applies to the Kirchhoff stresses  $\boldsymbol{\tau} = \boldsymbol{\tau}^T$  whereas the first Piola-Kirchhoff stress tensor  $\mathbf{P}$  is a non-symmetric tensor.

**2.3.4. Balance of Energy. First Axiom of Thermodynamics.** The energy  $E$  of a part  $\mathcal{P}_S$  of the material body is defined in terms of the specific energy  $e$  per unit mass and can be split up into a kinetic part  $K$  and an internal contribution  $U$  according to

$$E = \int_{\mathcal{P}_S} \rho e \, dv = \int_{\mathcal{P}_S} \frac{1}{2} \rho \mathbf{v} \cdot \mathbf{v} \, dv + \int_{\mathcal{P}_S} \rho u \, dv = K + U \quad (2.49)$$

with the specific internal energy  $u$  per unit mass. Focusing on thermo-mechanical investigations, the balance of energy states that the temporal change of the energy of a cut-out part  $\mathcal{P}_S$  of the body equals the sum of external mechanical and thermal power  $\mathcal{P}$  and  $\mathcal{Q}$

$$\frac{d}{dt} (K + U) = \mathcal{P} + \mathcal{Q} = \int_{\mathcal{P}_S} \mathbf{v} \cdot \bar{\boldsymbol{\gamma}} \, dv + \int_{\partial \mathcal{P}_{S_t}} \mathbf{v} \cdot \bar{\mathbf{t}} \, da + \int_{\mathcal{P}_S} \rho r \, dv + \int_{\partial \mathcal{P}_{S_h}} -\bar{q}_n \, da. \quad (2.50)$$

This balance equation is known as the first axiom of thermodynamics. The external mechanical power is governed by physical volume and surface forces whereas the thermal power consists of a volume part in terms of the heat supply  $r$  and a surface term based on the heat flux  $\bar{q}_n = \mathbf{q} \cdot \mathbf{n}$  with the spatial heat flux vector  $\mathbf{q}$ . The local counterparts of this global balance read in their Lagrangian and Eulerian representations

$$\rho_0 \frac{\partial}{\partial t} e = \text{Div} [\mathbf{v} \cdot \mathbf{P} - \mathbf{Q}] + \mathbf{v} \cdot \bar{\boldsymbol{\gamma}}_0 + \rho_0 r \quad \text{and} \quad \rho \frac{d}{dt} e = \text{div} [\mathbf{v} \cdot \boldsymbol{\sigma} - \mathbf{q}] + \mathbf{v} \cdot \bar{\boldsymbol{\gamma}} + \rho r \quad (2.51)$$

defined per unit mass of the reference or current configuration and the relation  $\partial e / \partial t = de / dt|_{X \text{ fixed}}$  being obvious.

The balance of kinetic energy is equivalent to the balance of linear momentum. In a purely mechanical context it is not an additional requirement to be satisfied but it is a consequence of the linear momentum balance. To exploit this fact in the thermo-mechanical

framework, the local spatial form of linear momentum (2.45)<sub>2</sub> is multiplied by the velocity  $\mathbf{v}$  and integrated over the cut-out volume. Some straightforward manipulations result in

$$\int_{\mathcal{P}_S} \rho \mathbf{v} \cdot \frac{d}{dt} \mathbf{v} \, dv = \int_{\mathcal{P}_S} \mathbf{v} \cdot \bar{\boldsymbol{\gamma}} \, dv + \int_{\partial \mathcal{P}_{S_t}} \mathbf{v} \cdot \bar{\mathbf{t}} \, dv - \int_{\mathcal{P}_S} \boldsymbol{\sigma} : \mathbf{g} \nabla_x \mathbf{v} \, dv. \quad (2.52)$$

The left hand side displays the time derivative  $dK/dt$  of the kinetic energy. The right hand side is governed by the mechanical power  $\mathcal{P}$  and a part in terms of the covariant spatial velocity gradient  $\mathbf{g} \nabla_x \mathbf{v} = \mathbf{gl}$ . Due to symmetry of the Cauchy stresses, its symmetric part arises, namely the rate of deformation tensor,  $\mathbf{d} = \frac{1}{2} [\mathbf{gl} + \mathbf{l}^T \mathbf{g}]$ , cf. (2.28). Recalling definition (2.37), the last term of (2.52) represents the global stress power recognizing that the integration over the current volume is achieved by means of the identities  $\boldsymbol{\sigma} = \boldsymbol{\tau}/J$  and  $dv = JdV$ . Finally, the global form of the balance of kinetic energy reads

$$\frac{d}{dt} K = \mathcal{P} - S \quad \text{with} \quad S := \int_{\mathcal{P}_S} \boldsymbol{\sigma} : \mathbf{d} \, dv. \quad (2.53)$$

Substitution into the balance of total energy (2.50) renders the balance of internal energy

$$\frac{d}{dt} U = Q + S. \quad (2.54)$$

again including the production term  $S$ . The localization procedure leads to

$$\rho_0 \frac{\partial}{\partial t} u = \rho_0 r - \text{Div} \mathbf{Q} + \tilde{\mathbf{P}} : \dot{\mathbf{F}} \quad \text{and} \quad \rho \frac{d}{dt} u = \rho r - \text{div} \mathbf{q} + \boldsymbol{\sigma} : \mathbf{d} \quad (2.55)$$

representing the local Lagrangian and Eulerian formats of the internal energy balance.

**2.3.5. Balance of Entropy. Second Axiom of Thermodynamics.** Entropy is one of the fundamental state variables of thermodynamics. It is regarded as a measure of disorder and randomness and governs the direction of a thermodynamical process. The entropy  $H$  is defined in terms of the specific entropy  $\eta$  per unit mass. The rate of entropy input  $Q$  bases on the entropy sources  $\tilde{r}$  and the Cauchy entropy flux  $\tilde{\mathbf{q}}$  defined per unit time and per unit mass and area of the current configuration. Typically, the entropy sources  $\tilde{r} = r/\theta$  and the entropy flux  $\tilde{\mathbf{q}} = \mathbf{q}/\theta$  are related to the heat source  $r$  and the heat flux vector  $\mathbf{q}$  via the absolute temperature  $\theta$

$$H = \int_{\mathcal{P}_S} \rho \eta \, dv, \quad Q = \int_{\mathcal{P}_S} \rho \frac{r}{\theta} \, dv - \int_{\partial \mathcal{P}_{S_h}} \frac{1}{\theta} \mathbf{q} \cdot \mathbf{n} \, da. \quad (2.56)$$

The difference between the temporal change of entropy and the rate of entropy input determines the total entropy production  $\Gamma$  per unit time. This quantity is governed by the specific entropy production  $\gamma$  per unit time and mass. The second law of thermodynamics states that the entropy of an isolated system not in equilibrium will tend to increase over the time. Thus, the entropy production is always greater than – or equal to – zero

$$\Gamma = \int_{\mathcal{P}_S} \rho \gamma \, dv = \frac{d}{dt} H - Q \geq 0. \quad (2.57)$$

Solving the local counterparts of this axiom for the entropy production  $\gamma$  yield the so-called Clausius-Duhem inequality in its material and spatial representations

$$\begin{aligned} \rho_0 \gamma &= \rho_0 \dot{\eta} - \rho_0 \frac{r}{\theta} + \frac{1}{\theta} \text{Div} \mathbf{Q} - \frac{1}{\theta^2} \mathbf{Q} \cdot \nabla_X \theta \geq 0 \\ \rho \gamma &= \rho \dot{\eta} - \rho \frac{r}{\theta} + \frac{1}{\theta} \text{div} \mathbf{q} - \frac{1}{\theta^2} \mathbf{q} \cdot \nabla_x \theta \geq 0. \end{aligned} \quad (2.58)$$

Introduction of the free Helmholtz energy  $\Psi$  per unit mass via the Legendre transformation  $\Psi = u - \theta\eta$  induces the rate expression  $\dot{u} = \dot{\Psi} + \dot{\eta}\theta + \eta\dot{\theta}$ . The rate  $\dot{u}$  is governed by the local format (2.55) of balance of internal energy. Substitution into (2.58) gives the alternative version of the Clausius-Duhem inequality

$$\begin{aligned}\rho_0\theta\gamma &= \tilde{\mathbf{P}} : \dot{\mathbf{F}} - \rho_0\dot{\Psi} - \rho_0\dot{\theta}\eta - \frac{1}{\theta}\mathbf{Q} \cdot \nabla_X\theta \geq 0 \\ \rho\theta\gamma &= \boldsymbol{\sigma} : \mathbf{d} - \rho\dot{\Psi} - \rho\dot{\theta}\eta - \frac{1}{\theta}\mathbf{q} \cdot \nabla_x\theta \geq 0.\end{aligned}\tag{2.59}$$

Finally, the mechanical dissipation  $\mathcal{D} := \theta\gamma$  per unit volume is introduced. Then, a stronger representation of (2.59) is obtained for separate consideration of the local dissipation  $\mathcal{D}_{loc}$  and the conductive dissipation  $\mathcal{D}_{con}$

$$\begin{aligned}\rho_0\mathcal{D}_{loc} &= \tilde{\mathbf{P}} : \dot{\mathbf{F}} - \rho_0\dot{\Psi} - \rho_0\dot{\theta}\eta \geq 0 & \text{and} & & \rho\mathcal{D}_{loc} &= \boldsymbol{\sigma} : \mathbf{d} - \rho\dot{\Psi} - \rho\dot{\theta}\eta \geq 0 \\ \rho_0\mathcal{D}_{con} &= -\frac{1}{\theta}\mathbf{Q} \cdot \nabla_X\theta \geq 0 & & & \rho\mathcal{D}_{con} &= -\frac{1}{\theta}\mathbf{q} \cdot \nabla_x\theta \geq 0\end{aligned}\tag{2.60}$$

denoted the Clausius-Planck and the Fourier inequalities, respectively. At last, based on representation (2.58) of the Clausius-Duhem inequality, the Clausius-Planck inequality for the local dissipation can alternatively be written as

$$\begin{aligned}\rho_0\mathcal{D}_{loc} &= \rho_0\left(\frac{\partial}{\partial t}\eta\right)\theta - \rho_0r + \text{Div}\mathbf{Q} \geq 0 \\ \rho\mathcal{D}_{loc} &= \rho\left(\frac{d}{dt}\eta\right)\theta - \rho r + \text{div}\mathbf{q} \geq 0,\end{aligned}\tag{2.61}$$

in which the precise notation for the time derivative of  $(\bullet)$  is used instead of  $(\dot{\bullet})$ . The Lagrangian representation  $(2.61)_1$  of the local dissipation is expressed in terms of the total time derivative of the entropy  $\partial\eta/\partial t = d\eta/dt|_{X \text{ fixed}}$  at fixed material positions.





### 3. Configurational Setting of Thermo-Inelasticity

It is the objective of this chapter to derive a versatile, thermodynamically consistent approach towards configurational mechanics with regard to the solution of thermo-mechanically coupled problems at finite inelastic deformations. The procedure to follow incorporates global energetic arguments to set up a global dissipation postulate. This postulate is used in the sense of a global Coleman-type exploitation method. The governing equations of configurational mechanics, i.e. the dual material and spatial balances of linear momentum or, for the time being, equilibrium conditions, are obtained in a natural fashion. Subsequent to some preliminary remarks, the investigations commence with the continuous setting. At first the geometric framework is presented whereupon the afore-mentioned dissipation postulate is introduced and exploited with regard to the formulation of the respective balance equations. For the thermo-mechanically coupled problem under consideration an evolution equation for the temperature field is developed starting from the balance of internal energy. The second part of this chapter is devoted to the algorithmic treatment and the numerical solution procedure in the sense of a staggered solution strategy. In this context particular attention is focused on the evaluation of discrete configurational nodal forces. Finally, the basic equations are specified in view of a model problem and a typical boundary value problem is discussed. It is of interest to point out that the configurational setting of (thermo-)inelasticity will be employed once more within the analyses of Section 6 including alternative constitutive formulations.

#### 3.1. Introductory Remarks

Even in the absence of true material inhomogeneities characterized for instance by a change in the material properties of the considered solid, the occurrence of thermal and/or inelastic effects act as a possible source of inhomogeneity. Hence the investigation of thermal and inelastic processes is naturally related to the study of configurational mechanics as this setting intrinsically originates from the analyses of forces acting on inhomogeneities. The influence of inelastic and thermal phenomena on the configurational representation of continuum mechanics and, more recently, concerning the application of the configurational setting in computational mechanics has been elaborated by numerous authors. Thereby the investigation of thermal effects is mainly concerned with the framework of thermo-elasticity. With regard to the theoretical description EPSTEIN & MAUGIN [38] worked out the material setting of thermo-elastic heat conductors. A different type of thermo-elastic material forces has been proposed by DASCALU & MAUGIN [34] who constructed a material momentum equation for thermo-elasticity based on the notion of so-called thermal displacements and in addition dealt with the application to fracture mechanics. In both articles the material balance law is derived by means of manipulations of the well-known spatial counterparts. This is in contrast to the previous work of FRANCFORT & GOLEBIEWSKA HERRMANN [48] in which the material balance is said to be inevitably of variational origin. However, as it was also emphasized within the above-mentioned quotations, the balance of material momentum even holds in the presence of dissipative processes and thus is not physically derivable from this type of a variational principle. An alternative approach which utilizes Gurtin's viewpoint of the derivation of configurational forces, but in fact not Gurtin's understanding of thermo-elasticity in this context, cf. e.g. GURTIN [61], is due to KALPAKIDES & DASCALU [74]. They combine Gurtin's ideas with the concept of thermal displacements and thus end up with a representation similar to that of DASCALU & MAUGIN [34]. The thermo-elastic case and above all its extension to

thermo-inelasticity and the fully dynamical framework has been developed by MAUGIN & BEREZOVSKI [108]. Also STEINMANN [174] investigated the combination of thermal and dynamical effects in elastic materials. The application of the thermo-mechanical formulations to the study of the movement of inhomogeneities or rather different types of singularities can be found e.g. in MAUGIN [104].

An thermo-mechanical approach to configurational inelasticity is presented in CLEJA-TIGOIU & MAUGIN [32] who considered the configurational framework of multiplicative elasto-plasticity. This description is conceptually in line with the notion of local rearrangement in terms of the introduction of a reference crystal as evoked e.g. by EPSTEIN & MAUGIN [37, 40, 39], however, the first one being devoted to the elastic case, see also STEINMANN [173]. The role of Eshelby's energy-momentum tensor in (elasto-)plasticity is investigated in a series of papers of the second author, namely MAUGIN [100, 101] including also inertial, i.e. dynamical effects, and the application to ductile fracture mechanics, as well as MAUGIN [105, 106] governing the influence of thermal effects as well. The work of MENZEL & STEINMANN [116] also relies on multiplicative elasto-plasticity and provides a variety of reformulations of the material balance equation. The material inhomogeneity forces incorporate gradients of distortions and dislocation density tensors. This characteristic is directly related to the above-mentioned concept of local structural rearrangement and enables to capture the representation of the well-established Peach-Koehler force.

The dual material-spatial setting of thermo-elasticity has been highlighted by KUHL, DENZER, BARTH & STEINMANN [84] who above all deal with the numerical treatment. A monolithic solution strategy is conceived with the spatial displacements and the temperature field being the primary unknowns. The evaluation of the ingredients of the material balance equations is performed in a postprocessing step. With respect to the solution of inelastic problems at first LIEBE, DENZER & STEINMANN [88] considered the model problem of finite continuum damage and introduced the scalar damage variable as an additional nodal degree. The same strategy has been adopted by MENZEL, DENZER & STEINMANN [115] in the context of small strain single-crystal-plasticity. Moreover, in this contribution an alternative solution procedure is discussed that avoids the introduction of additional global degrees. The latter approach has been extended by NGUYEN, GOVINDJEE, KLEIN & GAO [138] to the modeling of small-strain inelastic fracture processes. The application to ductile fracture is also investigated by NÄSER, KALISKE & MÜLLER [136], however in the finite strain context. To the author's knowledge the computational realization of the configurational setting in thermo-inelasticity is rare in existing literature. Recent attempts elaborated within the author's research group, cf. ZIMMERMANN & MIEHE [196] and additionally the report of YALÇINKAYA [189], deal with the numerical implementation of material forces in finite thermo-plasticity. A unified treatment of these investigations is derived in the subsequent sections and later on applied in the context of  $h$ -adaptive mesh refinement.

## 3.2. Formulation and Exploitation of a Global Dissipation Postulate

In this subsection the continuous framework is outlined starting with the geometric setting followed by the formulation and exploitation of a global dissipation postulate.

**3.2.1. Basic Geometry of a Solid with Structural Changes.** To set the state, some fundamental aspects of the deformation of a material body at finite strains are recapitulated shortly incorporating in addition thermal effects. Let  $\mathcal{B} \subset \mathbb{E}^3$  be the reference

configuration of the body subjected to thermo-mechanical loading. With respect to the mechanical problem, the exterior boundary  $\partial\mathcal{B}$  of the body is decomposed into a part  $\partial\mathcal{B}_\varphi$  with prescribed deformation by Dirichlet-type boundary conditions and a part  $\partial\mathcal{B}_\bar{\mathbf{t}}$  with given tractions by von Neumann-type boundary conditions. The decomposition of the boundary is unique due to  $\partial\mathcal{B} = \partial\mathcal{B}_\varphi \cup \partial\mathcal{B}_\bar{\mathbf{t}}$  with  $\partial\mathcal{B}_\varphi \cap \partial\mathcal{B}_\bar{\mathbf{t}} = \emptyset$ . For the thermal problem, in an analogous fashion the material boundary is decomposed into a part  $\partial\mathcal{B}_\theta$  with given temperature field  $\theta$  and a part  $\partial\mathcal{B}_{\bar{Q}_n}$  with prescribed heat flux  $\bar{Q}_n$  and the unique decomposition  $\partial\mathcal{B} = \partial\mathcal{B}_\theta \cup \partial\mathcal{B}_{\bar{Q}_n}$  with  $\partial\mathcal{B}_\theta \cap \partial\mathcal{B}_{\bar{Q}_n} = \emptyset$  being obvious. The material coordinates  $\mathbf{X} \in \mathcal{B}$  of the solid in the reference configuration  $\mathcal{B}$  are mapped onto the current coordinates  $\mathbf{x} \in \mathcal{S}$  by the deformation map at time  $t \in \mathcal{R}_+$

$$\varphi_t : \begin{cases} \mathcal{B} \rightarrow \mathcal{S} \\ \mathbf{X} \mapsto \mathbf{x} = \varphi_t(\mathbf{X}) \end{cases} \quad (3.1)$$

where  $\mathcal{S} \subset \mathbb{E}^3$  is the deformed configuration. Following the above discussion, this spatial deformation is prescribed on the part  $\partial\mathcal{B}_\varphi \subset \partial\mathcal{B}$  of the boundary by the Dirichlet condition

$$\varphi_t(\mathbf{X}) = \mathbf{X} + t\bar{\mathbf{v}}(\mathbf{X}) \quad \text{on} \quad \partial\mathcal{B}_\varphi \quad (3.2)$$

in a monotonous format with given velocity function  $\bar{\mathbf{v}}$  and the particular case  $\bar{\mathbf{v}} = \mathbf{0}$  for a stationary part  $\partial\mathcal{B}_\varphi$  of the boundary.

The kinematic setting outlined in Chapter 2 was restricted to time-independent material coordinates  $\mathbf{X} = \text{const.}$ , i.e. a time-independent reference configuration  $\mathcal{B}$ , recall Remark 2.1. In the subsequent investigations this restriction is omitted. In contrast, the procedure allows for temporal changes of the Lagrangian setting referred to as *material configurational changes*. To this end, in addition to the reference configuration  $\mathcal{B}$  and the current configuration  $\mathcal{S}$ , both being from now on time-dependent, a time-independent domain  $\Omega \subset \mathbb{E}^3$  with coordinates  $\boldsymbol{\theta} \in \Omega$  is introduced denoted the parameter space of the continuum. Consider then a one-to-one piecewise differentiable transformation  $\Xi_t : \Omega \rightarrow \mathcal{B}_t$  of the parameter space onto the reference configuration. This mapping is to be understood as the time-dependent parameterization of the solid describing material structural changes. It reflects a time-dependent change of the Lagrangian coordinates  $\boldsymbol{\theta} \in \Omega$  to  $\mathbf{X} \in \mathcal{B}_t$  in the sense of a change of the material structure. With this viewpoint at hand, it is straightforward to introduce the dual material and spatial coordinate maps

$$\Xi_t : \begin{cases} \Omega \rightarrow \mathcal{B}_t \\ \boldsymbol{\theta} \mapsto \mathbf{X} = \Xi_t(\boldsymbol{\theta}) \end{cases} \quad \text{and} \quad \xi_t : \begin{cases} \Omega \rightarrow \mathcal{S}_t \\ \boldsymbol{\theta} \mapsto \mathbf{x} = \xi_t(\boldsymbol{\theta}) \end{cases} \quad (3.3)$$

at time  $t$  and to express the deformation map (3.1) by the composition

$$\varphi_t(\mathbf{X}) = \xi_t(\boldsymbol{\theta}) \circ \Xi_t^{-1}(\mathbf{X}) \quad (3.4)$$

as visualized in Figure 3.1. Thus, a body  $\mathcal{B}$  including material inhomogeneities such as defects or inclusions undergoes two simultaneous and independent processes: The motion of material particles with respect to the ambient space described by the non-linear deformation map  $\varphi_t$  and the motion of inhomogeneities within the material governed by the material configurational map  $\Xi_t$ . In this sense, the material configuration  $\mathcal{B}$  acts as a reference for the motion of particles in space whereas the parameter space  $\Omega$  acts as a reference for the motion of inhomogeneities with respect to the material manifold. The spatial and material configurational maps are constrained by Dirichlet boundary conditions

$$\xi_t(\boldsymbol{\theta}) = \mathbf{x} = \bar{\mathbf{x}} = \mathbf{X} + t\bar{\mathbf{v}} \quad \text{on} \quad \partial\mathcal{B}_\varphi \quad \text{and} \quad \xi_t(\boldsymbol{\theta}) = \mathbf{X} = \text{const.} \quad \text{on} \quad \partial\mathcal{B}. \quad (3.5)$$

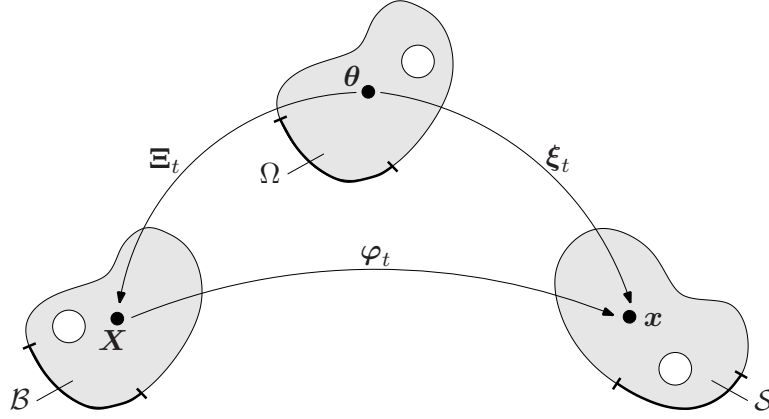


**Figure 3.1:** Kinematics of a body with structural changes. The *material coordinate map*  $\Xi_t$  maps the coordinates  $\theta \in \Omega$  of the parameter space onto the Lagrangian coordinates  $\mathbf{X} \in \mathcal{B}_t$ . The *spatial coordinate map*  $\xi_t$  maps the coordinates  $\theta \in \Omega$  onto the Eulerian coordinates  $\mathbf{x} \in \mathcal{S}_t$ . The reference coordinates  $\mathbf{X} \in \mathcal{B}_t$  are mapped onto the current coordinates  $\mathbf{x} \in \mathcal{S}_t$  via the *non-linear point or deformation map*  $\varphi_t(\mathbf{X}) = \xi_t(\theta) \circ \Xi_t^{-1}(\mathbf{X})$ .

Due to  $\mathbf{x} = \varphi_t$ , the first one, i.e. the spatial condition, exactly represents (3.2). The second one, i.e. the material condition, states that no change of the material boundary  $\partial\mathcal{B}$  occurs as all material positions on  $\partial\mathcal{B}$  are kept constant. Later on, this restriction can be reduced by allowing for a movement of the material coordinates along the boundary. Nevertheless, the shape of the material body in its reference configuration must still remain unaffected. Based on representation (3.4) of the non-linear point map the deformation gradient  $\mathbf{F} = \nabla_{\mathbf{X}}\varphi_t$  appears as the composition

$$\mathbf{F} = \mathbf{j} \mathbf{J}^{-1} \quad \text{with} \quad \mathbf{j} = \nabla_{\theta}\xi_t \quad \text{and} \quad \mathbf{J} = \nabla_{\theta}\Xi_t \quad (3.6)$$

in terms of the gradients of the material and spatial coordinate maps and the abbreviation  $\nabla_{\theta}(\bullet)$  indicating the partial derivative  $\partial(\bullet)/\partial\theta$  of  $(\bullet)$  with respect to the parameter coordinates  $\theta$ . The volume element of the Lagrangian configuration is related to that of the parameter space via the determinant of the gradient of the material coordinate map

$$dV = \det \mathbf{J} d\Omega. \quad (3.7)$$

For the subsequent rate formulation of the inelastic solid it is essential to evaluate the following time derivatives of the above kinematic objects

$$\mathbf{v} = \frac{\partial}{\partial t}\varphi = \dot{\xi} - \mathbf{F}\dot{\Xi}, \quad \frac{d}{dt}\mathbf{F} = \nabla_{\mathbf{X}}\dot{\xi} - \mathbf{F}\nabla_{\mathbf{X}}\dot{\Xi}, \quad \frac{d}{dt}dV = (\mathbf{1} : \nabla_{\mathbf{X}}\dot{\Xi}) dV. \quad (3.8)$$

They rely on the time derivatives of the spatial and material configurational maps

$$\dot{\xi} = \frac{\partial}{\partial t}\xi \circ \Xi_t^{-1}(\mathbf{X}) \quad \text{and} \quad \dot{\Xi} = \frac{\partial}{\partial t}\Xi \circ \Xi_t^{-1}(\mathbf{X}). \quad (3.9)$$

For a detailed derivation of these expressions the reader is referred to Appendix B. All the kinematic quantities are parameterized by the Lagrangian space-time  $(\mathbf{X}, t)$ . The composition with the inverse of the material configurational map induces this parameterization but will be omitted for the sake of abbreviation. The short cut  $(\dot{\bullet})$  for the total time derivative is still suitable as the material and spatial configurational maps themselves are

parameterized by the time-independent coordinates  $\boldsymbol{\theta}$  of the parameter space. The material velocity  $\dot{\mathbf{E}}$  depicts a change of the position of a particle with respect to the material manifold whereas the spatial counterpart  $\dot{\boldsymbol{\xi}}$  describes the movement of a particle with respect to the current configuration. Both fields can be interpreted as variations of the spatial and material positions of the particle. In this sense, the spatial and material velocity fields (3.9) act as point variations and govern possible variations of the Lagrangian and the Eulerian coordinates  $\mathbf{X} \in \mathcal{B}_t$  and  $\mathbf{x} \in \mathcal{S}_t$ . This characteristic brings the subsequent rate formulation close to a variational setting. The velocity fields are restricted by some typical boundary conditions. For the monotonous loading process (3.5)<sub>1</sub> the admissible spatial velocity is

$$\dot{\boldsymbol{\xi}} \in \{\dot{\boldsymbol{\xi}} \mid \dot{\boldsymbol{\xi}} = \bar{\mathbf{v}} \text{ on } \partial\mathcal{B}_\varphi\} \quad (3.10)$$

with given velocity function  $\bar{\mathbf{v}}$  and in particular  $\bar{\mathbf{v}} = \mathbf{0}$  for a stationary boundary  $\partial\mathcal{B}_\varphi$ . The homogeneous form of the essential material boundary condition (3.5)<sub>2</sub> defines the admissible material velocity field

$$\dot{\mathbf{E}} \in \{\dot{\mathbf{E}} \mid \dot{\mathbf{E}} = \mathbf{0} \text{ on } \partial\mathcal{B}\}. \quad (3.11)$$

As mentioned above, the restriction to constant material positions  $\mathbf{X}$  on the material boundary  $\partial\mathcal{B}$  can be reduced by allowing for a movement of the material coordinates along  $\partial\mathcal{B}$ . As the shape of the material body must not change, only such movements of the material positions are permitted which do not include structural changes normal to the external surface of the solid. This scenario is expressed by the alternative condition  $\dot{\mathbf{E}} \in \{\dot{\mathbf{E}} \mid \dot{\mathbf{E}} \cdot \mathbf{N} = 0 \text{ on } \partial\mathcal{B}\}$  in which  $\mathbf{N}$  characterizes the outward normal of  $\partial\mathcal{B}$ .

**3.2.2. Global Constitutive Response of an Inelastic Solid.** The analyses focus on a general inelastic response of the solid. A global dissipation postulate is established by means of a comparison between external and internal power produced during the thermo-mechanical deformation of the solid subjected to the restrictions of the second law of thermodynamics. The external power is given by the power of the physical loading. On the other hand, the internal power incorporates the evolution of the total energy storage and the global dissipation. The following subsection provides a straightforward approach towards the formulation of this global postulate using the statements of both the first as well as the second axiom of thermodynamics.

**3.2.2.1. Formulation of a global dissipation postulate.** For the quasi-static case the change  $dK/dt$  of kinetic energy vanishes and the balance of energy (2.50) reduces to

$$\frac{d}{dt}U = \mathcal{P} + Q. \quad (3.12)$$

The total internal energy  $U$  is governed by the specific internal energy  $\bar{u}_0 = \rho_0 u$ . By means of the Legendre transformation  $\psi = \bar{u}_0 - \theta \eta_0$  the free energy function  $\psi = \rho_0 \Psi$  is introduced where  $\eta_0 = \rho_0 \eta$  denotes the specific entropy. The free energy  $\psi$  is assumed to depend on the deformation gradient  $\mathbf{F}$ , the temperature  $\theta$  and a generalized vector  $\boldsymbol{\mathcal{I}} \in \mathcal{G}$  of internal variables describing locally the dissipative bulk response.  $\mathcal{G}$  indicates a vector space  $\mathcal{R}^n$  of  $n$  scalar functions of internal variables which may be constrained to a manifold, e.g. the Lie group  $SL(3)$  of unimodular tensors in isochoric finite plasticity. The

temperature and the internal variables are fields on the reference configuration  $\mathcal{B}$  and are parameterized by the Lagrangian space-time  $(\mathbf{X}, t)$

$$\theta = \theta(\mathbf{X}, t) \quad \text{and} \quad \mathcal{I} = \mathcal{I}(\mathbf{X}, t). \quad (3.13)$$

Both fields explicitly depend on the time  $t$  but also on the time-dependent position  $\mathbf{X} = \Xi_t(\boldsymbol{\theta}) \in \mathcal{B}$  of the reference configuration. According to (2.22)<sub>2</sub>, the total time derivatives

$$\frac{d}{dt}\theta = \frac{\partial}{\partial t}\theta(\mathbf{X}, t) + \nabla_{\mathbf{X}}\theta(\mathbf{X}, t) \cdot \dot{\Xi} \quad \text{and} \quad \frac{d}{dt}\mathcal{I} = \frac{\partial}{\partial t}\mathcal{I}(\mathbf{X}, t) + \nabla_{\mathbf{X}}\mathcal{I}(\mathbf{X}, t) \cdot \dot{\Xi} \quad (3.14)$$

split up into a local and a convective part with  $\dot{\Xi} = \partial\Xi/\partial t$  representing the time derivative of the material coordinates. As the focus is on a general inhomogeneous bulk response of the solid, the free energy function explicitly depends on the reference position  $\mathbf{X} = \Xi_t(\boldsymbol{\theta})$ . The energy storage function is assumed to satisfy the standard restriction of objectivity, i.e.  $\psi(\mathbf{Q}\mathbf{F}, \theta, \mathcal{I}, \mathbf{X}) = \psi(\mathbf{F}, \theta, \mathcal{I}, \mathbf{X})$  for all proper orthogonal tensors  $\mathbf{Q} \in SO(3)$ . Using the definition of the power  $\mathcal{P}$  of external physical forces and the thermal power  $Q$ , cf. (2.50), the energy balance reads

$$\frac{d}{dt} \int_{\mathcal{B}} \psi + \eta_0 \theta \, dV = \int_{\mathcal{B}} \mathbf{v} \cdot \bar{\gamma}_0 \, dV + \int_{\partial\mathcal{B}_{\bar{\mathbf{t}}}} \mathbf{v} \cdot \bar{\mathbf{t}} \, dA + \int_{\mathcal{B}} \rho_0 r \, dV - \int_{\partial\mathcal{B}_{\bar{Q}_n}} \bar{Q}_n \, dA \quad (3.15)$$

with the heat flux  $\bar{Q}_n = \mathbf{Q} \cdot \mathbf{N}$  and the Lagrangian heat flux vector  $\mathbf{Q}$ . By means of Gauss integration theorem the last surface integral can be transformed into a volume integral in terms of  $\text{Div}\mathbf{Q}$ . By substitution of the time derivative (3.8)<sub>3</sub> of the material volume element the left hand side of (3.15) is evaluated

$$\frac{d}{dt} \int_{\mathcal{B}} \psi + \eta_0 \theta \, dV = \frac{d}{dt} \int_{\mathcal{B}} \psi \, dV + \int_{\mathcal{B}} \frac{d}{dt}(\eta_0 \theta) \, dV + \int_{\mathcal{B}} \eta_0 \theta (\mathbf{1} : \nabla_{\mathbf{X}} \dot{\Xi}) \, dV. \quad (3.16)$$

Since the entropy  $\eta_0$  depends on the Lagrangian space-time, its total time derivative is performed in formally the same way as specified in (3.14). By application of integration by parts the last two terms of (3.16) can be expressed by

$$\int_{\mathcal{B}} \frac{d}{dt}(\eta_0 \theta) + \eta_0 \theta (\mathbf{1} : \nabla_{\mathbf{X}} \dot{\Xi}) \, dV = \int_{\mathcal{B}} \left( \frac{\partial}{\partial t} \eta_0 \right) \theta + \eta_0 \left( \frac{\partial}{\partial t} \theta \right) + \text{Div} \left[ \eta_0 \theta \dot{\Xi} \right] \, dV. \quad (3.17)$$

The last addend of the right hand side is transformed into a surface integral which in turn vanishes due to the boundary constraint (3.11) for the material velocity field. With these results at hand, the energy balance (3.15) boils down to

$$\int_{\mathcal{B}} \frac{\partial}{\partial t} \eta_0 \theta - \rho_0 r + \text{Div}\mathbf{Q} \, dV = \mathcal{P} - \frac{d}{dt} \Pi_{int} - \int_{\mathcal{B}} \eta_0 \frac{\partial}{\partial t} \theta \, dV \quad (3.18)$$

with the definition of the total bulk energy storage  $\Pi_{int}$  of the solid

$$\Pi_{int} := \int_{\mathcal{B}} \psi \, dV. \quad (3.19)$$

As the reference density  $\rho_0$  does not depend on time, the temporal change of entropy is  $\partial\eta_0/\partial t = \rho_0\partial\eta/\partial t$ . Hence, the integrand on the left hand side of (3.18) represents the local



dissipation  $\rho_0 \mathcal{D}_{loc}$  per unit reference volume specified in (2.61) as a local Lagrangian form of the balance of entropy, i.e. the second law of thermodynamics. The volume integral

$$\mathcal{D} := \int_{\mathcal{B}} \rho_0 \mathcal{D}_{loc} dV = \int_{\mathcal{B}} \left( \rho_0 \left( \frac{\partial}{\partial t} \eta \right) \theta - \rho_0 r + \text{Div} \mathbf{Q} \right) dV \geq 0 \quad (3.20)$$

represents the *global dissipation* and (3.18) sets up the *global dissipation postulate*

$$\mathcal{D} = \mathcal{P} - \frac{d}{dt} \Pi_{int} - \int_{\mathcal{B}} \eta_0 \frac{\partial}{\partial t} \theta dV \geq 0. \quad (3.21)$$

The global dissipation of a solid undergoing thermo-mechanically coupled inelastic deformation is evaluated as the difference between the power of external physical forces and the evolution of the total bulk energy storage and a temperature-dependent contribution. The postulate states that the global dissipation has to be always greater than or equal to zero. It is the demand of the second axiom of thermodynamics and reflects the global counterpart of the classical Clausius-Planck inequality of continuum thermo-mechanics, cf. Section 2.3.5. For the restriction to isothermal processes, i.e. the purely mechanical framework, the last integral vanishes. For elastic continua the dissipation of the system is equal to zero and it remains the reduced form of the global dissipation postulate

$$\mathcal{D} = \mathcal{P} - \frac{d}{dt} \Pi_{int} \equiv 0 \quad (3.22)$$

requiring the change of energy storage to be equal to the power of the external loading.

**3.2.2.2. Derivation of dual material and spatial balance equations.** The global dissipation postulate is employed to derive the dual material-spatial field equations by means a Coleman-type exploitation method. At first, the power of external physical forces is recast using the kinematic relationship (3.8)<sub>1</sub> for the velocity  $\mathbf{v}$

$$\mathcal{P} = \int_{\mathcal{B}} \mathbf{v} \cdot \bar{\boldsymbol{\gamma}}_0 dV + \int_{\partial \mathcal{B}_{\bar{\mathbf{t}}}} \mathbf{v} \cdot \bar{\mathbf{t}} dA = \int_{\mathcal{B}} \dot{\boldsymbol{\xi}} \cdot \bar{\boldsymbol{\gamma}}_0 - \mathbf{F}^T \bar{\boldsymbol{\gamma}}_0 \cdot \dot{\boldsymbol{\Xi}} dV + \int_{\partial \mathcal{B}_{\bar{\mathbf{t}}}} \dot{\boldsymbol{\xi}} \cdot \bar{\mathbf{t}} dA. \quad (3.23)$$

Observe that the material configurational map, or rather its rate, does not enter the surface integral due to the boundary condition (3.11). In analogy to (3.16) for the rate of the energy storage the following relation holds

$$\frac{d}{dt} \Pi_{int} = \frac{d}{dt} \int_{\mathcal{B}} \psi dV = \int_{\mathcal{B}} \frac{d}{dt} \psi dV + \int_{\mathcal{B}} \psi (\mathbf{1} : \nabla_X \dot{\boldsymbol{\Xi}}) dV. \quad (3.24)$$

Using the functional dependencies of the free energy function  $\psi$ , its evolution is given by

$$\frac{d}{dt} \psi = \frac{d}{dt} \psi(\mathbf{F}, \theta, \mathcal{I}, \mathbf{X}) = \partial_{\mathbf{F}} \psi : \frac{d}{dt} \mathbf{F} + \partial_{\theta} \psi \cdot \frac{d}{dt} \theta + \partial_{\mathcal{I}} \psi \cdot \frac{d}{dt} \mathcal{I} + \partial_{\mathbf{X}} \psi^{\text{expl}} \cdot \dot{\boldsymbol{\Xi}}. \quad (3.25)$$

Upon substitution of this derivative into (3.24) and by means of the kinematic relationships (3.8) and (3.14) the temporal change of the energy storage  $\Pi_{int}$  can be computed

$$\begin{aligned} \frac{d}{dt} \Pi_{int} &= \int_{\mathcal{B}} \mathbf{P} : \nabla_X \dot{\boldsymbol{\xi}} + (\psi \mathbf{1} - \mathbf{F}^T \mathbf{P}) : \nabla_X \dot{\boldsymbol{\Xi}} dV \\ &+ \int_{\mathcal{B}} (\partial_{\theta} \psi \nabla_X \theta + \partial_{\mathcal{I}} \psi \cdot \nabla_X \mathcal{I} + \partial_{\mathbf{X}} \psi^{\text{expl}}) \cdot \dot{\boldsymbol{\Xi}} - \mathcal{F} \cdot \frac{\partial}{\partial t} \mathcal{I} - \eta_0 \frac{\partial}{\partial t} \theta dV. \end{aligned} \quad (3.26)$$

This relation relies on the constitutive expressions for the first Piola-Kirchhoff stress tensor  $\mathbf{P} = \partial_{\mathbf{F}}\psi$ , the entropy  $\eta_0 = \rho_0\eta = -\partial_\theta\psi$  and the internal thermodynamical forces  $\mathcal{F} = -\partial_{\mathcal{I}}\psi$  and induces the definition of the *Eshelby stress* or *energy-momentum tensor*

$$\boldsymbol{\Sigma} = \psi \mathbf{1} - \mathbf{F}^T \partial_{\mathbf{F}}\psi = \psi \mathbf{1} - \mathbf{F}^T \mathbf{P} \quad (3.27)$$

being a purely material mixedvariant second order tensor. By substitution of the relation  $\mathbf{P} = \mathbf{F}\mathbf{S}$  the alternative representation  $\boldsymbol{\Sigma} = \psi \mathbf{1} - \mathbf{C}\mathbf{S}$  is obtained. Then,  $\boldsymbol{\Sigma}$  is symmetric in case the material is isotropic, i.e. the second Piola-Kirchhoff stresses  $\mathbf{S}$  and the right Cauchy Green tensor  $\mathbf{C}$  are coaxial,  $\mathbf{C}\mathbf{S} = \mathbf{S}\mathbf{C}$ , cf. CHADWICK [30].

It is a remarkable fact that the change  $d\Pi_{int}/dt$  of energy storage of the deforming solid including structural changes contains a deformation induced spatial stress power based on the first Piola-Kirchhoff stress tensor and a structural change induced material stress power based on the Eshelby stress tensor.

By combination of (3.26) and (3.23) the global dissipation postulate (3.21) results in

$$\begin{aligned} \mathcal{D} &= \int_{\mathcal{B}} \bar{\gamma}_0 \cdot \dot{\boldsymbol{\xi}} \, dV + \int_{\partial\mathcal{B}_t} \bar{\mathbf{t}} \cdot \dot{\boldsymbol{\xi}} \, dA - \int_{\mathcal{B}} \mathbf{P} : \nabla_{\mathbf{X}} \dot{\boldsymbol{\xi}} \, dV \\ &\quad + \int_{\mathcal{B}} (-\mathbf{F}^T \bar{\gamma}_0 - \partial_\theta\psi \nabla_{\mathbf{X}}\theta - \partial_{\mathcal{I}}\psi \cdot \nabla_{\mathbf{X}}\mathcal{I} - \partial_{\mathbf{X}}\psi^{\text{expl}}) \cdot \dot{\boldsymbol{\xi}} \, dV \\ &\quad - \int_{\mathcal{B}} \boldsymbol{\Sigma} : \nabla_{\mathbf{X}} \dot{\boldsymbol{\xi}} \, dV + \int_{\mathcal{B}} \mathcal{F} \cdot \frac{\partial}{\partial t} \mathcal{I} \, dV \geq 0. \end{aligned} \quad (3.28)$$

It is appropriate to define the *configurational* or *material force* vector per unit volume of the reference configuration

$$\bar{\boldsymbol{\Gamma}}_0 := -\bar{\gamma}_0 - \partial_\theta\psi \nabla_{\mathbf{X}}\theta - \partial_{\mathcal{I}}\psi \cdot \nabla_{\mathbf{X}}\mathcal{I} - \partial_{\mathbf{X}}\psi^{\text{expl}}. \quad (3.29)$$

As a matter of notation, the material volume force can be split into three different parts

$$\bar{\boldsymbol{\Gamma}}_\gamma := \mathbf{F}^T \bar{\gamma}_0, \quad \bar{\boldsymbol{\Gamma}}_{\mathcal{I}} := \partial_\theta\psi \nabla_{\mathbf{X}}\theta + \partial_{\mathcal{I}}\psi \cdot \nabla_{\mathbf{X}}\mathcal{I} \quad \text{and} \quad \bar{\boldsymbol{\Gamma}}_{\mathbf{X}} := \partial_{\mathbf{X}}\psi^{\text{expl}}. \quad (3.30)$$

By means of this split, the basic characteristic of the configurational volume force comes to light: The purely material object  $\bar{\boldsymbol{\Gamma}}_0$  displays the explicit,  $\bar{\boldsymbol{\Gamma}}_{\mathbf{X}}$ , and, via the temperature and the internal variable fields,  $\bar{\boldsymbol{\Gamma}}_{\mathcal{I}}$ , implicit dependence of the free energy function on the time-dependent material position  $\mathbf{X} \in \mathcal{B}$  besides the contribution  $\bar{\boldsymbol{\Gamma}}_\gamma$  arising from the pull-back of the physical volume forces  $\bar{\gamma}_0$ . It represents the dual material vector to these physical forces. In the sense of their original interpretation, cf. Appendix A, configurational forces are the driving forces on an inhomogeneity, like a crack or an inclusion, within the Lagrangian setting of a material body. For the time being, this property is represented by the true material inhomogeneity force  $\bar{\boldsymbol{\Gamma}}_{\mathbf{X}} := \partial_{\mathbf{X}}\psi^{\text{expl}}$ . Referring to (3.30), configurational forces  $\bar{\boldsymbol{\Gamma}}_0$  occur for the following cases:

- (i) For material bodies subjected to spatial volume forces  $\bar{\gamma}_0$ .
- (ii) For an evolving temperature field or for an evolution of inelastic deformation described by a gradient in the temperature or the internal variable field. Thus, the distribution of both the temperature field as well as the inelastic state variables act as a quasi-inhomogeneity within the material setting of the solid.



(iii) For truly inhomogeneous bodies indicated by an explicit dependence of the free energy function on the material coordinate  $\mathbf{X}$ . Anticipating one crucial result of Section 4, it has to be mentioned that the complete true inhomogeneity of a material body is exhibited by the explicit dependence of the free energy function  $\psi$  and the reference density  $\rho_0$  on the material position  $\mathbf{X}$ . However, the latter one is naturally linked to the dynamical framework as it only occurs in the inertia contribution.

Incorporating these definitions, equation (3.28) can be rewritten in the compact format

$$\begin{aligned} \mathcal{D} = & \int_{\mathcal{B}} \{ \bar{\gamma}_0 \cdot \dot{\boldsymbol{\xi}} - \mathbf{P} : \nabla_{\mathbf{X}} \dot{\boldsymbol{\xi}} + \bar{\Gamma}_0 \cdot \dot{\boldsymbol{\Xi}} - \boldsymbol{\Sigma} : \nabla_{\mathbf{X}} \dot{\boldsymbol{\Xi}} \} dV \\ & + \int_{\mathcal{B}} \mathcal{F} \cdot \frac{\partial}{\partial t} \mathcal{I} dV + \int_{\partial \mathcal{B}_{\bar{\mathbf{t}}}} \bar{\mathbf{t}} \cdot \dot{\boldsymbol{\xi}} dA \geq 0. \end{aligned} \quad (3.31)$$

By means of integration by parts and application of Gauss integration theorem the global dissipation is finally converted into the form

$$\begin{aligned} \mathcal{D} = & \int_{\mathcal{B}} (\text{Div} \mathbf{P} + \bar{\gamma}_0) \cdot \dot{\boldsymbol{\xi}} dV + \int_{\partial \mathcal{B}_{\bar{\mathbf{t}}}} (\bar{\mathbf{t}} - \mathbf{P} \mathbf{N}) \cdot \dot{\boldsymbol{\xi}} dA \\ & + \int_{\mathcal{B}} (\text{Div} \boldsymbol{\Sigma} + \bar{\Gamma}_0) \cdot \dot{\boldsymbol{\Xi}} dV + \int_{\mathcal{B}} \mathcal{F} \cdot \frac{\partial}{\partial t} \mathcal{I} dV \geq 0. \end{aligned} \quad (3.32)$$

This dissipation inequality is now exploited in the sense of a global Coleman-type procedure. It has to be satisfied for arbitrary admissible spatial and material velocity fields  $\dot{\boldsymbol{\xi}}$  and  $\dot{\boldsymbol{\Xi}}$  subjected to the homogeneous forms of the Dirichlet boundary conditions. Admissible arbitrary spatial velocity fields induce the local spatial equations

$$\text{Div} \mathbf{P} + \bar{\gamma}_0 = \mathbf{0} \text{ in } \mathcal{B} \quad \text{and} \quad \mathbf{P} \mathbf{N} = \bar{\mathbf{t}} \text{ on } \partial \mathcal{B}_{\bar{\mathbf{t}}}. \quad (3.33)$$

The first one represents the *spatial equilibrium condition*, i.e. the local form of balance of linear momentum, and the latter one is the traction boundary condition on the external traction boundary  $\partial \mathcal{B}_{\bar{\mathbf{t}}}$  with outward normal  $\mathbf{N}$ . This equation is valid in combination with the essential boundary condition (3.5) on the deformation boundary  $\partial \mathcal{B}_{\varphi}$ . Vice versa, admissible arbitrary material velocity fields induce the local material equation

$$\text{Div} \boldsymbol{\Sigma} + \bar{\Gamma}_0 = \mathbf{0} \text{ in } \mathcal{B}. \quad (3.34)$$

This equation is usually denoted the *material equilibrium condition* and constitutes the dual material counterpart of the spatial equilibrium condition (3.33)<sub>1</sub>. It is a completely material balance equation with all ingredients being purely material objects. Observe that no additional traction boundary condition occurs for this balance law as the boundary is entirely governed by the essential boundary condition  $\mathbf{X} = \text{const.}$  on  $\partial \mathcal{B}$ .

**Remark 3.1:** The material balance law (3.34) can be obtained from the spatial counterpart (3.33)<sub>1</sub> by premultiplication with  $\mathbf{F}^T$ , cf. MAUGIN [99, 103]. Geometrically, this transformation represents a pull-back of the Eulerian quantity  $\text{Div} \mathbf{P} + \bar{\gamma}$  onto the Lagrangian manifold, i.e. a mapping between the cotangent spaces  $T_{\mathbf{X}}^* \mathcal{B}$  and  $T_x^* \mathcal{S}$  of the material and spatial configuration as visualized in Figure 3.2. At first, the total derivative of the free energy  $\psi = \psi(\mathbf{F}, \theta, \mathcal{I}, \mathbf{X})$  with respect to the material coordinates is computed

$$\nabla_{\mathbf{X}} \psi = \text{Div} [\psi \mathbf{1}] = \mathbf{P} : \nabla_{\mathbf{X}} \mathbf{F} - \eta \nabla \theta - \mathcal{F} \cdot \nabla \mathcal{I} + \partial_{\mathbf{X}} \psi^{\text{expl}}. \quad (3.35)$$

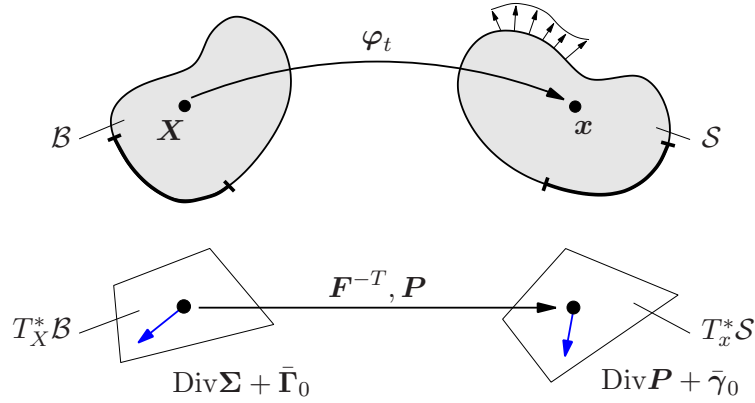


**Figure 3.2:** Dual balances in material and physical space. Pull-back of spatial equilibrium condition onto the material configuration.

Due to compatibility of the deformation gradient, the first term on the right hand side of (3.35) is rewritten as  $\mathbf{P} : \nabla_X \mathbf{F} = \text{Div} [\mathbf{F}^T \mathbf{P}] - \mathbf{F}^T \text{Div} \mathbf{P}$ . Substitution into the pull-back of the spatial balance equation (3.33) yields the dual material balance (3.34)

$$\mathbf{F}^T (\text{Div} \mathbf{P} + \bar{\gamma}_0) = \text{Div} \Sigma + \bar{\Gamma}_0 \quad (3.36)$$

in terms of the Eshelby tensor  $\Sigma$  and the material force  $\bar{\Gamma}_0$  defined in (3.27) and (3.29).

In a global scenario the local balance equation (3.34) corresponds to an equilibrium condition of global *material* or *configurational forces* being the dual statement to the equilibrium condition of global *physical forces*. These conditions represent the quasi-static versions of global momentum balances incorporating inertia terms due to dynamical effects. For a detailed discussion on global balances the reader is referred to Section 4.3.

**3.2.2.3. Thermo-mechanical coupling: Evolution of the temperature field.** The coupling of mechanical and thermal effects is displayed by two main characteristics. On the one hand, large deformations generate structural heating of the system denoted the Gough-Joule effect. On the other hand, the deformation of a structure depends on the temperature due to thermally induced stresses. Moreover, the presence of inelastic deformation or, more general, of arbitrary dissipative phenomena causes a degradation of energy into its thermal form and naturally involves changes in the temperature field.

To complete the set of governing equations of the thermo-mechanically coupled problem, an evolution equation for the temperature field  $\theta$  has to be formulated. The essential equation for this task is the local form (2.55)<sub>1</sub> of balance of internal energy

$$\rho_0 \frac{\partial}{\partial t} u = \rho_0 r - \text{Div} \mathbf{Q} + \tilde{\mathbf{P}} : \frac{\partial}{\partial t} \mathbf{F} \quad (3.37)$$

with the time derivative  $\partial(\bullet)/\partial t = d(\bullet)/dt|_{X \text{ fixed}}$  at fixed material positions. By means of the Legendre transformation the free energy is introduced,  $\psi = \rho_0 u - \theta \rho_0 \eta$ . Employing the Clausius-Planck inequality (2.60)<sub>1</sub> for the local dissipation one ends up with its alternative form (2.61)<sub>1</sub>, cf. (3.20). This inequality serves as an evolution equation for the entropy

$$\rho_0 \left( \frac{\partial}{\partial t} \eta \right) \theta = \rho_0 \mathcal{D}_{loc} + \rho_0 r - \text{Div} \mathbf{Q} \quad \text{with} \quad \rho_0 \mathcal{D}_{loc} \geq 0. \quad (3.38)$$

The entropy has been defined as the negative derivative of the free energy function with respect to the temperature field. Hence, its temporal change can alternatively be written

$$\rho_0 \left( \frac{\partial}{\partial t} \eta \right) \theta = \rho_0 \left( \frac{\partial}{\partial t} (-\partial_\theta \psi) \right) \theta = \rho_0 c \frac{\partial}{\partial t} \theta + \rho_0 \mathcal{H}. \quad (3.39)$$

Here, the heat capacity  $c$  and the thermo-elastic heating  $\mathcal{H}$  have been introduced

$$c := -\theta \partial_{\theta\theta}^2 \psi \quad \text{and} \quad \mathcal{H} := -\theta \left( \partial_{\theta \mathbf{F}}^2 \psi : \frac{\partial}{\partial t} \mathbf{F} + \partial_{\theta \mathcal{I}}^2 \psi : \frac{\partial}{\partial t} \mathcal{I} \right). \quad (3.40)$$

By combination of (3.38) and (3.39) an evolution equation for the temperature field  $\theta$  is conceived which is referred to as the *temperature evolution equation of thermo-inelasticity*

$$\rho_0 c \frac{\partial}{\partial t} \theta = -\text{Div} \mathbf{Q} + \rho_0 r - \rho_0 \mathcal{H} + \rho_0 \mathcal{D}_{loc}. \quad (3.41)$$

Physically,  $\mathcal{H}$  and  $\mathcal{D}_{loc}$  characterize the thermo-elastic coupling and dissipative effects. Following a standard argumentation of metal-plasticity, cf. MIEHE [120], the first contribution is small compared to the latter one,  $|\mathcal{H}| \ll \mathcal{D}_{loc}$ , and can be neglected,  $\mathcal{H} \approx 0$ . What remains unspecified up to now is a constitutive equation for the heat flux vector  $\mathbf{Q}$ . This quantity is assumed to be governed by an isotropic Fourier law

$$\mathbf{Q} = -k \nabla_{\mathbf{X}} \theta \quad (3.42)$$

where the material parameter  $k > 0$  represents the thermal conductivity.

**3.2.2.4. Inelastic response: Evolution of the internal variables.** The inelastic response of the solid is described by the internal variable field  $\mathcal{I}$ . For the subsequent investigations the focus is on fully rate-independent models of inelasticity. With the local balance equations (3.33) and (3.34) at hand the dissipation postulate (3.32) boils down to the reduced dissipation inequality

$$\mathcal{D} = \int_{\mathcal{B}} \delta \, dV \geq 0 \quad \text{with} \quad \delta := \mathcal{F} \cdot \frac{\partial}{\partial t} \mathcal{I} \quad (3.43)$$

with the dissipation  $\delta$  per unit volume of the inelastic solid. It is the inner product of the driving forces  $\mathcal{F} = -\partial_{\mathcal{I}} \psi$  and the local rate  $\partial \mathcal{I} / \partial t$  of the internal variable field at material position  $\mathbf{X} \in \mathcal{B}$ . The evolution  $\partial \mathcal{I} / \partial t$  has to be set up based on a constitutive assumption. To this end, consider a yield criterion function

$$\phi(\mathcal{F}) = f(\mathcal{F}) - y_0 \leq 0 \quad (3.44)$$

in terms of the yield stress  $y_0$  and the level set function  $f(\mathcal{F})$ . The yield criterion function governs the elastic domain

$$\mathbb{E} = \{ \mathcal{F} \mid \phi(\mathcal{F}) \leq 0 \} \quad (3.45)$$

which bounds the internal stress state. For  $\phi < 0$  the response is elastic, otherwise, for  $\phi = 0$ , the material behaves inelastically. In that case, the evolution of the internal variables has to be specified such that the second law of thermodynamics represented by the reduced dissipation inequality (3.43) is satisfied. For associated models of inelasticity the evolution equations can be derived from the principle of maximum dissipation

$$\delta := \max_{\mathcal{F} \in \mathbb{E}} \left\{ \mathcal{F} \cdot \frac{\partial}{\partial t} \mathcal{I} \right\} \quad (3.46)$$

stating that the current internal stress state maximizes the dissipation compared to all admissible internal stress states, i.e.

$$\mathcal{F} \cdot \frac{\partial}{\partial t} \mathcal{I} \geq \mathcal{F}^* \cdot \frac{\partial}{\partial t} \mathcal{I} \quad \text{for all} \quad \mathcal{F}^* \in \mathbb{E}. \quad (3.47)$$

The optimization principle (3.46) with the inequality constraint (3.45), i.e. the elastic domain, can be formulated by the Lagrange functional

$$\mathcal{L}(\mathcal{F}, \lambda) = -\mathcal{F} \cdot \frac{\partial}{\partial t} \mathcal{I} + \lambda \phi(\mathcal{F}) \rightarrow \text{stat} \quad (3.48)$$

where  $\lambda$  is the Lagrange multiplier. The necessary condition for the solution of this functional, i.e.  $\partial_{\mathcal{F}} \mathcal{L} = 0$ , induces the evolution equations for the internal variables

$$\frac{\partial}{\partial t} \mathcal{I} = \lambda \partial_{\mathcal{F}} \phi(\mathcal{F}) \quad (3.49)$$

typically denoted the flow rules along with the Karush-Kuhn-Tucker conditions of the optimization principle

$$\phi \leq 0, \quad \lambda \geq 0 \quad \text{and} \quad \phi \lambda = 0 \quad (3.50)$$

referred to as the loading-unloading conditions. According to these conditions the pair  $\phi < 0$  and  $\lambda = 0$  characterizes elastic material behavior whereas the pair  $\phi = 0$  and  $\lambda > 0$  indicates the occurrence of associated inelastic flow characterized by the evolution equation (3.49) with amount  $\lambda$  into the direction  $\partial_{\mathcal{F}} \phi$ .

**Remark 3.2:** Observe that the evolution equations for the temperature and the internal variable field refer just to the local part of the time derivatives (3.14) of these objects corresponding to the time derivative at fixed material position. This procedure anticipates an essential feature of the solution strategy to be discussed in detail within Section 3.4.

### 3.3. Discrete Finite Element Formulation

The discrete counterparts of the governing equations of configurational thermo-inelasticity are developed by application of the standard finite element approach for the three unknown fields, namely the material and spatial coordinates as well as the temperature.

**3.3.1. Spatial Discretization of the Inelastic Solid.** The approximation starts with the subdivision of the material body  $\mathcal{B}$  into a set of  $n_{ele}$  finite elements

$$\mathcal{B} \approx \mathcal{B}^h = \mathbf{A}_{e=1}^{n_{ele}} \mathcal{B}^e, \quad (3.51)$$

see also Figure 3.3 for a sketch of the procedure. The symbol  $\mathbf{A}_{e=1}^{n_{ele}}$  denotes the standard

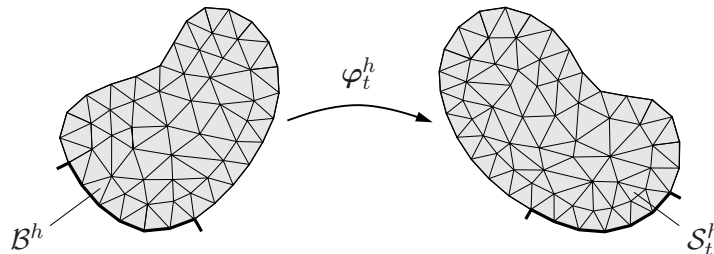


**Figure 3.3:** Spatial discretization of the inelastic solid. The material body  $\mathcal{B}$  is discretized with  $n_{ele}$  finite elements  $\mathcal{B}^e$  yielding an approximation of the body  $\mathcal{B} \approx \mathcal{B}^h$ .

finite element assembly operator. The material and spatial configurational maps  $\Xi_t$  and  $\xi_t$  (3.3) are approximated for each finite element via

$$\mathbf{x} \approx \xi_t^h(\boldsymbol{\theta}) = \mathbf{N}(\boldsymbol{\theta}) \mathbf{d}_t \quad \text{and} \quad \mathbf{X} \approx \Xi_t^h(\boldsymbol{\theta}) = \mathbf{N}(\boldsymbol{\theta}) \mathbf{D}_t. \quad (3.52)$$

Here,  $\mathbf{d}_t \in \mathcal{R}^{\mathcal{N}_t}$  and  $\mathbf{D}_t \in \mathcal{R}^{\mathcal{N}_t}$  characterize the discrete spatial and material coordinates at time  $t$  of all  $\mathcal{N}_t$  nodal points of the current finite element mesh.  $\mathbf{N}$  represents the matrix of shape functions parameterized by the local coordinates  $\boldsymbol{\theta} \in \Omega^e$  of the finite element parameter space  $\Omega^e$ . Without loss of generality the same interpolation functions are used for the spatial and material coordinates. Based on this fundamental approximation the discrete counterparts of the material and spatial gradients (3.6)<sub>2,3</sub> can be computed

$$\mathbf{j}_t^h = \tilde{\mathbf{B}}(\boldsymbol{\theta})\mathbf{d}_t \quad \text{and} \quad \mathbf{J}_t^h = \tilde{\mathbf{B}}(\boldsymbol{\theta})\mathbf{D}_t \quad (3.53)$$

in terms of the interpolation matrix  $\tilde{\mathbf{B}}$  which contains the derivative of the shape functions  $\mathbf{N}$  with respect to the coordinates  $\boldsymbol{\theta}$  of the parameter space. With the gradients (3.53) at hand, the discrete counterpart of the deformation gradient (3.6)<sub>1</sub> reads

$$\mathbf{F}_t^h = \mathbf{j}_t^h \mathbf{J}_t^{h-1} =: \mathbf{B}(\mathbf{X}^h)\mathbf{d}_t \quad (3.54)$$

where  $\mathbf{B}(\mathbf{X}^h)$  states the matrix of the derivatives of the shape functions  $\mathbf{N}$  with respect to the Lagrangian coordinates  $\mathbf{X}^h$ . Figure 3.4 provides a schematic visualization of the discretization process referring to one single element.

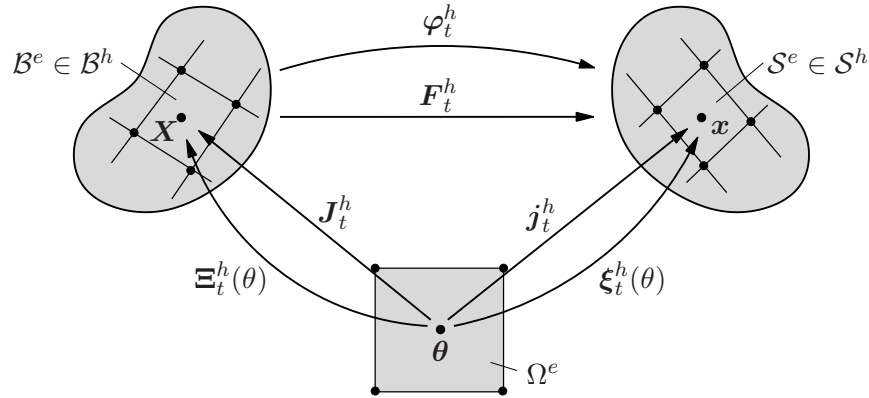


**Figure 3.4:** Mappings between the unit element parameter space  $\Omega^e$  and the associated Lagrangian and Eulerian finite elements  $\mathcal{B}^e \subset \mathcal{B}$  and  $\mathcal{S}^e \subset \mathcal{S}$ .

**3.3.2. Global Response of the Spatially Discretized Inelastic Solid.** The subsequent treatments follow the same processing used in the continuous setting. Attention is focused on the derivation of the discrete versions of the coupled field equations.

**3.3.2.1. Discrete version of the global dissipation postulate.** At first, a discrete counterpart of the global dissipation postulate is elaborated. Based on the finite element approximation (3.52) the material and spatial velocity fields can be computed by

$$\dot{\boldsymbol{\xi}}_t^h = \mathbf{N}\dot{\mathbf{d}}_t \quad \text{and} \quad \dot{\boldsymbol{\Xi}}_t^h = \mathbf{N}\dot{\mathbf{D}}_t \quad \text{with} \quad \dot{\mathbf{d}}_t = \frac{\partial}{\partial t}\mathbf{d}_t \quad \text{and} \quad \dot{\mathbf{D}}_t = \frac{\partial}{\partial t}\mathbf{D}_t \quad (3.55)$$

The global vectors  $\dot{\mathbf{D}}_t$  and  $\dot{\mathbf{d}}_t$  represent the discrete material and spatial nodal velocities. The discrete material gradients of these fields are evaluated by

$$\nabla_{\mathbf{X}}\dot{\boldsymbol{\xi}}_t^h = \mathbf{B}\dot{\mathbf{d}}_t \quad \text{and} \quad \nabla_{\mathbf{X}}\dot{\boldsymbol{\Xi}}_t^h = \mathbf{B}\dot{\mathbf{D}}_t \quad (3.56)$$

incorporating the interpolation matrix  $\mathbf{B}$  introduced in (3.54). Substitution of the finite element approximations of the kinematic objects into representation (3.31) of the global dissipation results in the discrete version of the global dissipation inequality

$$\mathcal{D}^h = \sum_{I=1}^{\mathcal{N}_t} \{ [\mathbf{p}_I + \mathbf{f}_I] \cdot \dot{\mathbf{d}}_I + [\mathbf{P}_I + \mathbf{F}_I] \cdot \dot{\mathbf{D}}_I \} + \mathcal{D}_{bulk}^h \geq 0. \quad (3.57)$$

In the discrete setting the global dissipation appears in a natural fashion as a sum of discrete nodal contributions evaluated at every node  $I = 1, \mathcal{N}_t$  of the mesh. In this equation the following definitions of nodal quantities have been introduced. For the spatial problem

$$\mathbf{p}_I := \mathbf{A}_{e=1}^{n_{ele}} \left\{ \int_{\mathcal{B}^e} \mathbf{N}_I^T \bar{\boldsymbol{\gamma}}_0 dV + \int_{\partial \mathcal{B}^e} \mathbf{N}_I^T \bar{\mathbf{t}} dA \right\} \quad (3.58)$$

displays the nodal vector of external physical forces in terms of the volume forces  $\bar{\boldsymbol{\gamma}}_0$  and the surface tractions  $\bar{\mathbf{t}}$ . The vector of internal spatial forces

$$\mathbf{f}_I := - \mathbf{A}_{e=1}^{n_{ele}} \int_{\mathcal{B}^e} \mathbf{B}_I^T \mathbf{P} dV \quad (3.59)$$

related to the discrete node  $I$  is governed by the first Piola-Kirchhoff stresses  $\mathbf{P}$ . With respect to the dual material problem

$$\mathbf{P}_I := \mathbf{A}_{e=1}^{n_{ele}} \int_{\mathcal{B}^e} \mathbf{N}_I^T \bar{\boldsymbol{\Gamma}}_0 dV \quad (3.60)$$

denotes the *discrete configurational* or *material nodal force* at node  $I$ . Recalling definition (3.29) of the continuous configurational force  $\bar{\boldsymbol{\Gamma}}_0$ , the configurational nodal force is a function of the material gradients of the temperature field  $\theta$  and the internal variable vector  $\boldsymbol{\mathcal{I}}$ , i.e.  $\nabla_X \theta$  and  $\nabla_X \boldsymbol{\mathcal{I}}$ . The latter dependence demands a particular treatment concerning the numerical implementation and is discussed in detail in Section 3.5 below. The *internal material nodal force*

$$\mathbf{F}_I := - \mathbf{A}_{e=1}^{n_{ele}} \int_{\mathcal{B}^e} \mathbf{B}_I^T \boldsymbol{\Sigma} dV \quad (3.61)$$

relies on Eshelby's energy-momentum tensor  $\boldsymbol{\Sigma}$  introduced in (3.27) as the purely material stress tensor dual to the nominal stresses  $\mathbf{P}$ . The finite element matrices  $\mathbf{N}_I$ ,  $\mathbf{B}_I$  refer to a particular node  $I$  of the mesh and represent the entries of the global matrices  $\mathbf{N}$ ,  $\mathbf{B}$ .

**3.3.2.2. Dual material and spatial nodal equilibrium conditions.** In analogy to the continuous framework, the discrete global dissipation postulate is exploited in the sense of a global Coleman method. To this end, consider the admissible material and spatial velocity fields originally introduced in (3.10) and (3.11). In the discrete setting, these conditions are represented by admissible spatial and material nodal velocities

$$\dot{\mathbf{d}}_I := \{ \dot{\mathbf{d}}_I \mid \dot{\mathbf{d}}_I = \dot{\bar{\mathbf{d}}}_I \text{ on } \partial \mathcal{B}_\varphi^h \} \quad \text{and} \quad \dot{\mathbf{D}}_I := \{ \dot{\mathbf{D}}_I \mid \dot{\mathbf{D}}_I = \mathbf{0} \text{ on } \partial \mathcal{B}^h \}. \quad (3.62)$$

The discrete version (3.57) of the dissipation postulate has to be satisfied for all admissible spatial and material velocity fields. Exploitation of the dissipation inequality for arbitrary admissible spatial fields results in the spatial equilibrium condition

$$\mathbf{f}_I + \mathbf{p}_I = \mathbf{0} \quad \text{in } \mathcal{B}^h \quad \text{and on } \partial \mathcal{B}_t^h. \quad (3.63)$$

This condition demands an equilibrium of internal and external physical forces in the discrete domain  $\mathcal{B}^h$  and on the material boundary  $\partial\mathcal{B}^h$ . It displays the discrete counterpart of (3.33). For arbitrary admissible material fields the dual material equilibrium condition

$$\mathbf{F}_I + \mathbf{P}_I = \mathbf{0} \quad \text{in } \mathcal{B}^h \quad (3.64)$$

is obtained being the discrete version of the material balance (3.34). This condition enforces the equilibration of internal material forces and discrete configurational forces at all interior nodes of the discrete domain  $\mathcal{B}^h$ . As it will be used several times in the upcoming paragraphs, this material condition is well applicable in the context of  $r$ - or  $h$ -adaptive refinement strategies and can be denoted a condition for an optimal mesh.

**3.3.2.3. Discretization of the temperature evolution equation.** To set up the discrete counterpart of the temperature evolution equation (3.41) in a first step a weak form expression is derived. The temperature equation is tested by any arbitrary test function  $\delta\theta$  which satisfies the homogeneous form of the essential boundary conditions, i.e.  $\delta\theta = 0$  on  $\partial\mathcal{B}_\theta$ . The whole equation is integrated over the material body  $\mathcal{B}$ . Application of Gauss integration theorem and substitution of the von Neumann boundary condition for the heat flux,  $\bar{Q}_n = \mathbf{Q} \cdot \mathbf{N}$  on  $\partial\mathcal{B}_{\bar{Q}_n}$ , gives the weak form equation

$$G_\vartheta := \int_{\mathcal{B}} \delta\theta \rho_0 \left( c \frac{\partial}{\partial t} \theta - \mathcal{D}_{loc} - r \right) - \nabla_{\mathbf{X}} \delta\theta \cdot \mathbf{Q} \, dV + \int_{\partial\mathcal{B}_{\bar{Q}_n}} \delta\theta \bar{Q}_n \, dA = 0. \quad (3.65)$$

The thermo-elastic heating  $\mathcal{H}$  has a priori been neglected due to the reasoning discussed in the context of equation (3.41).

The spatial discretization bases on the subdivision (3.51) of the body into  $n_{ele}$  finite elements  $\mathcal{B}^e$ . The scalar temperature field  $\theta$  is approximated in the element domain

$$\theta \approx \theta^h = \mathbf{N}^\theta(\boldsymbol{\theta}) \boldsymbol{\vartheta}_t. \quad (3.66)$$

where  $\mathbf{N}^\theta$  denotes the matrix of interpolation functions for the temperature problem. The superscript  $\theta$  indicates that in general different shape functions compared to the coordinate approximation (3.52) can be employed. The vector  $\boldsymbol{\vartheta}_t$  contains the temperatures at all  $\mathcal{N}_t$  nodal points of the current mesh at time  $t$ . The same approximation applies for the test function  $\delta\theta$  and its material gradient by using the virtual nodal value  $\delta\boldsymbol{\vartheta}$  instead

$$\delta\theta = \mathbf{N}^\theta \delta\boldsymbol{\vartheta} \quad \text{and} \quad \nabla_{\mathbf{X}} \delta\theta = \mathbf{N}_{,\mathbf{X}}^\theta \delta\boldsymbol{\vartheta}. \quad (3.67)$$

The matrix  $\mathbf{N}_{,\mathbf{X}}^\theta$  contains the derivatives of the shape functions  $N^\theta$  with respect to the material coordinates  $\mathbf{X}$ .

Turning next to the time discretization, the whole scalar time domain is subdivided into a finite number of discrete time steps  $\Delta t$ . The time derivative  $\partial\theta/\partial t$  of the temperature is approximated by the difference of the temperature at time  $t_{n+1}$  and  $t_n$  divided by the time increment, i.e.  $\partial\theta/\partial t = (\theta - \theta_n)/\Delta t$  with the abbreviation  $\theta_{n+1} =: \theta$ . At the end, the space-time discrete temperature evolution equation can be written as

$$G_\vartheta^h = \sum_{I=1}^{\mathcal{N}_t} \{ r_I \delta\vartheta_I \} = 0. \quad (3.68)$$



In analogy to the material and spatial equilibrium conditions the temperature evolution problem is governed by a sum of discrete nodal values or rather residuals  $r_I$  at node  $I$

$$r_I := \mathbf{A}_{e=1}^{n_{ele}} \left\{ \int_{\mathcal{B}^e} \mathbf{N}_I^{\theta T} \rho_0 \left( c \frac{\vartheta_I - \vartheta_{nI}}{\Delta t} - \mathcal{D}_{loc} - r \right) - \mathbf{N}_{,\mathbf{X}}^{\theta I T} \mathbf{Q} dV + \int_{\partial \mathcal{B}_{\bar{Q}_n}^e} \mathbf{N}_I^{\theta T} \bar{Q}_n dA \right\}. \quad (3.69)$$

For arbitrary admissible virtual temperatures  $\delta \vartheta_I$  one extracts the scalar-valued residual expression for the change of temperature at node  $I$

$$r_I = 0 \quad \text{in} \quad \mathcal{B}^h \quad (3.70)$$

to be solved for the current nodal temperature  $\vartheta_I$ .

**3.3.2.4. Inelastic response: Evolution of the internal variables.** Upon application of the Coleman-type exploitation method the global dissipation postulate boils down to the reduced dissipation inequality which reads in its discrete representation

$$\mathcal{D}^h = \int_{\mathcal{B}^h} \delta^h dV = \int_{\mathcal{B}^h} \mathcal{F}^h \cdot \frac{\partial}{\partial t} \mathcal{I}^h dV \geq 0. \quad (3.71)$$

The approximation  $\delta^h$  of the dissipation per unit reference volume is governed by the evolution  $\partial \mathcal{I}^h / \partial t$  of the internal variable field. Using the constitutive approach introduced in Subsection 3.2.2.4 this evolution is described by the associated flow rule (3.49)

$$\frac{\partial}{\partial t} \mathcal{I} = \lambda \partial_{\mathcal{F}} \phi(\mathcal{F}). \quad (3.72)$$

The algorithmic treatment starts with the integration of the evolution equation which, in an implicit scenario, is usually performed by means of a backward Euler integration scheme within the discrete time interval  $[t_n, t_{n+1}]$

$$\mathcal{I}_{n+1} = \mathcal{I}_n + \gamma (\partial_{\mathcal{F}} \phi)_{n+1}. \quad (3.73)$$

Here,  $\gamma = \lambda(t_{n+1} - t_n)$  denotes the incremental plastic multiplier. For the rate-independent case the decision on inelastic loading or elastic unloading is made via the Karush-Kuhn-Tucker conditions (3.50). The way to enforce these conditions will be crucial in view of the evaluation of discrete configurational nodal forces to be discussed in Section 3.5 below.

### 3.4. Summary of Governing Equations and Numerical Solution Procedure

The thermo-mechanically coupled problem is described by the local balance laws (3.33)<sub>1</sub> and (3.41) for the current spatial coordinates  $\mathbf{x}$  and the temperature field  $\theta$ . The evolution of the spatial deformation and the temperature is accompanied by the local realignment of inhomogeneities. This rearrangement of matter is described by a dual material motion which in a thermodynamical context is associated with the variation of material placements of material points with respect to the ambient material. Its unknowns are the material coordinates  $\mathbf{X}$  and again the temperature field. While the latter one is already described by the temperature evolution equation, the change of material coordinates is governed by the dual material balance law (3.34). Thus, the governing set of equations for the inelastic solid subjected to thermo-mechanical loading that in addition accounts



for structural changes of the material reference configuration reads

spatial equilibrium condition	$\text{Div} \mathbf{P} + \bar{\gamma}_0 = \mathbf{0}$	in $\mathcal{B}$	(3.74)
material equilibrium condition	$\text{Div} \Sigma + \bar{\Gamma}_0 = \mathbf{0}$	in $\mathcal{B}$	
temperature evolution equation	$-\text{Div} \mathbf{Q} + \rho_0 r + \rho_0 \mathcal{D}_{loc} = \rho_0 c \frac{\partial}{\partial t} \theta$	in $\mathcal{B}$ .	

These equations are valid for the respective boundary conditions for the spatial and material coordinates and the temperature field.

In strict analogy to the continuous setting, the discrete spatial and material nodal equilibrium conditions (3.63) and (3.64) in combination with the temperature equation (3.70) constitute the governing set of discrete nodal balances

equilibrium of spatial nodal forces	$\mathbf{f}_I + \mathbf{p}_I = \mathbf{0}$	in $\mathcal{B}^h$	(3.75)
equilibrium of configurational nodal forces	$\mathbf{F}_I + \mathbf{P}_I = \mathbf{0}$	in $\mathcal{B}^h$	
residual of temperature evolution	$r_I = 0$	in $\mathcal{B}^h$	

at every node  $I = 1, \mathcal{N}_t$  of the finite element mesh. These balances are subjected to the discrete versions of the respective essential boundary conditions.

A possible solution procedure of the thermo-mechanically coupled problem is given by the simultaneous solution of the three balance equations. This attempt may be referred to as a thermo-mechanically coupled arbitrary Lagrangian Eulerian formulation. This methodology will be discussed in Chapter 5 for the particular case of isothermal elasticity.

In the following, an alternative approach is elaborated. The flowchart in Figure 3.5 shows a descriptive sketch of the procedure. To be specific, the complete set of equations (3.75) is solved by means of a staggered solution strategy. The basic idea is to use the material equilibrium condition or, respectively, the discrete configurational nodal forces in the sense of a postprocessing tool. This algorithmic treatment exploits the most attractive feature of the material balance equation as it provides additional information about the present system without requiring the explicit solution of a new set of equations.

In a first step, the physical balance equation and for non-isothermal processes the temperature evolution equation are solved for the primary unknowns, namely the current spatial coordinates  $\mathbf{x}$  and the temperature  $\theta$ . For the solution of this coupled set of equations once more a staggered solution scheme is employed as it was proposed e.g. by SIMO & MIEHE [164], ARMERO & SIMO [6] or MIEHE [118, 120]. This means that the solution of (3.75)<sub>1,3</sub> is carried out by means of an operator split. In an isothermal predictor step the spatial deformation problem is solved at frozen temperature. Within a heat conduction thermal corrector step the temperature field is updated while the deformation is kept constant. This procedure allows for a decoupled solution of the governing system of equations and significantly reduces the numerical effort of the simulation. During the solution of this primary problem, the material positions are kept constant. Subjected to this condition, the convective parts in the total time derivatives (3.14) of the temperature field and internal state variables vanish and the update of these fields is performed by

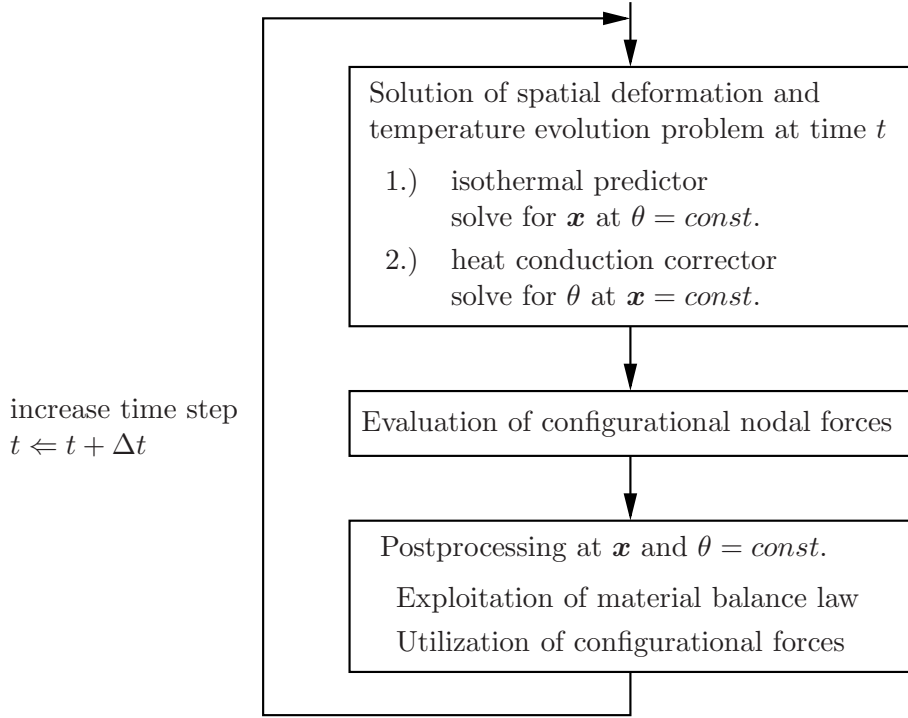


**Figure 3.5:** Flowchart of staggered solution procedure for the coupled non-isothermal deformation problem including a postprocessing step based on the material balance equation.

means of the algorithms introduced above exclusively based on the local time derivative  $\partial(\bullet)/\partial t = d(\bullet)/dt|_{X \text{ fixed}}$ , cf. Remark 3.2.

In the second step, with all the ingredients of the material nodal balance (3.75)<sub>2</sub> being available from the solution of the primary problem, the material postprocessing can be used at frozen spatial deformation and temperature e.g. for optimization strategies, for  $r$ -/ $h$ -adaptive refinement procedures and for the simulation of crack propagation defining the scope of the developments of the subsequent chapters.

### 3.5. Evaluation of Discrete Configurational Nodal Forces

In the sense of the above discussion, the evaluation of discrete configurational nodal forces does not pose a new boundary value problem but constitutes a postprocessing procedure of the non-isothermal spatial problem. For inelastic problems one crucial point needs to be investigated in detail. Recall definition (3.29) of the configurational force, i.e.  $\bar{\Gamma}_0 = -\mathbf{F}^T \bar{\gamma}_0 - \partial_\theta \psi \nabla_X \theta - \partial_{\mathcal{I}} \psi \cdot \nabla_X \mathcal{I} - \partial_{\mathbf{X}} \psi^{\text{expl}}$ . The evaluation of the second and third addends necessitates the material gradients of the temperature and the internal variable vector. Following finite element scheme these gradients are approximated via

$$\nabla_X \theta = \mathbf{N}_{,\mathbf{X}}^\theta \boldsymbol{\vartheta} \quad \text{and} \quad \nabla_X \mathcal{I} = \mathbf{N}_{,\mathbf{X}}^{\mathcal{I}} \tilde{\mathcal{I}}. \quad (3.76)$$

The matrices  $\mathbf{N}_{,\mathbf{X}}^\theta$  and  $\mathbf{N}_{,\mathbf{X}}^{\mathcal{I}}$  represent the derivatives of the shape functions with respect to the material coordinates  $\mathbf{X}$ . The order of the interpolation functions of the internal variables can be chosen independently from those of the spatial and material deformation and of the temperature problem. The global vectors  $\boldsymbol{\vartheta}$  and  $\tilde{\mathcal{I}}$  contain the discrete nodal values  $\vartheta_I$  and  $\tilde{\mathcal{I}}_I$  of the temperature and the internal variable field at every node  $I = 1, \mathcal{N}_t$  of the mesh. Hence, the evaluation of the gradients  $\nabla_X \theta$  and  $\nabla_X \mathcal{I}$  requires a global representation of the temperature and the internal variable field at the node point level of

the mesh. As the temperature is one of the primary variables of the coupled problem, the nodal values  $\vartheta_I$  are already known from the non-isothermal spatial solution. The global representation of the internal variable vector can be achieved in two different ways. On the one hand, the internal variables can be introduced as additional nodal degrees referred to as a *global formulation*. Alternatively, the internal variable field is computed at the integration point level within a standard *local formulation* and then, in a postprocessing procedure, is projected onto the nodal points by means of smoothing algorithms. With the nodal values at hand the material gradients (3.76) are readily computed whereupon the discrete configurational nodal force  $\mathbf{P}_I$  can be evaluated.

**3.5.1. Global Formulation: Introduction of Additional Nodal Degrees.** In a global scenario the internal variable vector  $\mathcal{I}$  is introduced as a primary variable in addition to the spatial coordinates and the temperature field. The approximation is carried out via the finite element approach

$$\mathcal{I} \approx \mathcal{I}^h = \mathbf{N}^{\mathcal{I}} \tilde{\mathcal{I}} \quad (3.77)$$

An illustrative sketch of this three field formulation is provided in Figure 3.6. A mixed

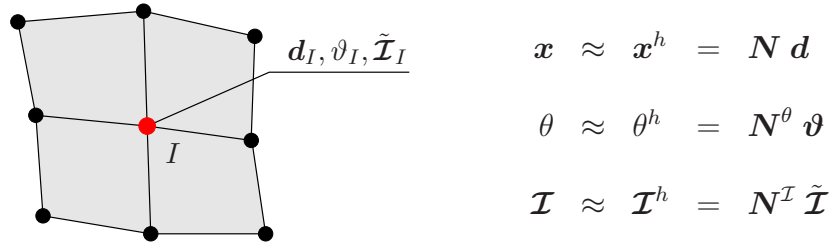


**Figure 3.6:** Global formulation. The internal variables are introduced as additional nodal degrees. This three-field approach is governed by the spatial equilibrium condition, the temperature evolution equation and an accompanying subproblem.

finite element formulation with an internal strain-like variable being discretized in addition to the displacement field has been set up by PINSKY [148], however, in a local context and at small strains. SIMO, KENNEDY & TAYLOR [163] developed an alternative treatment based on a complementary mixed finite element formulation. Within this concept the loading condition is enforced in a weak format on the element level. A similar procedure, namely a two-field finite element formulation for elasticity coupled to damage, can be found in FLOREZ-LOPEZ ET AL. [47]. An algorithmic formulation similar to the approach to be developed in the following has been elaborated by LIEBE, STEINMANN & BENALLAL [91] within the context of geometrically linear phenomenological gradient damage as well as LIEBE & STEINMANN [90] and LIEBE, MENZEL & STEINMANN [89] in view of gradient plasticity including additional boundary conditions. A global formulation for finite strain gradient crystal-plasticity is discussed by BECKER [13].

The change of the internal variables is governed by an evolution equation frequently denoted the flow rule. Adopting the basic feature of the global formulation, i.e. the finite element approximation (3.77), this evolution equation is discretized in space and time. This set of space-time-discrete equations constitutes in combination with the discrete weak form equations (3.75)<sub>1,3</sub> the overall system of equations to be solved for the current nodal values of the spatial coordinates, the temperature and each component of the internal variable vector. Regarding its numerical efficiency, the fundamental drawback of this

approach is rather obvious. Consider for instance the model problem of non-isothermal finite strain plasticity in the three-dimensional setting. The deformation gradient is multiplicatively decomposed into an elastic and a plastic part,  $\mathbf{F} = \mathbf{F}^e \mathbf{F}^p$ . Thereby,  $\mathbf{F}^p$  is a non-symmetric second order tensor containing nine independent components. Consequently, the global formulation introduces in total thirteen scalar nodal degrees, namely three spatial displacements, the temperature and the nine values of the internal variable vector. Hence, the full discretization of the internal variable field dramatically increases the numerical effort of the computation and turns out to be an unfavorable approach.

A numerically cheaper even though still extensive and costly attempt is applicable in case the direction of the inelastic evolution remains constant during inelastic flow. In that case solely the amount of inelastic flow, i.e. one scalar field, has to be introduced as an additional nodal degree. This reasoning also holds if the internal variable vector a priori consists of one scalar field, e.g. the damage parameter  $d$  of damage mechanics.

**Remark 3.3:** In order to make things more clear consider the evolution equation (3.49)

$$\frac{\partial}{\partial t} \mathcal{I} = \lambda \partial_{\mathcal{F}} \phi(\mathcal{F}). \quad (3.78)$$

The Lagrange multiplier  $\lambda$  characterizes the amount of inelastic flow in the direction  $\partial_{\mathcal{F}} \phi$ . For one scalar internal variable the direction  $\partial_{\mathcal{F}} \phi$  boils down to just a scaling of the amount  $\lambda$  and does not contribute in the sense of a coordinate-dependent quantity. On the contrary, if the direction depends on the Lagrangian coordinates, the evaluation of the material gradient of  $\mathcal{I}$  demands the consideration of the gradients of both the amount  $\lambda$  and the direction  $\partial_{\mathcal{F}} \phi$ . If the direction is constant, e.g. in crystal-plasticity where plastic slip occurs in the direction of given slip systems, the material gradient of the internal variable field is exclusively governed by the gradient of the amount of inelastic flow.

In the sense of a *reduced global formulation* the subsequent investigations concentrate on the particular case that the evolution of the internal variable vector is solely determined by the amount  $\lambda$  of inelastic flow apart from some scaling or a constant direction  $\partial_{\mathcal{F}} \phi = \text{const}$ . This approach requires an accompanying subproblem which enters the strong form equations (3.74). In the following, the loading-unloading conditions (3.50), i.e.

$$\phi \leq 0, \quad \dot{\gamma} \geq 0 \quad \text{and} \quad \phi \dot{\gamma} = 0, \quad (3.79)$$

set up this constitutive subproblem. This treatment is conceptually in line with the ideas proposed within the framework of configurational mechanics by LIEBE, DENZER & STEINMANN [88] for isothermal finite strain continuum damage and MENZEL, DENZER & STEINMANN [115] in view of isothermal single-crystal-plasticity at small strains. Compared to (3.78) the Lagrange multiplier  $\lambda$  has been substituted by the evolution  $\dot{\gamma}$  of a scalar quantity  $\gamma$  characterizing e.g. the damage variable of damage mechanics or the incremental plastic multiplier associated with one slip system in crystal-plasticity. With these supplementary equations at hand the strong form of the thermo-mechanically coupled boundary value problem can be summarized as follows

---

spatial equilibrium condition	$\text{Div} \mathbf{P} + \bar{\gamma}_0 = \mathbf{0}$	in $\mathcal{B}$	
temperature evolution equation	$-\text{Div} \mathbf{Q} + \rho_0 r + \rho_0 \mathcal{D}_{loc} = \rho_0 c \frac{\partial}{\partial t} \theta$	in $\mathcal{B}$	(3.80)
loading-unloading	$\phi \leq 0, \quad \dot{\gamma} \geq 0$	in $\mathcal{B}$	

---

valid for the essential and natural boundary conditions

---


$$\begin{aligned}
 \text{spatial deformation} \quad \varphi &= \bar{\varphi} \quad \text{on } \partial\mathcal{B}_\varphi, & \mathbf{PN} &= \bar{\mathbf{t}} \quad \text{on } \partial\mathcal{B}_\mathbf{t} \\
 \text{temperature evolution} \quad \theta &= \bar{\theta} \quad \text{on } \partial\mathcal{B}_\theta, & \mathbf{Q} \cdot \mathbf{N} &= \bar{Q}_n \quad \text{on } \partial\mathcal{B}_{\bar{Q}_n}.
 \end{aligned} \tag{3.81}$$


---

Based on the loading-unloading conditions (3.79) the whole domain is split up into a non-active part  $\mathcal{B}_{el}$  and an active part  $\mathcal{B}_{inel}$  completing the strong form equations

---


$$\begin{aligned}
 \text{non-active part} \quad \mathcal{B}_{el} &= \{ \mathbf{X} \in \mathcal{B} \mid \phi \leq 0 \wedge \dot{\gamma} = 0 \} \\
 \text{active part} \quad \mathcal{B}_{inel} &= \{ \mathbf{X} \in \mathcal{B} \mid \phi = 0 \wedge \dot{\gamma} > 0 \}.
 \end{aligned} \tag{3.82}$$


---

The algorithmic treatment of this three field approach is presented in Appendix C featuring an enhanced strain formulation. The numerical implementation of the global formulation demands a non-standard finite element data environment. Beyond this, the numerical effort of the computation is increased significantly by the introduction of additional nodal degrees which is only necessary for the postprocessing concerned with the evaluation of the discrete material nodal forces.

**Remark 3.4:** The global formulation is not to be confused with a truly *non-local formulation* in the context of higher order or generalized continua. Thereby, the inelastic mechanism can be conceptually described by order parameters governed by additional field equations along with respective boundary conditions. Without claim of completeness the reader is referred to the fundamental contribution of CAPRIZ [26] and the review article of MARIANO [97], see also the references cited therein, as well as the above-mentioned literature concerning strain gradient plasticity or non-local inelasticity. The link between these non-local theories and the concept of configurational mechanics can be found e.g. by MARIANO [96] and SVENDSEN [179] as well as the recent report of FRANKENREITER [49]. Nevertheless, the global approach presented above provides a conceptual means with regard to the numerical treatment of some cases of such truly non-local methods.

**3.5.2. Local Formulation. Application of Smoothing Algorithms.** The local formulation bases on a standard solution of the thermo-mechanically coupled problem. In this scenario the strong form equations are

---


$$\begin{aligned}
 \text{spatial equilibrium condition} \quad \text{Div} \mathbf{P} + \bar{\gamma}_0 &= \mathbf{0} \quad \text{in } \mathcal{B} \\
 \text{temperature evolution equation} \quad -\text{Div} \mathbf{Q} + \rho_0 r + \rho_0 \mathcal{D}_{loc} &= \rho_0 c \frac{\partial}{\partial t} \theta \quad \text{in } \mathcal{B}
 \end{aligned} \tag{3.83}$$


---

constrained by the respective Dirichlet and von Neumann boundary conditions (3.81). While the global procedure enforces the loading-unloading conditions (3.79) on the node point level of the finite element mesh, in the local setting the decision on inelastic loading is made on the integration point level during the constitutive stress update algorithm. Starting from (3.83), the corresponding weak form is deduced whereupon spatial and temporal discretization is applied as already described in Section 3.3. The resulting set of non-linear discrete equations can be formulated by the residual expressions

$$\mathbf{r}_u = \sum_{I=1}^{\mathcal{N}_t} \{ \mathbf{p}_I + \mathbf{f}_I \} = \mathbf{0} \quad \text{and} \quad \mathbf{r}_\theta = \sum_{I=1}^{\mathcal{N}_t} r_I = 0. \tag{3.84}$$

They display the global counterparts of the nodal balances (3.75)<sub>1,3</sub> in terms of the external and internal spatial nodal forces  $\mathbf{p}_I$  and  $\mathbf{f}_I$ , cf. (3.58), (3.59), and the temperature residual  $r_I$  defined in (3.69). For the solution of this coupled set of equations a Newton-Raphson-type iteration is employed requiring the consistent linearization with respect to the primary variables, namely the spatial displacements and the temperature. To this end, the approximation of the increments of these variables is introduced

$$\Delta \mathbf{u} \approx \mathbf{N} \Delta \mathbf{d} \quad \text{and} \quad \Delta \theta \approx \mathbf{N}^\theta \Delta \vartheta \quad (3.85)$$

with the global vector fields  $\Delta \mathbf{d}$ ,  $\Delta \vartheta$  containing the nodal increments of the respective variable at all  $\mathcal{N}_t$  nodal points. Taking into account the staggered solution strategy discussed in Section 3.4 the linearization ends up with the decoupled system of linear equations

$$\begin{bmatrix} \mathbf{k}_{uu} & \mathbf{0} \\ \mathbf{0} & \mathbf{k}_{\vartheta\vartheta} \end{bmatrix} \begin{bmatrix} \Delta \mathbf{d} \\ \Delta \vartheta \end{bmatrix} = \begin{bmatrix} \mathbf{r}_u \\ \mathbf{r}_\vartheta \end{bmatrix} \quad (3.86)$$

This system is solved for the increments  $\Delta \mathbf{d}$  of the spatial nodal displacements and  $\Delta \vartheta$  of the nodal temperature and the current nodal values are evaluated by the Newton-update

$$\mathbf{d} \Leftarrow \mathbf{d} + \Delta \mathbf{d} \quad \text{and} \quad \vartheta \Leftarrow \vartheta + \Delta \vartheta. \quad (3.87)$$

The components of the global stiffness matrix are given by

$$\begin{aligned} \mathbf{k}_{uu} &= \int_{\mathcal{B}^h} \mathbf{B}^T \partial_{\mathbf{F}} \mathbf{P} \mathbf{B} \, dV \\ \mathbf{k}_{\vartheta\vartheta} &= \int_{\mathcal{B}^h} \mathbf{N}^{\theta T} \rho_0 \left( \frac{c}{\Delta t} - \partial_{\vartheta} \mathcal{D}_{loc} \right) \mathbf{N}^\theta + \mathbf{N}_{,\mathbf{X}}^{\theta T} k \mathbf{N}_{,\mathbf{X}}^\theta \, dV. \end{aligned} \quad (3.88)$$

For the tangent operator  $\mathbf{k}_{\vartheta\vartheta}$  associated with the temperature problem the Fourier law (3.42) for the heat flux vector,  $\mathbf{Q} = -k \nabla_{\mathbf{X}} \theta$ , has been employed. The quantification of the local dissipation  $\mathcal{D}_{loc}$  is a difficult task. According to MIEHE [120] and the references quoted therein the dissipation of a plastic deformation process is given by a certain fraction  $\chi \in [0; 1]$  of the total plastic power. This quantity can be written as the product of the current yield stress  $\hat{y}(\mathcal{F}, \theta)$  and the evolution  $\dot{\gamma}$  of the amount of plastic flow. Based on this assumption the algorithmic expression for the local dissipation is

$$\mathcal{D}_{loc} := \chi(\hat{y}(\mathcal{F}, \theta_n)) \dot{\gamma} = \chi(\hat{y}(\mathcal{F}, \theta_n)) (\gamma_{n+1} - \gamma_n) / \Delta t. \quad (3.89)$$

In this approximative scenario the dissipation is evaluated in terms of the temperature  $\theta_n$  at time  $t_n$ . Thus, the sensitivity of the dissipation with respect to the current temperature vanishes,  $\partial_{\vartheta} \mathcal{D}_{loc} = 0$ , and the stiffness matrix of the temperature problem appears as a function just of the finite element matrices  $\mathbf{N}^\theta$  and  $\mathbf{N}_{,\mathbf{X}}^\theta$ , the material parameters  $c$  and  $k$  denoting the heat capacity and the conductivity, and the discrete time step  $\Delta t$ .

With the spatial and thermal solution at hand, the discrete configurational nodal forces are computed in a postprocessing step. The computation of the material gradient (3.76)<sub>2</sub> demands a global representation of the internal variable field which at the moment is only available at the integration points and has to be projected onto the node point level by means of smoothing algorithms, cf. MENZEL, DENZER & STEINMANN [115], NGUYEN,



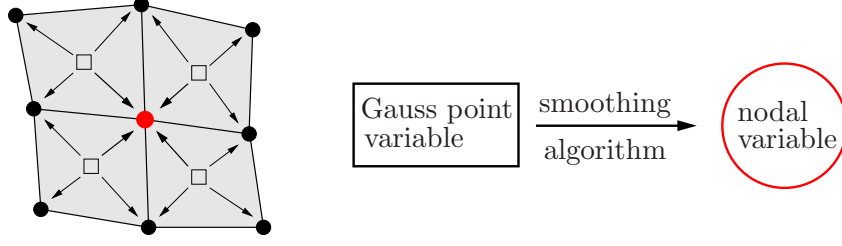


**Figure 3.7:** Local formulation. After a standard spatial computation the internal variable field is projected from the integration points onto the nodal points by means of smoothing algorithms fitting the idea of the material nodal force computation as a postprocessing step.

GOVINDJEE, KLEIN & GAO [138], and see Figure 3.7 for a sketch of the idea. In extension to these references two different smoothing algorithms are investigated.

The *L2-projection*, cf. e.g. ZIENKIEWICZ & TAYLOR [192], minimizes the difference between smoothed and original values of the Gauss point variables by the least square expression

$$\mathcal{L} := \int_{\mathcal{B}} (\mathcal{I}^* - \mathcal{I}_{\text{GP}})^T (\mathcal{I}^* - \mathcal{I}_{\text{GP}}) dV \rightarrow \text{Min.} \quad (3.90)$$

The smoothed Gauss point values  $\mathcal{I}^*$  are computed from projected nodal values  $\tilde{\mathcal{I}}$  via the finite element equation  $\mathcal{I}^* = \mathbf{N}^T \tilde{\mathcal{I}}$  in terms of the shape functions  $\mathbf{N}^T$ . These nodal values of the internal variables are obtained by solving a global system of equations

$$\int_{\mathcal{B}} \mathbf{N}^T \mathbf{N}^T dV \tilde{\mathcal{I}} = \int_{\mathcal{B}} \mathbf{N}^T \mathcal{I}_{\text{GP}} dV. \quad (3.91)$$

To reduce the numerical effort of the solution of this global system of equations, the coefficient matrix is diagonalized, e.g. by lumping schemes. Note that this diagonalization is reported to be sometimes critical in combination with higher order elements.

Alternatively, so-called *patch recovery techniques* can be used, developed by ZHU & ZIENKIEWICZ [190] and ZIENKIEWICZ & ZHU [194] in the context of a posteriori error estimation for adaptive strategies. The nodal values of the internal variables  $\tilde{\mathcal{I}}$  belong to a polynomial expansion  $\mathcal{I}_p$  of order  $p$  valid over an element patch surrounding the nodal point of interest. The  $i$ -th component of the polynomial is computed by

$$\mathcal{I}_p^i(\mathbf{X}) = \mathbf{P}(\mathbf{X}) \mathbf{a} \quad \text{with} \quad \mathbf{P}(\mathbf{X}) = [1 \ X \ Y \ \dots \ X^p \ Y^p] \quad (3.92)$$

with the polynomial terms  $\mathbf{P}$  up to the order of  $p$  listed here for the two-dimensional setting. The unknown parameters  $\mathbf{a}$  are determined by the least square expression

$$\mathcal{L} := \sum_{i=1}^n (\mathcal{I}_{\text{GP}}^i - \mathcal{I}_p^i)^2 = \sum_{i=1}^n (\mathcal{I}_{\text{GP}}^i - \mathbf{P}(\mathbf{X}) \mathbf{a})^2 \rightarrow \text{Min.} \quad (3.93)$$

minimizing the difference between the  $i$ -th component of the internal variable vector at the integration point and the  $i$ -th component of the polynomial. The necessary condition of (3.93) states that the derivative of  $\mathcal{L}$  with respect to the parameters  $\mathbf{a}$  vanishes,  $\partial \mathcal{L} / \partial \mathbf{a} = \mathbf{0}$ . Enforcing this condition, the patch recovery technique results in a system of equations to be solved for the coefficient vector  $\mathbf{a}$  locally at the element patch

$$\mathbf{a} = \left[ \sum_{i=1}^n \mathbf{P}^T \mathbf{P} \right]^{-1} \left[ \sum_{i=1}^n \mathbf{P}^T \mathcal{I}_{\text{GP}}^i \right]. \quad (3.94)$$

With known coefficient vector at hand the polynomial expansion  $\mathcal{I}_p$  is computed directly and the nodal values  $\tilde{\mathcal{I}}$  follow just by function evaluation. The polynomial terms  $\mathbf{P}$  remain unchanged for the computation of the coefficients  $\mathbf{a}$  for each component  $\mathcal{I}_p^i$  and consequently have to be evaluated only once for each element patch. In case higher order non-linear finite element shape functions are applied the following turned out to be appropriate. At first, for an internal node under consideration the average obtained from the recovery process of all patches containing this node should be used. Furthermore, the order  $p$  of the polynomial terms should be chosen in accordance with the order of the finite element interpolation functions as in that case the ideal convergence properties at the integration points are also achieved for the smoothed solution.

The local formulation avoids the introduction of additional degrees and therefore is numerically much more effective. Its characteristic perfectly fits the idea of the application of discrete configurational nodal forces in a postprocessing procedure.

### 3.6. Specification and Numerical Example

The above concepts are applied to thermo-crystal-plasticity. The constitutive framework is outlined shortly and Cook's membrane is analyzed as a boundary value problem.

**3.6.1. Model Problem: Thermo-Crystal-Plasticity.** The subsequent treatments follow the work of MIEHE [120], see also MIEHE [119] and MIEHE & SCHRÖDER [126], but, for simplicity, are restricted to one single slip system. The continuum slip theory bases on the multiplicative split of the deformation gradient into an elastic and a plastic part

$$\mathbf{F} = \mathbf{F}^e \mathbf{F}^p \quad (3.95)$$

in the local neighborhood of every material point  $\mathbf{X} \in \mathcal{B}$ . In crystal-plasticity the plastic part  $\mathbf{F}^p$  describes shear on a given slip system  $(\mathbf{S}, \mathbf{N})$  including both a stretch and a rotation whereas the elastic part  $\mathbf{F}^e$  governs elastic lattice distortions and rigid body motions. The slip system is characterized by the orthonormal vector pair  $(\mathbf{S}, \mathbf{N})$  with  $\mathbf{S}$  denoting the slip direction and  $\mathbf{N}$  being the slip normal. The energy storage mechanism of the material is assumed to depend on the lattice distortion  $\mathbf{F}^e$ , the temperature  $\theta$  and a scalar internal variable  $A$  describing isotropic hardening

$$\psi = \psi(\mathbf{F}^e, \theta, A) = \psi(\mathbf{F}, \mathbf{F}^p, \theta, A). \quad (3.96)$$

From the latter representation the internal variable vector is identified as  $\mathcal{I} = [\mathbf{F}^p, A]^T$ . The numerical example to be analyzed below presumes the particular free energy function

$$\begin{aligned} \psi = & \frac{1}{2} \kappa \ln^2 J - \kappa \alpha \ln J (\theta - \theta_0) + c (\theta - \theta_0 - \theta \ln \frac{\theta}{\theta_0}) + \frac{1}{2} \mu (\text{tr} \bar{\mathbf{b}}^e - 3) \\ & + \left[ (y_\infty - y_0) \left( A + \frac{1}{\omega} (\exp(-\omega A) - 1) \right) + \frac{1}{2} h A^2 \right] (1 - w(\theta - \theta_0)). \end{aligned} \quad (3.97)$$

It consists of a microscopic part in terms of the hardening variable  $A$  and the temperature  $\theta$  and a macroscopic part subdivided into a volumetric contribution depending on the determinant of the deformation gradient and the temperature, a heat capacity term depending only on the temperature, and an isochoric part in terms of the unimodular part  $\bar{\mathbf{b}}^e$  of the elastic Finger tensor

$$\mathbf{b}^e = \mathbf{F}^e \bar{\mathbf{G}}^{-1} \mathbf{F}^{eT} \quad \text{and} \quad \bar{\mathbf{b}}^e = \bar{\mathbf{F}}^e \bar{\mathbf{G}}^{-1} \bar{\mathbf{F}}^{eT} \quad \text{with} \quad \bar{\mathbf{F}}^e = J^{-\frac{1}{3}} \mathbf{F}^e. \quad (3.98)$$



Note that the plastic incompressibility condition  $J^p = \det \mathbf{F}^p = 1$  allows for the identifications  $\bar{\mathbf{F}}^p = \mathbf{F}^p$  and  $J = J^e J^p = J^e$ . The material parameters introduced in (3.97) are specified in Table 3.1 below. Coleman's exploitation of the Clausius-Planck-inequality (2.60) for the local dissipation gives the constitutive relations

$$\mathbf{P} = \partial_{\mathbf{F}}\psi = \partial_{\mathbf{F}^e}\psi \mathbf{F}^{p-T} \quad \text{and} \quad \rho_0 \eta = \eta_0 = -\partial_{\theta}\psi \quad (3.99)$$

for the first Piola-Kirchhoff stress tensor  $\mathbf{P}$  and the entropy  $\eta_0$  per unit volume of the reference configuration. What remains is the reduced dissipation inequality

$$\rho_0 \mathcal{D}_{loc} = \mathbf{P}^p : \dot{\mathbf{F}}^p + B \dot{A} \geq 0 \quad \text{with} \quad \mathbf{P}^p := -\partial_{\mathbf{F}^p}\psi, \quad B = -\partial_A \psi \quad (3.100)$$

in terms of the conjugate forces  $\mathcal{F} = [\mathbf{P}^p, B]^T$ . Instead of the plastic stresses  $\mathbf{P}^p$  a modified thermodynamical force  $\Sigma^p$  is used referred to as the Mandel stress tensor. This mixed-variant second order tensor represents – except for its sign – the Eshelby stress tensor associated with the intermediate configuration, see Remark 3.5 below for a detailed explanation. The dual object work conjugate to the Mandel stresses is the plastic evolution tensor  $\mathbf{L}^p$ , frequently denoted the velocity gradient of the intermediate configuration

$$\Sigma^p := \mathbf{P}^p \mathbf{F}^{pT} = \mathbf{F}^{eT} \partial_{\mathbf{F}^e}\psi \quad \text{and} \quad \mathbf{L}^p := \dot{\mathbf{F}}^p \mathbf{F}^{p-1}. \quad (3.101)$$

In a concise geometric setting these tensors can be considered as mappings within the tangent and cotangent spaces  $\bar{T}_X \mathcal{B}$  and  $\bar{T}_X^* \mathcal{B}$  of the intermediate configuration as depicted in Figure 3.8. Following Section 3.2.2.4, the yield criterion function  $\phi$  is introduced as the

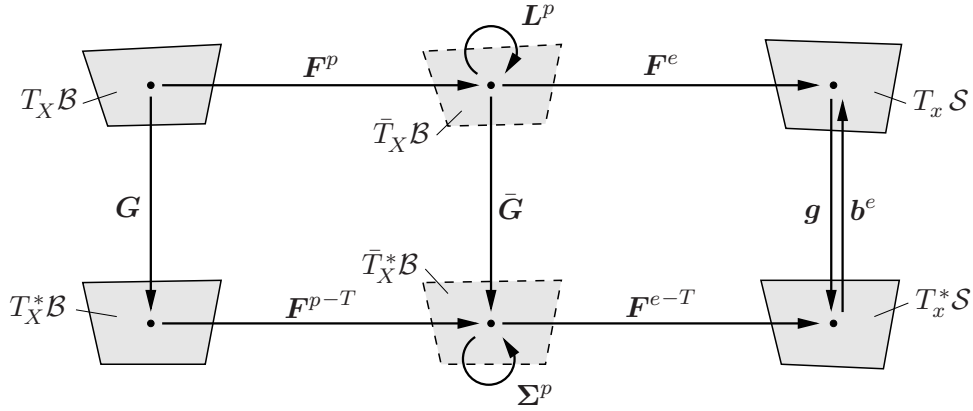


**Figure 3.8:** Mappings in terms of the plastic part  $\mathbf{F}^p$  and elastic part  $\mathbf{F}^e$  of the deformation gradient, the Mandel stress tensor  $\Sigma^p$  and the work conjugate plastic evolution tensor  $\mathbf{L}^p$ .

difference between the level set function  $f(\mathcal{F}, \theta) = f(\Sigma^p, B, \theta)$  and a material parameter  $\tau_c(\theta)$  denoted the slip resistance. To set up the level set function  $f$ , the Mandel stress tensor is projected onto the slip system defining Schmid's resolved shear stress

$$\tau^{Sch} = \Sigma^p : (\mathbf{S} \otimes \mathbf{N}) = \text{dev } \Sigma^p : (\mathbf{S} \otimes \mathbf{N}). \quad (3.102)$$

Due to orthogonality of  $\mathbf{S}$  and  $\mathbf{N}$  the resolved shear stress incorporates only the deviatoric part of the Mandel stresses. The particular form of yield criterion function is given by

$$\phi = \tau^{Sch} + B - \tau_c = \tau^{Sch} - (\tau_c - B). \quad (3.103)$$

The critical shear stress is described by the initial flow stress function  $\tau_c = y_0(1 - w_0(\theta - \theta_0))$  with  $w_0$  being the flow stress softening coefficient. In view to the derivation of the evolution

equations for the internal variables  $\mathbf{L}^p$  and  $A$ , attention is focused on an associated flow response. In that case the evolution equations are obtained from the principle of maximum dissipation. The necessary condition of the optimization problem yields

$$\mathbf{L}^p = \lambda \partial_{\Sigma^p} \phi = \lambda \mathbf{S} \otimes \mathbf{N} \quad \text{and} \quad \dot{A} = \lambda \partial_B \phi = \lambda \quad (3.104)$$

in combination with the Karush-Kuhn-Tucker loading-unloading conditions (3.50), i.e.  $\phi \leq 0$ ,  $\lambda \geq 0$  and  $\phi\lambda = 0$ . The primary identification of the internal variable vector  $\mathcal{I} = [\mathbf{F}^p, A]^T$  uses the plastic part  $\mathbf{F}^p$  of the deformation gradient. Its evolution equation is directly obtained from (3.104)<sub>1</sub>, namely  $\dot{\mathbf{F}}^p = \lambda \partial_{\Sigma^p} \phi \mathbf{F}^p$ . Based on this relation it can easily be shown that the following closed form representation holds

$$\mathbf{F}^p = \mathbf{1} + \gamma \mathbf{S} \otimes \mathbf{N}. \quad (3.105)$$

Physically, it is interpreted as a simple shearing of the crystallographic lattice with the amount of slip  $\gamma = \lambda(t_{n+1} - t_n)$  in the direction of  $\mathbf{S}$ .

Turning next to the evaluation of the discrete configurational forces, the material gradient of the internal variable vector has to be computed

$$\nabla_X \mathcal{I} = \begin{bmatrix} \nabla_X \mathbf{F}^p \\ \nabla_X A \end{bmatrix} = \begin{bmatrix} (\mathbf{S} \otimes \mathbf{N}) \otimes \nabla_X \gamma \\ \nabla_X A \end{bmatrix}. \quad (3.106)$$

Integration of (3.104)<sub>2</sub> by means of an implicit backward Euler integration scheme in the discrete time interval  $[t_n; t_{n+1}]$  yields the scalar hardening variable at time  $t_{n+1}$

$$A_{n+1} = A_n + \lambda(t_{n+1} - t_n) = A_n + \gamma. \quad (3.107)$$

Hence, for the evaluation of  $\nabla_X \mathcal{I}$  only the scalar variable  $A$  needs to be provided on the node point level of the finite element mesh. The amount of slip is described by the closed form update  $\gamma_{n+1} = \gamma_n + (A_{n+1} - A_n)$  to be performed on the node point level as well for known nodal values  $A_{n+1}$ ,  $A_n$  of the hardening variable.

**Remark 3.5:** It is an intrinsic feature of multiplicative crystal-plasticity that the negative Mandel stress tensor coincides with the purely intermediate representation of the Eshelby tensor. This can be proven by means of the notion of local rearrangement as discussed for instance by EPSTEIN & MAUGIN [37, 40]. Consider the representations of the free energy function  $\hat{\psi}$  and  $\tilde{\psi}$  with respect to the reference and intermediate configuration. Both are linked via the determinant  $J^p$  of the plastic part of the deformation gradient

$$\hat{\psi}(\mathbf{F}, \mathbf{X}) = J^p \tilde{\psi}(\mathbf{F}^e, \mathbf{X}) = \psi(\mathbf{F}, \mathbf{F}^{p-1}, \mathbf{X}) \quad (3.108)$$

with  $J^p = \det \mathbf{F}^p = (\det[\mathbf{F}^{p-1}])^{-1}$ . The first Piola-Kirchhoff stress tensor is the derivative of the free energy function with respect to the deformation gradient. The Eshelby tensor  $\hat{\Sigma}$  with respect to the intermediate configuration is defined by the negative derivative of the free energy with respect to the inverse of the plastic part of the deformation gradient

$$\mathbf{P} = \partial_{\mathbf{F}} \hat{\psi} \quad \text{and} \quad \hat{\Sigma} = -\partial_{(\mathbf{F}^{p-1})} \hat{\psi}. \quad (3.109)$$

Both objects are two-point tensors respectively related to the spatial and material as well as the material and intermediate configurations. Substituting the free energy function

(3.108)<sub>2</sub> into the definition of the Eshelby tensor  $\hat{\Sigma}$  and taking into account the product rule as well as the rule for the derivative of the determinant it follows

$$\hat{\Sigma} = (\hat{\psi} \mathbf{1} - \mathbf{F}^T \mathbf{P}) \mathbf{F}^{pT} = \Sigma \mathbf{F}^{pT} \quad (3.110)$$

with the well-established purely material Eshelby tensor  $\Sigma$ . For plastic incompressible materials,  $J^p = 1$ , (3.110) boils down to

$$\hat{\Sigma} = -\mathbf{F}^T \mathbf{P} \mathbf{F}^{pT} = -\mathbf{F}^T (\partial_{\mathbf{F}^e} \hat{\psi} \mathbf{F}^{p-T}) \mathbf{F}^{pT} = -\mathbf{F}^T \partial_{\mathbf{F}^e} \hat{\psi} \quad (3.111)$$

since the chain rule does not have to be applied within the above derivative. In the last parts an alternative representation of the first Piola-Kirchhoff stresses, cf. (3.99), has been used. The two-point tensor  $\hat{\Sigma}$  is transformed onto the intermediate configuration by a pull-back operation in terms of the transpose inverse of the plastic part of the deformation gradient. By this manipulation a modified Eshelby tensor  $\bar{\Sigma}$  arises

$$\bar{\Sigma} = \mathbf{F}^{p-T} \hat{\Sigma} = -\mathbf{F}^T (\partial_{\mathbf{F}^e} \hat{\psi} \mathbf{F}^{p-T}) \mathbf{F}^{pT} = -\mathbf{F}^{eT} \partial_{\mathbf{F}^e} \hat{\psi} = -\Sigma^p \quad (3.112)$$

exclusively related to the intermediate configuration. By comparison with (3.101) this purely intermediate Eshelby tensor appears as the negative Mandel stress tensor  $\Sigma^p$ .

**3.6.2. Numerical Example: Cook's Membrane Problem.** The example deals with the comparison of the global and local procedures discussed in Section 3.5. Cook's membrane is investigated as a model problem. The use of Cook's membrane within the context of the evaluation of discrete configurational nodal forces is provided e.g. by NÄSER & KALISKE [135]. The system with boundary conditions is visualized in Figure 3.9, the

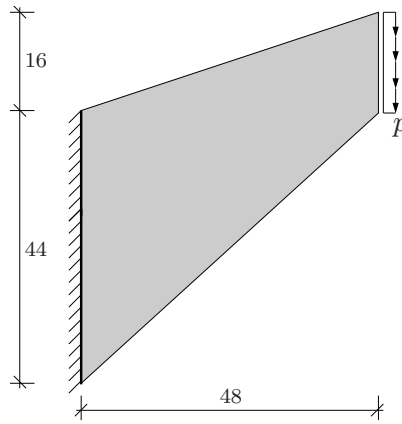


**Figure 3.9:** System and boundary conditions of Cook's membrane problem. The dimensions are given in [mm]. The specimen is discretized with 25x15 bilinear quadrilaterals. An enhanced strain formulation is adopted for the spatial deformation problem.

material parameters are summarized in Table 3.1. The orientation  $\epsilon_{\mathbf{S}}$  of the slip direction  $\mathbf{S}$  is specified with respect to the horizontal axis. The particular choice of the material parameters  $\alpha$ ,  $c$  and  $w$  is such that the influence of the temperature is overstated. This does not pose any restriction to the applicability of the proposed procedures but is adopted just for the sake of a better accentuation of the effects to be shown. A distributed vertical load of a total of  $p = 0.084$  kN/mm is applied within 42 load increments. Spatial volume forces  $\bar{\gamma}_0$  and the heat source  $r$  have been neglected. The specimen is discretized with 25x15 four-noded quadrilaterals. Bilinear shape functions are used for the temperature

**Table 3.1:** Material parameters for thermo-crystal-plasticity

bulk modulus	$\kappa$	49.98	kN/mm <sup>2</sup>
shear modulus	$\mu$	21.1	kN/mm <sup>2</sup>
initial yield stress	$y_0$	0.06	kN/mm <sup>2</sup>
infinite yield stress	$y_\infty$	0.115	kN/mm <sup>2</sup>
hardening modulus	$h$	0.015	kN/mm <sup>2</sup>
saturation parameter	$\omega$	10.764	–
thermal expansion coefficient	$\alpha$	$1 \cdot 10^{-4}$	1/K
conductivity	$k$	0.045	1/K
reference temperature	$\theta_0$	293.0	K
heat capacity	$c$	$3.558 \cdot 10^{-5}$	kN/(s·K)
hardening softening	$w$	0.002	1/K
flow stress softening	$w_0$	0.002	1/K
orientation of slip direction	$\epsilon_S$	60.0	°

evolution problem and, in case of the global formulation, the supplementary constitutive subproblem. For the spatial deformation problem an enhanced strain formulation is employed using bilinear interpolation functions as well but in addition containing four internal degrees. The denotations Q1E4Q1Q1 and Q1E4Q1 seem to be appropriate. A detailed treatment of this finite element formulation is outlined in Appendix C.

Figure 3.10 shows a comparison of the distribution of the change  $\Delta\theta$  in the temperature field  $\theta$  plotted over the deformed structure. The results obtained from a) the global and

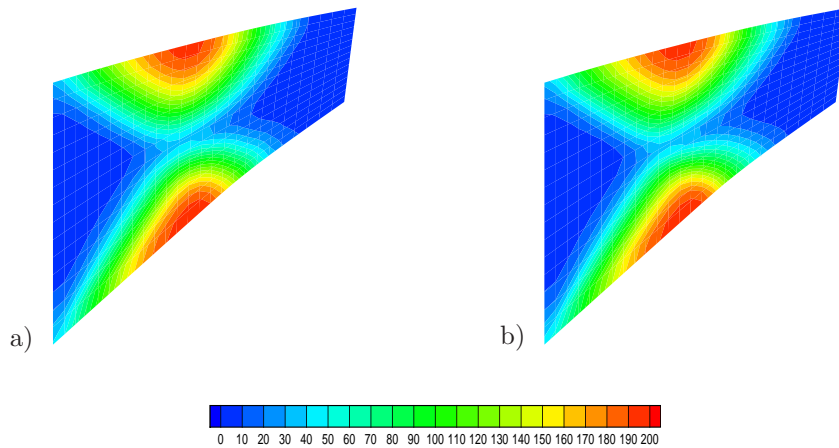


**Figure 3.10:** Distribution of change  $\Delta\theta$  of temperature field  $\theta$  for a) global solution and b) local solution.

b) the local formulation are almost identical. The temperature increases by a maximum value of  $\Delta\theta = 198.37$  K in the global and  $\Delta\theta = 198.35$  K in the local simulation. A comparison of the overall structural response reveals the same characteristic. For the final load step the maximum nodal displacements for the global solution are  $u_{max}^x = 2.99$  mm and  $u_{max}^y = -3.41$  mm. The local scheme ends up with  $u_{max}^x = 3.01$  mm and  $u_{max}^y = -3.43$  mm.

The very good agreement of the results obtained from the different solution strategies is confirmed when considering the distribution of the scalar hardening variable  $A$  visualized

in Figure 3.11. Three scenarios have to be compared. Within the global formulation the

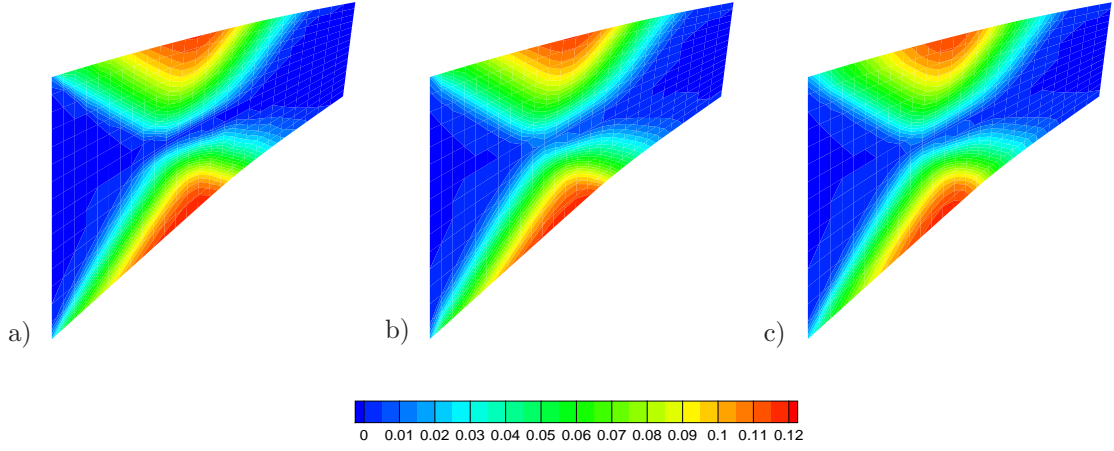


**Figure 3.11:** Distribution of hardening variable  $A$  for a) global solution, b) local solution combined with patch recovery, and c) local solution utilizing  $L2$ -projection.

hardening variable is introduced as an additional nodal degree. In this sense, Figure 3.11a) provides the contour plot of this additional node point variable. Within a local simulation the internal variable field is available on the integration point level and is projected onto the nodal points in a postprocessing step. The contour plot in Figure 3.11b) is obtained by the patch recovery whereas that one received from the  $L2$ -projection is depicted in Figure 3.11c). The differences between the alternative approaches are again negligible. The maximum values deviate from  $A_{max} = 0.1192$  for the patch recovery to  $A_{max} = 0.1175$  for the  $L2$ -projection. The global solution lies in between at  $A_{max} = 0.1188$ . By comparison of the distributions of the hardening variable  $A$  and the increase  $\Delta\theta$  in temperature it is well detectable that the evolution of plastic deformation, which directly governs the local dissipation  $\mathcal{D}_{loc}$ , is the driving quantity for the evolution of the temperature.

Finally, the computation of the discrete configurational nodal forces is investigated. The results gained from the alternative solution strategies are very close to each other. For this reason only the results of the global analysis are displayed in Figure 3.12. Three different

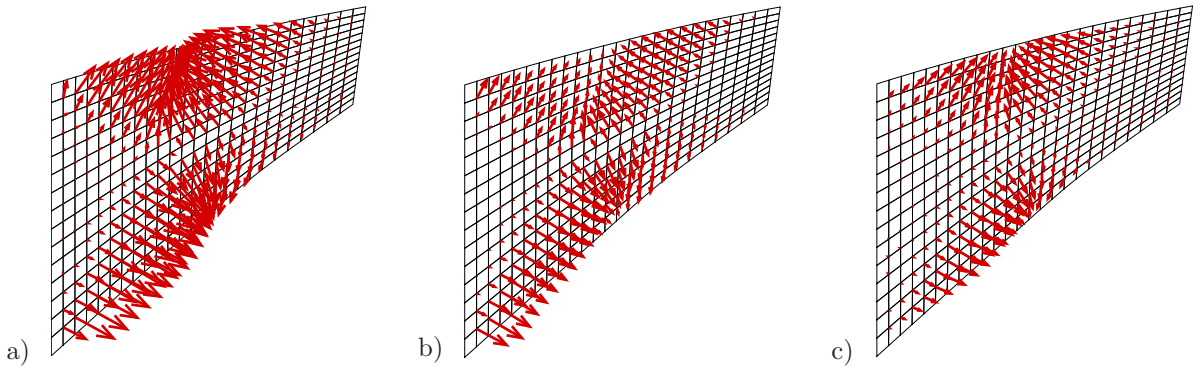


**Figure 3.12:** Discrete material nodal forces obtained by the global simulation. a) Internal part based on the Eshelby tensor  $\Sigma$  pointing in the negative direction. Contributions to discrete configurational forces in terms of the gradients b)  $\nabla_X \mathcal{I}$  of the internal variables and c)  $\nabla_X \theta$  of the temperature. Forces along the discrete boundary are omitted.

contributions are plotted. In Figure 3.12a) the internal material forces  $\mathbf{F}_I$  in terms of the Eshelby tensor  $\Sigma$  are presented, cf. (3.61). On the other hand, the configurational, or

rather quasi-inhomogeneity forces  $\mathbf{P}_I$  are a function of the material gradients of the internal variables and the temperature field, see (3.60) and (3.29). These two contributions of  $\mathbf{P}_I$  are depicted in Figure 3.12b), c). Note that the internal forces are plotted pointing in their negative direction for the sake of comparison. In contrast to the interior nodes large discrete surface forces appear at the boundary nodes of the finite element mesh. These forces are essential to maintain the shape of the material boundary of the structure, i.e. to prevent the material configuration of the body from shrinking. As they are not needed for the current investigations, these nodal forces on the discrete boundary  $\partial\mathcal{B}^h$  are set to zero and only the nodal forces  $\mathbf{F}_I, \mathbf{P}_I$  at the interior nodes  $I \in \mathcal{B}^h$  are plotted in the figures. The configurational forces are computed in terms of the material gradients of the hardening variable  $A$  and the temperature field  $\theta$  and thus are perpendicular to the isolines of  $A$  and  $\theta$ . The distribution of these fields acts as an inhomogeneity within the material body. Since configurational forces point in the direction of an energy increase upon movement of the material node point position, they try to inhibit any further evolution of these quantities which would cause an energy decrease of the system. The negative internal material forces display the same characteristic as they constitute the direct counterpart of the configurational forces within the discrete nodal balance (3.75)<sub>2</sub>.

This discrete equilibrium condition reflects the discrete version of the material balance law (3.74)<sub>2</sub> and demands vanishing resultant forces  $(\mathbf{F}_I + \mathbf{P}_I) = \mathbf{0}$  at all interior nodes of the mesh. This means that from the theoretical point of view all the contributions to the nodal forces sum up to zero inside the discrete domain  $\mathcal{B}^h$ . The resultant forces are visualized in Figure 3.13. As expected, these forces almost vanish inside the material

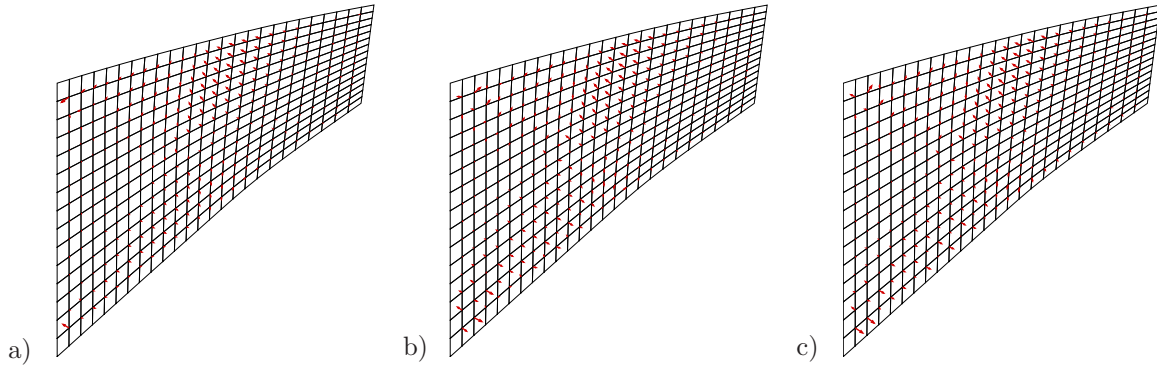


**Figure 3.13:** Resultant nodal forces obtained by the sum of internal contribution and the discrete configurational nodal forces in terms of the gradients of the internal variables and the temperature field for a) global formulation, b) patch recovery and c)  $L_2$ -projection. All the forces along the discrete boundary have been omitted.

body irrespective of the applied solution procedure. However, some numerically caused, often denoted spurious forces remain at the interior nodes. Thereby, only minor deviations between the three approaches are detectable. These forces occur due to an insufficient triangulation and can be used as an indicator for mesh refinement. This argument will be exploited in the forthcoming sections.

In summary, all approaches reveal completely the same characteristics concerning the distribution of the hardening variable, the temperature field and the resultant material forces. Recalling the advantages with respect to the numerical effort of the simulation, it has to be emphasized that the local approach turns out to be more favorable and will be applied for problems of finite inelasticity to come up in the subsequent chapters.



## 4. Configurational Solid Dynamics

The aim of this section is to present a variational approach to configurational solid dynamics based on Hamilton's principle. Hereby, the variations with respect to the spatial and material positions as well as the time are performed. The corresponding Euler-Lagrange equations of the variational setting appear as the local forms of the spatial balance of linear momentum, the balance of material pseudomomentum, which itself relies on the definition of the dynamical extension of the Eshelby tensor, and the balance of kinetic energy. The corresponding global balance laws are introduced as well. In the first step a brief review of selected literature on the topic is provided. Subsequently, the variational setting of configurational dynamics is discussed at full length. Attention is restricted to the purely elastic, non-dissipative case. Next, the discrete setting is elaborated. At first, the spatial deformation problem is investigated. Space discretization in terms of standard finite element scheme results in a semi-discrete representation of the equation of spatial motion. This expression is solved by means of the classical Newmark- $\alpha$  method. In the sense of a staggered solution strategy, the equation of material motion is implemented in a postprocessing step. Finally, an illustrative numerical example is discussed. Further applications of configurational forces within the dynamical framework will be presented in the forthcoming paragraphs.

### 4.1. Preliminary Aspects

A variety of literature dealing with the dynamical setting of configurational mechanics and material forces is available. Basically, the influence of dynamical effects on the forces acting on defects has already been studied by ESHELBY [43] himself and later on also by ROGULA [153]. It is a remarkable circumstance that many publications on the field of Eshelbian mechanics include the dynamical formulation of the fundamental field equations. Hence, the quotations given below are just a brief compendium dealing with various aspects of the topic. In general, two different conceptual approaches can be used to derive the fundamental material balance equation referred to as the dual balance of material momentum or pseudomomentum, namely either the pull-back of the spatial balance equation or a true variational formulation. A detailed discussion can be found in MAUGIN [99, 100] or more recently in the works of STEINMANN [172, 174] where thermo-mechanical aspects are included as well. The theoretical basis of configurational dynamics has been studied by e.g. MAUGIN & TRIMARCO [110], MAUGIN [102], and GURTIN & SHVARTSMAN [64], see also MAUGIN, EPSTEIN & TRIMARCO [109] including the application to fracture mechanics and even the consequences with regard to electromagnetoelasticity. The numerical treatment which in particular results in the evaluation of discrete configurational nodal forces has been elaborated by e.g. KOLLING & MÜLLER [81], and TIMMEL, KALISKE, KOLLING & MÜLLER [184]. The analyses performed within these contributions are concerned with high-frequency loading of the systems under consideration and therefore incorporate an explicit time integration scheme for the solution of the spatially discretized or semi-discrete equation of motion. With regard to the variational setting KUHL & STEINMANN [85] address an arbitrary Lagrangian Eulerian (ALE) formulation of hyperelastodynamics. Thereby, the total variation of the variational principle appears as the sum of variations with respect to the spatial coordinates at fixed material positions and, vice versa, with respect to the material coordinates at fixed spatial positions. In the recent work of ZIELONKA [191] the variational ALE technique has been successfully applied to mesh adaption. It is mentioned by now that the application of the variational

ALE approach to mesh adaption and topology optimization is going to be considered in detail in Paragraph 5 for the particular case of quasi-static problems. An alternative approach to mesh adaptivity using discrete material forces as a refinement indicator will be presented in Section 6. Within these analyses the dynamical case is going to be taken into account as well, see also the recent report of HOFACKER [70].

#### 4.2. Variational Formulation of Configurational Solid Dynamics

This paragraph is concerned with the variational setting of configurational hyperelastodynamics based on Hamilton's principle. To recapitulate briefly the geometric scenario, cf. Section 2, consider the reference and current configurations  $\mathcal{B}$  and  $\mathcal{S}$  of a material body related by the non-linear deformation map  $\varphi(\mathbf{X}, t)$ , see Figure 4.1 below. This point map is parameterized by the Lagrangian space-time  $(\mathbf{X}, t)$ . The partial derivatives of the motion  $\varphi$  define the deformation gradient and the spatial velocity

$$\mathbf{F} = \frac{\partial}{\partial \mathbf{X}} \varphi(\mathbf{X}, t) = \nabla_{\mathbf{X}} \varphi(\mathbf{X}, t) \quad \text{and} \quad \mathbf{v} = \frac{\partial}{\partial t} \varphi(\mathbf{X}, t). \quad (4.1)$$

The partial time derivative of an arbitrary material object  $(\bullet)$  parameterized by the Lagrangian space-time equals the total time derivative  $d(\bullet)/dt|_{\mathbf{X} \text{ fixed}}$  for time-independent reference coordinates,  $\mathbf{X} = \text{const}$ . In contrast, the partial derivative of the deformation map  $\varphi$  with respect to the material coordinate  $\mathbf{X}$  corresponds to the total derivative,  $d\varphi/d\mathbf{X} = \partial\varphi/\partial\mathbf{X}$ . With these arguments at hand, the following relations hold

$$\frac{d}{d\mathbf{X}} \mathbf{v} = \frac{\partial}{\partial \mathbf{X}} \mathbf{v} = \frac{\partial}{\partial \mathbf{X}} \left( \frac{\partial}{\partial t} \varphi \right) = \frac{\partial^2}{\partial t \partial \mathbf{X}} \varphi = \frac{\partial}{\partial t} \nabla_{\mathbf{X}} \varphi = \frac{\partial}{\partial t} \mathbf{F} = \frac{d}{dt} \Big|_{\mathbf{X} \text{ fixed}} \mathbf{F}. \quad (4.2)$$

Consider now the perturbation of both the reference and the spatial configuration of the material body in terms of variations  $\delta\mathbf{X}$  and  $\delta\mathbf{x}$  of the material and spatial coordinates as visualized in Figure 4.1. The material variation accounts for a change of the reference

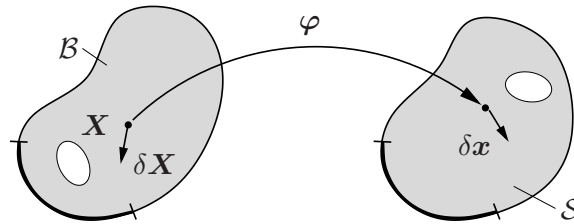


**Figure 4.1:** Perturbation of reference and current configurations by variations  $\delta\mathbf{X}$  and  $\delta\mathbf{x}$  of the material and spatial coordinates. The variation of the material position characterizes a movement of an inhomogeneity, indicated by the void, with respect to the material setting.

coordinates and allows for the description of structural changes within the Lagrangian setting of the body, e.g. the movement of a void or inclusion. Hence, the material and spatial variations  $\delta\mathbf{X}$  and  $\delta\mathbf{x} = \delta\varphi$  which are central to the subsequent variational formulation of solid dynamics act in the same way as the rates of the material and spatial configurational maps  $\Xi$  and  $\xi$  introduced in Chapter 3 providing the kinematic basis for the rate formulation of configurational thermo-elasticity. This analogy brings both approaches close to each other. In addition to the variations of the space-coordinates, a variation  $\delta t$  of the time-coordinate  $t$  is taken into account.

The variational formulation rests upon energetic arguments. The fundamental ingredient



is the Lagrangian functional  $L$  defined by the difference between kinetic energy  $K$  and potential energy  $\Pi$

$$L = K - \Pi = \int_{\mathcal{B}} \mathcal{L} dV + \int_{\partial\mathcal{B}_{\bar{\mathbf{i}}}} \bar{\mathcal{L}} dA. \quad (4.3)$$

In contrast to Section 2.3.4, it is preferable to formulate  $K$  with respect to unit volume of the reference configuration

$$K = \int_{\mathcal{B}} \frac{1}{2} \rho_0(\mathbf{X}) \mathbf{v}(\mathbf{X}, t) \cdot \mathbf{v}(\mathbf{X}, t) dV. \quad (4.4)$$

with the Lagrangian density  $\rho_0(\mathbf{X})$ . The total potential energy of an elastic system is given by the sum of the internal and the external potential energy,  $\Pi = \Pi_{int} + \Pi_{ext}$ . On the one hand, the internal contribution characterizes the total strain energy

$$\Pi_{int} = \int_{\mathcal{B}} \psi(\mathbf{F}, \mathbf{X}) dV, \quad (4.5)$$

in terms of the free energy function  $\psi(\mathbf{F}, \mathbf{X})$  per unit volume of the reference configuration. The dependence of the reference density and the free energy function on the material coordinates  $\mathbf{X}$  governs possible inhomogeneities of the material body. On the other hand, the external part describes the potential energy of the external physical loading

$$\Pi_{ext} = - \int_{\mathcal{B}} \boldsymbol{\varphi}(\mathbf{X}, t) \cdot \bar{\boldsymbol{\gamma}}_0(\mathbf{X}) dV - \int_{\partial\mathcal{B}_{\bar{\mathbf{i}}}} \boldsymbol{\varphi}(\mathbf{X}, t) \cdot \bar{\mathbf{t}} dA \quad (4.6)$$

defined by the physical forces acting on the body, namely the spatial volume forces  $\bar{\boldsymbol{\gamma}}_0$  per unit reference volume and spatial surface tractions  $\bar{\mathbf{t}}$ .

**Remark 4.1:** For the particular case, these potentials governing the external power  $\mathcal{P}$  and the stress power  $S$ , both likewise defined in Section 2.3.4, via the total time derivatives

$$\mathcal{P} = -\frac{d}{dt} \Pi_{ext} \quad \text{and} \quad S = \frac{d}{dt} \Pi_{int}, \quad (4.7)$$

the mechanical system is denoted a conservative system.

With all these definitions at hand, the Lagrangian functional  $L$  reads

$$L = \int_{\mathcal{B}} \frac{1}{2} \rho_0 \mathbf{v} \cdot \mathbf{v} - \psi + \boldsymbol{\varphi} \cdot \bar{\boldsymbol{\gamma}}_0 dV + \int_{\partial\mathcal{B}_{\bar{\mathbf{i}}}} \boldsymbol{\varphi} \cdot \bar{\mathbf{t}} dA. \quad (4.8)$$

As indicated in equation (4.3), the Lagrangian  $L$  can alternatively be expressed by the Lagrangian densities  $\mathcal{L}$  and  $\bar{\mathcal{L}}$  per unit volume and unit area of the reference configuration. By comparison of both representations, the Lagrangian densities appear as

$$\mathcal{L} = \mathcal{L}(t, \mathbf{X}, \boldsymbol{\varphi}, \mathbf{v}, \mathbf{F}) = \frac{1}{2} \rho_0 \mathbf{v} \cdot \mathbf{v} - \psi + \boldsymbol{\varphi} \cdot \bar{\boldsymbol{\gamma}}_0 \quad \text{and} \quad \bar{\mathcal{L}} = \bar{\mathcal{L}}(t, \mathbf{X}, \boldsymbol{\varphi}) = \boldsymbol{\varphi} \cdot \bar{\mathbf{t}}. \quad (4.9)$$

For the subsequent treatments it is convenient to differentiate between independent and dependent variables interchangeably referred to as variables and fields. Basically, the time  $t$  and the reference coordinates  $\mathbf{X}$ , i.e. the Lagrangian space-time, constitute the independent variables whereas the spatial coordinates  $\boldsymbol{x} = \boldsymbol{\varphi}$  characterize the dependent variables or fields. The Lagrangian densities (4.8) are parameterized by the time, the material and spatial coordinates and, in addition, the derivatives of the field with respect to the variables, i.e. the spatial velocity field and the deformation gradient  $\mathbf{v} = \partial\boldsymbol{\varphi}/\partial t$  and  $\mathbf{F} = \partial\boldsymbol{\varphi}/\partial\mathbf{X}$ . Apparently, to set up a framework capable of describing structural changes within the material setting of the body, the Lagrangian coordinates  $\mathbf{X}$  are time-dependent but are still regarded as independent variables.

**4.2.1. Hamilton's Principle.** For elastic systems, the scalar-valued Lagrangian functional  $L$ , or rather the kinetic and potential energies, contain the complete dynamics of that system, subjected to the condition that they are used as the basis of a mechanical principle. In general, variational principles are concerned with the stationary, in particular cases even minimal value of a definite integral. For more details on variational principles, the reader is referred to the fundamental monograph of LANCZOS [86].

The basis of the variational formulation to follow is Hamilton's principle. Its key quantity is the action integral

$$H = \int_{t_1}^{t_2} K - \Pi dt = \int_{t_1}^{t_2} L dt \quad (4.10)$$

being the definite time integral of the difference between kinetic and potential energies, i.e. the Lagrangian functional  $L$ . The motion of a mechanical system between two points in time  $t_1$  and  $t_2$  is analyzed. It is presumed, that at these points in time the state of the system is prescribed and no variations are admitted. For discrete mechanical systems, the action integral is parameterized by a set of  $n$  generalized coordinates  $\mathbf{q}$  and their temporal change  $\dot{\mathbf{q}}$  with  $n$  denoting the number of degrees of freedom of the system. The generalized coordinates and the time  $t$  span a  $(n + 1)$ -dimensional space usually denoted the configuration space. Carefully observe that this notation must not be confused with the expression configurational space corresponding in a rather abstract meaning to the material or Lagrangian space. The fundamental interpretation of this geometric idealization of dynamical problems is that the motion of the system between its prescribed initial and final states appears as a sequence of points and therefore as a curve or path within the configuration space, see Figure 4.2 for a sketch of this scenario. This path can

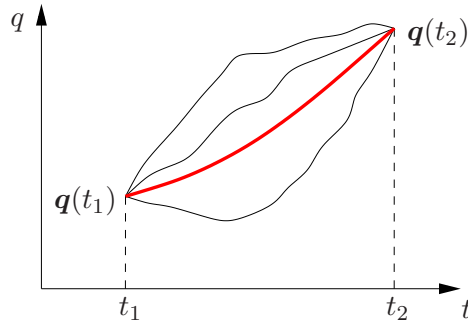


**Figure 4.2:** The generalized coordinates  $\mathbf{q}$  and the time  $t$  define the  $(n + 1)$ -dimensional configuration space. The motion of the system between the prescribed initial and final states appears as a path through the configuration space. Hamilton's principle states that the motion occurs along that path, for which the action functional becomes stationary.

be seen as the geometric visualization of the whole history of the motion as every point of this path characterizes the state of the system at the corresponding time  $t$ .

Hamilton's principle states that the motion of the system is such that the action integral becomes stationary with respect to all admissible variations of the state of the system

$$H = \int_{t_1}^{t_2} L dt \rightarrow \text{stat.} \quad (4.11)$$

Since the initial and final states of the system are prescribed, the variations at these points vanish,  $\delta\mathbf{q}(t_1) = \delta\mathbf{q}(t_2) = \mathbf{0}$ , and the variation just occurs between these definite limits.

In view of the geometric interpretation Hamilton's principle asserts that the current path in the configuration space corresponds to that path that renders the action functional stationary. Hence, the dynamical system always finds the, say, optimal path from its initial state at time  $t_1$  to its final state at time  $t_2$ . By this procedure, the problem of the motion of mechanical system boils down the exploitation of a scalar integral.

In the following, Hamilton's principle is used to derive the fundamental equations of configurational solid dynamics. The considerations are devoted to continuous systems. Therefore, the generalized coordinates are replaced by space-continuous state variables resulting in an infinite number of degrees of freedom. In addition to the temporal change of these variables, their change with respect to space given by the material gradient enters the action functional

$$H = \int_{t_1}^{t_2} K - \Pi \, dt = \int_{t_1}^{t_2} \left\{ \int_{\mathcal{B}} \mathcal{L} \, dV + \int_{\partial\mathcal{B}_t} \bar{\mathcal{L}} \, dA \right\} dt \quad (4.12)$$

with the Lagrangian densities  $\mathcal{L}$ ,  $\bar{\mathcal{L}}$  being defined in (4.9). This functional is valid for the initial conditions, which demand that the initial and final configurations of the system are given, and for prescribed spatial and material essential Dirichlet boundary conditions

$$\varphi = \bar{\varphi} \text{ on } \partial\mathcal{B}_\varphi \quad \text{and} \quad \mathbf{X} = \text{const. on } \partial\mathcal{B}. \quad (4.13)$$

The first condition governs that part  $\partial\mathcal{B}_\varphi$  of the boundary where the spatial position or deformation  $\bar{\mathbf{x}} = \bar{\varphi}$  is prescribed. The second condition for the material coordinates on the whole boundary  $\partial\mathcal{B}$  states that the material boundary remains completely unaltered.

**Remark 4.2:** Recalling the discussions in the context of equations (3.5) and (3.11) within Section 3.2.1, a reduced form of the essential material boundary condition (4.13)<sub>2</sub> allows for a variation of the Lagrangian coordinates along the material boundary. This movement of the material positions must not change the original shape of the body and thus must not contain any contribution in the direction of the outward normal  $\mathbf{N}$ .

Hamilton's principle requires that the action functional  $H$  needs to be stationary with respect to variations of the spatial and material coordinates and time. Thus the necessary condition of (4.11) reads

$$\delta H = \delta_\varphi H + \delta_{\mathbf{X}} H + \delta_t H = 0 \quad (4.14)$$

and demands that the first variation of the action functional has to vanish. The subscript  $\delta_{(\bullet)} H$  indicates with respect to which variable ( $\bullet$ ) the variation is performed. Adopting the notation of e.g. ZIELONKA [191] and KHAREVYCH ET AL. [75], variations of the action functional with respect to the spatial positions at fixed material configuration and time are denoted vertical variations. Vice versa, variations with respect to the reference positions and time at fixed spatial coordinates are referred to as horizontal variations.

**4.2.2. Variation with respect to Spatial Coordinate.** At first, the variation of the action functional (4.12) with respect to the current coordinates  $\mathbf{x} = \varphi$  is investigated. Consider an arbitrary field  $\delta\varphi$  denoted the variation of  $\varphi$  or the virtual deformation map satisfying the homogeneous form of the Dirichlet-type boundary conditions (4.13)<sub>1</sub>

$$\delta\varphi \in \{\delta\varphi \mid \delta\varphi = \mathbf{0} \text{ on } \partial\mathcal{B}_\varphi\}. \quad (4.15)$$

Upon variation of the spatial coordinates, the time  $t$  and the material position  $\mathbf{X}$  and therefore the integration limits remain unaffected. By means of the Gateaux derivative the variation of the action functional can be expressed by

$$\begin{aligned} \delta_\varphi H &= \int_{t_1}^{t_2} \left\{ \int_{\mathcal{B}} \frac{d}{d\epsilon} \mathcal{L}(t, \mathbf{X}, \varphi + \epsilon \delta \varphi, \frac{\partial}{\partial t}(\varphi + \epsilon \delta \varphi), \frac{\partial}{\partial \mathbf{X}}(\varphi + \epsilon \delta \varphi)) \Big|_{\epsilon=0} dV \right. \\ &\quad \left. + \int_{\partial \mathcal{B}_{\bar{t}}} \frac{d}{d\epsilon} \bar{\mathcal{L}}(t, \mathbf{X}, \varphi + \epsilon \delta \varphi) \Big|_{\epsilon=0} dA \right\} dt \\ &= \int_{t_1}^{t_2} \left\{ \int_{\mathcal{B}} \frac{\partial \mathcal{L}}{\partial \varphi} \cdot \delta \varphi + \frac{\partial \mathcal{L}}{\partial \mathbf{v}} \cdot \frac{\partial}{\partial t} \delta \varphi + \frac{\partial \mathcal{L}}{\partial \mathbf{F}} : \frac{\partial}{\partial \mathbf{X}} \delta \varphi dV \right. \\ &\quad \left. + \int_{\partial \mathcal{B}_{\bar{t}}} \frac{\partial \bar{\mathcal{L}}}{\partial \varphi} \cdot \delta \varphi dA \right\} dt = 0. \end{aligned} \quad (4.16)$$

Note that the derivatives of the variation  $\delta \varphi$  with respect to time and material position could be replaced by variations  $\delta \mathbf{v} := \partial \delta \varphi / \partial t$  of the velocity field and  $\delta \mathbf{F} := \partial \delta \varphi / \partial \mathbf{X}$  of the deformation gradient. For the second and third addends integration by parts with respect to time or, respectively, material coordinates is applied

$$\begin{aligned} \delta_\varphi H &= \int_{t_1}^{t_2} \left\{ \int_{\mathcal{B}} \left\{ \frac{\partial \mathcal{L}}{\partial \varphi} \cdot \delta \varphi + \frac{\partial}{\partial t} \left[ \frac{\partial \mathcal{L}}{\partial \mathbf{v}} \cdot \delta \varphi \right] - \frac{\partial}{\partial t} \left[ \frac{\partial \mathcal{L}}{\partial \mathbf{v}} \right] \cdot \delta \varphi + \text{Div} \left[ \delta \varphi \frac{\partial \mathcal{L}}{\partial \mathbf{F}} \right] \right. \right. \\ &\quad \left. \left. - \text{Div} \left[ \frac{\partial \mathcal{L}}{\partial \mathbf{F}} \right] \cdot \delta \varphi \right\} dV + \int_{\partial \mathcal{B}_{\bar{t}}} \frac{\partial \bar{\mathcal{L}}}{\partial \varphi} \cdot \delta \varphi dA \right\} dt = 0. \end{aligned} \quad (4.17)$$

With regard to the second addend time and space integration commute for fixed material positions. Time integration and differentiation cancel out each other but the integrand has to be evaluated at the integration limits. Thereupon this term vanishes as the state variables remain unchanged at the end points of the time interval,  $\delta \varphi(t_1) = \delta \varphi(t_2) = \mathbf{0}$ . The last component in the first line is transferred into a surface integral by means of Gauss integration theorem. According to the Dirichlet-type boundary conditions (4.15) the variation  $\delta \varphi$  vanishes on  $\partial \mathcal{B}_\varphi$  and the necessary condition reduces to

$$\begin{aligned} \delta_\varphi H &= \int_{t_1}^{t_2} \left\{ \int_{\mathcal{B}} \left( \frac{\partial \mathcal{L}}{\partial \varphi} - \frac{\partial}{\partial t} \left[ \frac{\partial \mathcal{L}}{\partial \mathbf{v}} \right] - \text{Div} \left[ \frac{\partial \mathcal{L}}{\partial \mathbf{F}} \right] \right) \cdot \delta \varphi dV \right. \\ &\quad \left. + \int_{\partial \mathcal{B}_{\bar{t}}} \left( \frac{\partial \bar{\mathcal{L}}}{\partial \mathbf{F}} \mathbf{N} + \frac{\partial \bar{\mathcal{L}}}{\partial \varphi} \right) \cdot \delta \varphi dA \right\} dt = 0. \end{aligned} \quad (4.18)$$

Here,  $\mathbf{N}$  represents the outward normal of the material boundary  $\partial \mathcal{B}$ . This equation has to be fulfilled for all admissible variations  $\delta \varphi$  which allows for the identification of the spatial Euler-Lagrange equation of the variational formulation

$$- \text{Div} \left[ \frac{\partial \mathcal{L}}{\partial \mathbf{F}} \right] + \frac{\partial \mathcal{L}}{\partial \varphi} = \frac{\partial}{\partial t} \left[ \frac{\partial \mathcal{L}}{\partial \mathbf{v}} \right] \quad \text{in } \mathcal{B} \quad (4.19)$$

and the natural boundary conditions valid on the traction boundary

$$- \frac{\partial \mathcal{L}}{\partial \mathbf{F}} \mathbf{N} = \frac{\partial \bar{\mathcal{L}}}{\partial \varphi} \quad \text{on } \partial \mathcal{B}_{\bar{t}}. \quad (4.20)$$

Upon substitution of the Lagrangian densities (4.9) the Euler-Lagrange equation (4.19) appears as the Lagrangian version (2.45) of the local format of balance of physical or spatial linear momentum

$$\operatorname{Div} \mathbf{P} + \bar{\gamma}_0 = \rho_0 \frac{\partial}{\partial t} \mathbf{v} \quad \text{in } \mathcal{B} \quad (4.21)$$

with the constitutive relation  $\mathbf{P} = \partial_{\mathbf{F}} \psi$  for the first Piola-Kirchhoff stress tensor. Note that the partial time derivative  $\partial \mathbf{v} / \partial t$  of the spatial velocity field coincides with its total one  $d\mathbf{v} / dt|_{X \text{ fixed}}$  at fixed material positions. The traction boundary condition changes to

$$\mathbf{P} \mathbf{N} = \bar{\mathbf{t}} \quad \text{on } \partial \mathcal{B}_{\bar{\mathbf{t}}} \quad (4.22)$$

in terms of the given physical traction field  $\bar{\mathbf{t}}$ .

**4.2.3. Variation with respect to Material Coordinate.** Turning next to the variation of the action functional (4.12) with respect to the material position  $\mathbf{X}$ , attention is focused on possible changes of the material structure of the solid described by an arbitrary field  $\delta \mathbf{X}$  referred to as the variation of  $\mathbf{X}$ . According to the essential boundary conditions (4.13)<sub>2</sub>, this rearrangement of matter is restricted to the bulk material while the boundary must remain unaffected,  $\mathbf{X} = \text{const.}$  on  $\partial \mathcal{B}$ . In this sense, the material variation  $\delta \mathbf{X}$  is constrained by the homogeneous form of the boundary conditions

$$\delta \mathbf{X} \in \{ \delta \mathbf{X} \mid \delta \mathbf{X} = \mathbf{0} \text{ on } \partial \mathcal{B} \} \quad (4.23)$$

Recalling Remark 4.2 as well as the discussion outlined in the context of equation (3.11) in Section 3.2.1, a movement of material positions along the boundary  $\partial \mathcal{B}$  could be permitted inducing the alternative boundary condition  $\delta \mathbf{X} \in \{ \delta \mathbf{X} \mid \delta \mathbf{X} \cdot \mathbf{N} = \mathbf{0} \text{ on } \partial \mathcal{B} \}$  with the outward normal  $\mathbf{N}$  already introduced above. Performing the variation with respect to the material coordinates, the time  $t$  is kept constant

$$\begin{aligned} \delta_{\mathbf{X}} H = & \int_{t_1}^{t_2} \left\{ \int_{\mathcal{B}} \left\{ \frac{d}{d\epsilon} \mathcal{L}(t, \mathbf{X} + \epsilon \delta \mathbf{X}, \boldsymbol{\varphi}(\mathbf{X} + \epsilon \delta \mathbf{X}), \mathbf{v}(\mathbf{X} + \epsilon \delta \mathbf{X}), \mathbf{F}(\mathbf{X} + \epsilon \delta \mathbf{X})) \right\} \Big|_{\epsilon=0} \right. \\ & \left. + \mathcal{L}(\mathbf{1} : \nabla_{\mathbf{X}} \delta \mathbf{X}) \right\} dV + \int_{\partial \mathcal{B}_{\bar{\mathbf{t}}}} \left. \frac{d}{d\epsilon} \bar{\mathcal{L}}(t, \mathbf{X} + \epsilon \delta \mathbf{X}, \boldsymbol{\varphi}(\mathbf{X} + \epsilon \delta \mathbf{X})) \Big|_{\epsilon=0} dA \right\} dt = 0. \end{aligned} \quad (4.24)$$

By now, the variation  $\delta_{\mathbf{X}} dV$  of the integration limit of the volume integral has to be considered. This variation is computed in analogy to the time derivative of the spatial and material volume elements, cf. Section 2.1.5 and Appendix B, and leads to the first contribution in the second line of (4.24). In contrast, the material boundary remains constant,  $\delta_{\mathbf{X}} dA = 0$ . The derivative with respect to the perturbation  $\epsilon$  results in

$$\begin{aligned} \delta_{\mathbf{X}} H = & \int_{t_1}^{t_2} \left\{ \int_{\mathcal{B}} \left\{ \frac{\partial \mathcal{L}^{\text{expl}}}{\partial \mathbf{X}} \cdot \delta \mathbf{X} + \frac{\partial \mathcal{L}}{\partial \boldsymbol{\varphi}} \cdot \frac{\partial \boldsymbol{\varphi}}{\partial \mathbf{X}} \delta \mathbf{X} + \frac{\partial \mathcal{L}}{\partial \mathbf{v}} \cdot \frac{\partial \mathbf{v}}{\partial \mathbf{X}} \delta \mathbf{X} + \frac{\partial \mathcal{L}}{\partial \mathbf{F}} \cdot \frac{\partial \mathbf{F}}{\partial \mathbf{X}} \delta \mathbf{X} \right\} dV \right. \\ & \left. + \int_{\mathcal{B}} \mathcal{L}(\mathbf{1} : \nabla_{\mathbf{X}} \delta \mathbf{X}) dV + \int_{\partial \mathcal{B}_{\bar{\mathbf{t}}}} \frac{\partial \bar{\mathcal{L}}}{\partial \mathbf{X}} \cdot \delta \mathbf{X} dA \right\} dt = 0. \end{aligned} \quad (4.25)$$

Due to the homogeneous boundary condition (4.23) the surface integral is eliminated. By virtue of relation (4.2) the third component can be expressed in terms of the time

derivative of the deformation gradient. Application of integration by parts with respect to time and reference coordinate yields

$$\begin{aligned} \delta_{\mathbf{X}}H = & \int_{t_1}^{t_2} \left\{ \int_{\mathcal{B}} \left\{ \frac{\partial \mathcal{L}^{\text{expl}}}{\partial \mathbf{X}} \cdot \delta \mathbf{X} + \mathbf{F}^T \frac{\partial \mathcal{L}}{\partial \boldsymbol{\varphi}} \cdot \delta \mathbf{X} + \frac{\partial}{\partial t} \left[ \mathbf{F}^T \frac{\partial \mathcal{L}}{\partial \mathbf{v}} \right] \cdot \delta \mathbf{X} \right. \right. \\ & - \left( \mathbf{F}^T \frac{\partial}{\partial t} \left[ \frac{\partial \mathcal{L}}{\partial \mathbf{v}} \right] \right) \cdot \delta \mathbf{X} + \text{Div} \left[ \mathbf{F}^T \frac{\partial \mathcal{L}}{\partial \mathbf{F}} \right] \cdot \delta \mathbf{X} - \left( \mathbf{F}^T \text{Div} \left[ \frac{\partial \mathcal{L}}{\partial \mathbf{F}} \right] \right) \cdot \delta \mathbf{X} \\ & \left. \left. + \text{Div} \left[ \mathcal{L} \delta \mathbf{X} \right] - \text{Div} \left[ \mathcal{L} \mathbf{1} \right] \cdot \delta \mathbf{X} \right\} dV \right\} dt = 0. \end{aligned} \quad (4.26)$$

Using Gauss integration theorem, the first component of the third line is transformed into a surface integral which also vanishes due to the boundary conditions (4.23). Finally, the variation of the action functional with respect to the material coordinates reads

$$\begin{aligned} \delta_{\mathbf{X}}H = & \int_{t_1}^{t_2} \left\{ \int_{\mathcal{B}} \left\{ \left( \text{Div} \left[ -\mathcal{L} \mathbf{1} + \mathbf{F}^T \frac{\partial \mathcal{L}}{\partial \mathbf{F}} \right] + \frac{\partial \mathcal{L}^{\text{expl}}}{\partial \mathbf{X}} - \frac{\partial}{\partial t} \left[ -\mathbf{F}^T \frac{\partial \mathcal{L}}{\partial \mathbf{v}} \right] \right) \cdot \delta \mathbf{X} \right. \right. \\ & \left. \left. + \mathbf{F}^T \left( -\text{Div} \left[ \frac{\partial \mathcal{L}}{\partial \mathbf{F}} \right] + \frac{\partial \mathcal{L}}{\partial \boldsymbol{\varphi}} - \frac{\partial}{\partial t} \left[ \frac{\partial \mathcal{L}}{\partial \mathbf{v}} \right] \right) \cdot \delta \mathbf{X} \right\} dV \right\} dt = 0. \end{aligned} \quad (4.27)$$

The second expression represents the spatial Euler-Lagrange equation (4.19) being multiplied by the transpose of the deformation gradient in order to generate a purely material quantity. The variational form has to be satisfied for arbitrary admissible material variations  $\delta \mathbf{X}$ . Subjected to the condition that the spatial balance is fulfilled, the dual material or configurational Euler-Lagrange equation can be extracted

$$\text{Div} \left[ -\mathcal{L} \mathbf{1} + \mathbf{F}^T \frac{\partial \mathcal{L}}{\partial \mathbf{F}} \right] + \frac{\partial \mathcal{L}^{\text{expl}}}{\partial \mathbf{X}} = \frac{\partial}{\partial t} \left[ -\mathbf{F}^T \frac{\partial \mathcal{L}}{\partial \mathbf{v}} \right] \quad \text{in } \mathcal{B}. \quad (4.28)$$

For the material branch of the variational setting no natural boundary condition arises since the whole boundary is governed by the Dirichlet condition  $\mathbf{X} = \text{const.}$  on  $\partial \mathcal{B}$ . The material Euler-Lagrange equation can be reformulated by insertion of the Lagrangian density (4.9)<sub>1</sub>. On the one hand, consider the specification of the divergence term

$$\text{Div} \left[ -\mathcal{L} \mathbf{1} + \mathbf{F}^T \frac{\partial \mathcal{L}}{\partial \mathbf{F}} \right] = \text{Div} \left[ (\psi - \frac{1}{2} \rho_0 \mathbf{v} \cdot \mathbf{v}) \mathbf{1} - \mathbf{F}^T \mathbf{P} \right] - \mathbf{F}^T \bar{\boldsymbol{\gamma}}_0 - \boldsymbol{\varphi} \nabla_{\mathbf{X}} \bar{\boldsymbol{\gamma}}_0 \quad (4.29)$$

with the first Piola-Kirchhoff stress tensor  $\mathbf{P} = \partial_{\mathbf{F}} \psi$ . On the other hand, the explicit derivative of the Lagrangian density with respect to the material coordinates reads

$$\frac{\partial \mathcal{L}^{\text{expl}}}{\partial \mathbf{X}} = \frac{1}{2} \nabla_{\mathbf{X}} \rho_0 \mathbf{v} \cdot \mathbf{v} - \partial_{\mathbf{X}} \psi^{\text{expl}} + \boldsymbol{\varphi} \nabla_{\mathbf{X}} \bar{\boldsymbol{\gamma}}_0. \quad (4.30)$$

Upon summation, the last addends of (4.29) and (4.30) cancel and the configurational Euler-Lagrange equation is recast into the form of the local material balance equation

$$\text{Div} \boldsymbol{\Sigma} + \bar{\boldsymbol{\Gamma}}_0 = \frac{\partial}{\partial t} \boldsymbol{\mathcal{P}} \quad \text{in } \mathcal{B}. \quad (4.31)$$

This purely material balance law is denoted the *balance of material pseudomomentum* and states the dual material counterpart to the spatial balance law (4.21). It relies on the definition of the *dynamic Eshelby tensor*

$$\boldsymbol{\Sigma} := (\psi - \frac{1}{2} \rho_0 \mathbf{v} \cdot \mathbf{v}) \mathbf{1} - \mathbf{F}^T \mathbf{P} = -\tilde{\mathcal{L}} \mathbf{1} - \mathbf{F}^T \mathbf{P} \quad \text{with} \quad \tilde{\mathcal{L}} := \frac{1}{2} \rho_0 \mathbf{v} \cdot \mathbf{v} - \psi \quad (4.32)$$

in terms of the reduced Lagrangian density  $\tilde{\mathcal{L}}$  and the material vector fields

$$\mathbf{P} := -\rho_0 \mathbf{F}^T \mathbf{v} \quad \text{and} \quad \bar{\boldsymbol{\Gamma}}_0 := \frac{1}{2} \nabla_X \rho_0 \mathbf{v} \cdot \mathbf{v} - \partial_{\mathbf{X}} \psi^{\text{expl}} - \mathbf{F}^T \bar{\boldsymbol{\gamma}}_0 \quad (4.33)$$

denoted the *material pseudomomentum* and the *configurational* or *material volume force*, respectively. From (4.33)<sub>2</sub> it follows that configurational forces occur for the case that (i) spatial volume forces  $\bar{\boldsymbol{\gamma}}_0$  take effect, and/or the material body exhibits a material inhomogeneity which can be characterized by an explicit dependence of the (ii) free energy function  $\psi$  and (iii) the reference density  $\rho_0$  on the material position  $\mathbf{X}$ .

**Remark 4.3:** For the restriction to the quasi-static case, the pseudomomentum vector vanishes,  $\mathbf{P} = \mathbf{0}$ , and the dynamical Eshelby tensor  $\boldsymbol{\Sigma}$  boils down to its quasi-static counterpart (3.27) as the modified Lagrangian density reduces to the free energy function,  $-\tilde{\mathcal{L}} = \psi$ . Thus, the equation (4.31) of material motion passes into the material equilibrium condition (3.34) derived in the previous chapter and, on the one hand, appears as the dynamical generalization of the quasi-static material balance law. On the other hand, due to the fact that the current investigations are restricted to the isothermal elastic case, the configurational force  $\bar{\boldsymbol{\Gamma}}_0$  specified in (4.33)<sub>2</sub> does not include any contributions from the gradients of the temperature or internal variable field and consequently turns out to be a particular format of the more general expression (3.29). This expression basically captures the fundamental interpretation of a configurational force as an inhomogeneity force, or, more precisely, the driving force acting on an inhomogeneity embedded in a material body. It is of interest to point out that the full material inhomogeneity, including the explicit dependence of the density  $\rho_0$  and, as usual, of the free energy  $\psi$  on the material coordinates  $\mathbf{X}$  can be exhibited only in the dynamical framework because it is naturally related to the inertial contribution.

**Remark 4.4:** The derivation of the material balance equation in terms of a Lagrangian density  $\mathcal{L}$  directly refers to the classical approach of ESHELBY [43]. This procedure starts with the evaluation of the material gradient of the Lagrangian density (4.9)

$$\nabla_X \mathcal{L} = \frac{1}{2} \nabla_X \rho_0 \mathbf{v} \cdot \mathbf{v} + \rho_0 \nabla_X^T \mathbf{v} \mathbf{v} - \partial_{\mathbf{F}} \psi : \nabla_X \mathbf{F} - \partial_{\mathbf{X}} \psi^{\text{expl}} + \mathbf{F}^T \bar{\boldsymbol{\gamma}}_0 \quad (4.34)$$

Using the constitutive expression for the first Piola-Kirchhoff stress tensor,  $\mathbf{P} = \partial_{\mathbf{F}} \psi$ , the spatial balance equation (4.21) as well as the kinematic compatibility conditions  $\nabla_X \mathbf{F} = F_{iJ,K} = F_{iK,J}$  and  $\nabla_X \mathbf{v} = \partial \mathbf{F} / \partial t$ , this relation can be recast into the material balance law (4.31). For the sake of completeness, it has to be mentioned that ESHELBY [43] used the parameterization of the Lagrangian density in terms of the displacement gradient  $\nabla \mathbf{u} = u_{i,J}$  instead of the deformation gradient  $\mathbf{F} = F_{iJ}$  and thus ended up with the following representation of the energy-momentum tensor

$$\boldsymbol{\Sigma}_O := -\tilde{\mathcal{L}} \mathbf{1} + \nabla_X^T \mathbf{u} \frac{\partial \mathcal{L}}{\partial \nabla_X \mathbf{u}}. \quad (4.35)$$

Referring to Remark 3.1, the material balance equation is related to its spatial counterpart by a pull-back operation via premultiplication of the latter one with  $\mathbf{F}^T$ . While the link



between the left hand sides of both equations is obtained by the algebraic manipulations outlined in Remark 3.1 based on the material gradient (4.34), the pull-back transformation of the right hand side yielding the pseudomomentum  $\mathcal{P}$  is rather obvious.

**4.2.4. Variation with respect to Time.** With the objective of providing a comprehensive variational framework, in the final step the variation of the action functional with respect to time  $t$  is derived. As the Lagrangian space-time coordinates  $(\mathbf{X}, t)$  are assumed to be independent variables, the temporal change of  $\mathbf{X}$  is not explicitly included. On the contrary, the dependence of the deformation map, the velocity field and the deformation gradient on the time  $t$  needs to be taken into account

$$\begin{aligned} \delta_t H = & \int_{t_1}^{t_2} \left\{ \int_{\mathcal{B}} \frac{d}{d\epsilon} \mathcal{L}(t + \epsilon \delta t, \mathbf{X}, \boldsymbol{\varphi}(t + \epsilon \delta t), \mathbf{v}(t + \epsilon \delta t), \mathbf{F}(t + \epsilon \delta t)) \Big|_{\epsilon=0} dV \right. \\ & \left. + \int_{\partial \mathcal{B}_{\bar{i}}} \frac{d}{d\epsilon} \bar{\mathcal{L}}(t + \epsilon \delta t, \mathbf{X}, \boldsymbol{\varphi}(t + \epsilon \delta t)) \Big|_{\epsilon=0} dA \right\} dt \\ & + \int_{t_1}^{t_2} \left\{ \int_{\mathcal{B}} \mathcal{L} dV + \int_{\partial \mathcal{B}_{\bar{i}}} \bar{\mathcal{L}} dA \right\} \delta_t dt = 0. \end{aligned} \quad (4.36)$$

As the reference coordinates are kept unchanged, no variations of the integration limits concerning the bulk and the material boundary occur,  $\delta_t dV = \delta_t dA = 0$ . In contrast, the variation  $\delta_t dt$  of the infinitesimal time increment is evaluated in analogy to the variation of an infinitesimal volume element resulting in  $\delta_t dt = \partial \delta t / \partial t = d\delta t / dt|_{X \text{ fixed}}$ . Next, the variation of the action functional is evaluated

$$\begin{aligned} \delta_t H = & \int_{t_1}^{t_2} \left\{ \int_{\mathcal{B}} \left\{ \frac{\partial \mathcal{L}^{\text{expl}}}{\partial t} \delta t + \frac{\partial \mathcal{L}}{\partial \boldsymbol{\varphi}} \cdot \frac{\partial \boldsymbol{\varphi}}{\partial t} \delta t + \frac{\partial \mathcal{L}}{\partial \mathbf{v}} \cdot \frac{\partial \mathbf{v}}{\partial t} \delta t + \frac{\partial \mathcal{L}}{\partial \mathbf{F}} : \frac{\partial \mathbf{F}}{\partial t} \delta t \right\} dV \right. \\ & \left. + \int_{\partial \mathcal{B}_{\bar{i}}} \left\{ \frac{\partial \bar{\mathcal{L}}}{\partial t} \delta t \right\} dA \right\} dt + \int_{t_1}^{t_2} \left\{ \int_{\mathcal{B}} \mathcal{L} dV + \int_{\partial \mathcal{B}_{\bar{i}}} \bar{\mathcal{L}} dA \right\} \frac{d}{dt} \Big|_{X \text{ fixed}} \delta t dt = 0. \end{aligned} \quad (4.37)$$

Both time integrals, say  $\delta_t H_1$  and  $\delta_t H_2$ , are analyzed separately. Regarding the first integral, the partial time derivative in the surface integral coincides with the total one at fixed material position. The time derivative of the deformation gradient is replaced by the space derivative of the velocity field. In the next step, integration by parts with respect to time and reference coordinates is applied

$$\begin{aligned} \delta_t H_1 = & \int_{t_1}^{t_2} \left\{ \int_{\mathcal{B}} \left\{ \frac{\partial \mathcal{L}^{\text{expl}}}{\partial t} \delta t + \frac{\partial \mathcal{L}}{\partial \boldsymbol{\varphi}} \cdot \mathbf{v} \delta t + \frac{\partial}{\partial t} \left[ \frac{\partial \mathcal{L}}{\partial \mathbf{v}} \cdot \mathbf{v} \right] \delta t - \frac{\partial}{\partial t} \left[ \frac{\partial \mathcal{L}}{\partial \mathbf{v}} \right] \cdot \mathbf{v} \delta t \right. \right. \\ & \left. \left. + \text{Div} \left[ \mathbf{v} \frac{\partial \mathcal{L}}{\partial \mathbf{F}} \right] \delta t - \mathbf{v} \cdot \text{Div} \left[ \frac{\partial \mathcal{L}}{\partial \mathbf{F}} \right] \delta t \right\} dV + \int_{\partial \mathcal{B}_{\bar{i}}} \left\{ \frac{d}{dt} \Big|_{X \text{ fixed}} \bar{\mathcal{L}} \delta t \right\} dA \right\} dt. \end{aligned} \quad (4.38)$$

Turning next to the second integral, integration by parts with respect to time is performed

$$\begin{aligned} \delta_t H_2 = & \int_{t_1}^{t_2} \left\{ \frac{d}{dt} \Big|_{X \text{ fixed}} \left[ \left( \int_{\mathcal{B}} \mathcal{L} dV + \int_{\partial \mathcal{B}_{\bar{i}}} \bar{\mathcal{L}} dA \right) \delta t \right] \right\} dt \\ & - \int_{t_1}^{t_2} \left\{ \left( \frac{d}{dt} \Big|_{X \text{ fixed}} \left[ \int_{\mathcal{B}} \mathcal{L} dV + \int_{\partial \mathcal{B}_{\bar{i}}} \bar{\mathcal{L}} dA \right] \right) \delta t \right\} dt. \end{aligned} \quad (4.39)$$



In the first expression time integration and differentiation cancel out each other whereupon the argument is to be evaluated at the integration limits. As the motion of the system between two fixed points in time  $t_1$  and  $t_2$  is investigated,  $\delta t(t_1) = \delta t(t_2) = 0$ , this term is eliminated. With regard to the second term, time and space integration commute because the material coordinates are kept constant. Using the same reasoning, the variation  $\delta t$  can be written inside of the volume and boundary integrals

$$\delta_t H_2 = - \int_{t_1}^{t_2} \left\{ \int_{\mathcal{B}} \left( \frac{d}{dt} \Big|_{X \text{ fixed}} \mathcal{L} \right) \delta t \, dV + \int_{\partial \mathcal{B}_i} \left( \frac{d}{dt} \Big|_{X \text{ fixed}} \bar{\mathcal{L}} \right) \delta t \, dA \right\} dt. \quad (4.40)$$

By comparison of (4.38) and (4.40) the surface integral vanishes. Combining all the results, the variation of the action functional with respect to time can be expressed in the form

$$\begin{aligned} \delta_t H = \int_{t_1}^{t_2} \left\{ \int_{\mathcal{B}} \left\{ \left( \text{Div} \left[ \mathbf{v} \frac{\partial \mathcal{L}}{\partial \mathbf{F}} \right] + \frac{\partial \mathcal{L}^{\text{expl}}}{\partial t} - \frac{d}{dt} \Big|_{X \text{ fixed}} \mathcal{L} + \frac{\partial}{\partial t} \left[ \frac{\partial \mathcal{L}}{\partial \mathbf{v}} \cdot \mathbf{v} \right] \right) \delta t \right. \right. \\ \left. \left. + \mathbf{v} \cdot \left( -\text{Div} \left[ \frac{\partial \mathcal{L}}{\partial \mathbf{F}} \right] + \frac{\partial \mathcal{L}}{\partial \varphi} - \frac{\partial}{\partial t} \left[ \frac{\partial \mathcal{L}}{\partial \mathbf{v}} \right] \right) \delta t \right\} dV \right\} dt = 0 \end{aligned} \quad (4.41)$$

to be fulfilled for all admissible variations  $\delta t$ . The second contribution displays the spatial Euler-Lagrange equation multiplied by the velocity field to obtain a power expression. In case the spatial balance law is satisfied, the first term is identified as the temporal Euler-Lagrange equation

$$\text{Div} \left[ \mathbf{v} \frac{\partial \mathcal{L}}{\partial \mathbf{F}} \right] + \frac{\partial \mathcal{L}^{\text{expl}}}{\partial t} - \frac{d}{dt} \Big|_{X \text{ fixed}} \mathcal{L} = - \frac{\partial}{\partial t} \left[ \frac{\partial \mathcal{L}}{\partial \mathbf{v}} \cdot \mathbf{v} \right] \quad \text{in } \mathcal{B}. \quad (4.42)$$

Note that the explicit partial time derivative  $\partial \mathcal{L}^{\text{expl}} / \partial t$  does not coincide with the total time derivative  $d\mathcal{L}/dt|_{X \text{ fixed}}$  at fixed material positions since the latter one accounts for the implicit time-dependence of the Lagrangian density  $\mathcal{L}$  via the deformation map, the velocity field and the deformation gradient. Observe furthermore that the specific choice of the Lagrangian density is such that no explicit time-dependence of  $\mathcal{L}$  and  $\bar{\mathcal{L}}$  is assumed, see also the comments at the end of Section 4.2.5 below. Opening all the terms, the temporal Euler-Lagrange equation can be transferred to the more compact form

$$\mathbf{v} \cdot \text{Div} \left[ \frac{\partial \mathcal{L}}{\partial \mathbf{F}} \right] - \mathbf{v} \cdot \frac{\partial \mathcal{L}}{\partial \varphi} = - \mathbf{v} \cdot \frac{\partial}{\partial t} \left[ \frac{\partial \mathcal{L}}{\partial \mathbf{v}} \right] \quad \text{in } \mathcal{B}. \quad (4.43)$$

By substitution of the Lagrangian density (4.9)<sub>1</sub> this equation passes into the local form of the balance of kinetic energy

$$\mathbf{v} \cdot \text{Div} \mathbf{P} + \mathbf{v} \cdot \bar{\gamma}_0 = \rho_0 \mathbf{v} \cdot \frac{\partial}{\partial t} \mathbf{v} \quad \text{in } \mathcal{B} \quad (4.44)$$

which is already known from the investigations within Section 2.3.4.

**4.2.5. Additional Remarks. Noether's Theorem.** Starting from Hamilton's principle, the variations with respect to spatial and material coordinates and time are performed in a completely analogous way. At first, the variation is expressed by the Gateaux derivative whereupon integration by parts with respect to the Lagrangian coordinates and time

is applied. Subsequently, the corresponding Euler-Lagrange equations of the variational principle are extracted. Upon specification of the Lagrangian density these Euler-Lagrange equations are identified as the local formats of the balances of spatial linear momentum, material pseudomomentum and kinetic energy. The material and energetic balances are related to the spatial equation of motion by premultiplication with the transpose of the deformation gradient or the velocity field, respectively. Therefore, in the continuous setting all equations are entirely equivalent in the sense that the remaining equations are automatically fulfilled in case one balance is satisfied.

Within the derivations of the material and temporal balance equations, the spatial Euler-Lagrange equation arises as well. Subjected to the condition that this equation is satisfied, the corresponding balances can be extracted. This reasoning directly exploits so-called Noether's first theorem which dates back to the trendsetting work of NOETHER [139]. Noether considered variational problems having the property that the action integral remains invariant with respect to a group of transformations, applied either to the dependent or the independent variables. Then, every parameter associated with such transformations leads to a corresponding conservation law. Following this argumentation, the variational formulation deals with two types of equations. The first group arises due to the requirement that the variation of the action functional has to be zero with respect to a variation of the dependent variables or fields, i.e. the current position  $\boldsymbol{x} = \boldsymbol{\varphi}$ . The second group, called conservation laws, are the result of the variation of the parameterization, namely the independent variables, i.e. the material coordinates  $\boldsymbol{X}$  and the time  $t$ , and therefore a simultaneous transformation of both the dependent and the independent variables. A formally slightly different procedure is, in the author's opinion, closer to the formalism of Noether, however, on the other hand, appears to be more abstract in nature. It conceptually follows the processing proposed by KIENZLER & HERRMANN [76] and is presented in Appendix D. Further literature on the application of Noether's theorem and its relevance in the context of configurational mechanics have been proposed e.g. by KNOWLES & STERNBERG [78], CHADWICK [30], OLVER [143, 144], LI [94], related to the quasi-static case, as well as GUPTA [58], LI & GUPTA [93], see also MAUGIN [99] among others.

Irrespective of the methodological approach, the variational formulation results in the standard Euler-Lagrange equation, the notation  $EL_{\boldsymbol{\varphi}}$  has been introduced in Appendix D, associated with the variation with respect to the field, i.e. the current position, which represents the spatial balance of linear momentum. On account of Noether's reasoning, by variation of the action functional with respect to the independent variables and provided that the above field equation is satisfied,  $EL_{\boldsymbol{\varphi}} = \boldsymbol{0}$ , the procedure implies the existence of conservation laws. These are the local balances of material pseudomomentum and energy also denoted the canonical equations of momentum and energy, see e.g. the recent contribution of MAUGIN [107]. Typically, Noether's procedure ends up with so-called strict conservation laws. The accentuated expression *strict* induces that no source term enters the balance law. On the contrary, the balance equations derived above do contain some source terms arising from the explicit dependence of the Lagrangian functional on the independent variables. Hence, they are just denoted conservation laws. Within the present analyses, the independent variables are given by the Lagrangian space-time  $(\boldsymbol{X}, t)$  and therefore the general case, where source terms are present, is characterized by the dependence of both the reference density  $\rho_0$  and the free energy function  $\psi$  on  $(\boldsymbol{X}, t)$ . The dependence on  $\boldsymbol{X}$  indicates an inhomogeneous material body and results in the occurrence

of the configurational inhomogeneity force within the balance of pseudomomentum

$$-\frac{\partial}{\partial t}\mathbf{P} + \text{Div}\boldsymbol{\Sigma} - \mathbf{F}^T\bar{\boldsymbol{\gamma}}_0 = -\frac{1}{2}\nabla_X\rho_0\mathbf{v}\cdot\mathbf{v} + \partial_{\mathbf{X}}\psi^{\text{expl}} =: \bar{\boldsymbol{\Gamma}}_{\mathbf{X}}, \quad (4.45)$$

cf. Remark 4.3. In contrast, within the current investigations neither the reference density  $\rho_0$ , cf. equation (2.41)<sub>1</sub> in Section 2.3.1, nor the free energy function  $\psi$  explicitly depend on time. This is due to the fact that the description of the phenomena of growth or resorption, related to a time-dependent field  $\rho_0$ , and of ageing, indicated by a time-dependent free energy  $\psi$ , are out of the scope of this work. In this sense, the local format of the kinetic energy balance can be classified as a strict conservation law.

### 4.3. Global Material and Spatial Balance Equations

The three Euler-Lagrange equations of the variational formulation represent local balance laws. The notation local is adopted as the balance equations constitute partial differential equations governing the response at every material point of the solid. Focusing on the variation with respect to the spatial and material coordinates, the local formats of spatial linear momentum and material pseudomomentum are given by (4.21) and (4.31)

$$\text{Div}\mathbf{P} + \bar{\boldsymbol{\gamma}}_0 = \rho_0\frac{d}{dt}\Big|_{X \text{ fixed}}\mathbf{v} \quad \text{and} \quad \text{Div}\boldsymbol{\Sigma} + \bar{\boldsymbol{\Gamma}}_0 = \frac{d}{dt}\Big|_{X \text{ fixed}}\mathbf{P} \quad \text{in } \mathcal{B}. \quad (4.46)$$

Observe that the partial time derivative employed before characterizes the total time derivative at frozen material position,  $\partial(\bullet)/\partial t = d(\bullet)/dt|_{X \text{ fixed}}$ . Recalling the results outlined within Section 2.3.2, the first equation has been derived from the global balance of linear momentum (2.43). During these former investigations the global balance has been formulated with respect to a cut-out part  $\mathcal{P}_{\mathcal{S}}$  of the current configuration  $\mathcal{S}$  but is now formally related to  $\mathcal{S}$  itself

$$\frac{d}{dt}\int_{\mathcal{S}}\rho\mathbf{v}dv = \int_{\mathcal{S}}\bar{\boldsymbol{\gamma}}dv + \int_{\partial\mathcal{S}_{\bar{\mathbf{t}}}}\bar{\mathbf{t}}da. \quad (4.47)$$

The Eulerian object  $\rho\mathbf{v}$  denotes the physical linear momentum per unit volume of  $\mathcal{S}$ . The balance states that the temporal change of the global momentum equals the resultant physical force acting on the body. Starting from this global statement, the local balance law has been obtained. This procedure is now applied the other way round. The local spatial balance (4.46)<sub>1</sub> is integrated over the reference configuration  $\mathcal{B}$  whereupon the divergence term is recast into a surface integral by means of Gauss integration theorem. As the time differentiation is performed at fixed material coordinates, it commutes with the integration over the reference configuration. Finally, the analyses end up with the Lagrangian, or rather two-point formulation of the *global balance of physical linear momentum*

$$\frac{d}{dt}\Big|_{X \text{ fixed}}\int_{\mathcal{B}}\rho_0\mathbf{v}dV = \int_{\mathcal{B}}\bar{\boldsymbol{\gamma}}_0dV + \int_{\partial\mathcal{B}}\mathbf{P}\mathbf{N}dA. \quad (4.48)$$

This equation still constitutes an Eulerian expression as all the ingredients are spatial objects. The surface integral can be rewritten in terms of the prescribed physical tractions due to the natural boundary conditions (4.22), i.e.  $\mathbf{P}\mathbf{N} = \bar{\mathbf{t}}$  on  $\partial\mathcal{B}_{\bar{\mathbf{t}}}$ .

The same procedure is now applied to the local material balance (4.46)<sub>2</sub>. The resulting expression characterizes the *global balance of material pseudomomentum*

$$\left. \frac{d}{dt} \right|_{X \text{ fixed}} \int_{\mathcal{B}} \mathcal{P} dV = \int_{\mathcal{B}} \bar{\Gamma}_0 dV + \int_{\partial \mathcal{B}} \Sigma \mathbf{N} dA \quad (4.49)$$

being the material counterpart of (4.48). In analogy to the spatial setting, the right hand side is governed by a resultant global configurational or material force which in turn consists of a volume contribution and a surface part in terms of the configurational volume force  $\bar{\Gamma}_0$  and the Eshelby tensor  $\Sigma$ , respectively. The left hand side is formed by the temporal change of the global pseudomomentum. All these balances are also referred to as conservation laws. If no source terms are present, i.e.  $\bar{\gamma}_0 = \mathbf{0}$  and  $\bar{\Gamma}_0 = \mathbf{0}$ , the notation strict conservation laws is used instead. Upon restriction to the quasi-static case, the left hand sides of the global balance equations vanish inducing the *dual spatial and material equilibrium conditions* of physical Newtonian and configurational Eshelbian forces

$$\int_{\mathcal{B}} \bar{\gamma}_0 dV + \int_{\partial \mathcal{B}} \mathbf{P} \mathbf{N} dA = \mathbf{0} \quad \text{and} \quad \int_{\mathcal{B}} \bar{\Gamma}_0 dV + \int_{\partial \mathcal{B}} \Sigma \mathbf{N} dA = \mathbf{0}. \quad (4.50)$$

These global statements render in their local representation the balance equations (3.33)<sub>1</sub> and (3.34) introduced in Chapter 3. Configurational volume forces  $\bar{\Gamma}_0$  occur if the material body contains any arbitrary type of inhomogeneities which is why its global format is also denoted the inhomogeneity force, see e.g. MAUGIN [99]. Vice versa, in case of a homogeneous body, the local and global configurational force cancels. The material balance law reduces to the surface-independent integral which, on the local level, coincides with the demand for a divergence free Eshelby stress

$$\int_{\partial \mathcal{B}} \Sigma \mathbf{N} dA = \mathbf{0} \quad \xrightarrow{\text{localization}} \quad \text{Div} \Sigma = \mathbf{0} \quad \text{in } \mathcal{B} \quad (4.51)$$

representing a strict conservation law. It is of interest to point out that the identity (4.50)<sub>2</sub> allows for the computation of the inhomogeneity force by evaluation of the surface-independent integral. This result has been in some way anticipated in Appendix A where the surface-independent integral, introduced on account of Eshelby's reasoning in (A.6) and (A.17), has been denoted the driving force on a singularity or an inhomogeneity.

**Remark 4.5:** The third balance equation (4.44), namely the local form of the balance of kinetic energy, can also be transformed to a global counterpart in the afore-mentioned way. This has already been discussed in detail within Section 2.3.4.

#### 4.4. Numerical Treatment: Discretization in Space and Time

Attention is focused on the numerical implementation. Subsequent to some brief introductory comments, space and time discretization of the governing equations is performed.

**4.4.1. General Aspects and Numerical Solution Procedure.** The continuous formulation of configurational solid dynamics ends up with three field equations, namely the equations of spatial and material motion and the balance of kinetic energy. It has been shown that in the continuous setting all these equations are equivalent. This means, that in case the spatial balance of linear momentum is satisfied, the two other equations are fulfilled automatically. This equivalence does not hold in the discrete setting. For this reason, in the most general context, all three equations have to be considered within the

numerical framework. Following for instance the ideas proposed by ZIELONKA [191], a promising approach towards the numerical implementation appears when the solution of these three equations is performed simultaneously by means of a time-dependent variational arbitrary Lagrangian Eulerian formulation.

In the present work an alternative procedure is incorporated. However, the balance of kinetic energy is not explicitly enforced as a strong form equation but just assumed to be satisfied at the spatial solution state. Thus, the dynamical problem is given by the material and spatial momentum balances (4.21) and (4.31)

equation of spatial motion	$\text{Div} \mathbf{P} + \bar{\gamma}_0 = \rho_0 \frac{\partial}{\partial t} \mathbf{v}$	in $\mathcal{B}$	(4.52)
equation of material motion	$\text{Div} \boldsymbol{\Sigma} + \bar{\Gamma}_0 = \frac{\partial}{\partial t} \mathcal{P}$	in $\mathcal{B}$	

constrained by the essential boundary conditions for the current and reference coordinates

$$\varphi = \bar{\varphi} \quad \text{on } \partial \mathcal{B}_\varphi \quad \text{and} \quad \mathbf{X} = \text{const.} \quad \text{on } \partial \mathcal{B}. \quad (4.53)$$

Recall that the prescribed spatial deformation  $\bar{\varphi}$  can be expressed by a prescribed velocity  $\bar{\mathbf{v}}$  according to  $\bar{\varphi} = \mathbf{X} + t\bar{\mathbf{v}}$ . In view of the spatial problem, the remaining part of the boundary is governed by the natural boundary conditions

$$\mathbf{PN} = \bar{\mathbf{t}} \quad \text{on } \partial \mathcal{B}_{\bar{\mathbf{t}}} \quad (4.54)$$

with the given traction field  $\bar{\mathbf{t}}$ . The processing employed for the forthcoming investigations coincides with that proposed in Chapter 3 for thermo-mechanically coupled problems at finite inelastic deformations. To be specific, a staggered solution strategy is used wherein the field equations are not treated contemporaneously, i.e. in the sense of an ALE approach, but successively at frozen state with respect to the dual problem, cf. Figure 3.5 within Section 3.4 for a sketch of this idea. In the first step, the standard spatial motion problem is analyzed by solving the spatial balance of linear momentum (4.52)<sub>1</sub> for the primary unknowns, i.e. the current Eulerian coordinates. Once the spatial problem is solved, the equation of material motion is investigated in a postprocessing step directly related to the evaluation of discrete configurational nodal forces.

**4.4.2. Solution of Equation of Spatial Motion.** Several approaches exist for the numerical implementation of this standard problem of structural dynamics. The first class is concerned with Galerkin-type schemes, in which the discretization with respect to space and time is performed via the finite element method. A second class, used in the following, is posed by Newmark-type schemes. The temporal discretization is carried out via finite step size integration algorithms usually denoted finite differences, see e.g. the textbook of BELYTSCHKO, LIU & MORAN [14] and the references given therein.

**4.4.2.1. Space Discretization by Finite Element Method.** Starting point is the weak form of the boundary value problem or the variational formulation. By substitution of the Lagrangian densities  $\mathcal{L}$  and  $\bar{\mathcal{L}}$  given in (4.9) the variation (4.16)<sub>2</sub> of the action functional with respect to the spatial coordinates reads

$$\delta_\varphi H = \int_{t_1}^{t_2} \left\{ \int_{\mathcal{B}} \left( \frac{\partial}{\partial t} \delta \varphi \right) \cdot \rho_0 \mathbf{v} - \nabla_X \delta \varphi : \mathbf{P} + \delta \varphi \cdot \bar{\gamma}_0 \, dV + \int_{\partial \mathcal{B}_{\bar{\mathbf{t}}}} \delta \varphi \cdot \bar{\mathbf{t}} \, dA \right\} dt = 0 \quad (4.55)$$

with  $\nabla_X(\bullet) = \partial(\bullet)/\partial\mathbf{X}$ . After some straightforward manipulations using integration by parts with respect to time and the fact that the motion of the system between two fixed points in time is considered,  $\delta\boldsymbol{\varphi}(t_1) = \delta\boldsymbol{\varphi}(t_2) = \mathbf{0}$ , the following integral is obtained

$$\delta_\varphi H_t = \int_{\mathcal{B}} -\delta\boldsymbol{\varphi} \cdot \left(\rho_0 \frac{\partial^2}{\partial t^2} \boldsymbol{\varphi}\right) - \nabla_X \delta\boldsymbol{\varphi} : \mathbf{P} + \delta\boldsymbol{\varphi} \cdot \bar{\boldsymbol{\gamma}}_0 \, dV + \int_{\partial\mathcal{B}_t} \delta\boldsymbol{\varphi} \cdot \bar{\mathbf{t}} \, dA = 0. \quad (4.56)$$

This represents the variational or weak formulation at every point in time within the interval  $t \in [t_1, t_2]$  indicated by the subscript  $t$ . For the solution of this non-linear equation Newton-Raphson-type iteration is adopted demanding its consistent linearization

$$\text{Lin } \delta_\varphi H_t = \delta_\varphi H_t + \int_{\mathcal{B}} -\delta\boldsymbol{\varphi} \cdot \left(\rho_0 \frac{\partial^2}{\partial t^2} \Delta\boldsymbol{\varphi}\right) - \nabla_X \delta\boldsymbol{\varphi} : \mathbb{C} : \nabla_X \Delta\boldsymbol{\varphi} \, dV = 0 \quad (4.57)$$

in terms of the fourth order nominal elasticity moduli  $\mathbb{C}$ . Within a typical Newton step, this equation has to be solved for the incremental deformation  $\Delta\boldsymbol{\varphi}$ .

In the next step space discretization is applied. The continuous body  $\mathcal{B}$  is subdivided into  $n_{ele}$  finite elements  $\mathcal{B}^e$ , cf. equation (3.51),

$$\mathcal{B} \approx \mathcal{B}^h = \bigtriangleup_{e=1}^{n_{ele}} \mathcal{B}^e. \quad (4.58)$$

The spatial deformation map as well as its variation and increment are approximated on the element level

$$\boldsymbol{\varphi} \approx \mathbf{N} \mathbf{d}_t, \quad \delta\boldsymbol{\varphi} \approx \mathbf{N} \delta\mathbf{d}_t \quad \text{and} \quad \Delta\boldsymbol{\varphi} \approx \mathbf{N} \Delta\mathbf{d}_t \quad (4.59)$$

in terms of an overall matrix of shape functions  $\mathbf{N}$  and the global vectors  $\mathbf{d}_t$ ,  $\delta\mathbf{d}_t$ ,  $\Delta\mathbf{d}_t$  representing the discrete nodal values of the spatial displacements as well as their variations and increments at all  $\mathcal{N}_t$  nodal points of the current mesh. With the discrete motion  $\boldsymbol{\varphi}$  at hand, the derivatives with respect to the Lagrangian space-time can be evaluated

$$\frac{\partial^2}{\partial t^2} \boldsymbol{\varphi} \approx \mathbf{N} \ddot{\mathbf{d}}_t \quad \text{and} \quad \nabla_X \boldsymbol{\varphi} \approx \mathbf{B} \mathbf{d}_t. \quad (4.60)$$

Here,  $\ddot{\mathbf{d}}_t$  denotes the global vector of discrete spatial nodal accelerations and the matrix  $\mathbf{B}$  contains the derivatives of the shape functions with respect to the material coordinates. The same relationships apply for the derivatives of the variation and the increment of  $\boldsymbol{\varphi}$ . By substitution of the finite element interpolation into the weak form (4.56) the approximation of the variational expression appears as a sum of discrete nodal contributions

$$\delta_\varphi H_t^h = \sum_{I=1}^{\mathcal{N}_t} \{[-\mathbf{a}_I + \mathbf{f}_I + \mathbf{p}_I] \cdot \delta\mathbf{d}_I\} = 0. \quad (4.61)$$

The nodal quantities  $\mathbf{f}_I$  and  $\mathbf{p}_I$  have already been introduced in Section 3.3.2.1 within the quasi-static framework

$$\mathbf{f}_I := - \bigtriangleup_{e=1}^{n_{ele}} \int_{\mathcal{B}^e} \mathbf{B}_I^T \mathbf{P} \, dV \quad \text{and} \quad \mathbf{p}_I := \bigtriangleup_{e=1}^{n_{ele}} \left\{ \int_{\mathcal{B}^e} \mathbf{N}_I^T \bar{\boldsymbol{\gamma}}_0 \, dV + \int_{\partial\mathcal{B}^e} \mathbf{N}_I^T \bar{\mathbf{t}} \, dA \right\}. \quad (4.62)$$



They represent the discrete nodal vectors of external and internal spatial forces governed by the volume forces  $\bar{\gamma}_0$ , the surface tractions  $\bar{\mathbf{t}}$  and the first Piola-Kirchhoff stresses  $\mathbf{P}$ . In the dynamical setting, an additional nodal vector  $\mathbf{a}_I$  arises denoted the inertia force

$$\mathbf{a}_I := \mathbf{m}_{IJ} \ddot{\mathbf{d}}_J \quad \text{with} \quad \mathbf{m}_{IJ} := \mathbf{A} \int_{\mathcal{B}^e} \mathbf{N}_I^T \rho_0 \mathbf{N}_J dV. \quad (4.63)$$

It is defined by the contraction of the nodal accelerations  $\ddot{\mathbf{d}}_J$  and the mass matrix  $\mathbf{m}_{IJ}$  which in the given format is a natural result of the discretization process and usually referred to as consistent mass matrix. In many cases a diagonalization of this matrix, so-called lumping, has proven to be reasonable, see e.g. ZIENKIEWICZ & TAYLOR [192] and Section 3.5.2 regarding the lumping procedure. Equation (4.61) has to be fulfilled for all admissible variations  $\delta \mathbf{d}_I$  resulting in the semi-discrete equation of spatial motion

$$-\mathbf{a}_I + \mathbf{f}_I + \mathbf{p}_I = \mathbf{0} \quad \text{in } \mathcal{B}^h \text{ and on } \partial \mathcal{B}_t^h \quad (4.64)$$

to be satisfied at every node  $I = 1, \mathcal{N}_t$  of the mesh. For the quasi-static case inertia forces do not exist,  $\mathbf{a}_I = \mathbf{0}$ , and (4.64) boils down to the spatial equilibrium condition (3.63). The equation of spatial motion can be recast into the more familiar format

$$\mathbf{M} \ddot{\mathbf{d}}_t - \mathbf{P}^{int} = \mathbf{P}^{ext} \quad (4.65)$$

based on the global internal and external load vectors and the system mass matrix

$$\mathbf{P}^{int} = \sum_{I=1}^{\mathcal{N}_t} \mathbf{f}_I, \quad \mathbf{P}^{ext} = \sum_{I=1}^{\mathcal{N}_t} \mathbf{p}_I \quad \text{and} \quad \mathbf{M} = \sum_{I,J=1}^{\mathcal{N}_t} \mathbf{m}_{IJ}. \quad (4.66)$$

The linearized system of equations is obtained by substitution of the finite element approximation into the linearization (4.57)

$$\mathbf{M} \Delta \ddot{\mathbf{d}}_t + \mathbf{K} \Delta \mathbf{d}_t = \mathbf{P}^{ext} + \mathbf{P}^{int} - \mathbf{M} \ddot{\mathbf{d}}_t \quad (4.67)$$

where  $\Delta \mathbf{d}_t$  and  $\Delta \ddot{\mathbf{d}}_t$  denote the global vectors of incremental nodal displacements and accelerations and

$$\mathbf{K} = \sum_{I,J=1}^{\mathcal{N}_t} \mathbf{k}_{IJ} = \sum_{I,J=1}^{\mathcal{N}_t} \left\{ \mathbf{A} \int_{\mathcal{B}^e} \mathbf{B}_I^T \mathbb{C} \mathbf{B}_J dV \right\} \quad (4.68)$$

characterizes the global tangential stiffness matrix.

**4.4.2.2. Time Discretization by Finite Difference Method.** Upon spatial discretization by means of finite elements, the weak form passes into a semi-discrete system of equations (4.65) being still continuous in time. For the solution of this system of second order ordinary differential equations in time the implicit Newmark method, cf. NEWMARK [137], is used. This type of solution algorithms possesses algorithmic damping. To handle this problem, CHUNG & HULBERT [31] proposed the generalized- $\alpha$  method, also referred to as Newmark- $\alpha$  method, characterized by an improved numerical dissipation. Unfortunately, it has been found to be just conditionally stable in the context of non-linear dynamics. For particular choices of the parameters that guarantee stability, the algorithm is too dissipative and violates the requirement of energy conservation. Hence, it

appears not suitable for long-run analysis. Improved unconditionally stable algorithms are provided for instance by the energy-momentum method, SIMO & TARNOW [166, 167], so-called energy conserving/decaying schemes, ARMERO & PETÖCZ [5], or the generalized energy-momentum method, KUHLE & CRISFIELD [82]. Long-run computations are out of the scope of the present work but attention is focused on the evaluation and utilization of configurational forces within the dynamical framework. Thus, the Newmark- $\alpha$  method is supposed to be an appropriate solution strategy in view of the forthcoming studies.

The basic feature of a step-by-step integration scheme is the subdivision of the continuous time interval  $[t_1, t_2]$  into  $n_t$  discrete time steps  $\Delta t$

$$[t_1, t_2] = \bigcup_{n=1}^{n_t} [t_n, t_{n+1}] \quad \text{with} \quad \Delta t = t_{n+1} - t_n. \quad (4.69)$$

The current nodal velocities and accelerations are expressed in terms of the current nodal displacements and the respective values of the previous time step via the classical Newmark-approximation

$$\begin{aligned} \dot{\mathbf{d}}_{n+1} &= \frac{\gamma}{\beta\Delta t}(\mathbf{d}_{n+1} - \mathbf{d}_n) - \frac{\gamma - \beta}{\beta}\dot{\mathbf{d}}_n - \frac{\gamma - 2\beta}{2\beta}\Delta t \ddot{\mathbf{d}}_n \\ \ddot{\mathbf{d}}_{n+1} &= \frac{1}{\beta\Delta t^2}(\mathbf{d}_{n+1} - \mathbf{d}_n) - \frac{1}{\beta\Delta t}\dot{\mathbf{d}}_n - \frac{1 - 2\beta}{2\beta}\ddot{\mathbf{d}}_n \end{aligned} \quad (4.70)$$

with the algorithmic parameters  $\gamma$  and  $\beta$  of the Newmark method and the subscripts  $n+1$  and  $n$  referring to times  $t_{n+1}$  and  $t_n$ , respectively. Following CHUNG & HULBERT [31], the current kinematic quantities are modified in the sense of a mid point approximation

$$\ddot{\mathbf{d}}_{n+1-\alpha_m} = (1 - \alpha_m)\ddot{\mathbf{d}}_{n+1} + \alpha_m\ddot{\mathbf{d}}_n \quad \text{and} \quad \dot{\mathbf{d}}_{n+1-\alpha_f} = (1 - \alpha_f)\dot{\mathbf{d}}_{n+1} + \alpha_f\dot{\mathbf{d}}_n \quad (4.71)$$

involving an averaging of the previous and current values controlled by the algorithmic parameters  $\alpha_m$  and  $\alpha_f$ . The nodal displacements  $\mathbf{d}_{n+1-\alpha_f}$  are given in the same format as the velocities (4.71)<sub>2</sub>. The generalized- $\alpha$  method bases on the representation of the semi-discrete equation of spatial motion (4.65) at times  $t_{n+1-\alpha_m}$  and  $t_{n+1-\alpha_f}$

$$M\ddot{\mathbf{d}}_{n+1-\alpha_m} - \mathbf{P}_{n+1-\alpha_f}^{int} = \mathbf{P}_{n+1-\alpha_f}^{ext}. \quad (4.72)$$

This system of non-linear equations has to be linearized with respect to the nodal displacements  $\mathbf{d}_{n+1}$  at the endpoint of the time interval. Taking into account that due to (4.70)<sub>2</sub> the incremental accelerations are directly related to the incremental displacements, i.e.  $\Delta\ddot{\mathbf{d}}_{n+1} = \Delta\mathbf{d}_{n+1}/(\beta\Delta t^2)$ , the governing system of linear equations is obtained

$$\mathbf{K}^{\text{eff}}(\mathbf{d}_{n+1}^k)\Delta\mathbf{d}_{n+1} = \mathbf{R}^{\text{eff}}(\mathbf{d}_{n+1}^k). \quad (4.73)$$

The effective stiffness matrix and residual vector are respectively defined by

$$\begin{aligned} \mathbf{K}^{\text{eff}} &= M\frac{1 - \alpha_m}{\beta\Delta t^2} + (1 - \alpha_f)\mathbf{K}(\mathbf{d}_{n+1-\alpha_f}(\mathbf{d}_{n+1}^k)) \\ \mathbf{R}^{\text{eff}} &= \mathbf{P}_{n+1-\alpha_f}^{ext} + \mathbf{P}_{n+1-\alpha_f}^{int}(\mathbf{d}_{n+1-\alpha_f}(\mathbf{d}_{n+1}^k)) - M\ddot{\mathbf{d}}_{n+1-\alpha_m}(\ddot{\mathbf{d}}_{n+1}(\mathbf{d}_{n+1}^k)) \end{aligned} \quad (4.74)$$

and depend on the actual displacements  $\mathbf{d}_{n+1}^k$  associated with the  $k$ -th step of the Newton iteration. The global external and internal load vectors as well as the global mass and stiffness matrices have been introduced in (4.66) and (4.68). The effective space-time discrete system of linear equations is solved for the incremental nodal displacements  $\Delta\mathbf{d}$  whereupon the current nodal values are evaluated by the Newton update  $\mathbf{d} \leftarrow \mathbf{d} + \Delta\mathbf{d}$ .



**4.4.3. Treatment of Equation of Material Motion.** In the sense of the staggered solution strategy, the numerical treatment of the material balance equation (4.52)<sub>2</sub> does not pose a new boundary value problem. Nevertheless, recalling the investigations of Section 3.5, some additional effort had to be done within the framework of inelasticity to generate the material gradient of the internal variable field. This is no longer required in the current context of hyperelastodynamics since at every time step all the ingredients to compute the Eshelby tensor, the pseudomomentum and the configurational force are obtained by the solution of the equation of spatial motion. Therefore, the numerical implementation of the balance of material motion is captured by its space discretization which in turn offers a postprocessing tool to be exploited at the end of every time step. Space discretization by the finite element method demands a weak counterpart of the equation of material motion. This is intrinsically provided by the variational formulation upon variation of the action functional with respect to the reference coordinates  $\delta \mathbf{X} H$ , cf. (4.24), subjected to the condition that the standard Euler-Lagrange equation, i.e. the equation of spatial motion, is fulfilled. Alternatively, the weak form can be derived by standard Galerkin procedure. The strong form equation (4.52)<sub>2</sub> is multiplied by some arbitrary test functions or variations  $\delta \mathbf{X}$  satisfying the homogeneous form (4.23) of the essential boundary conditions. This expression is integrated over the reference volume

$$\delta_{\mathbf{X}} H_t = \int_{\mathcal{B}} \delta \mathbf{X} \cdot \left( -\frac{\partial}{\partial t} \mathcal{P} + \text{Div} \Sigma + \bar{\Gamma}_0 \right) dV = 0. \quad (4.75)$$

The subscript  $t$  again indicates this relation holding at every time  $t \in [t_1, t_2]$ . Integration by parts with respect to the Lagrangian coordinates  $\mathbf{X}$  and application of Gauss integration theorem along with the boundary conditions render the weak form

$$\delta_{\mathbf{X}} H_t = \int_{\mathcal{B}} -\delta \mathbf{X} \cdot \frac{\partial}{\partial t} \mathcal{P} - \nabla_{\mathbf{X}} \delta \mathbf{X} : \Sigma + \delta \mathbf{X} \cdot \bar{\Gamma}_0 dV = 0. \quad (4.76)$$

It formally displays the same structure compared to the weak form (4.56) of the spatial balance law apart from the surface integral which does not appear for the material problem as the whole boundary is governed by the essential boundary conditions.

Using finite element scheme, the Lagrangian coordinates  $\mathbf{X}$  and their variations  $\delta \mathbf{X}$  are approximated via global nodal vectors  $\mathbf{D}_t$  and  $\delta \mathbf{D}_t$  containing the discrete material nodal positions and variations at every node  $I = 1, \mathcal{N}_t$  of the mesh

$$\mathbf{X} \approx \mathbf{N} \mathbf{D}_t, \quad \delta \mathbf{X} \approx \mathbf{N} \delta \mathbf{D}_t \quad \text{and} \quad \nabla_{\mathbf{X}} \delta \mathbf{X} \approx \mathbf{B} \delta \mathbf{D}_t. \quad (4.77)$$

Without loss of generality, the same shape functions  $\mathbf{N}$  are employed for the material and the spatial problem which is why the matrix  $\mathbf{B}$  remains unchanged as well. Upon insertion of these relations into the weak form (4.76) its space-discrete counterpart is obtained

$$\delta_{\mathbf{X}} H_t^h = \sum_{I=1}^{\mathcal{N}_t} \{ [-\mathbf{A}_I + \mathbf{F}_I + \mathbf{P}_I] \cdot \delta \mathbf{D}_I \} = 0. \quad (4.78)$$

This equation has to be satisfied for arbitrary admissible nodal variations  $\delta \mathbf{D}_I$ . Thus, the bracket term has to vanish and it remains the discrete equation of material motion in the format of a nodal balance equation

$$-\mathbf{A}_I + \mathbf{F}_I + \mathbf{P}_I = \mathbf{0} \quad \text{in } \mathcal{B}^h \quad (4.79)$$

to be enforced at all nodes  $I = 1, \mathcal{N}_t$  at every time  $t$ . The vectorial quantities  $\mathbf{F}_I$  and  $\mathbf{P}_I$  denote the material internal nodal force and the discrete configurational nodal force. Their definitions formally coincide with those introduced in the quasi-static setting

$$\mathbf{F}_I := - \mathbf{A} \int_{\mathcal{B}^e} \mathbf{B}_I^T \boldsymbol{\Sigma} dV \quad \text{and} \quad \mathbf{P}_I := \mathbf{A} \int_{\mathcal{B}^e} \mathbf{N}_I^T \bar{\boldsymbol{\Gamma}}_0 dV. \quad (4.80)$$

Despite the formal analogy, these nodal vectors are naturally associated to the dynamical framework as they base on the dynamical Eshelby stress tensor  $\boldsymbol{\Sigma}$  and the continuous configurational volume force  $\bar{\boldsymbol{\Gamma}}_0$  specified in equations (4.32) and (4.33)<sub>2</sub>. Additionally, the discrete counterpart  $\mathbf{A}_I$  of the pseudomomentum vector  $\mathcal{P}$ , (4.33)<sub>1</sub>, reads

$$\mathbf{A}_I := \mathbf{A} \int_{\mathcal{B}^e} \mathbf{N}_I^T \frac{\partial}{\partial t} \mathcal{P} dV = \mathbf{A} \int_{\mathcal{B}^e} \mathbf{N}_I^T \rho_0 \frac{\partial}{\partial t} (-\mathbf{F}^T \mathbf{v}) dV. \quad (4.81)$$

Rather than solving explicitly for the Lagrangian coordinates  $\mathbf{X}$ , the material nodal balance (4.79) is used in a postprocessing step according to the staggered solution strategy. The different nodal contributions are obtained just by function evaluation with all the ingredients being provided by the solution of the equation of spatial motion.

#### 4.5. Specification and Numerical Example

The numerical procedures elaborated in the previous chapter are applied to a descriptive boundary value problem. The oscillation of a strip is analyzed focusing in particular on the effects arising from the treatment of the equation of material motion.

**4.5.1. Material Model and Constitutive Relations.** Before starting with the discussion of the numerical example, a material model of finite elasticity is introduced. This specific model will be employed for all analyses concerned with elastic material response throughout this thesis. The constitutive behavior of an elastic system is governed by the free Helmholtz energy  $\psi$  representing the energy storage of the material. A compressible Neo-Hookean type storage function is assumed

$$\psi(\mathbf{F}) = \frac{\mu}{2} (\text{tr} [\mathbf{F}^T \mathbf{g} \mathbf{F}] - 3) + \frac{\mu}{\beta} ((\det \mathbf{F})^{-\beta} - 1). \quad (4.82)$$

The elastic constants are the shear modulus  $\mu$  and an additional constant  $\beta$  which can be expressed in terms of Poisson's ratio  $\nu$ , i.e.  $\beta = 2\nu/(1-2\nu)$ . Based on this function the first Piola-Kirchhoff stress tensor and the fourth-order nominal elasticity moduli are readily obtained by the derivatives  $\mathbf{P} = \partial_{\mathbf{F}} \psi$  and  $\mathbb{A} = \partial_{\mathbf{F}\mathbf{F}}^2 \psi$ . The free energy  $\psi$  and the nominal stresses  $\mathbf{P}$  establish the constitutive ingredients of the material balance equation as they directly contribute to Eshelby's energy-momentum tensor  $\boldsymbol{\Sigma} = (-\frac{1}{2} \rho_0 \mathbf{v} \cdot \mathbf{v} + \psi) \mathbf{1} - \mathbf{F}^T \mathbf{P}$ .

**4.5.2. Numerical Example: Oscillation of a Strip.** The oscillation of a two-dimensional strip is examined as an elementary but very illustrative benchmark problem. A schematic sketch of the system is given in Figure 4.3. The reference density is chosen by  $\rho_0 = 1000 \text{ kg/m}^3$ . The strip is assumed to be homogeneous and no spatial volume forces take effect. Regarding the material parameters  $\mu = 80.19 \text{ kN/mm}^2$  and  $\beta$  is set to a very small number. By this choice the boundary value problem turns out to be close to an one-dimensional setting. For the spatial triangulation 15x75 bilinear quadrilaterals are used. At the lower boundary the body is entirely fixed in axial direction and the midpoint

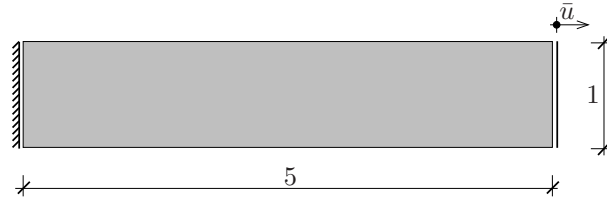


**Figure 4.3:** System and boundary conditions of two-dimensional strip. All dimensions are given in [mm]. The specimen is discretized with four-noded quadrilaterals.

is constrained in lateral direction as well. The specimen is pre-stretched by a top surface displacement of one fifth of the original height with the deformation being continuously distributed along the body. No external loading or deformation are applied during the simulation but the system performs a free oscillation. A time step of  $\Delta t = 0.001$  s has been chosen. The simulation terminates after 2000 time steps when the body reaches its initial pre-stretched configuration.

At first the spatial problem is solved. The motion of the system is visualized in Figure 4.4. Two phenomena can be observed. On the one hand, consider the deformation of the strip.

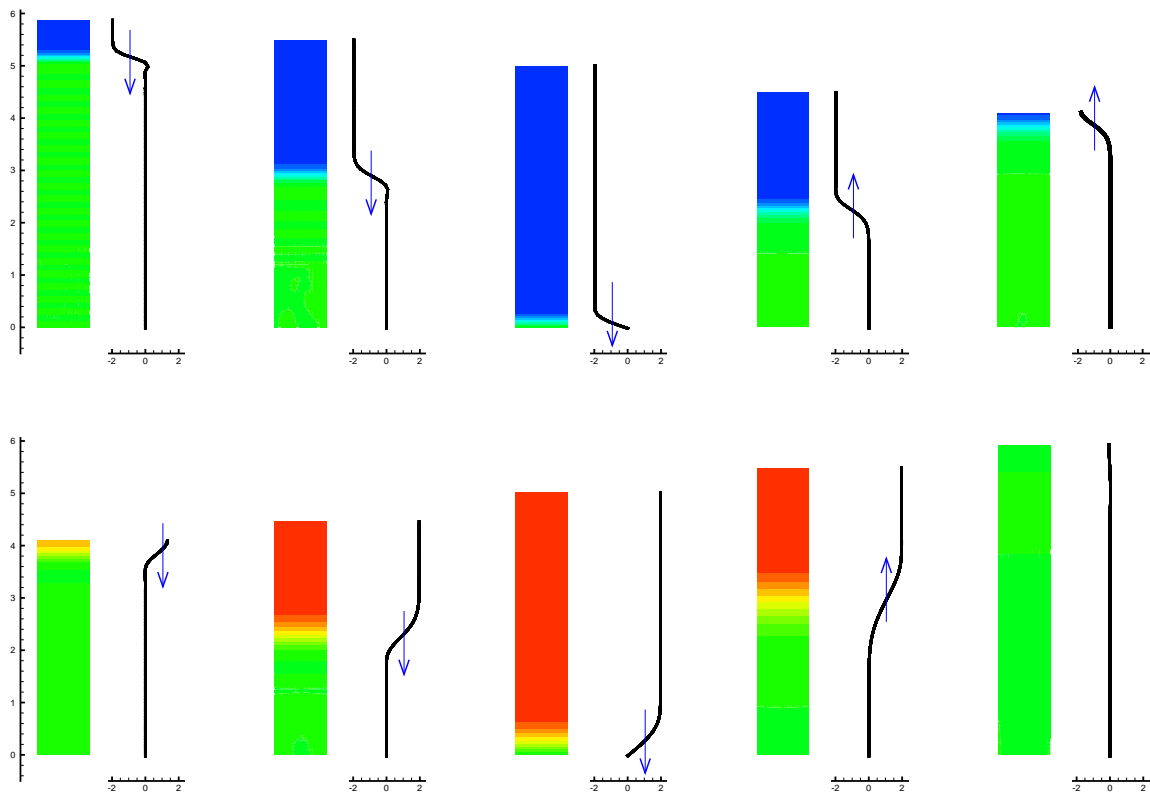


**Figure 4.4:** Contour and profile of axial velocity for one oscillation period plotted in terms of the current configuration. The jump in the velocity field characterizes the wave front moving through the strip. The arrow indicates the direction of this movement.

Starting from the deflected position at height  $H = 6$  mm, the specimen relaxes. Passing the undeformed configuration at  $H = 5$  mm, it changes into the compressed state with maximum compression at  $H \approx 4$  mm. The direction of the motion switches and the body elongates up to the initial deformation at  $H \approx 6$  mm. On the other hand, this deformation is accompanied by the change in the axial velocity field depicted in Figure 4.4 by means of a contour plot and its profile. This profile is characterized by a jump moving through the

material body. This jump is identified as the wave front of the oscillation. Note that the arrows shown in the figure do not refer to the sign of the velocity but indicate the direction of the movement of the wave front. The deformation of the body and the movement of the wave front are linked in the following way. During the downward motion, outlined in the first line of the figure, the velocity has a negative value of  $v_y = -2$  mm/s. The wave front reaches the bottom of the body when the deformation passes the undeformed configuration. The direction of the movement of the wave front changes and hits the top surface of the specimen at the state of maximum compression. The upward motion, see the second line of the figure, comes along with a positive velocity  $v_y = 2$  mm/s. The wave front moves downwards and matches the bottom of the strip in its undeformed state  $H = 5$  mm. The orientation of the movement of the wave front again changes and the wave front reaches the top surface at the initial deformation at  $H \approx 6$  mm.

Turning next to the description of the material motion, the discrete nodal forces are evaluated in a postprocessing step subsequent to each time increment. Since the body is assumed to be homogeneous and no spatial volume forces exist, the configurational forces are expected to vanish at all interior nodes. Referring to (4.79), this condition reads

$$\mathbf{P}_I = \mathbf{A}_I - \mathbf{F}_I = \mathbf{0} \quad \text{for all } I \text{ inside } \mathcal{B}^h. \quad (4.83)$$

On the contrary, true material forces occur at the discrete boundary  $\partial\mathcal{B}^h$  of the body. As the outer shape of the body must remain unchanged during the deformation process, material forces occur as reaction forces to this constraint. The development of these boundary forces is presented in Figure 4.5 for the same time steps used in the previous

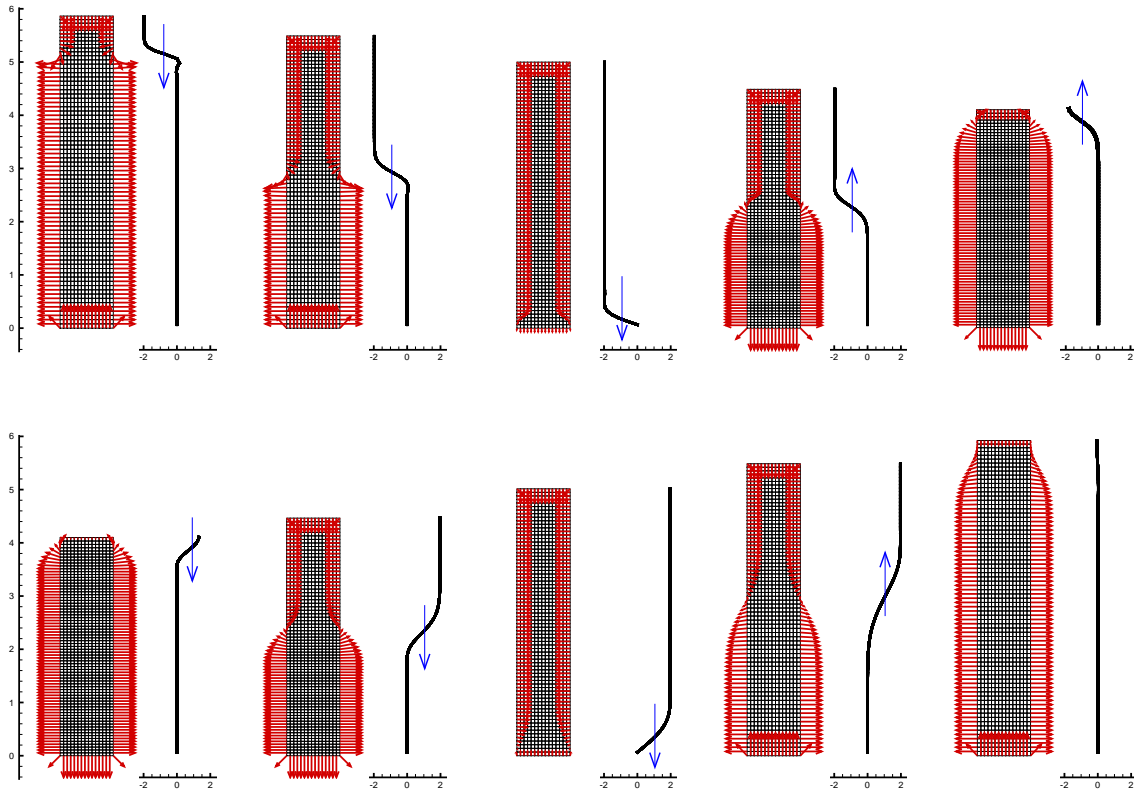


**Figure 4.5:** Configurational forces at the discrete boundary. Their orientation changes according to the jump in the axial velocity whose profile is visualized alongside. Boundary forces at the lower support are scaled by 0.2.

figure. The profile of the velocity field is plotted alongside to allow for a link to the spatial motion. The main characteristic of these boundary forces is their changing in orientation according to the movement of the wave front. With regard to the forces at the lower support it has to be mentioned that they are scaled by the factor 0.2 and consequently are much larger than those at the vertical edges. For the spatial downward motion they show in the opposite direction compared to the orientation of the movement of the wave front. On the contrary, for the upward motion their orientation is in accordance with the movement. The boundary forces at the vertical edges behave quite different. They point in the outward direction in those parts where the axial velocity is equal to zero. Vice versa, in zones where the velocity field is non-zero the orientation of the boundary forces is opposite irrespective of the sign of the velocity. It is a remarkable circumstance that the configurational forces especially at the vertical boundary are mainly governed by the dynamical effects. Since a lateral spatial deformation is almost excluded due to the specific choice of the material parameters, the main ingredient controlling the dynamic and internal material nodal forces  $\mathbf{A}_I$  and  $\mathbf{F}_I$  at the boundary is the axial velocity field. The final discussion is devoted to the situation in the interior of the strip. For this purpose in Figure 4.6 the three components of the equation of material motion are displayed for two different time steps. Again, the profile of the velocity field is included to visualize the

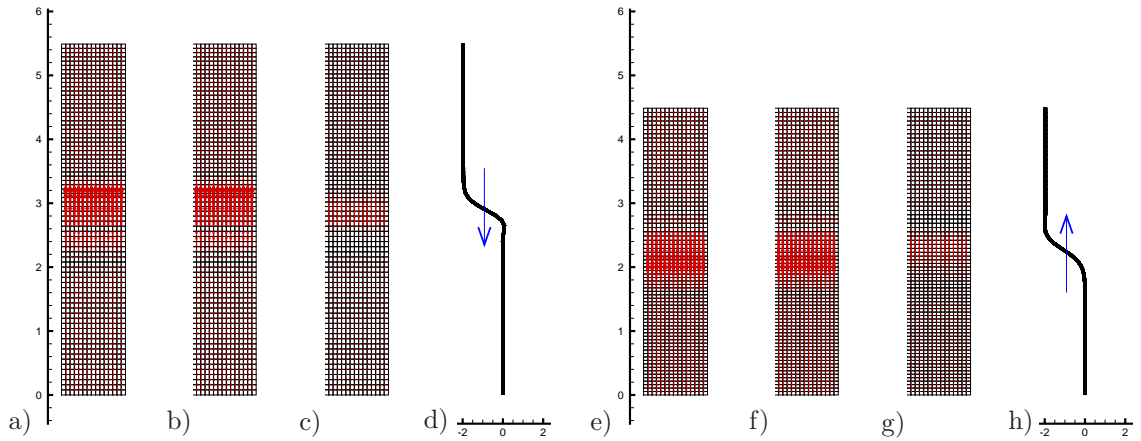


**Figure 4.6:** Configurational forces in the interior of the homogeneous body for two typical time steps. a), e) Internal part  $\mathbf{F}_I$  and b), f) dynamical part  $\mathbf{A}_I$ . c), g) Sum of both contributions governing the discrete configurational nodal forces. d), h) Profile of axial velocity.

current location of the wave front. The first columns, Figure 4.6a), e), show the internal contribution  $\mathbf{F}_I$  based on the energy-momentum tensor while the second columns, Figure 4.6b), f) deal with the dynamic part  $\mathbf{A}_I$  in terms of the pseudomomentum. Both quantities concentrate in the region of the wave front and point in the same direction. The orientation is opposite to the movement of the wave front. Turning to the third columns, Figure 4.6c), g), the resulting configurational nodal forces evaluated by the sum of both components are plotted. As required by the discrete nodal balance (4.83), these nodal forces vanish in the interior of the strip. However, some spurious forces appear due to an insufficient triangulation. These out of balance forces quantify the deviation from the material nodal balance (4.83) and are exploited to set up adaptive refinement procedures within the forthcoming sections.



## 5. Material-Force-Based Optimization Strategies

In this section configurational forces are employed in the context of optimization. The theoretical basis is provided by a dual variational formulation of isothermal finite elastostatics. Within this scenario, the fundamental equations can be derived in a variational framework based on the principle of minimum potential energy. The objective function of the optimization problem is the potential energy and accordingly, the optimization process results in a structural response exhibiting an optimal energetic state. The formulation to follow appears as the quasi-static counterpart of the variational setting of solid dynamics established in the previous chapter. Adopting a similar conceptual proceeding, the variation is carried out with respect to both the Eulerian as well as the Lagrangian coordinates. The corresponding Euler-Lagrange equations are the quasi-static analogs of the spatial and material equations of motion and represent dual spatial and material equilibrium conditions. Hence, the variational formulation leads to a simultaneous equilibration of physical and configurational forces. Subsequent to some preliminary notes the continuous setting of the dual variational formulation is discussed briefly. Afterwards various aspects concerning the numerical solution procedure of the dual or rather coupled spatial-material problem are investigated. Finally, the entire framework is adjusted to mesh improvement and structural optimization. The capability of the proposed strategies is demonstrated by the analyses of representative boundary value problems.

### 5.1. General Remarks

Without doubt, it is far beyond the scope of this thesis to capture the problem area of optimization as it per se constitutes a wide field of scientific research activities. Without claim of completeness, the author refers to the monographs of HAFTKA, GURDAL & KAMAT [65] with respect to structural optimization and BENDSØE & SIGMUND [15] with regard to topology optimization. Further fundamentals as well as quotations of related literature can be found in the review articles of KIRSCH [77] and ROZVANY, ZHOU & SIGMUND [155] on optimal topologies of structures, ROZVANY, BENDSØE & KIRSCH [154] on layout optimization and MAUTE, SCHWARZ & RAMM [111] on structural optimization, to name but a few. In this section the optimization process is related in a rather natural fashion to the notion of configurational forces. In Section 5.4 and Section 5.5 a spectrum of relevant literature on this particular field of the application of material forces is provided, see also the recent report of BRUSS [23] for further informations.

It is supposed to be appropriate to introduce some basic features of the terminology of optimization in order to embed the subsequent analyses into a more general framework. In applied mechanics, optimization means a combination of mechanical problems, variational or differential calculus and mathematical programming. Typical examples are the optimization of the shape or the topology of a structure or the optimization of the distribution of material within a mechanical system. The notation optimization implies that there exists the possibility to vary certain parameters describing the particular system under consideration. These parameters are called the designvariables and may be continuous or discrete in nature. The branch of mathematical programming refers to the minimization or maximization of a specific function usually denoted the objective function of the optimization problem. This function is parameterized by the designvariables. Typically, the optimization process is restricted by some equality or inequality constraints that evoke the domain of feasible solutions and govern possible variations of the designvariables. Familiar examples are geometric constraints such as the dimensions of a system



or restrictions concerning the mechanical response of the structure such as maximal displacements or stresses. In an abstract setting, the optimization problem of an objective function  $f$  parameterized by the designvariables  $\mathbf{x}$  subjected to certain constraints is expressed by

$$\begin{aligned} \text{minimize } f(\mathbf{x}) \quad \text{subjected to } \quad & h_i(\mathbf{x}) = 0 \quad i = 1, \dots, n_e \\ & g_j(\mathbf{x}) \leq 0 \quad j = 1, \dots, n_i \end{aligned} \quad (5.1)$$

with  $n_e$  and  $n_i$  indicating the number of equality and inequality constraints, respectively. As analytical solution can be obtained only for very few special cases, (5.1) is normally solved by means of numerical strategies adopted from mathematical programming, cf. Section 5.3 below for two particular algorithms.

## 5.2. Dual Variational Formulation of Finite Elastostatics

For problems of isothermal finite elastostatics, the current state of a material body subjected to an arbitrary deformation is governed by the principle of minimum potential energy. This principle states, that the work of deformation done to the solid reaches a minimum at the solution point. For the elastic case the work of deformation coincides with the potential energy stored in the solid. Hence, the principle reads

$$\Pi = \Pi_{int} + \Pi_{ext} \rightarrow \text{Min} \quad (5.2)$$

and  $\Pi$  is identified to be the objective function of the optimization problem. The potential energy of an elastic system is the sum of the total strain energy and the potential of the external physical loading. Recalling definitions (4.5) and (4.6) in Section 4.2, i.e.

$$\Pi_{int} = \int_{\mathcal{B}} \psi(\nabla_{\mathbf{X}} \boldsymbol{\varphi}_t, \mathbf{X}) dV \quad \text{and} \quad \Pi_{ext} = - \int_{\mathcal{B}} \boldsymbol{\varphi}_t \cdot \bar{\boldsymbol{\gamma}}_0(\mathbf{X}) dV - \int_{\partial \mathcal{B}_{\bar{\mathbf{t}}}} \boldsymbol{\varphi}_t \cdot \bar{\mathbf{t}} dA, \quad (5.3)$$

these quantities are formulated in terms of the free energy function  $\psi$  per unit reference volume and the physical forces acting on the body, namely the spatial volume forces  $\bar{\boldsymbol{\gamma}}_0$  and surface tractions  $\bar{\mathbf{t}}$ . The free energy is a function of the deformation gradient  $\mathbf{F} = \nabla_{\mathbf{X}} \boldsymbol{\varphi}_t$  and of the material coordinates  $\mathbf{X}$ . By means of the latter dependence possible inhomogeneities of the material body are taken into account. Referring to Remark 4.1, it is of interest to point out that for conservative systems the external power  $\mathcal{P}$  and the stress power  $S$ , see Section 2.3.4 for their definitions, are obtained from the external and internal potentials by their time derivatives,  $\mathcal{P} = -d\Pi_{ext}/dt$  and  $S = d\Pi_{int}/dt$ .

Due to the fundamental kinematic identity  $\mathbf{x} = \boldsymbol{\varphi}_t(\mathbf{X})$ , the material and spatial coordinates constitute the designvariables of the optimization problem and govern the parameterization of the functional  $\Pi = \Pi(\mathbf{x}, \mathbf{X})$ . Starting from (5.2), a dual variational formulation in terms of the spatial position  $\mathbf{x}$  and simultaneously the material position  $\mathbf{X}$  can be derived. This treatment follows conceptually the dynamical framework outlined within Chapter 4 and the works of KNOWLES & STERNBERG [78], OLVER [143, 144] and KIENZLER & HERRMANN [76] based on Noether's theorem, NOETHER [139].

The minimization principle (5.2) is valid for the essential boundary conditions

$$\mathbf{x} = \bar{\mathbf{x}} \quad \text{on } \partial \mathcal{B}_{\boldsymbol{\varphi}} \quad \text{and} \quad \mathbf{X} = \text{const.} \quad \text{on } \partial \mathcal{B} \quad (5.4)$$

introduced in (3.5) and (4.13) within the previous chapters, see also Remark 4.2 for further comments. These boundary conditions characterize the equality constraints of the



optimization problem. The crucial point of the simultaneous variational formulation is that the energy functional  $\Pi$  needs to be stationary with respect to variations of both the spatial as well as the material coordinates to attain a global minimum. The necessary condition of (5.2) requires that the first variation of the energy functional vanishes

$$\delta\Pi = \delta_{\mathbf{x}}\Pi + \delta_{\mathbf{X}}\Pi = 0. \quad (5.5)$$

Here,  $\delta_{\mathbf{x}}\Pi$  and  $\delta_{\mathbf{X}}\Pi$  denote the first variations of  $\Pi$  with respect to the spatial and material coordinates  $\mathbf{x}$  and  $\mathbf{X}$ . The resulting variational expressions are obtained in an intuitive fashion from the investigations of the previous chapters upon restriction to the particular case of isothermal finite elastostatics. Nevertheless, the derivation of the fundamental equations is recapitulated shortly. Two alternative procedures are adopted, namely the true variational formulation, Section 5.2.1, and a rate formulation based on the exploitation of the global dissipation postulate, Section 5.2.2, displaying the two fundamental approaches previously used in Chapter 3 and Chapter 4.

**5.2.1. Variational Formulation.** To start with, consider the variation with respect to the spatial coordinates. Upon introduction of the variation  $\delta\mathbf{x}$  instead of  $\delta\boldsymbol{\varphi}$  employed in Section 4.2.2 satisfying the homogeneous form of the essential boundary conditions (5.4)<sub>1</sub>, cf. (4.15), the variational expression is readily obtained

$$\delta\Pi_{\mathbf{x}} = \int_{\mathcal{B}} \mathbf{P} : \nabla_{\mathbf{X}}\delta\mathbf{x} \, dV - \int_{\mathcal{B}} \bar{\boldsymbol{\gamma}}_0 \cdot \delta\mathbf{x} \, dV - \int_{\partial\mathcal{B}_{\bar{\mathbf{t}}}} \bar{\mathbf{t}} \cdot \delta\mathbf{x} \, dA = \mathbf{0}. \quad (5.6)$$

with the nominal stresses  $\mathbf{P} = \partial\psi/\partial\mathbf{F}$ . Turning next to the variation of  $\Pi$  with respect to the material positions, the variation  $\delta\mathbf{X}$  is introduced, constrained by the homogeneous form of the boundary conditions (5.4)<sub>2</sub>, cf. (4.23). The variational form is given by

$$\begin{aligned} \delta\Pi_{\mathbf{X}} = & \int_{\mathcal{B}} \mathbf{P} : \nabla_{\mathbf{X}}\mathbf{F}\delta\mathbf{X} + \partial_{\mathbf{X}}\psi^{\text{expl}} \cdot \delta\mathbf{X} + \psi\mathbf{1} : \nabla_{\mathbf{X}}\mathbf{F}\delta\mathbf{X} \, dV \\ & - \int_{\mathcal{B}} \bar{\boldsymbol{\gamma}}_0 \cdot \mathbf{F}\delta\mathbf{X} + \mathbf{x} \cdot \nabla_{\mathbf{X}}\bar{\boldsymbol{\gamma}}_0\delta\mathbf{X} + \bar{\boldsymbol{\gamma}}_0 \cdot \mathbf{x} (\psi\mathbf{1} : \nabla_{\mathbf{X}}\delta\mathbf{X}) \, dV = \mathbf{0} \end{aligned} \quad (5.7)$$

By means of integration by parts and substitution of the homogeneous boundary conditions, this equation can be reformulated in the format

$$\delta\Pi_{\mathbf{X}} = \int_{\mathcal{B}} -\mathbf{F}^T \left\{ \text{Div}\mathbf{P} + \bar{\boldsymbol{\gamma}}_0 \right\} \cdot \delta\mathbf{X} \, dV + \int_{\mathcal{B}} \boldsymbol{\Sigma} : \nabla_{\mathbf{X}}\delta\mathbf{X} \, dV - \int_{\mathcal{B}} \bar{\boldsymbol{\Gamma}}_0 \cdot \delta\mathbf{X} \, dV = \mathbf{0} \quad (5.8)$$

Anticipating the results of Section 5.2.3, the first contribution includes the Euler-Lagrange equation of the spatial branch of the variational formulation. Subjected to the condition, that this equation is satisfied, the variation with respect to the material coordinates reads

$$\delta\Pi_{\mathbf{X}} = \int_{\mathcal{B}} \boldsymbol{\Sigma} : \nabla_{\mathbf{X}}\delta\mathbf{X} \, dV - \int_{\mathcal{B}} \bar{\boldsymbol{\Gamma}}_0 \cdot \delta\mathbf{X} \, dV = \mathbf{0}. \quad (5.9)$$

This equation constitutes the material counterpart of (5.6) but does not contain any surface part because the whole boundary is governed by the Dirichlet conditions (5.4)<sub>2</sub>. It relies on the definitions of the Eshelby stress tensor and the configurational volume force

$$\boldsymbol{\Sigma} = \psi\mathbf{1} - \mathbf{F}^T\mathbf{P} \quad \text{and} \quad \bar{\boldsymbol{\Gamma}}_0 = -\partial_{\mathbf{X}}\psi^{\text{expl}} - \mathbf{F}^T\bar{\boldsymbol{\gamma}}_0. \quad (5.10)$$

It is convenient, to reformulate the variational expressions in the compact matrix format

$$\delta\Pi = \int_{\mathcal{B}} \begin{bmatrix} \nabla_X \delta \mathbf{x} \\ \nabla_X \delta \mathbf{X} \end{bmatrix} \cdot \begin{bmatrix} \mathbf{P} \\ \boldsymbol{\Sigma} \end{bmatrix} dV - \int_{\mathcal{B}} \begin{bmatrix} \delta \mathbf{x} \\ \delta \mathbf{X} \end{bmatrix} \cdot \begin{bmatrix} \bar{\boldsymbol{\gamma}}_0 \\ \bar{\boldsymbol{\Gamma}}_0 \end{bmatrix} dV - \int_{\partial \mathcal{B}_t} \delta \mathbf{x} \cdot \bar{\mathbf{t}} dA = 0 \quad (5.11)$$

representing the necessary condition of the dual spatial-material minimization problem.

**5.2.2. Exploitation of Global Dissipation Postulate.** An alternative way to derive the variational expression (5.11) is provided by the exploitation of the global dissipation postulate. To this end, recall its representation (3.22) for the elastic case

$$\mathcal{D} = \mathcal{P} - \frac{d}{dt} \Pi_{int} = 0. \quad (5.12)$$

It demands that for elastic processes no dissipation occurs and consequently the power of the external physical loading equals the change of energy storage. By substitution of the definition of the external power and the internal energy this condition becomes

$$\mathcal{D} = \int_{\mathcal{B}} \mathbf{v} \cdot \bar{\boldsymbol{\gamma}}_0 dV + \int_{\mathcal{B}_t} \mathbf{v} \cdot \bar{\mathbf{t}} dA - \int_{\mathcal{B}} \frac{d}{dt} \psi dV - \int_{\mathcal{B}} \psi \frac{d}{dt} dV = 0. \quad (5.13)$$

Possible changes of the bulk material have been taken into account via the time derivative of the integration limit. The motion of the material body is parameterized with respect to a parameter space  $\Omega$  by the material and spatial configurational maps  $\Xi$  and  $\xi$ , cf. (3.3) and Figure 3.1 in Section 3.2.1. The time derivatives of the geometric objects

$$\mathbf{v} = \frac{\partial}{\partial t} \boldsymbol{\varphi} = \dot{\boldsymbol{\xi}} - \mathbf{F} \dot{\Xi}, \quad \frac{d}{dt} \mathbf{F} = \nabla_X \dot{\boldsymbol{\xi}} - \mathbf{F} \nabla_X \dot{\Xi}, \quad \frac{d}{dt} dV = (\mathbf{1} : \nabla_X \dot{\Xi}) dV \quad (5.14)$$

are formulated in terms of the time derivatives  $\dot{\Xi}$  and  $\dot{\boldsymbol{\xi}}$ . These rates are restricted by homogeneous boundary conditions (3.10) and (3.11) in a completely analogous fashion to those for the variations  $\delta \mathbf{X}$  and  $\delta \mathbf{x}$ . The time derivative of the free energy function is

$$\frac{d}{dt} \psi = \mathbf{P} : \frac{d}{dt} \mathbf{F} + \partial_{\mathbf{X}} \psi^{\text{expl}} \cdot \dot{\Xi}. \quad (5.15)$$

By substitution of these intermediate results into (5.13) and application of integration by parts the dissipation postulate appears in the form

$$\begin{aligned} \mathcal{D} &= \int_{\mathcal{B}} -\mathbf{P} : \nabla_X \dot{\boldsymbol{\xi}} dV + \int_{\mathcal{B}} \dot{\boldsymbol{\xi}} \cdot \bar{\boldsymbol{\gamma}}_0 dV + \int_{\mathcal{B}_t} \dot{\boldsymbol{\xi}} \cdot \bar{\mathbf{t}} dA \\ &+ \int_{\mathcal{B}} -\boldsymbol{\Sigma} : \nabla_X \dot{\Xi} dV + \int_{\mathcal{B}} \dot{\Xi} \cdot \bar{\boldsymbol{\Gamma}}_0 dV = 0 \end{aligned} \quad (5.16)$$

with the Eshelby tensor  $\boldsymbol{\Sigma} = \psi \mathbf{1} - \mathbf{F}^T \mathbf{P}$  and the material force  $\bar{\boldsymbol{\Gamma}}_0 = -\partial_{\mathbf{X}} \psi^{\text{expl}} - \mathbf{F}^T \bar{\boldsymbol{\gamma}}_0$ . The link to the variational formulation is as follows. For conservative systems the external power coincides with the time derivative of the external potential  $\mathcal{P} = -d\Pi_{ext}/dt$  and condition (5.12) can be expressed by the negative time derivative of the total energy  $\Pi$ . As the rates of the spatial and material configurational maps describe the change of the coordinates with respect to a change in time, they can be identified with their variations. Thus, the change of the energy functional coincides with its first variation

$$\mathcal{D} = \mathcal{P} - \frac{d}{dt} \Pi_{int} = 0 \iff \frac{d}{dt} \Pi = \frac{d}{dt} \Pi_{int} + \frac{d}{dt} \Pi_{ext} = 0 \iff \delta\Pi = 0 \quad (5.17)$$

and the necessary condition of the minimization principle is written in matrix notation

$$\int_{\mathcal{B}} \begin{bmatrix} \nabla_X \dot{\boldsymbol{\xi}} \\ \nabla_X \dot{\boldsymbol{\Xi}} \end{bmatrix} \cdot \begin{bmatrix} \mathbf{P} \\ \boldsymbol{\Sigma} \end{bmatrix} dV - \int_{\mathcal{B}} \begin{bmatrix} \dot{\boldsymbol{\xi}} \\ \dot{\boldsymbol{\Xi}} \end{bmatrix} \cdot \begin{bmatrix} \bar{\boldsymbol{\gamma}}_0 \\ \bar{\boldsymbol{\Gamma}}_0 \end{bmatrix} dV - \int_{\partial\mathcal{B}_t} \dot{\boldsymbol{\xi}} \cdot \bar{\mathbf{t}} dA = 0. \quad (5.18)$$

This condition equals (5.11) for the identification  $\dot{\boldsymbol{\xi}} \leftarrow \delta \mathbf{x}$  and  $\dot{\boldsymbol{\Xi}} \leftarrow \delta \mathbf{X}$  of the rate expressions in the sense of point variations.

**5.2.3. Dual Euler-Lagrange Equations of the Variational Formulation.** The dual Euler-Lagrange equations are obtained from the variational expression (5.18) or (5.11) by application of Gauss theorem and the lemma of variational calculus. For arbitrary spatial rates  $\dot{\boldsymbol{\xi}}$  or variations  $\delta \mathbf{x}$  and fixed material position,  $\dot{\boldsymbol{\Xi}} = \delta \mathbf{X} = \mathbf{0}$ , the standard spatial equilibrium condition and the traction boundary condition arise

$$\text{Div} \mathbf{P} + \bar{\boldsymbol{\gamma}}_0 = \mathbf{0} \quad \text{in } \mathcal{B} \quad \text{and} \quad \mathbf{P} \mathbf{N} = \bar{\mathbf{t}} \quad \text{on } \partial\mathcal{B}_t \quad (5.19)$$

valid in combination with the essential boundary conditions. Vice versa, for arbitrary material rates  $\dot{\boldsymbol{\Xi}}$  or variations  $\delta \mathbf{X}$  at fixed spatial position,  $\dot{\boldsymbol{\xi}} = \delta \mathbf{x} = \mathbf{0}$ , the procedure ends up with the dual material equilibrium condition

$$\text{Div} \boldsymbol{\Sigma} + \bar{\boldsymbol{\Gamma}}_0 = \mathbf{0} \quad \text{in } \mathcal{B}. \quad (5.20)$$

For the material problem no natural boundary condition appears because the essential boundary condition governs the whole material boundary.

### 5.3. Discussion of Numerical Solution Procedures

The solution of the dual variational problem is performed by means of the finite element method. It directly starts with the variational expression (5.18). This relation coincides with the weak formulations of the local balance expressions (5.19), (5.20) obtained by testing these balance laws with some arbitrary test functions  $\dot{\boldsymbol{\xi}}$  or  $\dot{\boldsymbol{\Xi}}$  and integrating over the body  $\mathcal{B}$ . The subsequent representations use the above rate formulation and adopt the notation outlined in Chapter 3.3 but can be alternatively reformulated in terms of the true variational expressions as shown within Section 4.4.

Applying finite element discretization, the Lagrangian configuration is subdivided into a set of  $n_{ele}$  finite elements. The spatial and material positions are approximated on the element level in terms of the global vectors  $\mathbf{d} \in \mathcal{R}^{\mathcal{N}_t}$  and  $\mathbf{D} \in \mathcal{R}^{\mathcal{N}_t}$  of discrete spatial and material nodal coordinates of all  $\mathcal{N}_t$  nodes of the finite element mesh, see (3.52), i.e.

$$\mathbf{x} \approx \boldsymbol{\xi}_t^h(\boldsymbol{\theta}) = \mathbf{N}(\boldsymbol{\theta}) \mathbf{d} \quad \text{and} \quad \mathbf{X} \approx \boldsymbol{\Xi}_t^h(\boldsymbol{\theta}) = \mathbf{N}(\boldsymbol{\theta}) \mathbf{D}. \quad (5.21)$$

The approximations of the rates  $\dot{\boldsymbol{\xi}}$ ,  $\dot{\boldsymbol{\Xi}}$  and their gradients  $\nabla_X \dot{\boldsymbol{\xi}}$ ,  $\nabla_X \dot{\boldsymbol{\Xi}}$  are specified in (3.55) and (3.56) using the global vectors  $\dot{\mathbf{d}} \in \mathcal{R}^{\mathcal{N}_t}$  and  $\dot{\mathbf{D}} \in \mathcal{R}^{\mathcal{N}_t}$  of discrete nodal velocities instead of the real positions. The shape functions for the interpolation of the material and spatial positions do not necessarily coincide but are chosen identically.

By substitution of the finite element approximation into (5.18) the discrete weak form is obtained. The range of feasible spatial and material rates  $\dot{\mathbf{d}}$ ,  $\dot{\mathbf{D}}$  is defined by the discrete versions (3.62) of the homogeneous forms of the essential boundary conditions (5.4). For admissible spatial and material rates the formulation ends up with the system of equations

$$\hat{\mathbf{R}} = - \sum_{I=1}^{\mathcal{N}_t} \begin{bmatrix} \mathbf{f}_I + \mathbf{p}_I \\ \mathbf{F}_I + \mathbf{P}_I \end{bmatrix} = - \sum_{I=1}^{\mathcal{N}_t} \begin{bmatrix} \mathbf{r}_I \\ \mathbf{R}_I \end{bmatrix} = \mathbf{0}. \quad (5.22)$$

The global spatial-material residual vector  $\hat{\mathbf{R}}$  consists of  $\mathcal{N}_t$  discrete spatial and material nodal residuals,  $\mathbf{r}_I$  and  $\mathbf{R}_I$ , associated with every node  $I$  of the mesh. The different nodal contributions represent the internal and external spatial forces

$$\mathbf{f}_I := - \mathbf{A}_{e=1}^{n_{ele}} \int_{\mathcal{B}^e} \mathbf{B}_I^T \mathbf{P} dV \quad \text{and} \quad \mathbf{p}_I := \mathbf{A}_{e=1}^{n_{ele}} \left\{ \int_{\mathcal{B}^e} \mathbf{N}_I^T \bar{\gamma}_0 dV + \int_{\partial \mathcal{B}^e} \mathbf{N}_I^T \bar{\mathbf{t}} dA \right\} \quad (5.23)$$

as well as the dual material counterparts

$$\mathbf{F}_I := - \mathbf{A}_{e=1}^{n_{ele}} \int_{\mathcal{B}^e} \mathbf{B}_I^T \Sigma dV \quad \text{and} \quad \mathbf{P}_I := \mathbf{A}_{e=1}^{n_{ele}} \int_{\mathcal{B}^e} \mathbf{N}_I^T \bar{\Gamma}_0 dV \quad (5.24)$$

denoted the material internal force and the discrete configurational nodal force.

**Remark 5.1:** Focusing on the Lagrangian subproblem, the material residual expression

$$\mathbf{R}_I = \mathbf{F}_I + \mathbf{P}_I = \mathbf{0} \quad \iff \quad \mathbf{F}_I = -\mathbf{P}_I \quad (5.25)$$

is extracted. This identity encourages that the material internal force  $\mathbf{F}_I$  can be denoted the discrete configurational nodal force as well. This will be adopted in the absence of inhomogeneities, i.e. in case the continuous configurational force vanishes,  $\bar{\Gamma}_0 = \mathbf{0}$ .

Recalling the strong form equations (5.19), (5.20) as local counterparts of global balances, cf. Section 4.3, the solution of the necessary condition (5.22) of the minimization problem (5.2) coincides with the simultaneous equilibration of global spatial and configurational forces. The set of equations (5.22) is highly non-linear in both the spatial and material nodal coordinates  $\mathbf{d}$  and  $\mathbf{D}$ . For the solution, two different procedures are elaborated, namely a non-linear conjugate gradient method and a Newton-Raphson iteration scheme.

**5.3.1. Polak-Ribière Non-Linear Conjugate Gradient Method.** The dual problem (5.22) can be solved by an iterative non-linear conjugate gradient method. In an abstract framework, the algorithm is as follows. Consider the minimization of a function  $f(\mathbf{Q})$  with computable gradient  $f'$ . In the present case,  $f$  is the total energy  $\Pi$  and the gradient  $f' = \mathbf{R}$  is given by the residual expression (5.22). The global vector  $\mathbf{Q} = [\mathbf{d}, \mathbf{D}]^T$  contains the primary variables, i.e. the spatial and material nodal positions  $\mathbf{d}$  and  $\mathbf{D}$ . The solution procedure is initialized by an initial guess  $\mathbf{Q}_0$  with the associated residual vector

$$\hat{\mathbf{R}}_0 = -\hat{\mathbf{R}}(\mathbf{Q}_0). \quad (5.26)$$

Based on this residual, the direction  $\mathbf{q}_0 = \hat{\mathbf{R}}_0$  of the first iteration is evaluated governing an additional parameter  $\beta_0 = \mathbf{q}_0^T \mathbf{q}_0$ . The new solution  $\mathbf{Q}$  is computed via the update

$$\mathbf{Q} \leftarrow \mathbf{Q}_n + \alpha \mathbf{q}_n \quad (5.27)$$

where the subscript  $n$  refers to the old iteration step. The step size  $\alpha$  minimizes the function  $\Pi(\mathbf{Q}_n + \alpha \mathbf{q}_n)$ . To satisfy this requirement, the gradient  $\hat{\mathbf{R}}$  has to be perpendicular to the direction  $\mathbf{q}_n$ ,  $[\hat{\mathbf{R}}(\mathbf{Q}_n + \alpha \mathbf{q}_n)]^T \mathbf{q}_n = 0$ . The new residual  $\hat{\mathbf{R}}(\mathbf{Q})$  is evaluated and in case its norm falls below a certain tolerance,  $|\hat{\mathbf{R}}| \leq tol$ , convergence is achieved and the procedure stops. This convergence condition coincides with the approximative solution of the necessary condition (5.18) of the minimization principle (5.2). For  $|\hat{\mathbf{R}}| > tol$ , the current value of  $\beta$  is computed by the Polak-Ribière update

$$\beta^{PR} = \frac{\hat{\mathbf{R}}^T (\hat{\mathbf{R}} - \hat{\mathbf{R}}_n)}{\hat{\mathbf{R}}_n^T \hat{\mathbf{R}}_n}. \quad (5.28)$$

The parameter  $\beta$  determines the new direction  $\mathbf{q} = \hat{\mathbf{R}} + \beta \mathbf{q}_n$ . Convergence of the Polak-Ribière method is guaranteed for the specific choice  $\beta = \max\{\beta^{PR}, 0\}$ , which coincides with a restart of the procedure for  $\beta^{PR} < 0$ . A flowchart of the conjugate gradient method similar to that presented in PRESS ET AL. [149] is shown in Box 5.1.

To compute the step size  $\alpha$  introduced in equation (5.27), the root of the expression

**Box 5.1:** Non-linear conjugate gradient method

1. *Initialization*  
Initial guess of solution vector and initial direction
 
$$\mathbf{Q}_0, \quad \mathbf{R}_0 = \mathbf{R}(\mathbf{Q}_0), \quad \mathbf{q}_0 = \mathbf{R}_0 \quad \text{and} \quad \beta_0 = \mathbf{q}_0^T \mathbf{q}_0$$
2. *Iteration loop*
  - (i) Compute step size  $\alpha$  and update solution vector
 
$$[\mathbf{R}(\mathbf{Q}_n + \alpha \mathbf{q}_n)]^T \mathbf{q}_n = 0 \quad \text{and} \quad \mathbf{Q} \leftarrow \mathbf{Q}_n + \alpha \mathbf{q}_n$$
  - (ii) Compute residual and check convergence
 
$$\mathbf{R} = \mathbf{R}(\mathbf{Q}), \quad \text{IF } |\mathbf{R}| < \text{tol} \quad \text{THEN} \quad \text{Exit}$$
  - (iii) Perform Polak-Ribière update and determine new direction
 
$$\beta^{PR} = \mathbf{R}^T (\mathbf{R} - \mathbf{R}_n) / \mathbf{R}_n^T \mathbf{R}_n \quad \text{and} \quad \mathbf{q} = \mathbf{R} + \beta^{PR} \mathbf{q}_n$$
  - (iv) Increase iteration counter and perform next step
 
$$n \leftarrow n + 1 \quad \text{GOTO (i)}$$

$[\hat{\mathbf{R}}(\mathbf{Q}_n + \alpha \mathbf{q}_n)]^T \mathbf{q}_n = 0$  needs to be evaluated. This is done by an iterative secant method. Although this procedure demands that the second derivative of the objective function does exist, its explicit evaluation is not required but it is approximated by function evaluation at two different points  $\alpha = 0$  and  $\alpha = \sigma$ . Finally, the step size is obtained by

$$\alpha = -\sigma \frac{[\hat{\mathbf{R}}(\mathbf{Q}_n)]^T \mathbf{q}_n}{[\hat{\mathbf{R}}(\mathbf{Q}_n + \alpha \mathbf{q}_n)]^T \mathbf{q}_n - [\hat{\mathbf{R}}(\mathbf{Q}_n)]^T \mathbf{q}_n}. \quad (5.29)$$

with  $\sigma$  being a small number not equal to zero.

It has to be mentioned, that non-linear conjugate gradient methods include some drawbacks. The result depends on the initial guess  $\mathbf{Q}_0$  of the solution vector and the algorithm does not guarantee convergence to a global minimum and might not even find a local minimum in case the goal function  $f = \Pi$  does not have a lower bound, see THOUTIREDDY & ORTIZ [182] for a more detailed discussion. Nevertheless, non-linear conjugate gradient methods are widely used due to their numerical efficiency. This efficiency can be enhanced if some pre-conditioner  $\mathbf{M}$  is used. Instead of evaluating the second derivative of the potential  $\Pi$  a diagonal matrix can be used approximatively but it has to be ensured that this matrix is positive definite, see SHEWCHUK [158].

**5.3.2. Newton-Raphson Iteration Scheme.** To solve the discrete version (5.22) of the necessary condition (5.18) of the dual problem by a monolithic Newton-Raphson-type iteration, the non-linear function  $\delta\Pi$  has to be linearized with respect to its primary variables, namely the spatial and material positions  $\mathbf{x}$  and  $\mathbf{X}$ . In a first step the continuous setting is considered. The linearization is performed for fixed values of the material and spatial positions in the direction of incremental changes  $\Delta\mathbf{x}$  and  $\Delta\mathbf{X}$ . Based on these incremental quantities the increments  $\Delta\mathbf{F}$  of the deformation gradient and  $\Delta(dV)$  of the material volume element are computed in analogy to the rate expressions (5.14)<sub>2,3</sub>

$$\Delta\mathbf{F} = \nabla_{\mathbf{X}}\Delta\mathbf{x} - \mathbf{F}\nabla_{\mathbf{X}}\Delta\mathbf{X} \quad \text{and} \quad \Delta(dV) = (\mathbf{1} : \nabla_{\mathbf{X}}\Delta\mathbf{X})dV. \quad (5.30)$$

As the gradients  $\nabla_{\mathbf{X}}\dot{\boldsymbol{\xi}}$  and  $\nabla_{\mathbf{X}}\dot{\boldsymbol{\Xi}}$  refer to the non-constant material coordinates  $\mathbf{X}$ , their linearization has to be taken into account as well requiring their increments

$$\Delta(\nabla_{\mathbf{X}}\dot{\boldsymbol{\xi}}) = -\nabla_{\mathbf{X}}\dot{\boldsymbol{\xi}}\nabla_{\mathbf{X}}\Delta\mathbf{X} \quad \text{and} \quad \Delta(\nabla_{\mathbf{X}}\dot{\boldsymbol{\Xi}}) = -\nabla_{\mathbf{X}}\dot{\boldsymbol{\Xi}}\nabla_{\mathbf{X}}\Delta\mathbf{X}. \quad (5.31)$$

Assuming that the material and spatial volume forces and the surface tractions do not contribute, the linear increment of the variation (5.18) can be written as

$$\begin{aligned} \Delta(\delta\Pi) &= \int_{\mathcal{B}} \left[ \nabla_{\mathbf{X}}\dot{\boldsymbol{\xi}} : \{\Delta\mathbf{P} + \mathbf{P}(\mathbf{1} : \nabla_{\mathbf{X}}\Delta\mathbf{X})\} - (\nabla_{\mathbf{X}}\dot{\boldsymbol{\xi}}\nabla_{\mathbf{X}}\Delta\mathbf{X}) : \mathbf{P} \right] dV \\ &+ \int_{\mathcal{B}} \left[ \nabla_{\mathbf{X}}\dot{\boldsymbol{\Xi}} : \{\Delta\boldsymbol{\Sigma} + \boldsymbol{\Sigma}(\mathbf{1} : \nabla_{\mathbf{X}}\Delta\mathbf{X})\} - (\nabla_{\mathbf{X}}\dot{\boldsymbol{\Xi}}\nabla_{\mathbf{X}}\Delta\mathbf{X}) : \boldsymbol{\Sigma} \right] dV. \end{aligned} \quad (5.32)$$

Substitution of the increments of the dual stress tensors  $\mathbf{P}$ ,  $\boldsymbol{\Sigma}$  renders the coupled relation

$$\Delta(\delta\Pi) = \int_{\mathcal{B}} \begin{bmatrix} \nabla_{\mathbf{X}}\dot{\boldsymbol{\xi}} \\ \nabla_{\mathbf{X}}\dot{\boldsymbol{\Xi}} \end{bmatrix} \begin{bmatrix} \mathbb{C} & \mathbb{K} \\ \mathbb{K}^T & \mathbb{M} \end{bmatrix} \begin{bmatrix} \nabla_{\mathbf{X}}\Delta\mathbf{x} \\ \nabla_{\mathbf{X}}\Delta\mathbf{X} \end{bmatrix} dV \quad (5.33)$$

with the fourth-order nominal elasticity moduli  $\mathbb{C} = \partial_{\mathbf{F}}\mathbf{P} = \partial_{\mathbf{F}\mathbf{F}}^2\psi$  and the definitions

$$\begin{aligned} \mathbb{K} &:= -\mathbb{C} \overset{\circ}{\bullet} \mathbf{F} - \mathbf{P} \odot \mathbf{1} + \mathbf{P} \otimes \mathbf{1} \\ \mathbb{M} &:= \mathbb{C} \overset{\circ}{\bullet} \mathbf{F} \overset{\circ}{\bullet} \mathbf{F} - \boldsymbol{\Sigma} \odot \mathbf{1} + \boldsymbol{\Sigma} \otimes \mathbf{1} + \mathbf{1} \odot (\mathbf{F}^T \mathbf{P}) - \mathbf{1} \otimes (\mathbf{F}^T \mathbf{P}). \end{aligned} \quad (5.34)$$

Here, the following abbreviations have been introduced:  $(\bullet) \overset{\circ}{\bullet} \mathbf{F}$  means the composition of the  $i$ -th component of  $(\bullet)$  with  $\mathbf{F}$  while  $(\mathbf{a} \odot \mathbf{b})_{ijkl} = a_{il}b_{jk}$  and  $(\mathbf{a} \otimes \mathbf{b})_{ijkl} = a_{ij}b_{kl}$  denote tensorial dyadic products. Due to the variational structure of the formulation, the coupled tangent matrix is symmetric.

**Remark 5.2:** Due to the dependence of the volume element  $dV$  and the gradients  $\nabla_{\mathbf{X}}\dot{\boldsymbol{\xi}}$ ,  $\nabla_{\mathbf{X}}\dot{\boldsymbol{\Xi}}$  on the material coordinates  $\mathbf{X}$  the linearization of the dual problem consists of a material tangent and a geometric part. The geometric part only occurs for the mixed material-spatial or purely material contributions whereas for the purely spatial part just the material tangent arises. Within the two-point setting of a purely spatial formulation only the increment of the stresses  $\mathbf{P}$  has to be evaluated and consequently just the material tangent occurs. The split of the increment into a material tangent and a geometric part corresponds to the structure of alternative representations of the finite deformation



framework, i.e. the Lagrangian or the Eulerian setting based on the work conjugated objects  $(\mathbf{S}, \mathbf{C})$  and  $(\boldsymbol{\tau}, \mathbf{g})$ . In these approaches a geometric contribution already appears for the purely spatial problem due to the linearization of the non-linear deformation measures.

In the next step, the algorithmic scenario is discussed. The approximation  $\delta\Pi^h$  of the first variation of the energy functional is solved via the linear expression

$$\text{Lin } \delta\Pi^h = \delta\Pi^h + \Delta(\delta\Pi)^h = 0. \quad (5.35)$$

By introduction of the finite element approximation of the gradients of the increments of the material and spatial coordinates, i.e.  $\nabla_X \Delta \mathbf{x} = \mathbf{B} \Delta \mathbf{d}$  and  $\nabla_X \Delta \mathbf{X} = \mathbf{B} \Delta \mathbf{D}$ , the linear set of equations (5.35) can be written in the compact format

$$\hat{\mathbf{R}} + \hat{\mathbf{K}} \Delta \mathbf{Q} = \mathbf{0}. \quad (5.36)$$

The global solution vector  $\Delta \mathbf{Q} = [\Delta \mathbf{d}, \Delta \mathbf{D}]^T$  contains the increments of the spatial and material nodal coordinates while  $\hat{\mathbf{R}}$  and  $\hat{\mathbf{K}}$  denote the global residual and stiffness matrix

$$\hat{\mathbf{R}} = - \sum_{I=1}^{\mathcal{N}_t} \begin{bmatrix} \mathbf{r}_I \\ \mathbf{R}_I \end{bmatrix} = - \sum_{I=1}^{\mathcal{N}_t} \begin{bmatrix} \mathbf{f}_I + \mathbf{p}_I \\ \mathbf{F}_I + \mathbf{P}_I \end{bmatrix} \quad \text{and} \quad \hat{\mathbf{K}} = \sum_{I,J=1}^{\mathcal{N}_t} \begin{bmatrix} \mathbf{k}_{IJ} & \mathbf{m}_{IJ} \\ \mathbf{m}_{IJ}^T & \mathbf{K}_{IJ} \end{bmatrix}. \quad (5.37)$$

The nodal contributions of the residual are defined in (5.23) and (5.24) whereas the components of the coupled stiffness matrix rely on the above tangent operators

$$\mathbf{k}_{IJ} = \mathbf{A} \int_{\mathcal{B}^e} \mathbf{B}_I^T \mathbb{C} \mathbf{B}_J dV, \quad \mathbf{m}_{IJ} = \mathbf{A} \int_{\mathcal{B}^e} \mathbf{B}_I^T \mathbb{K} \mathbf{B}_J dV, \quad \mathbf{K}_{IJ} = \mathbf{A} \int_{\mathcal{B}^e} \mathbf{B}_I^T \mathbb{M} \mathbf{B}_J dV. \quad (5.38)$$

Within a typical Newton step equation (5.36) is solved for the nodal increments  $\Delta \mathbf{Q}$  and the current material and spatial nodal positions  $\mathbf{Q} = [\mathbf{d}, \mathbf{D}]^T$  are updated according to

$$\mathbf{Q} \leftarrow \mathbf{Q} + \Delta \mathbf{Q} \quad (5.39)$$

until convergence is obtained, i.e.  $|\hat{\mathbf{R}}| < \text{tol}$  with given tolerance  $\text{tol}$ . As mentioned above, this convergence condition represents the approximative solution of the discrete version (5.22) of the necessary condition (5.18) of the variational principle and therefore states the approximative solution of the minimization problem (5.2).

**5.3.3. Viscous-Type Relaxation of Configurational Forces.** The dual variational setting appears to be very promising as it extends the well-known variational framework of finite elasticity to the modern notion of configurational mechanics. Despite this conceptual attraction, a robust numerical implementation displays some major drawbacks whereupon the Newton-Raphson iteration fails to converge in general. Consider for instance the tangent matrix (5.37) of the linearized functional for the particular case of zero deformation, i.e.  $\mathbf{F} = \mathbf{1}$ . Evaluating the sub-operators  $\mathbb{K}$  and  $\mathbb{M}$ , the stiffness matrix is detected to be singular and the linearized problem cannot be solved. In addition, and this is probably the essential difficulty, the resulting minimization problem is non-convex in general and thus possesses a variety of local minima. Due to this lack of convexity, in particular circumstances the tangent operator is found to have negative eigenvalues.

To overcome these problems, ASKES, KUHLE & STEINMANN [8] proposed a dynamic constraint for eliminating the rank deficiency of the tangent operator. Configurational forces



are associated with a variation of the material coordinates  $\mathbf{X}$  at fixed spatial positions  $\mathbf{x}$ . A zero material residual allows for arbitrarily large variations of  $\mathbf{X}$  implying a vanishing stiffness of the material problem that is why a singularity of the whole system exists. Hence, if the absolute value of a component of the material residual is lower than a numerical tolerance, the corresponding equation is eliminated from the iteration step. However, this procedure only works in special cases, in general the null subspace of the stiffness matrix needs not to coincide with the space spanned by the degrees of freedom in material equilibrium and the rank deficiency is not eliminated by restricting the latter one. In addition, the modes corresponding to negative eigenvalues are not stabilized.

Alternatively, it is proposed to add temporarily a unit matrix on the material stiffness. This approach is close to another procedure elaborated by MOSLER & ORTIZ [130]. Viscous damping is used to regularize the problem. Upon discretization the minimization principle (5.2) appears as a function of the current discrete material and spatial nodal coordinates,  $\Pi \approx \Pi^h(\mathbf{d}, \mathbf{D}) \rightarrow \text{Min}$ . This functional is penalized by an additional term

$$\bar{\Pi} := \Pi^h(\mathbf{d}, \mathbf{D}) + \epsilon |\mathbf{D} - \mathbf{D}_n|^2 \quad (5.40)$$

where  $\epsilon$  is a positive parameter and  $|\mathbf{D} - \mathbf{D}_n|$  denotes the Euclidean norm of the difference between the current material coordinates and their values of the previous solution step. Based on (5.37), the only terms that have to be modified are the material residual  $\mathbf{R}_I$  and its linearization  $\mathbf{K}_{IJ}$  with respect to the material coordinates

$$\bar{\mathbf{R}}_I = \mathbf{R}_I + 2\epsilon (\mathbf{D}_I - \mathbf{D}_{In}) \quad \text{and} \quad \bar{\mathbf{K}}_{IJ} = \mathbf{K}_{IJ} + 2\epsilon \mathbf{1}. \quad (5.41)$$

The parameter  $\epsilon$  is used to ensure the positive definiteness of the tangent operator, i.e. to enforce a strictly convex energy functional. The smallest possible value of  $\epsilon$  is chosen. For the particular case that the energy functional is a priori convex, no regularization is needed,  $\epsilon = 0$ . As  $\epsilon$  is a small number and above all convergence of the Newton-Raphson iteration is guaranteed, by what  $|\mathbf{D} - \mathbf{D}_n| \rightarrow \mathbf{0}$ , the penalty term of the modified energy functional (5.40) becomes very small and the value of  $\Pi$  is not affected.

#### 5.4. Topology Optimization of Finite Element Meshes

The dual variational setting is exploited in view of the topology optimization of finite element meshes or, more precise, adjusted to  $r$ -adaptive mesh improvement. Subsequent to the theoretical discussion, descriptive numerical examples are studied.

**5.4.1.  $r$ -Adaptive Mesh Optimization.** In general, mesh optimization is used to generate an improved finite element mesh. The optimization criterion is formulated with respect to particular criteria concerning the accuracy of the triangulation by means of a finite element mesh, or rather the solution obtained by a certain mesh. For example, the element shape or the ratio between the edge lengths of neighboring elements may constitute such a quality criterion.

Upon discretization, a material body is subdivided into a set of finite elements. In what follows, the number of elements and correspondingly the number of nodal points is kept unchanged during the optimization process. In the sense of the dual variational formulation, the objective function is the potential energy parameterized, in the discrete setting, by the discrete spatial and material nodal coordinates  $\mathbf{d}_I$  and  $\mathbf{D}_I$ . A variation of the objective function with respect to the coordinates renders the optimal structure. In the current scenario, the structure means the topology of the finite element mesh while optimal refers to the minimum of the potential energy associated with that mesh. The work

conjugate objects of the nodal coordinates are the discrete spatial and configurational nodal forces, or rather nodal residuals  $\mathbf{r}_I$  and  $\mathbf{R}_I$  representing the discrete counterparts of the dual local equilibrium conditions (5.19) and (5.20).

Assuming a material body without spatial forces acting on it,  $\bar{\boldsymbol{\gamma}}_0 = \bar{\mathbf{t}} = \mathbf{0}$ , the discrete representation of the spatial balance equation boils down to

$$\mathbf{r} = \sum_{I=1}^{N_t} \mathbf{r}_I = \sum_{I=1}^{N_t} \mathbf{f}_I = \mathbf{0} \quad \text{with} \quad \mathbf{f}_I = - \mathbf{A} \int_{\mathcal{B}^e} \mathbf{B}_I^T \mathbf{P} \, dV \quad (5.42)$$

corresponding to the strict conservation law  $\text{Div} \mathbf{P} = \mathbf{0}$  in the continuous case. The solution of this subproblem yields the spatial nodal positions of the deformed mesh.

Even in the absence of spatial volume forces, the material balance equation still includes a configurational volume force  $\bar{\boldsymbol{\Gamma}}_0 = -\partial_{\mathbf{X}} \psi^{\text{expl}}$  due to a possible inhomogeneity of the material. In the subsequent investigations the material is assumed to be homogeneous and the configurational force vanishes as well,  $\bar{\boldsymbol{\Gamma}}_0 = \mathbf{0}$ . Thus, the material residual reads

$$\mathbf{R} = \sum_{I=1}^{N_t} \mathbf{R}_I = \sum_{I=1}^{N_t} \mathbf{F}_I = \mathbf{0} \quad \text{with} \quad \mathbf{F}_I = - \mathbf{A} \int_{\mathcal{B}^e} \mathbf{B}_I^T \boldsymbol{\Sigma} \, dV. \quad (5.43)$$

and reflects the discrete version of the strict material conservation law  $\text{Div} \boldsymbol{\Sigma} = \mathbf{0}$ . In reference to Remark 5.1,  $\mathbf{R}_I$  represents the discrete configurational forces at point  $I$ .

In the continuous setting, the solution of the spatial equilibrium condition automatically guarantees the fulfillment of the material balance equation by what both conditions are entirely equivalent. Consequently, (5.43) is expected to be satisfied as well for a solution of (5.42). However, the finite element triangulation induces an artificial inhomogeneity of the system and breaks the equivalence between the dual branches of the coupled problem. Using finite element scheme, the coordinates are approximated by  $\mathcal{C}^0$ -continuous shape functions which is why the strains and all the dependent quantities are discontinuously distributed over the mesh. This discontinuity evokes numerically caused, non-vanishing material nodal forces,  $\mathbf{R}_I \neq \mathbf{0}$ . Vice versa, the deviation from the material equilibrium indicates an inhomogeneity arising from an insufficient triangulation.

As the configurational force and the material position associated with a certain node are conjugated objects, a reduction of the material residual is achieved by a rearrangement of the nodal coordinates. This  $r$ -adaptive alignment of the finite element mesh renders an improved approximation of the material subproblem (5.43). The configurational force points into the direction of an energy increase upon movement of the material node point position. Thus, the change of the material nodal coordinates into the opposite direction enforces a decrease of the energetic state of the mesh.

A possible attempt towards the numerical realization has been proposed in the seminal work of BRAUN [21] and latter on by MÜLLER & MAUGIN [134]. Subsequent to the solution of the spatial problem, the  $r$ -adaptive mesh optimization, i.e. the solution of the material subproblem, is performed in a postprocessing procedure step.

In the present contribution an alternative approach is adopted, cf. KUHLE, ASKES & STEINMANN [83], ASKES, KUHLE & STEINMANN [8], ASKES, BARGMANN, KUHLE & STEINMANN [7], THOUTIREDDY & ORTIZ [182], THOUTIREDDY [183] and MOSLER & ORTIZ [130]. The coupled material and spatial problem in terms of the dual variational formulation is solved in a monolithic fashion using the solution procedures discussed in Section 5.3. In this scenario, the solution of the spatial problem, i.e. the equilibration of

physical forces in the sense of Newton, and the solution of the material problem, i.e. the equilibration of configurational forces in the sense of Eshelby, are carried out simultaneously. The procedure results in the optimal mesh associated with its minimal energetic state as demanded by the governing minimization principle. The spatial problem provides the current Eulerian coordinates while the material problem gives the optimal referential coordinates reducing the inhomogeneity induced upon discretization.

An extension of this method to the inelastic setting is proposed in the recent work of MOSLER & ORTIZ [131] based on an incremental variational formulation.

The  $r$ -adaptive method exploits the configurational forces as an indicator for the accuracy of the current triangulation. The mesh improvement is achieved in a natural way during the solution step without employing an additional error estimator. The procedure may be denoted a (variational) Arbitrary-Lagrangian-Eulerian (ALE) formulation identifying the spatial equations with the Lagrangian description and the material equations with the Eulerian description of the motion including the adaption of the underlying triangulation.

The material model used for the ensuing analyses has been introduced within Section 4.5.1. It relies on the assumption of a compressible Neo-Hookean type free energy function

$$\psi(\mathbf{F}) = \frac{\mu}{2} (\text{tr} [\mathbf{F}^T \mathbf{g} \mathbf{F}] - 3) + \frac{\mu}{\beta} ((\det \mathbf{F})^{-\beta} - 1) \quad (5.44)$$

formulated in terms of the shear modulus  $\mu$  and an additional constant  $\beta$  linked to Poisson's ratio  $\nu$  via  $\beta = 2\nu/(1 - 2\nu)$ . In the simulations discussed below, these parameters are set to  $\mu = 80.19 \text{ kN/mm}^2$  and  $\nu = 0.29$  corresponding to  $\beta = 1.4$ .

**5.4.2. Numerical Example: Plane Sheet in Tension.** In the first example, a squared two-dimensional sheet with edge length  $h = 1.0 \text{ mm}$  is considered. This boundary value problem has been studied by MÜLLER & MAUGIN [134] and ASKES, KUHL & STEINMANN [8]. The slab is assumed to be homogeneous,  $\partial_{\mathbf{x}} \psi^{\text{expl}} = \mathbf{0}$  and spatial volume forces are set to zero,  $\bar{\gamma}_0 = \mathbf{0}$ . Consequently, the configurational force vanishes as well,  $\bar{\Gamma}_0 = \mathbf{0}$ . The slab is discretized by sixteen four-noded quadrilateral elements with bilinear shape functions for both the spatial and the material problem. The computations were performed under plane strain conditions. With regard to the spatial problem, the upper and lower edges of the slab are clamped and subjected to prescribed vertical displacement increments  $\Delta \bar{u} = 0.025 \text{ mm}$  up to a total deformation of 50% of the original height. For the material problem, three different boundary conditions have been investigated.

In the first step, all the nodes are constrained in view of the material problem coinciding with a purely spatial computation. For the underlying assumptions, the solution of the spatial problem is expected to satisfy the material equilibrium condition automatically. However, the discretization procedure induces an inhomogeneity of the system resulting in a non-vanishing material residual  $\mathbf{R}$ . In other words, as any changes of the material node point positions are forbidden, the material equilibrium of the whole structure cannot be achieved. In Figure 5.1a), d) the remaining material residual or rather the configurational nodal forces are plotted with respect to the reference configuration after the first and the final spatial deformation step. As the boundary of the system does not change its material position, physically motivated configurational forces occur at the boundary nodes in order to maintain the shape of the specimen in the reference configuration, i.e. to prevent the body from shrinking. In contrast, the forces at the interior nodes are just numerically caused and for this reason are used for the  $r$ -adaptive mesh improvement. These interior forces are by some magnitudes smaller than the boundary forces. In the

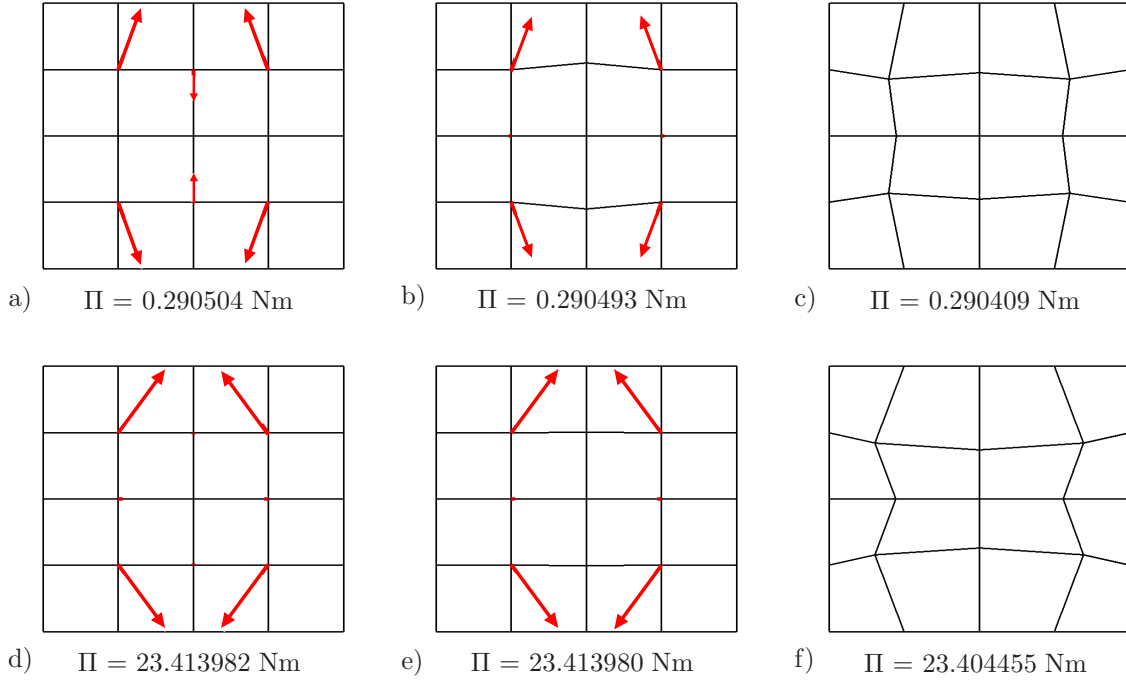


**Figure 5.1:** Configurational nodal forces at the interior nodes of the mesh for a), d) the purely spatial problem, b), e) 2 and c), f) 18 material degrees of freedom. a), b), c) visualize the forces after the first deformation step scaled by 250, and d), e), f) after the final step scaled by 5.5. In the plots c), f) no material residual occurs indicating an optimal energetic state. The values of the potential  $\Pi$  are given below.

figure, only the nodal forces at the interior nodes of the mesh are depicted. Observe that the forces on the boundary also include inaccuracy due to an insufficient triangulation. This effect is reported on in detail in the next example.

In the second step, two material degrees of freedom are introduced. To be specific, the upper and lower interior node on the vertical middle axis of the slab are allowed to move in vertical direction with respect to the reference configuration. Figure 5.1b), e) shows the reference configuration of the body including the configurational nodal forces for the respective spatial deformation states. The two crucial nodes have moved in the opposite direction of the configurational force obtained for the previous computation. Additionally, as the magnitude of the node point force after the first load step is larger than after the final one, the amount of the material displacement decreases as well. Recalling that the configurational forces point into the direction of an energy increase upon movement of the node point position, the change in the opposite direction coincides with a decrease of the potential energy  $\Pi$ . This reasoning is verified by a comparison of the values of the energy listed beneath the pictures. However, the difference between the corresponding values is very small. While the forces at the nodes with material degrees of freedom are now zero according to the material equilibrium condition, numerically caused configurational forces still occur at those interior nodes being not allow to change their material position.

In the third step, all interior nodes are allowed to move with respect to the material setting of the slab. This scenario incorporates 18 material degrees of freedom. Now, the material coordinates of the interior nodes are able to achieve their equilibrium state, i.e. the particular positions for which the material residual vanishes,  $\mathbf{R} = \mathbf{0}$ , or, respectively, no numerically caused configurational forces occur. In Figure 5.1c), f) the corresponding optimized referential meshes are shown. Considering the amount of energy stored in the

specimen reported beneath the pictures, a further decrease of the energetic state of the body has taken effect, even though the differences are still small. This observation holds for the comparison with the case of two material degrees of freedom or, more distinct, with the purely spatial computation. To be precise, the energetic state decreases by  $\approx 0.038\%$  and  $\approx 0.041\%$  for the first and final deformation step, respectively.

**5.4.3. Numerical Example: Homogeneous Block in Tension.** The investigations are extended to the three-dimensional context. To this end the deformation of a block of dimensions  $h \times h \times h/4$  with  $h = 1.0$  mm is analyzed. A similar example has been discussed by MOSLER & ORTIZ [130]. The body is discretized with 152 tetrahedral elements with linear interpolation functions for the material and the spatial problem. Again, spatial volume forces are neglected and the specimen is assumed to be homogeneous by what no configurational forces occur,  $\bar{\Gamma}_0 = \mathbf{0}$ . In the spatial setting, the upper and lower surfaces of the body are clamped. The upper surface is subjected to prescribed incremental displacements  $\Delta \bar{u} = 0.0075$  mm. The specimen is deformed up to a total deformation of approximately 7% of the original height.

In the first step, a purely spatial computation has been performed, see Figure 5.2a) for the undeformed and Figure 5.2c) for the deformed configuration. The energetic state of

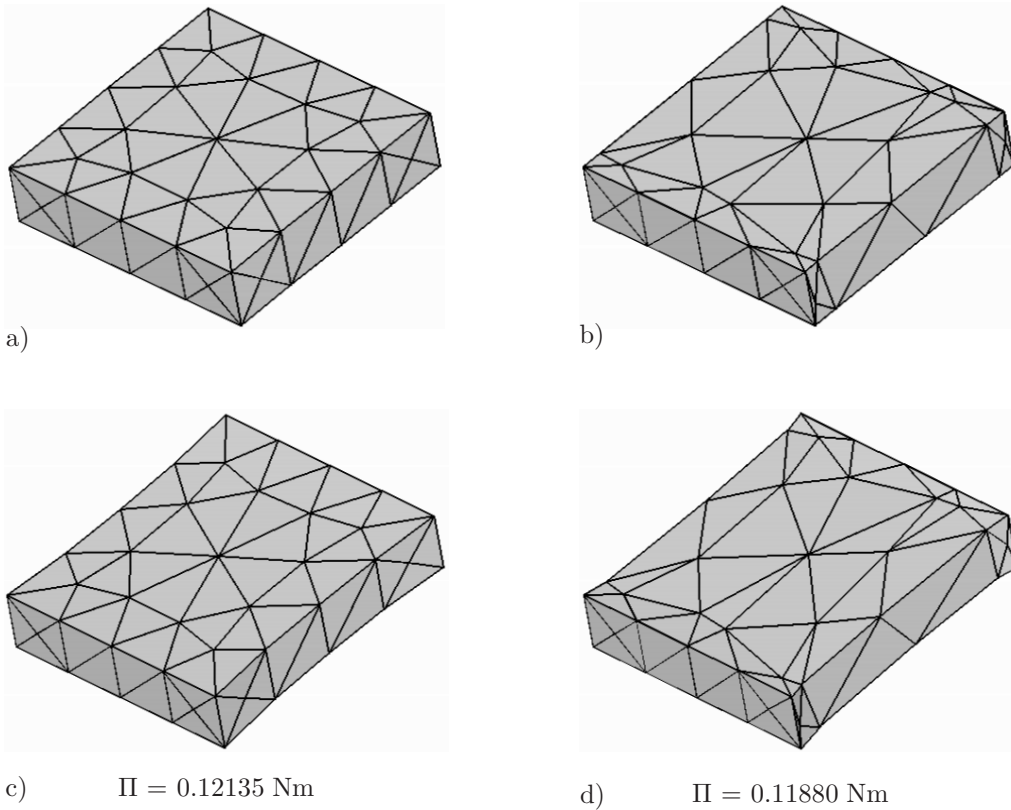


**Figure 5.2:** Lagrangian and Eulerian configuration of a), c) the purely spatial and b), d) the coupled problem. The nodes are allowed to change their material position in any tangential direction of the respective surface corresponding to 95 material degrees of freedom. The values of the potential  $\Pi$  are given for the final deformation state.

the deformed structure is  $\Pi = 0.12135 \text{ Nm}$ .

Following the procedure of the above example, material degrees of freedom are introduced within the reference setting of the mesh. However, the goal of the subsequent investigations



is different. As the current triangulation only consists of one single node lying entirely inside the volume, i.e. only one node does not belong to any surface of the slab, a movement of that single node will not result in a considerable change of the energetic state of the system. Hence, and this is in contrast to the previous studies, attention is focused on the situation on the material boundary of the specimen. To be specific, all the nodes of the surfaces are allowed to move within that surface. In other words, only a change of the material position in the direction of the respective normal vector of the surface is forbidden. For the current triangulation, this scenario leads to a total number of 95 material degrees of freedom (including the three of the single interior node). The improved mesh in both its undeformed and spatially deformed state, is depicted in Figure 5.2b),d). Apparently, the movement of the material node point positions is in the direction of the spatially constrained surfaces of the body whereas no changes of the material coordinates occur on these surfaces themselves. The potential energy of the deformed system is given by  $\Pi = 0.11880 \text{ Nm}$  which coincides with a significant reduction of  $\approx 2.1\%$  compared to that of the purely spatial computation.

In the sense of the dual variational setting based on the principle of minimum potential energy, the simultaneous equilibration of spatial and material forces results in a  $r$ -adaptively improved mesh or rather material configuration that minimizes the energy of the system. The consideration of a movement of the material node point positions along the material boundary is found to increase the accuracy of the triangulation.

## 5.5. Topology Optimization of Truss Structures

The dual variational formulation is applied to the topology optimization of truss structures whereupon the  $r$ -adaption appears as a concept of structural optimization. At first, the dual variational setting is adopted to the particular situation of truss systems. Afterwards a representative boundary value problem is examined.

**5.5.1. Structural Optimization of Truss Systems.** Several approaches exist in view of the optimization of truss structures. The objective function may characterize the entire weight of the structure or displacements at some particular joints. Typical designvariables are for instance the cross sections of the pin-jointed bars.

For a given connectivity, the variational  $r$ -adaption renders the optimal mesh, i.e. the optimal material and spatial nodal positions, with respect to its energetic state. Extending this method to the optimization of truss structures, originally proposed by ASKES, BARGMANN, KUHLE & STEINMANN [7], the mesh means the structure or rather geometry of the system. The unknowns are the material and spatial coordinates of the truss joints. The material equilibrium is associated with the optimal truss geometry in the undeformed state. This geometry is obtained by moving the joints into the opposite direction of the configurational force acting on the respective node. Exploiting the duality of the variational setting, the spatial problem is solved simultaneously for the current nodal positions of the deformed system. The resulting truss exhibits a minimal energetic state compared to all admissible configurations. Note that only the truss geometry is analyzed but no change of the cross sections of the bars or of the connectivity is taken into account.

In order to specify the fundamental equations of the dual variational formulation with regard to truss structures, consider the parameterization of a single pin-jointed bar with constant cross section  $A = \text{const.}$  in terms of the time-independent parameter space  $\mathcal{A}$  as depicted in Figure 5.3. The time-dependent Lagrangian and Eulerian configurations  $\mathcal{B}$  and  $\mathcal{S}$  are obtained via the material and spatial configurational maps  $\Xi$  and  $\xi$ , cf. (3.3),

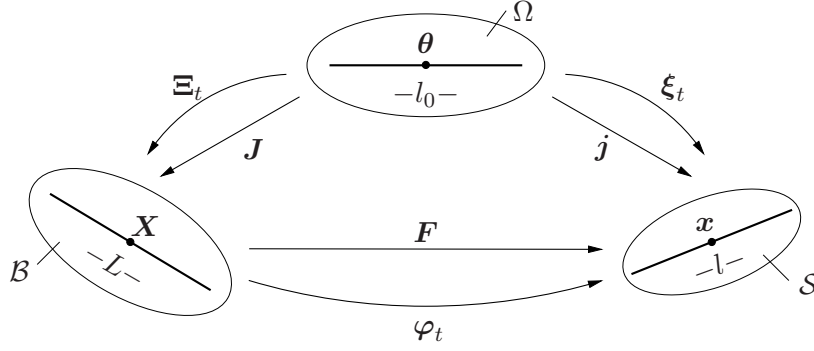


**Figure 5.3:** Kinematics of a pin-jointed bar. Parameter space  $\Omega$  with time-independent coordinates  $\theta$ . The reference and current configurations are obtained via the material and spatial configurational maps  $\Xi_t, \xi_t$ . Their composition defines the non-linear point map  $\varphi_t$ .

governing the non-linear deformation map  $\varphi_t = \xi \circ \Xi^{-1}$ . By definition, only axial forces occur in a pin-jointed bar and consequently just the 11-component of the gradients of the basic kinematic objects need to be taken into account,  $J_{11} =: J$ ,  $j_{11} =: j$  and  $F_{11} =: F$ . The minimization principle (5.2) is recast into the one-dimensional format

$$\Pi = \int_{l_B} \psi A dl_B \rightarrow \text{Min.} \quad (5.45)$$

The fictitious integration limit  $l_B$  indicates the integration over all pin-jointed bars of the entire truss structure. For simplicity, spatial volume forces and surface tractions have been neglected. Assuming a homogeneous material, the free energy exclusively depends on the deformation gradient,  $\psi(F_{11}) = \psi(F)$ . The length of every single bar in each configuration is evaluated using the respective coordinates of the truss joints

$$l_0 = |\theta_2 - \theta_1|, \quad L = |\mathbf{X}_2 - \mathbf{X}_1|, \quad l = |\mathbf{x}_2 - \mathbf{x}_1|. \quad (5.46)$$

The ratio of the respective lengths describes the scalar valued gradients of the material and spatial configurational maps,  $J = L/l_0$  and  $j = l/l_0$ , constituting the deformation gradient  $F = jJ^{-1} = l/L$ . The investigations to follow once more rely on the rate formulation based on the global dissipation postulate which has proven to be close to a variational setting. To perform the time derivative of the energy functional (5.45), the time derivatives of the deformation gradient and of the infinitesimal line element have to be computed

$$\dot{F} = \dot{l}L^{-1} - FL^{-1}\dot{L} \quad \text{and} \quad \overline{\dot{dl}_B} = L^{-1}\dot{L}dl_B. \quad (5.47)$$

The spatial and material rates  $\dot{l}, \dot{L}$  are governed by the rates of the respective coordinates

$$\dot{l} = \overline{\dot{|\mathbf{x}_2 - \mathbf{x}_1|}} = \mathbf{n} (\dot{\xi}_2 - \dot{\xi}_1) \quad \text{and} \quad \dot{L} = \overline{\dot{|\mathbf{X}_2 - \mathbf{X}_1|}} = \mathbf{N} (\dot{\Xi}_2 - \dot{\Xi}_1) \quad (5.48)$$

with the Eulerian and Lagrangian direction vectors  $\mathbf{n} = (\mathbf{x}_2 - \mathbf{x}_1)/|\mathbf{x}_2 - \mathbf{x}_1|$  and  $\mathbf{N} = (\mathbf{X}_2 - \mathbf{X}_1)/|\mathbf{X}_2 - \mathbf{X}_1|$  of the bar. The spatial and material velocities  $\dot{\xi}, \dot{\Xi}$  of the truss joints have to satisfy the homogeneous forms (3.10), (3.11) of the essential boundary conditions.

The time derivative  $d\Pi/dt$  of the energy functional governs its first variation inducing the following representation of the necessary condition of the minimization principle

$$\delta\Pi = 0 \quad \Longleftrightarrow \quad \int_{l_B} (P \dot{l}L^{-1} + \Sigma \dot{L}L^{-1})A dl_B = 0 \quad (5.49)$$



in terms of the scalar valued first Piola-Kirchhoff stress  $P = \partial_F \psi$  and the Eshelby stress  $\Sigma = \psi - FP$ . As the deformation gradient  $F$  is constant along the bar, the stresses  $P$  and  $\Sigma$  are constant as well. For a constant cross section  $A$ , the integral (5.49) is reformulated as a sum over all  $n_b$  bars of the structure

$$\delta\Pi = 0 \iff \sum_{e=1}^{n_b} [(P \dot{l} + \Sigma \dot{L})A] = 0. \quad (5.50)$$

Substituting the rate expressions (5.48), the procedure results for arbitrary admissible spatial and material rates in a discrete set of non-linear equations

$$\hat{\mathbf{R}} = \begin{bmatrix} \mathbf{r} \\ \mathbf{R} \end{bmatrix} = \mathbf{0} \quad \text{with} \quad \mathbf{r} = \mathbf{A}_{e=1}^{n_b} \{PA \begin{bmatrix} -\mathbf{n} \\ \mathbf{n} \end{bmatrix}\} \quad \text{and} \quad \mathbf{R} = \mathbf{A}_{e=1}^{n_b} \{\Sigma A \begin{bmatrix} -\mathbf{N} \\ \mathbf{N} \end{bmatrix}\} \quad (5.51)$$

where  $\mathbf{r}$  and  $\mathbf{R}$  denote the dual spatial and material residuals and the assembly operator  $\mathbf{A}$  accounts for the connectivity of the truss. The coupled problem (5.51) has to be solved for the current coordinates of the truss joints in both the material and the spatial configuration by means of the numerical solution procedures discussed in Section 5.3.

Applying the Newton-Raphson scheme, the consistent linearization of (5.51) has to be evaluated. This linearization consists of a material tangent part arising from the nonlinearities of the stress measures and a geometric part due to the linearization of the direction vectors upon their projection onto the global coordinate system. The analyses end up with the coupled system of linear equations

$$\mathbf{R} + \mathbf{K}\Delta\mathbf{Q} = \mathbf{0}. \quad (5.52)$$

After having solved for the nodal increments  $\Delta\mathbf{Q} = [\Delta\mathbf{x}, \Delta\mathbf{X}]$ , the Newton update yields the current spatial and material coordinates  $\mathbf{Q} \leftarrow \mathbf{Q} + \Delta\mathbf{Q}$  with  $\mathbf{Q} = [\mathbf{x}, \mathbf{X}]^T$ . A detailed derivation of this relation is provided in Appendix E.

Irrespective of the solution procedure, the algorithm stops if convergence is achieved, i.e. if the residual norm falls below a given tolerance,  $|\hat{\mathbf{R}}| < tol$ . This criterion corresponds to the approximative simultaneous equilibration of physical and configurational forces.

**5.5.2. Numerical Example: Optimization of a Truss Structure.** Exemplarily, the optimization of a truss bridge is discussed. This model problem has been investigated in a similar fashion by ASKES, BARGMANN, KUHL & STEINMANN [7]. At first, the constitutive model based on the free energy function (5.44) is adjusted to the one-dimensional setting. On condition that only stresses  $P_{11}$  in the axial direction of the pin-jointed bars occur, i.e.  $P_{22} = P_{33} = 0$ , the components  $F_{22}, F_{33}$  of the deformation gradient are computed in terms of the axial component  $F_{11}$ . Then, the axial stress can be evaluated

$$F_{22} = F_{33} = F_{11}^{(-\beta/(2(\beta+1)))} \quad \text{and} \quad P_{11} = \mu(F_{11} - F_{11}^{((-2\beta+1)/(\beta+1))}). \quad (5.53)$$

The material parameters are  $\mu = 80.19 \text{ kN/mm}^2$  and  $\beta = 1.4$ . The truss structure and its spatial boundary conditions are shown in Figure 5.4. The length is set to  $L = 100 \text{ mm}$  while the cross section of the bars is given by  $A = 10 \text{ mm}^2$ . The system is subjected to a concentrated load  $P = 100 \text{ N}$  at the joints along the lower edge of the bridge. For the numerical simulation, the Newton-Raphson solution procedure has been adopted. A purely spatial computation results in a maximum vertical displacement of  $u_{max} = 16.12 \text{ mm}$  at the lower midnode and an energetic state of  $\Pi = 0.146668 \text{ Nm}$ .

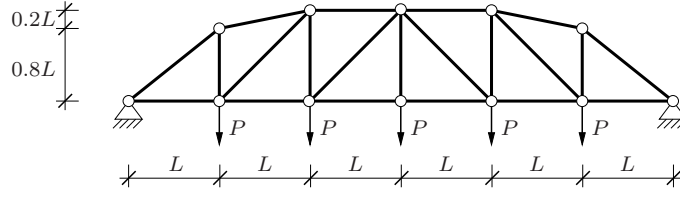


**Figure 5.4:** Spatial boundary conditions of the truss bridge. The length is  $L = 100$  mm. The bridge is loaded by concentrated loads  $P = 100$  N at the joints along the lower edge.

In what follows, the optimal material structure of the truss bridge is to be found for the case that the joints along the upper chord of the system are allowed to change their material position in vertical direction. This scenario coincides with a number of five material degrees of freedom. The optimized truss structure in its spatially undeformed and deformed state is presented in Figure 5.5. The displacements of two particular joints are

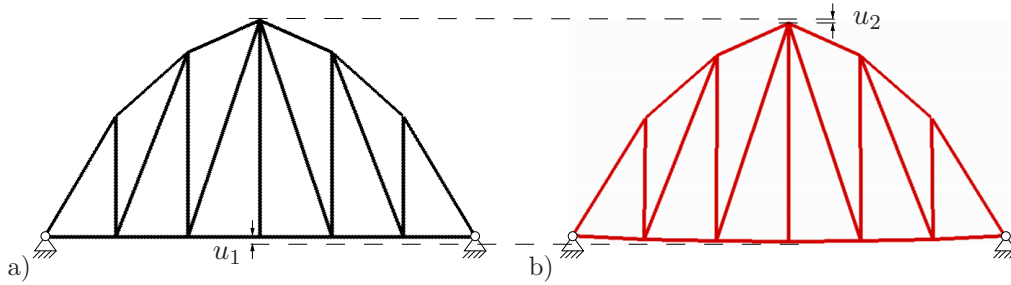


**Figure 5.5:** Improved truss structure in its spatially a) undeformed and b) deformed state. The displacements of the midnodes of the lower and the upper chords are specified, namely  $u_1 = 7.48$  mm and  $u_2 = 6.02$  mm.

indicated. To be specific, the displacements of the lower and upper midnodes are  $u_1 = 7.48$  mm and  $u_2 = 6.02$  mm. Comparing the first one to the maximum displacement  $u_{max}$  gained from the purely spatial computation, a decrease of more than 50% is achieved. The evolution of the norm of the dual spatial-material residual  $\hat{\mathbf{R}}$  during the equilibrium iteration of the Newton-Raphson scheme is given in Table 5.1. As expected, the algorithm

**Table 5.1:** Norm of dual residual, potential, displacement of lower midnode

iteration 1	$ \mathbf{R}  = 2.2360680\text{E}+02$	$\Pi = 0.115225$ Nm	$u_1 = 13.7415$ mm
2	$7.9967532\text{E}+01$	$0.052922$ Nm	$8.0452$ mm
3	$1.9247672\text{E}+02$	$0.035374$ Nm	$6.5295$ mm
4	$1.7094751\text{E}+02$	$0.036986$ Nm	$7.2951$ mm
5	$3.6053893\text{E}+01$	$0.039251$ Nm	$7.4755$ mm
6	$1.9736807\text{E}+00$	$0.039230$ Nm	$7.4827$ mm
7	$3.3212359\text{E}-02$	$0.039231$ Nm	$7.4828$ mm
8	$6.4764280\text{E}-07$	$0.039231$ Nm	$7.4828$ mm

shows a quadratic convergence in the near of the solution point. In addition, the table deals with the evolution of the amount of the energy potential  $\Pi$ . Considering the energy stored in the system after the final deformation step, the value of  $\Pi = 0.039231$  Nm for the optimized system corresponds to a reduction of almost 75% compared to the purely spatial case. Furthermore, the change of the displacement  $u_1$  of the lower midnode is

presented. The reduction of the maximum value has already been emphasized. However, the evolution  $u_2$  is of particular interest from the structural engineering point of view. After the first iteration step, the displacement is  $u_2 = 13.7415$  mm. Then, the material positions of the joints of the upper chord move upwards by what the moment arm of the axial forces in the upper and lower chord increases. This effect results in an increase of the stiffness of the structure and therefore in a decrease of the displacement  $u_2$ . After the fourth iteration only minor changes in the material node point positions occur and no major changes of the displacement  $u_2$  arise as well.

In the final step, the influence of the initial geometry on the optimization process is to be investigated. To this end, the truss structure shown in Figure 5.4 is replaced by a non-symmetric system displayed in Figure 5.6a). Only the initial coordinates of two nodes of

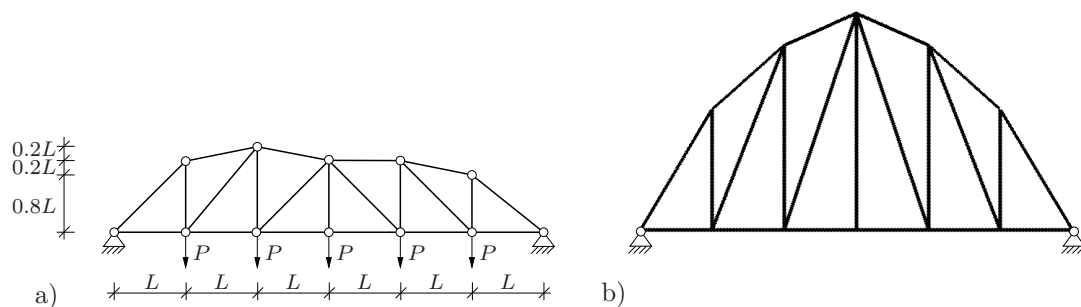


**Figure 5.6:** a) Non-symmetric initial geometry and b) optimized material configuration which is identical to that obtained starting from a symmetric initial system.

the upper chord have been modified. All the material data as well as the spatial boundary conditions, loads and dimensions remain unchanged. Again, quadratic convergence of the Newton-Raphson iteration is achieved and one finally ends up with the optimized structure depicted in Figure 5.6b) in its undeformed state. The resulting material configuration coincides identically with that obtained when starting from a symmetric geometry. Hence, the optimal reference configuration of the truss does not depend on the initial geometry but is exclusively governed by the material node point positions that belong to a vanishing material residual, or, respectively, to vanishing discrete configurational nodal forces.



## 6. Material-Force-Based $h$ -Adaptive Refinement Procedures

This chapter focuses on a configurational-force-based refinement indicator in  $h$ -adaptive finite element strategies. The material balance equation corresponds to an equilibrium of discrete configurational nodal forces and discrete internal material forces based on the energy-momentum tensor and, in dynamics, a contribution arising from the pseudomomentum. However, due to insufficient discretization, or rather triangulation by means of a finite element mesh, numerically caused forces occur at the interior nodes of the mesh. These nodal forces can be utilized as an indicator for mesh refinement. In this scenario, the accuracy of the finite element solution is determined in a postprocessing procedure which is referred to as an *a posteriori strategy*. Following the argumentation of elasticity where configurational forces have a clear energetic meaning the magnitude of the remaining discrete nodal forces is interpreted as an energetic misfit of the current triangulation. The section starts with a short overview on existing literature and some general remarks. Then, exploiting the energetic interpretation of configurational forces, a global criterion is defined which is used for the decision on mesh refinement. In the next step a criterion on the element level is set up governing the local refinement procedure within a  $h$ -adaptive strategy. Afterwards some aspects of the algorithmic treatment and the numerical implementation are discussed. Finally, the proposed procedure is applied to a representative variety of model problems. In addition to the adaptive simulations some benchmark solutions are performed for the sake of comparison.

### 6.1. General Aspects

Methodologically, two fundamental approaches exist to measure the accuracy of a finite element solution. The *a priori* error estimation deals with predictions about existence of solutions, properties of finite element approximations and convergence criteria without specification to a particular boundary value problem, see e.g. SZABO & BABUŠKA [180] or BRAESS [20] among others. On the other hand, the so-called *a posteriori* error estimation bases on the approximative finite element solution and consequently allows for an assessment of the accuracy of the solution of a particular boundary value problem under consideration. The very first treatments date back to the work of BABUŠKA & RHEINBOLDT [9] for linear problems. The error estimation based on smoothing algorithms has been proposed by ZIENKIEWICZ & ZHU [193]. Therein, solution variables, typically stress- or strain-measures, directly obtained from the finite element approximation are compared to their improved counterparts generated by the application of smoothing algorithms, e.g. the patch recovery technique presented within Section 3.5.2 of this work. Mathematical analyses of this kind of error estimation can be found in AINSWORTH, ZHU, CRAIG & ZIENKIEWICZ [3] or, more recently, CARSTENSEN & FUNKEN [27, 28, 29]. The adaption of this technique to small strain inelasticity has been investigated for instance by PERIC, YU & OWEN [146], LI & BETTESS [92] and BOROOMAND & ZIENKIEWICZ [17] in which the smoothing procedure is applied to incremental quantities.

An extension to finite deformation problems is provided by RHEINBOLDT [151] and later on by STEIN, SEIFERT, OHNIMUS & CARSTENSEN [170]. In addition, RADOVITZKY & ORTIZ [150] proposed an adaptive procedure for non-linear dynamical problems. Approaches to the construction of adaptive strategies to finite inelasticity have been established e.g. by ORTIZ & QUIGLEY [145] and MOLINARI & ORTIZ [129]. In the recent work of KOCH [79] a detailed discussion about adaptive strategies is provided including a broad spectrum of citations to corresponding literature.

In general, adaptive strategies in the context of the finite element method may be classified as follows. In  $r$ -adaptive strategies the number of nodal points and elements remains unchanged during the adaption process. The material node point positions of the finite element mesh are moved to optimize the element size with respect to a certain criterion, cf. Section 5. The structure and the dimension of the governing system of equations remains unchanged. However, due to the constant number of elements an appropriate resolution of complex geometries is not possible. In  $p$ -adaptive strategies higher order interpolation functions are introduced on the element level. Consequently, the total number of degrees of freedom of the finite element mesh increases. In what follows, the methodology of  $h$ -adaptivity will be applied. Here, the parameter  $h$  characterizes the edge length of a typical finite element. This refinement technique again yields an increase of the total number of degrees of freedom because elements are replaced by smaller elements of the same type and the refined mesh exhibits regions with high element density.

Basically, two different ways exist to generate partially refined meshes. In the context of *hierarchical refinement* the current mesh is refined locally by introducing additional nodal points at the element edges resulting in a reduced element edge length  $h$ . Using the procedure of complete *remeshing*, a new mesh is generated. The element edge length  $h$  of the improved mesh is controlled by a specific local criterion.

The use of configurational nodal forces within adaptive procedures dates back to the seminal work of BRAUN [21]. Referring to Section 5, configurational-force-based mesh improvement can also be embedded into a dual variational setting of elasticity. This approach is denoted a variational arbitrary Lagrangian Eulerian formulation and can be classified as a  $r$ -adaptive strategy. A combination of both a  $r$ - and a  $h$ -adaptive scheme is proposed by GANGADHARAN, RAJAGOPAL & SIVAKUMAR [51] in which the  $r$ -adaptive part is governed by the dual variational formulation. The application of configurational forces in the context of an adaptive strategy in fracture mechanics is discussed by HEINTZ, LARSSON, HANSBO & RUNESSON [68]. A purely  $h$ -adaptive procedure based on configurational forces has been presented by MÜLLER, GROSS & MAUGIN [132] using their magnitude to assign new mesh sizes. The subsequent treatments follow the recent contribution of MIEHE & ZIMMERMANN [127] where a complete procedure of  $h$ -adaptivity based on configurational forces is set up. The material nodal forces serve as the key quantities for the evaluation of a global criterion governing the decision on mesh refinement as well as a local criterion used for the control of the local refinement process.

## 6.2. Refinement Criterion Based on Discrete Material Nodal Forces

The change of Lagrangian coordinates or, say, the material motion is described by the material balance equation, i.e. the balance of material pseudomomentum. At first the considerations are restricted to the quasi-static case whereas the extension to the dynamical setting is done in Subsection 6.6 below. Consequently, for the time being the material balance law reduces to the material equilibrium condition (3.74)<sub>2</sub>

$$\text{Div}\Sigma + \bar{\Gamma}_0 = \mathbf{0}. \quad (6.1)$$

In this equation with all contributions being purely material objects

$$\Sigma = \psi \mathbf{1} - \mathbf{F}^T \mathbf{P} \quad \text{and} \quad \bar{\Gamma}_0 = -\mathbf{F}^T \bar{\gamma}_0 - \partial_\theta \psi \nabla_X \theta - \partial_{\mathcal{I}} \psi \cdot \nabla_X \mathcal{I} - \partial_{\mathbf{X}} \psi^{\text{expl}} \quad (6.2)$$

denote Eshelby's energy-momentum tensor and the continuous configurational force, respectively. The formulation to follow presumes homogeneous bodies  $\mathcal{B}$  which means that

the free energy function  $\psi$  does not explicitly depend on the material coordinates  $\mathbf{X}$ ,  $\partial_{\mathbf{X}}\psi^{\text{expl}} = \mathbf{0}$ . Furthermore, spatial volume forces are neglected,  $\bar{\gamma}_0 = \mathbf{0}$ . Nevertheless, in general the material balance law still includes a contribution of the configurational force arising from the material gradients of the temperature field  $\theta$  and the internal variable vector  $\mathcal{I}$ . Turning next to the discrete setting, attention is focused on a nodal representation of the material equilibrium condition. According to (3.75)<sub>2</sub>, it reads

$$\mathbf{F}_I + \mathbf{P}_I(\nabla_{\mathbf{X}}\theta, \nabla_{\mathbf{X}}\mathcal{I}) = \mathbf{0} \quad (6.3)$$

and has to be satisfied at all interior nodes  $I$  of the finite element mesh. This condition demands the equilibration of the internal material contribution  $\mathbf{F}_I$  defined by (3.61) in terms of Eshelby's energy-momentum tensor and the discrete configurational nodal force  $\mathbf{P}_I$  given in (3.60) being a function of the material gradients of the temperature and the internal variable fields. Referring to Remark 3.1, the pull-back relationship between the dual spatial-material balance laws states that in the continuous setting both balances are equivalent in the sense that if one equation is satisfied the other one is automatically satisfied as well. Thus, condition (6.3) is expected to be fulfilled identically for homogeneous bodies or in the discrete setting for an optimal mesh that perfectly resolves the homogeneous structure of the body. However, this property is not preserved in the continuous setting. In contrast, upon discretization, i.e. by introduction of a triangulation of the material body by means of an arbitrary finite element mesh, an artificial inhomogeneity is introduced. Due to this inhomogeneity the discrete form of the material equilibrium condition is violated. This means that the triangulation breaks the equivalence between the material and spatial balance equations. In other words, due to an insufficient triangulation, numerically caused, often also denoted spurious, nodal forces occur originating from the fact that the triangulation is not smooth with respect to strain and stresses. These out of balance discrete forces which actually preclude the satisfaction of the material balance law indicate that the current triangulation is not yet optimal and serve as a measure for the inaccuracy of the triangulation. Therefore, they may be used as an indicator for mesh improvement.

The procedure provided in the previous Section 5, which in fact is restricted to elastic problems, is classified as a  $r$ -adaptive strategy. It enforces the fulfillment of the material equilibrium condition by means of a rearrangement of the material node point positions for a fixed number of nodal points within the mesh.

For now, the material equilibrium condition or, to be precise, the remaining spurious forces are employed as a refinement indicator within a  $h$ -adaptive strategy. To this end, recall the fundamental energetic interpretation of configurational forces in inhomogeneous elastic bodies. They describe the change of energy within the material configuration of the body upon movement of the material coordinates. In this sense, the norm of all numerically caused nodal forces is assumed as an energetic misfit of the current triangulation. Incorporating this methodology into the more general context of thermo-inelasticity, it is straightforward to define an estimate of the inaccuracy of the current triangulation by the sum of all non-vanishing nodal forces of the discrete body

$$\Delta\Pi = \left(1 + \frac{n_{\text{bnd}}}{n_{\text{int}}}\right) \sum_{I=1}^{n_{\text{int}}} |(\mathbf{F}_I + \mathbf{P}_I)|. \quad (6.4)$$

Here,  $n_{\text{int}}$  and  $n_{\text{bnd}}$  denote the number of interior nodes and of the nodes on the discrete boundary. Obviously,  $\mathcal{N}_t = n_{\text{int}} + n_{\text{bnd}}$  represents the total number of nodal points of



the current finite element mesh. The computation of the energetic misfit  $\Delta\Pi$  demands a more detailed explanation. As pointed out before, on account of the discrete material equilibrium condition (6.3), the sum  $\mathbf{F}_I + \mathbf{P}_I$  of nodal forces has to vanish at all  $n_{int}$  interior nodes of the finite element mesh. In contrast, true physically motivated nodal forces  $(\mathbf{F}_I + \mathbf{P}_I)_{bnd}^{real}$  occur at all  $n_{bnd}$  nodes on the discrete boundary  $\partial\mathcal{B}^h$  of the body. These forces are essential to maintain the original material shape of the body which means to prevent the material configuration of the body from shrinking. However, due to discretization the approximation  $(\mathbf{F}_I + \mathbf{P}_I)_{bnd}$  of these boundary forces also includes

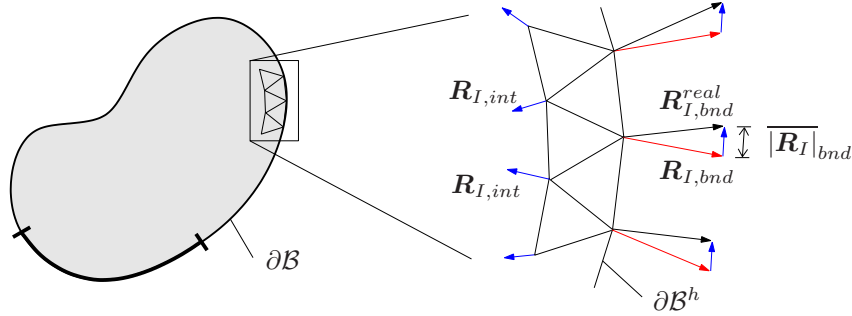


**Figure 6.1:** Treatment of nodal forces on discrete boundary. Physically motivated forces  $\mathbf{R}_{I,bnd}^{real} := (\mathbf{F}_I + \mathbf{P}_I)_{bnd}^{real}$  occur maintaining the material shape of the body. By assumption, the inaccuracy  $|\overline{\mathbf{R}_I}|_{bnd} := |(\mathbf{F}_I + \mathbf{P}_I)_{bnd}|$  of the approximated counterparts  $\mathbf{R}_{I,bnd} := (\mathbf{F}_I + \mathbf{P}_I)_{bnd}$  equals an averaged value of the forces  $\mathbf{R}_{I,int} := (\mathbf{F}_I + \mathbf{P}_I)_{int}$  at the interior nodes.

an inaccuracy, see Figure 6.1. This inaccuracy  $|\overline{(\mathbf{F}_I + \mathbf{P}_I)}|_{bnd}$  is assumed to coincide with the average value of the norm of the nodal forces at all interior nodes with respect to the number of interior nodes

$$\overline{|(\mathbf{F}_I + \mathbf{P}_I)|}_{bnd} := \frac{1}{n_{int}} \sum_{J=1}^{n_{int}} |(\mathbf{F}_J + \mathbf{P}_J)|. \quad (6.5)$$

Multiplying this quantity with the number  $n_{bnd}$  of boundary nodes and adding the sum of the norm of all spurious interior forces defines the energetic misfit  $\Delta\Pi$  as specified in (6.4) in terms of the weighting factor  $(1 + n_{bnd}/n_{int})$ .

Based on this estimate of the inaccuracy of the current triangulation a *relative global criterion* is set up as the ratio between the energetic misfit  $\Delta\Pi$  and the elastically stored energy  $\Pi^e$  of the body, i.e.

$$\eta = \frac{\Delta\Pi}{\Pi^{elast}} \quad \text{with} \quad \Pi^{elast} = \int_{\mathcal{B}} \psi^{elast} dV. \quad (6.6)$$

Based on this global criterion the decision on mesh refinement is carried out in the following manner. For the case that the accuracy of the current triangulation is said to be sufficient which means that the global criterion is lower than a given admissible criterion,  $\eta \leq \eta_{perm}$ , no refinement of the current mesh is needed. Otherwise,  $\eta > \eta_{perm}$ , the accuracy of the current triangulation is insufficient and mesh refinement is required.

In order to set up a local refinement procedure, in the first step a modified element quantity  $\xi^e$  is constructed. This value is the key ingredient of the data-processing that governs the local refinement within the strategy of complete remeshing. The element criterion  $\xi^e$  is defined as the ratio between an energetic defect  $\Delta\pi^e$  of the current element under

consideration and an averaged element value  $\pi_m$

$$\xi^e = \left[ \frac{\Delta\pi^e}{\pi_m} \right]^{1/p} \quad \text{with} \quad \pi_m = \eta_{perm} f_S \frac{\Delta\Pi}{n_{ele}}. \quad (6.7)$$

Here,  $n_{ele}$  denotes the total number of elements of the current mesh and  $p$  indicates the order of the finite element shape functions. Furthermore,  $\eta_{perm}$  is the admissible global threshold and  $f_S$  a safety factor. The global misfit  $\Delta\Pi$  has been defined in (6.4). The contribution  $\Delta\pi^e$  of the current element  $e$  is evaluated as the amount of all nodal forces belonging to that element

$$\Delta\pi^e = \left( 1 + \frac{n_{bnd}^e}{n_{int}^e} \right) \sum_{I=1}^{n_{int}^e} |(\mathbf{F}_I + \mathbf{P}_I)^e|. \quad (6.8)$$

In analogy, the overall quantities,  $n_{int}^e$  is the number of interior nodes per element whereas  $n_{bnd}^e$  denotes the number of nodes of the current element belonging to the discrete boundary  $\partial\mathcal{B}^h$  of the entire body, and  $n^e = n_{int}^e + n_{bnd}^e$  being obvious. Computing this element value the particular situation at the boundary needs to be taken into account as well. Recalling the above discussion, along the discrete boundary physically based nodal forces occur preserving the material shape of the body. As schematically depicted in Figure

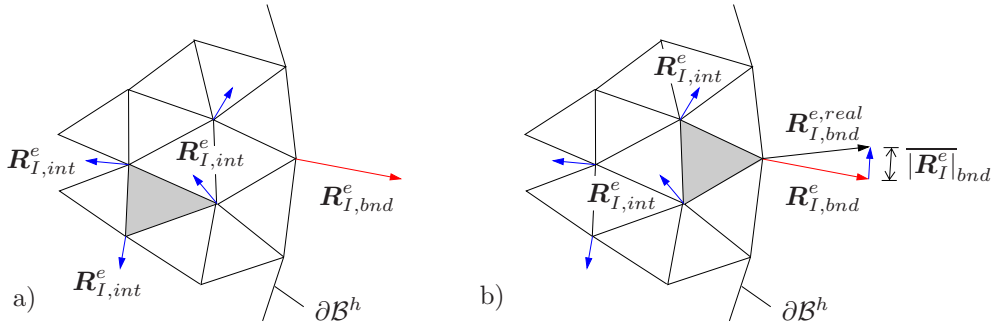


**Figure 6.2:** Computation of element criterion. a) Element  $e$  within the body  $\mathcal{B}$ . The element criterion is defined as the average of the norm of the discrete nodal forces  $\mathbf{R}_{I,int}^e := (\mathbf{F}_I + \mathbf{P}_I)^e$  of the current element  $e$ . b) Situation on material boundary  $\partial\mathcal{B}$ . Physically motivated forces  $\mathbf{R}_{I,bnd}^{e,real} := (\mathbf{F}_I + \mathbf{P}_I)_{bnd}^{e,real}$  appear. By assumption, the inaccuracy  $\overline{|\mathbf{R}_{I,bnd}^e|} := \overline{|(\mathbf{F}_I + \mathbf{P}_I)^e|_{bnd}}$  of these forces equals the averaged value of the norm of the resultant forces  $\mathbf{R}_{I,int}^e := (\mathbf{F}_I + \mathbf{P}_I)^e$  at the interior nodes of element  $e$ .

6.2, the approximative element nodal forces  $(\mathbf{F}_I + \mathbf{P}_I)_{bnd}^e$  differ from their true counterparts  $(\mathbf{F}_I + \mathbf{P}_I)_{bnd}^{e,real}$  due to an insufficient triangulation. Conceptually in line with the treatments provided for the global criterion, the formulation to follow presumes this inaccuracy  $\overline{|(\mathbf{F}_I + \mathbf{P}_I)^e|_{bnd}}$  to coincide with an averaged value of the amount of all nodal forces belonging to each element  $e$

$$\overline{|(\mathbf{F}_I + \mathbf{P}_I)^e|_{bnd}} := \frac{1}{n_{int}^e} \sum_{J=1}^{n_{int}^e} |(\mathbf{F}_J + \mathbf{P}_J)^e|. \quad (6.9)$$

Summing up all contributions the weighting factor  $(1 + n_{bnd}^e/n_{int}^e)$  enters the element misfit (6.8). The configurational-force-based global and local criteria are central to the  $h$ -adaptive strategy to be elaborated in the next subsection.

### 6.3. Algorithms and Numerical Implementation

The overall goal of an adaptive strategy is a self-controlled simulation providing at different time or loads steps an appropriate triangulation including a suitable resolution of crucial regions within the system. The general procedure of the proposed  $h$ -adaptive strategy acts in the following steps, cf. BRENNER & CARSTENSEN [22]:

---

<i>Solve:</i>	Perform load step $i$ on mesh or triangulation $j$ : Enforce spatial equilibrium condition.
<i>Estimate:</i>	Evaluate global criterion $\eta$ and decide on mesh refinement: Check material equilibrium condition.
<i>Mark:</i>	Compute element criterion $\xi^e$ .
<i>Refine/ Coarsen:</i>	Generate an improved triangulation $j \Leftarrow j + 1$ : Enforce better approximation of material balance equation.
<i>Map Solution Data:</i>	Transfer solution data onto new mesh.

---

To be precise, after the solution of load step  $i$  on mesh  $j$  by a standard local spatial computation the internal variables are projected from the integration point level onto the node point level of the current mesh by means of smoothing algorithms, cf. Section 3.5.2. Within a further element loop the elastic energy storage and the contributions to the discrete configurational nodal forces are computed according to (3.60) and (3.61). Afterwards, the global criterion (6.6) can be evaluated directly. If no mesh refinement is required, the next load step  $i \Leftarrow i + 1$  is going to be solved on the same mesh  $j$ . In case the global criterion violates the admissible threshold, i.e. the global criterion assesses the current triangulation to be inaccurate, the element criterion (6.7) is computed. The new mesh  $j \Leftarrow j + 1$  is generated with the local criterion informing about the element refinement factor. Prior to the next analysis, the solution variables of the last accepted load step have to be transferred onto the new mesh. Basically, the nodal variables, i.e. the spatial displacements and the temperature field as well as, for inelastic problems, the projected internal variables, cf. Section 6.5.1, of the old mesh are mapped onto the nodes of the new mesh. Obviously, the data evaluated on the old mesh does not necessarily constitute an equilibrium state for the new mesh. This demands that the same load step  $i$  has to be solved for the new mesh until the global criterion states the triangulation to be sufficiently accurate. The load step is increased  $i \Leftarrow i + 1$  and the analysis continues with the accepted mesh. The entire procedure recurs until a maximum load or deformation step is reached. The flowchart provided in Figure 6.3 schematically illustrates the overall scenario. In the following, two particular topics of the above procedure are considered, namely the mesh generation and the mapping of the solution variables.

**6.3.1. Mesh Generation.** In case the triangulation was assessed to be inappropriate for the current load step, the mesh has to be improved in certain regions. Thus, a locally refined mesh has to be generated. This local refinement can be performed by hierarchical mesh adaption or via remeshing of the geometry model. For the two-dimensional simulations both strategies have been adopted, a comparative study in the context of a numerical example is provided in Section 6.4.3 below. The three-dimensional examples solely incorporate complete remeshing. Irrespective of the refinement strategy, the key part of both

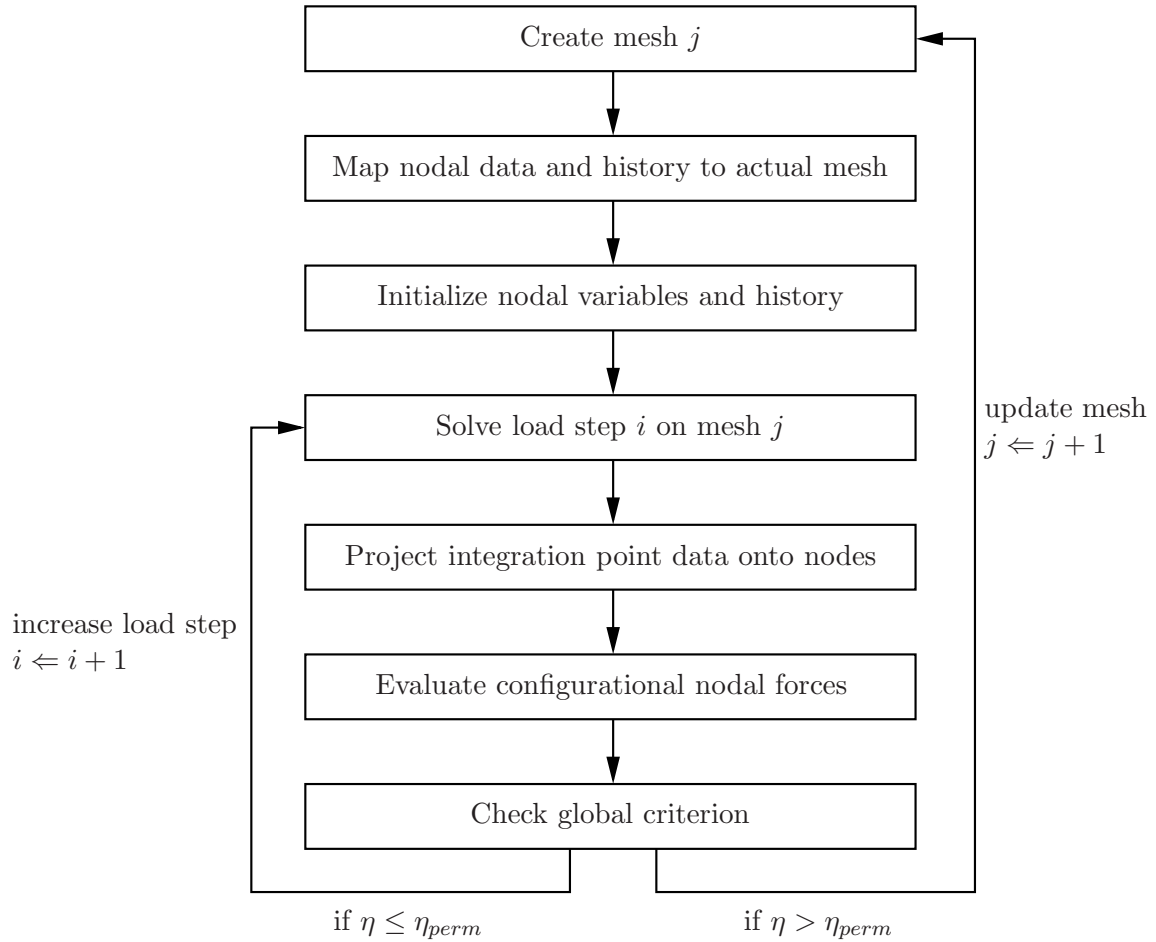


**Figure 6.3:** Flowchart of the general procedure for the configurational-force-based  $h$ -adaptive refinement procedure.  $\eta_{perm}$  denotes the admissible threshold for which the triangulation is said to be sufficiently accurate.

approaches is the generation of an at least primary finite element mesh. Within all the analyses to follow unstructured meshes consisting of quadratic elements are used.

In view of the two-dimensional setting six-noded triangular elements have been employed. The strategy of remeshing bases on the construction of a density function  $\varphi(\mathbf{X})$  evaluated in terms of the local criterion  $\xi^e$ . The density function covers the interval  $\varphi \in [0; 1]$  and assigns the element edge lengths of the new mesh in the sense that for  $\varphi = 1$  no refinement occurs whereas  $\varphi < 1$  determines the grade of refinement. For the hierarchical strategy a bisection method is used. The algorithms for the mesh generation have been developed and described at full length by KOCH [79], see also WELSCHINGER [187] for some more detailed informations. They base on a Delaunay-triangulation of the geometry model in the sense of the ideas of RUPPERT [156], SHEWCHUK [157], and SLOAN [168], [169].

With regard to three-dimensional setting, the adaptive strategy is embedded into an overall solution procedure based on the coupling of different software packages controlled by means of Python-scripts. In the following only the basic concepts are presented, a more detailed discussion of the algorithmic treatment and the numerical implementation can be found in the recent report of FÜRLE [50]. The preprocessing including the mesh generation is performed by the commercial software package Abaqus and controlled by the Python-based scripting interface of Abaqus, see the reference manual ABAQUS [1]. The preprocessing of an analysis consists of three major parts, namely the creation of the

geometry, the partitioning of the body and finally the mesh generation. The geometry is created within the non-graphical CAE-environment of Abaqus by exploitation of the program's Python-based scripting capabilities. Next, partitioning means the subdivision of the geometry model into smaller regions in order to assign different element sizes at different locations of the body. This is achieved by the introduction of planes intersecting with the model. Due to this partitioning process, new edges occur inside the body and on its surface in case a plane intersects with an existing edge or with another plane. After the body is partitioned sufficiently, all the edges which arose from the actual partitioning can be used to seed the model differently, dependent on the location of the edge. Seeding means to define a certain element size on a certain edge which coincides with the assignment of a particular element size to every single edge. This seeding procedure is governed by the element criterion  $\xi^e$  evaluated in terms of the numerically caused configurational nodal forces and therefore guarantees a local refinement of the critical regions of the material body. In particular, the element criteria  $\xi^e$  are scaled with respect to a certain interval that allows to use them directly as scaling factors for future element sizes or rather element edge lengths. To this end, at first the minimum and maximum element values  $\xi_{min}^e$  and  $\xi_{max}^e$  are determined. Based on these values the scaled criterion reads

$$\bar{\xi}^e = \frac{\xi^e - \xi_{min}^e}{\xi_{max}^e - \xi_{min}^e}(\alpha - \beta) + \beta \quad (6.10)$$

with  $\alpha, \beta$  representing the lower and upper bounds of the desired interval. In the numerical studies, the values  $\alpha \approx 1.0$  and  $\beta = 2.0$  have proven to be reasonable. This particular choice means that the element sizes in areas of the lowest local criterion remain unchanged,  $\bar{\xi}_{min}^e = \alpha = 1.0$ . In those areas of the highest indicator, the element edge lengths will be half the size because the old values are divided by  $\bar{\xi}_{max}^e = \beta = 2.0$ . For  $\alpha < 1.0$  coarsening in regions with small element values  $\xi^e$  can be taken into account. The final step is to mesh the body by ten-noded tetrahedrons whereupon the mesh data, i.e. the nodal coordinates and the element connectivity, can be written to an input file in an arbitrary format depending on which finite element processing software is employed for the execution of the analysis of the respective load or deformation step.

**6.3.2. Mapping of Solution Variables.** In order to restart the analysis at the last accepted load increment, the solution variables of that step have to be initialized. However, the solution data of the last accepted analysis belongs to a different mesh. To be able to perform the initialization all the solution data has to be transferred onto the actual new mesh. This demands the development of a mapping algorithm to perform that data transfer. The solution variables to be mapped are the current spatial nodal displacements and, in the event of the simulation of inelastic problems, the history data. The treatment of the latter one will be highlighted in Section 6.5.1 below. In any case, the data transfer results in the mapping of nodal values of the last accepted old mesh onto the nodal points of the new mesh. The crucial point of the algorithm is to evaluate for every point of the new triangulation the local element coordinates within the old mesh. This at first requires to find this unique element of the old mesh containing the physical coordinates of the new node. This task is carried out by application of a specific search algorithm. With the unique element at hand, the local coordinates  $\xi_I$  of an arbitrary point, for the time being the new node  $I$ , in an element  $\tilde{e}$  are computed in the following way. The physical coordinates  $\mathbf{X}_I^{new}$  of the point  $I$  are evaluated by the isoparametric geometry approach

in terms of the nodal coordinates  $\mathbf{X}_i^{old,\tilde{e}}$  of the element belonging to the old mesh

$$\mathbf{X}_I^{new} = \sum_{i=1}^{n^{\tilde{e}}} N_i(\boldsymbol{\xi}_I) \mathbf{X}_i^{old,\tilde{e}}. \quad (6.11)$$

As the coordinates of the point of interest as well as the element coordinates of the element of the old mesh are given, the unknowns in this equation are the local element coordinates  $\boldsymbol{\xi}_I$  which actually need to be evaluated. Since quadratic shape functions are employed, the non-linear system of equations (6.11) is solved by standard Newton-type iteration. The solution of this non-linear system of equations is constrained by the condition that all three coordinates of the solution  $\boldsymbol{\xi}_I$  have to be within the interval  $[0; 1]$  otherwise the new node lies outside the element. Therefore, the solution of (6.11) serves as a check whether the search algorithm has found the correct element. Now, with the unique element  $\tilde{e}$  of the old mesh containing the physical coordinates  $\mathbf{X}_I^{new}$  of the new node and in addition with the local element coordinates  $\boldsymbol{\xi}_I$  of that point at hand, the nodal displacements  $\mathbf{d}_I^{new}$  of node  $I$  of the new mesh are computed by the standard finite element approach

$$\mathbf{d}_I^{new} = \mathbf{u}^h(\boldsymbol{\xi}_I) = \sum_{i=1}^{n^{\tilde{e}}} N_i(\boldsymbol{\xi}_I) \mathbf{d}_i^{old,\tilde{e}}. \quad (6.12)$$

Here,  $\mathbf{d}_i^{old,\tilde{e}}$  represents the nodal displacements at every node  $i$  of the particular element  $\tilde{e}$  within the old mesh. Obviously, if the node of the new triangulation appears to have identical coordinates as a node of the old mesh, as it occurs for instance in the corners of the model, no mapping has to be done, since the displacements stay the same

$$\mathbf{d}_I^{new} = \mathbf{d}_i^{old}. \quad (6.13)$$

Consequently, the respective node  $I$  is not to be treated by the above procedure. At that point, all the ingredients for the material-force-based  $h$ -adaptive finite element simulation have been elaborated. In order to demonstrate the capability and versatility of the proposed method it is now applied to a variety of model problems starting from finite deformation elasticity up to finite plasticity and thermo-plasticity.

## 6.4. Application to Finite Elasticity

The fundamental equations of the material-force-based strategy are adjusted to purely elastic problems. Subsequently, two different aspects are elaborated. On the one hand, within the two-dimensional framework, a comparison of the proposed configurational-force-based procedure to a rather well-established recovery-based method is highlighted. Some essential aspects of the latter approach are recapitulated briefly. Then, the results of the simulations of a representative boundary value problem obtained from both strategies are discussed. On the other hand, the material-force-based technique is analyzed in more detail within the general three-dimensional setting. Thereby, the quality of the results is examined by means of comparison with fine and coarse mesh solutions. The constitutive basis of the subsequent treatments is provided by the assumption of a Neo-Hookean type free Helmholtz energy  $\psi$  introduced in equation (4.82) within Section 4.5.1.

**6.4.1. Material-Force-Based Refinement Indicator in Finite Elasticity.** In order to assign the adaptive strategy proposed in Section 6.2 to problems of finite elasticity



recall the dual material equilibrium condition (6.1). It states

$$\text{Div}\boldsymbol{\Sigma} + \bar{\boldsymbol{\Gamma}}_0 = \mathbf{0} \quad (6.14)$$

with Eshelby's energy-momentum tensor  $\boldsymbol{\Sigma}$  and the configurational force  $\bar{\boldsymbol{\Gamma}}_0$ . Now, the same argumentation that has been adopted within the context of topology optimization in Chapter 5 allows for the subsequent reformulations. Within the setting of isothermal elasticity no change of temperature occurs and no internal variables need to be accounted for. Hence, the configurational force boils down to  $\bar{\boldsymbol{\Gamma}}_0 = -\mathbf{F}^T \bar{\boldsymbol{\gamma}}_0 - \partial_{\mathbf{X}} \psi^{\text{expl}}$ . Furthermore, spatial volume forces are neglected,  $\bar{\boldsymbol{\gamma}}_0 = \mathbf{0}$ . Finally, the material body is assumed to be homogeneous which means that the free energy does not depend explicitly on the material coordinates,  $\partial_{\mathbf{X}} \psi^{\text{expl}} = \mathbf{0}$ . Consequently, the configurational force vanishes,  $\bar{\boldsymbol{\Gamma}}_0 = \mathbf{0}$ , and the material equilibrium condition reduces to the strict conservation law

$$\text{Div}\boldsymbol{\Sigma} = \mathbf{0}. \quad (6.15)$$

Upon discretization this balance equation is reformulated in a nodal expression corresponding to (6.3) that has to be enforced at every interior node  $I$  of the current mesh,

$$\mathbf{F}_I = \mathbf{0}. \quad (6.16)$$

Thereby,  $\mathbf{F}_I$  is defined according to (3.61). This statement obviously coincides with the nodal entries of the material residual arising in the discrete version of the dual variational formulation presented in Section 5. On account of the discussion provided in Remark 5.1 and in the sense of a discrete representation of the governing material balance law (6.14), the internal material nodal force  $\mathbf{F}_I$  can evidently be denoted the discrete configurational node point force. The essential criteria of the material-force-based strategy, i.e. the global criterion (6.6),  $\eta = \Delta\Pi/\Pi^{\text{elast}}$ , and the local element criterion (6.7),  $\xi^e = (\Delta\pi^e/\pi_m)^{1/p}$ , conceptually remain unchanged. The global energetic misfit  $\Delta\Pi$  given in (6.4) as well as its counterpart on the element level  $\Delta\pi^e$ , see (6.8), are slightly modified in that way that the discrete quasi-inhomogeneity, or rather configurational nodal force vanishes,  $\mathbf{P}_I = \mathbf{0}$ .

**6.4.2. A Short Review of Recovery-Based Error Estimation.** For finite deformation problems the error  $\mathbf{e}$  of a finite element solution is defined as the difference between the exact and the approximative spatial positions  $\mathbf{x} = \boldsymbol{\varphi}_t(\mathbf{X})$  and  $\mathbf{x}^h = \boldsymbol{\varphi}_t^h(\mathbf{X})$ , see also Figure 6.4 for a sketch of this definition. This coincides with the difference between the exact displacement field  $\mathbf{u}$  and the finite element solution  $\mathbf{u}^h$

$$\mathbf{e} := \mathbf{x} - \mathbf{x}^h = \mathbf{u} - \mathbf{u}^h. \quad (6.17)$$

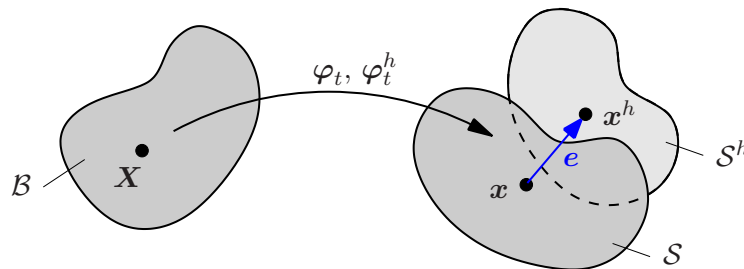


**Figure 6.4:** Definition of the error  $\mathbf{e}$  of the finite element solution as the difference between exact spatial position  $\mathbf{x}$  and approximative spatial position  $\mathbf{x}^h$ .



The methodology of error estimation employed for the comparative study within Section 6.4.3 goes back to the work of ZIENKIEWICZ & ZHU [193] and is referred to as *recovery-based error estimation*. A detailed discussion and especially its extension to finite deformations is provided by KOCH [79]. Based on energetic arguments it can be shown that the error of the energy norm equals the energy norm of the error  $B_C(\Delta \mathbf{e}, \Delta \mathbf{e})$  and, furthermore, that the finite element solution  $\mathbf{u}^h$  minimizes this quantity. The bilinear functional  $B_C$  corresponds to the linear increment of the linearization of the variational expression obtained from the principle of minimum potential energy, cf. the spatial branch of the variational setting outlined in Section 5. It is defined by

$$B_{C(\tilde{\mathbf{u}})}(\Delta \mathbf{u}, \delta \mathbf{u}) := \int_{\mathcal{B}} \delta \mathbf{F} : \mathbb{C}(\tilde{\mathbf{u}}) : \Delta \mathbf{F} \, dV \quad (6.18)$$

with the fourth order nominal moduli  $\mathbb{C} = \partial_{\mathbf{F}\mathbf{F}}^2 \psi(\mathbf{F})$ . The energy norm of error is obtained by function evaluation in terms of the incremental error

$$B_C(\Delta \mathbf{e}, \Delta \mathbf{e}) := B_C(\Delta \mathbf{u} - \Delta \mathbf{u}^h, \Delta \mathbf{u} - \Delta \mathbf{u}^h) = B_C(\Delta \mathbf{u}, \Delta \mathbf{u}) - B_C(\Delta \mathbf{u}^h, \Delta \mathbf{u}^h). \quad (6.19)$$

In what follows, the energy norm of the error will be used to determine the error of the finite element mesh. In this scenario, the relative global refinement criterion reads

$$\eta = \sqrt{\frac{B_C(\Delta \mathbf{e}, \Delta \mathbf{e})}{B_C(\Delta \mathbf{u}, \Delta \mathbf{u})}}. \quad (6.20)$$

In general, the exact solution of a boundary value problem is not known. Thus, the energy norm of the error can not be computed directly. Hence, the error may be estimated based on the approximative finite element solution. This approach is referred to as *a posteriori* error estimation. Instead of the exact solution, an improved approximative solution  $\mathbf{u}^*$  is used to evaluate the energy norm of the error. Considering the gradient  $\nabla_X \Delta \mathbf{u}$  of the increments of the displacement field it can be observed, that at the integration points of a typical finite element this quantity has a better rate of convergence than elsewhere in the element. Therefore, the gradient is said to be superconvergent, cf. ZIENKIEWICZ & ZHU [194, 195]. The improved gradient  $\nabla_X \Delta \mathbf{u}^*$  is computed via a so-called patch recovery technique, see Section 3.5.2. Based on definition (6.18) an approximation of the energy norm of the error can be expressed in terms of the gradient of the incremental displacement field  $\nabla_X \Delta \mathbf{u}^h$  and its improved counterpart  $\nabla_X \Delta \mathbf{u}^*$  via

$$B_C(\Delta \mathbf{e}, \Delta \mathbf{e}) \approx \int_{\mathcal{B}} [\nabla_X \Delta \mathbf{u}^* - \nabla_X \Delta \mathbf{u}^h] : \mathbb{C}(\tilde{\mathbf{u}}) : [\nabla_X \Delta \mathbf{u}^* - \nabla_X \Delta \mathbf{u}^h] \, dV. \quad (6.21)$$

**Remark 6.1:** The recovery-based error estimation demands the application of the patch recovery technique. In contrast, for elastic problems the global and local criteria of the material-force-based strategy are evaluated just in terms of the internal material nodal force  $\mathbf{F}_I$ . This quantity, however, only depends on Eshelby's energy-momentum tensor  $\Sigma$ . Due to the fact that the ingredients of this field are directly obtained by a standard spatial computation, the nodal forces  $\mathbf{F}_I$  can be evaluated by just one more element loop without employing any further algorithms. Consequently, the numerical effort with respect to the assessment of the accuracy of the current triangulation is significantly smaller compared to that of the recovery-based approach.

**6.4.3. Numerical Example: Plate with a Circular Hole.** At first, a circular plate with a hole is considered. System and boundary conditions are taken from MÜLLER, GROSS & MAUGIN [132] and are depicted in Figure 6.5. The ratio of the diameter of the hole with respect to the edge length is 0.4. The material parameters are  $\mu = 400.0 \text{ kN/mm}^2$

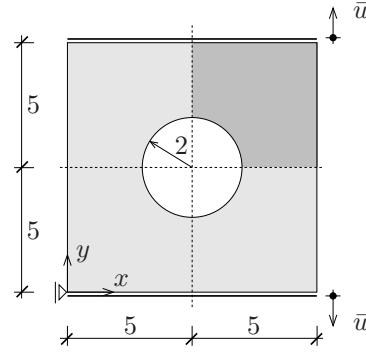


**Figure 6.5:** System and boundary conditions of a plate with a circular hole. All dimensions are given in [mm]. Due to symmetry only a quarter of the specimen is discretized.

and  $\nu = 0.3571$ , i.e.  $\beta = 2.5$ . Due to symmetry only a quarter of the specimen is discretized with a primary number of 36 six-noded quadratic triangular elements. Plane strain conditions are assumed for the analyses. A total displacement  $\bar{u} = 5 \text{ mm}$  of the top edge corresponding to a deformation of 100% of the original height is applied using ten increments  $\Delta\bar{u} = 0.5 \text{ mm}$ . By means of this boundary value problem the proposed configurational-force-based strategy is compared to the well proven recovery-based procedure. In addition, both refinement strategies, namely the hierarchical refinement as well as the complete remeshing are considered. However, the recovery-based approach is only used in combination with the hierarchical procedure for the sake of abbreviation whereas the material-force-based refinement indicator is employed with regard to both strategies. Figure 6.6 deals with the evolution of the relative global criterion  $\eta$  versus the number of

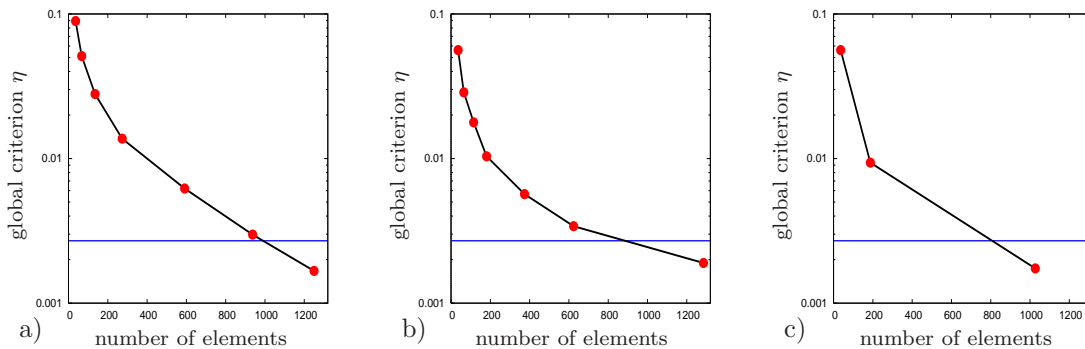


**Figure 6.6:** Plate with circular hole: Global criterion versus number of elements during first deformation step at  $\bar{u} = 0.5 \text{ mm}$ . Hierarchical refinement for a) recovery- and b) material-force-based method. c) Material-force-based procedure using remeshing. Permitted value is depicted as straight line.

elements during the first deformation step at  $\bar{u} = 0.5 \text{ mm}$ . The axis of the global criterion is plotted in logarithmic scale and the number of elements refers to the discretized quarter of the specimen. Using the hierarchical procedure combined with either the recovery-based or the material-force-based refinement indicator, Figure 6.6a), b), the mesh is refined in six

steps until the global criterion falls below the permitted threshold  $\eta_{perm}^{zz} = \eta_{perm}^{mf} = 0.27\%$ . For the recovery-based estimation the number of elements increases from 36 up to 1250 while the material-force-based method yields a total number of 1285 elements which coincides with a difference of less than 3%. The third method, i.e. the material-force-based refinement indicator utilizing the strategy of complete remeshing, is shown in Figure 6.6c). It ends up with 1027 elements received after just two refinement steps. In Figure 6.7 the progress of mesh refinement is presented for the three different method-

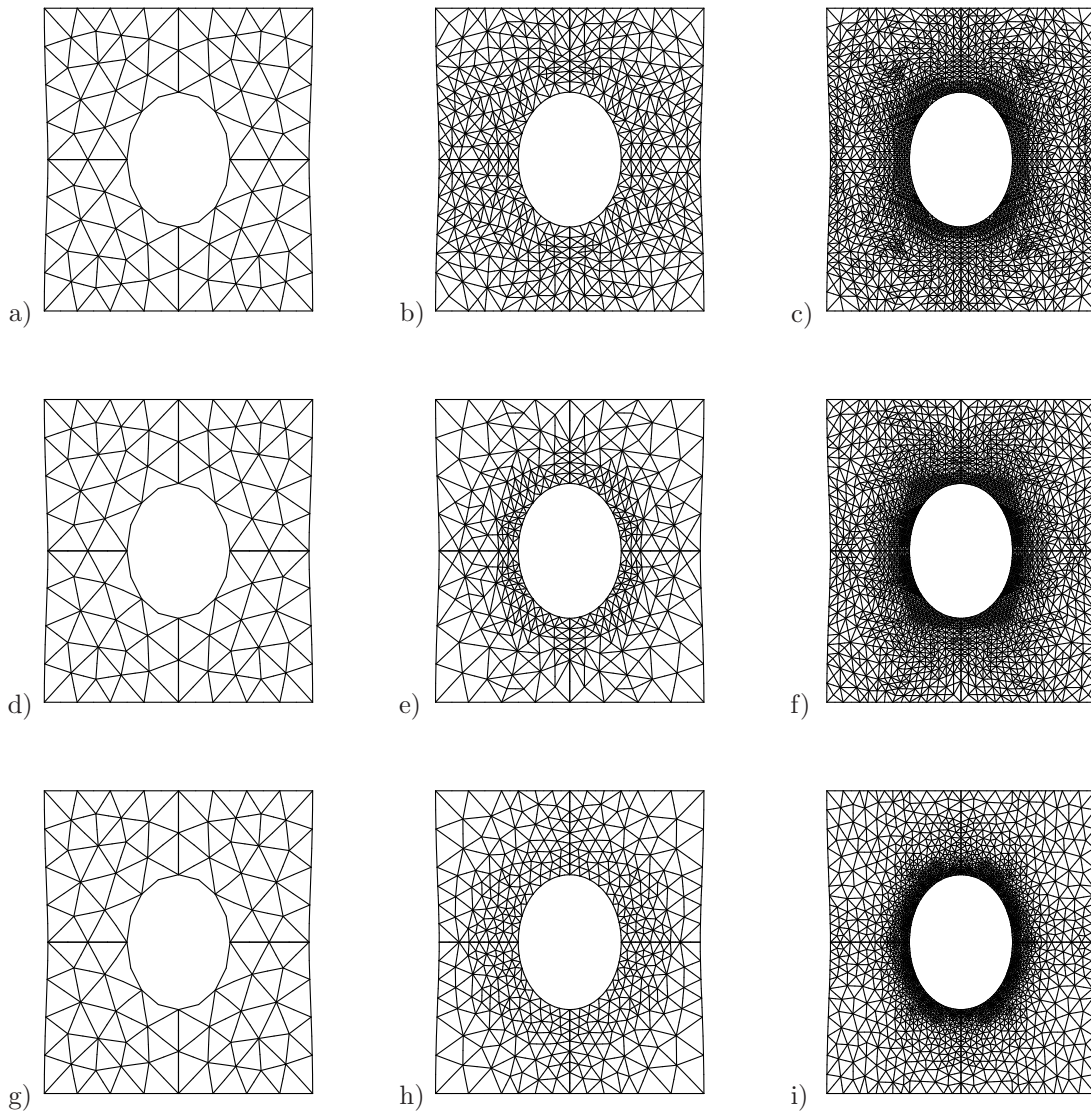


**Figure 6.7:** Mesh refinement during first deformation step at  $\bar{u} = 0.5$  mm. Hierarchical refinement for a)–c) recovery- and d)–f) material-force-based indicator. g)–i) Remeshing for material-force-based approach. Primary mesh, intermediate state and final triangulation.

ologies within the first deformation step at  $\bar{u} = 0.5$  mm. All approaches display the same characteristics in the refined meshes. To be specific, the mesh is highly densified around the circular hole whereas the mesh at the outer edges of the specimen remains relatively coarse. The process of hierarchical mesh refinement is very well observable in Figure 6.7a)–f). Starting from a coarse primary triangulation, the mesh is refined locally by introducing additional nodes at the midpoints of single elements. Considering the element shapes, the remeshing procedure, Figure 6.7g)–i), turns out to give the most regular mesh.

The distribution of the  $yy$ -component of the first Piola-Kirchhoff stress tensor is visualized in Figure 6.8 for the final state of deformation. The contour plots display no difference

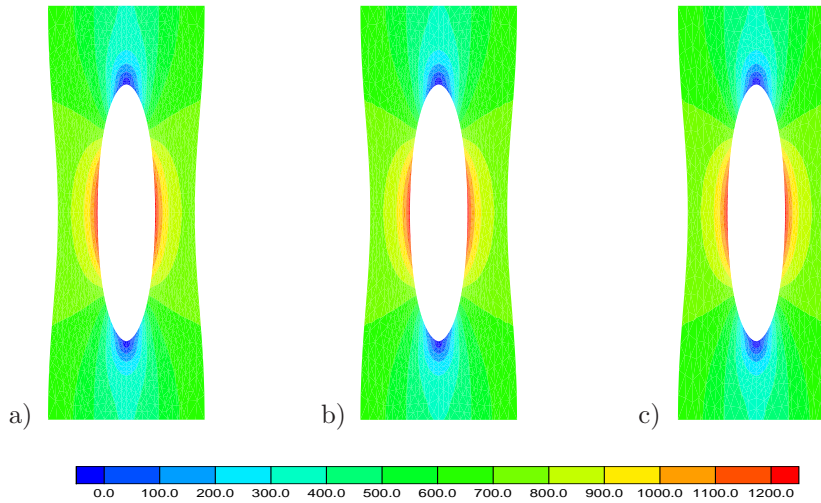


**Figure 6.8:** Distribution of  $P_{yy}$ -component of first Piola-Kirchhoff stress tensor for a) recovery-based, b) material-force-based method in terms of hierarchical refinement, and c) the material-force-based approach in combination with remeshing for final deformation state.

in the results of all approaches. This observation is confirmed when comparing the absolute values of the stresses. In view of the minimum  $P_{yy}$ -values  $-65.77 \text{ N/mm}^2$  for the recovery-based and  $-66.77 \text{ N/mm}^2$  for the material-force-based procedure using remeshing are obtained. Additionally the maximum  $P_{yy}$ -stresses are between  $1265.20 \text{ N/mm}^2$  for the recovery-based and  $1265.30 \text{ N/mm}^2$  for the material-force-based approach combined with hierarchical refinement. Hence, the maximum difference is less than 1.0%.

Consequently, within this comparative study the material-force-based procedure deals with results that are almost identical to those obtained from the well-known recovery-based error estimation. Taking into account the advantages of the configurational-force-based method regarding the numerical efficiency emphasized in Remark 6.1, the proposed strategy turns out to be more favorable.

**6.4.4. Numerical Example: Buckling of a Circular Bar.** The objective of the second example is to capture the three-dimensional case. To this end a circular bar subjected to compression is considered. The geometry and boundary conditions are illustrated in Figure 6.9. The ratio between the diameter  $d$  and the length  $l$  of the bar is  $d/l = 1/10$ .

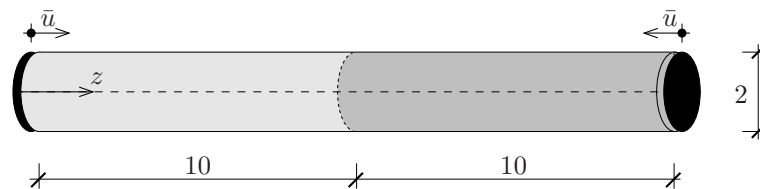


**Figure 6.9:** Buckling of a circular bar: Geometry and boundary conditions. All dimensions are given in [mm]. Exploiting symmetry only half of the specimen is discretized.

Exploiting symmetry, only one half of the bar has to be investigated. Consequently, at the middle plane of the entire specimen symmetry boundary conditions are enforced which permit motion in lateral direction. The upper end of half the system is clamped. Within a deformation-driven process an axial displacement of the top surface is applied within

52 increments  $\Delta\bar{u} = 0.1$  mm up to a maximum of  $\bar{u} = 5.2$  mm corresponding to a deformation of 52% of the original height. The longitudinal axis of the bar is slightly off-center by an angle of  $0.57^\circ$  with respect to the  $z$ -axis. This prescribed horizontal deflection of the middle of the entire bar serves as a geometric perturbation and basically induces the particular buckling-type shape of the deformed structure. For the analysis the following material parameters were chosen:  $\mu = 100.0$  kN/mm<sup>2</sup> and  $\beta = 0.667$  corresponding to  $\nu = 0.2$ . The primary triangulation of the upper half of the bar used for the adaptive analysis is depicted in Figure 6.10a). This initial mesh consists of 164 ten-noded tetrahedron

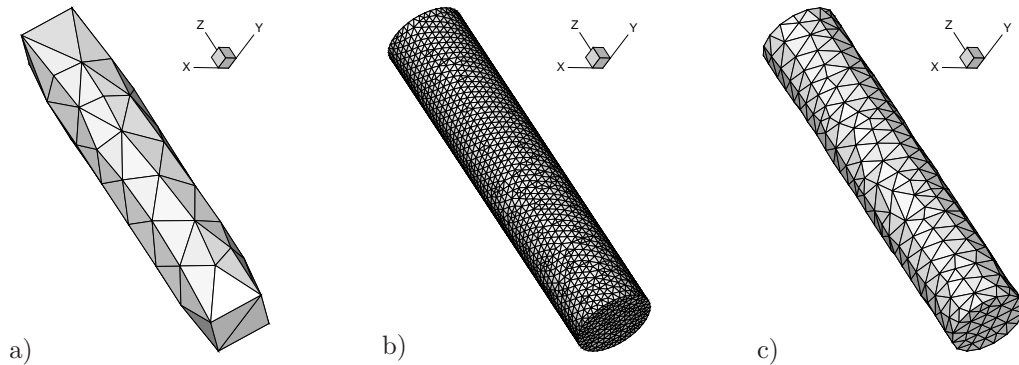


**Figure 6.10:** a) Initial mesh for adaptive simulation containing 164 elements, 345 nodes. b) Fine mesh with 39855 elements, 58278 nodes, c) coarse mesh holding 2254 elements, 3743 nodes. Only that part of the specimen is shown which has been used for the computations.

elements resulting in 345 nodes. In addition, Figure 6.10b) and c) show the triangulation used for the benchmark analyses to be considered below.

**Remark 6.2:** Observe that the software package utilized for the visualization of the simulation data is only capable of displaying linear finite element interpolations. As a matter of course, the CAE-model of the bar considers the real cylindrical shape of the structure. Hence, the rough even though weird topology that appears especially in Figure 6.10a) is exclusively a result of that drawback of the software tool. However, one should recognize that even for the case that higher-order interpolation functions could be treated, the real structure of the bar still would be approximated by a combination of piecewise linear polygons as the curvature of the outer shape of the body is exclusively available within the CAE-model.

The development of both the deformation of the system as well as the evolution of the adaptively refined mesh during the analysis is shown in Figure 6.11. To be precise, the structure at a deformation of 3%, 11%, 18%, 25%, 39% and for the the final deformation state at 52% are exemplarily depicted. Initiated by the slight perturbation of the geometry a deformed structure evolves which displays a typical buckling-mode shape. Obviously, this is accompanied with large elastic deformations. The local mesh refinement is well observable. In the areas of high tension and pressure, that are sections of maximum curvature, the mesh is significantly finer than in the areas between those points. For the whole bar under consideration, this refinement results in three regions with high element density characterized by small element edge lengths  $h$ . These zones are at the top and the bottom as well as in the middle of the bar. In contrast, in the two regions in-between the mesh remains relatively coarse. Starting from the primary triangulation with just 164 tetrahedrons, the development of the mesh refinement passes the states of 242, 393, 1552, 3797, 6930 and 10500 elements and reaches its maximum at 17930 elements. This coin-



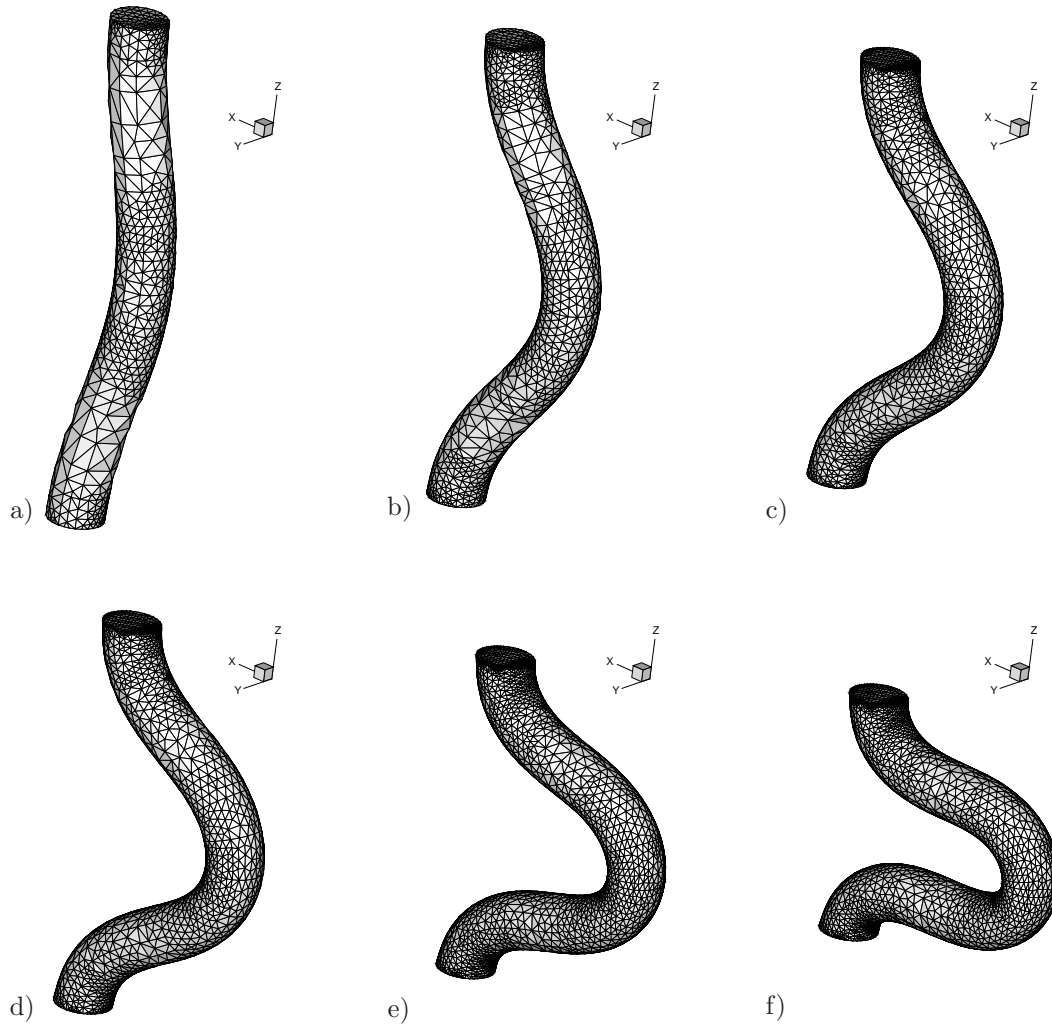


**Figure 6.11:** Evolution of mesh during adaptive analysis. The whole bar is obtained by mirroring at the  $xy$ -plane. a) Mesh with 6105 nodes at 3%, b) 10779 nodes at 11%, c), d) 16164 nodes at 18% and 25%, and e), f) 26877 nodes at 39% and 52% deformation.

cides with a number of 26877 nodes or, respectively, 78030 degrees of freedom.

The adaptive procedure is controlled by the global criterion  $\eta$ . The evolution of this relative quantity versus the deformation of the top surface is presented in Figure 6.12. The admissible value was set to  $\eta_{perm} = 4.0\%$  and is depicted by the straight line. Whenever the global criterion violates the permissible value the current analysis is discarded. The geometry is remeshed with a more accurate mesh at those locations where the local element criterion demands mesh refinement. Subsequently, the same load, or rather incremental deformation step has to be re-computed in order to obtain spatial equilibrium. This procedure recurs until the global criterion falls below the admissible threshold. Then, the load level is increased in the sense that the next increment of deformation is applied. Considering the diagram in detail, it turns out that the solution of the first deformation step is accepted whereas the solution of the second and third increment violate the global criterion. This holds in particular for the latter one which necessitates three refinement steps until the mesh is assessed to be appropriate. After a vertical displacement of the top surface of about 4%, remeshing has to be done less frequently. To be precise, to two more

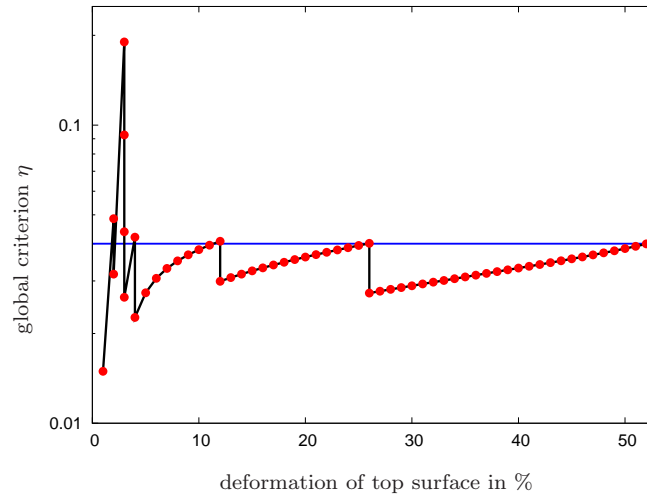


**Figure 6.12:** Buckling of a circular bar: Evolution of global criterion versus deformation. If the global criterion  $\eta$  violates the permitted value  $\eta_{perm} = 4\%$  mesh refinement is applied and the same deformation increment is computed until  $\eta$  falls below the admissible value.

refinement steps have to be performed at 12% and 26% deformation. For the final time step corresponding to 52% deformation, the global criterion reaches a value of  $\eta \approx 3.9\%$  which is still somewhat below the admissible threshold.

In the next step, the change of the discrete material nodal forces prior and subsequent to a remeshing event is discussed. In Figure 6.13 half of the bar is presented at a defor-

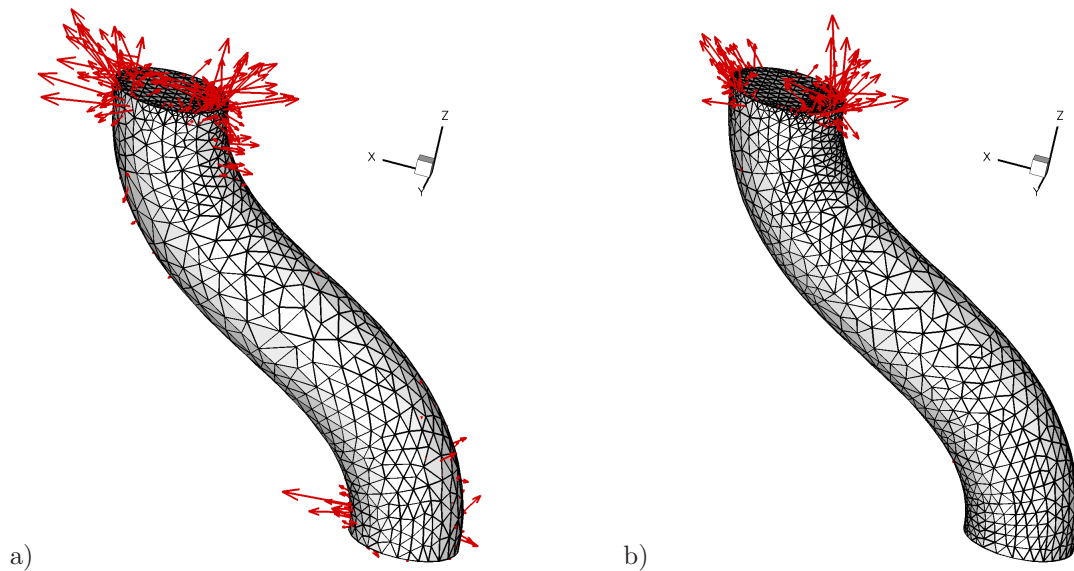


**Figure 6.13:** Material nodal forces at vertical displacement of 2.6 mm a) prior to and b) after refinement. Discarded mesh possessed 16164 nodes, new triangulation holds 26877 nodes. Energetic misfit decreases from  $\Delta\Pi = 1.532$  N to  $\Delta\Pi = 1.04$  N, i.e. a reduction of more than 30%. Boundary forces have been omitted as they do not contribute to the global criterion.

mation state of 26%. The mesh shown in Figure 6.13a) consists of 10500 elements and 16164 nodes. In the Figure the out of balance configurational nodal forces are presented which appear at the interior nodes of the mesh due to an insufficient triangulation. Note that the boundary forces do not contribute to the global criterion and have therefore been



omitted. Furthermore, for the sake of a better visualization the specimen is shaded by what, however, the comparatively smaller forces are blinded out. What remains visible are those forces that penetrate the shading. Thereby their magnitude is scaled by factor 750 which clearly demonstrates that they are undoubtedly numerically caused and therefore spurious in nature. Concentrations of material forces occur at the points of maximum curvature above all in the region around the top surface. The energetic misfit of the triangulation, i.e. the sum of the magnitude of all the material nodal forces, is evaluated by  $\Delta\Pi = 1.53$  N. Taking into account the elastically stored energy  $\Pi^{elast} = 38.184$ , the global relative criterion is  $\eta = \Delta\Pi/\Pi^{elast} = 0.040134$  Nm violating the admissible criterion  $\eta_{perm} = 4\%$ . Consequently, mesh refinement is required. The adaptively refined mesh which is constructed in terms of the local configurational-force-based element criterion  $\xi^e$  contains 17930 elements and 26877 nodes. The same deformation step is computed for this new mesh whereupon once more the configurational nodal forces are computed. They are visualized in Figure 6.13b). A considerable decrease of those forces compared to the discarded mesh is very well observable. The same scaling by factor 750 is adopted. Around the top surface a concentration of material forces still remains which nevertheless is conspicuously reduced. Focusing attention to the middle section of the bar, which apparently coincides to the lower part of the analyzed half of the system, they even vanished in total. The resulting energetic misfit is given by  $\Delta\Pi = 1.04$  N corresponding to a reduction of more than 30%. This effect is accompanied by a slight decrease in the elastic energy down to  $\Pi^{elast} = 38.06$  Nm. Based on these values, the global criterion is estimated by  $\eta = 0.027325$  and falls below the permissible value  $\eta_{perm} = 4\%$ . Thus, the new mesh is said to be sufficiently accurate and therefore appropriate for the current deformation step. Hence, the next displacement increment can be applied.

Finally, in order to quantify the performance of the adaptive simulation by means of a comparative study two benchmark analyses were accomplished. The respective triangu-

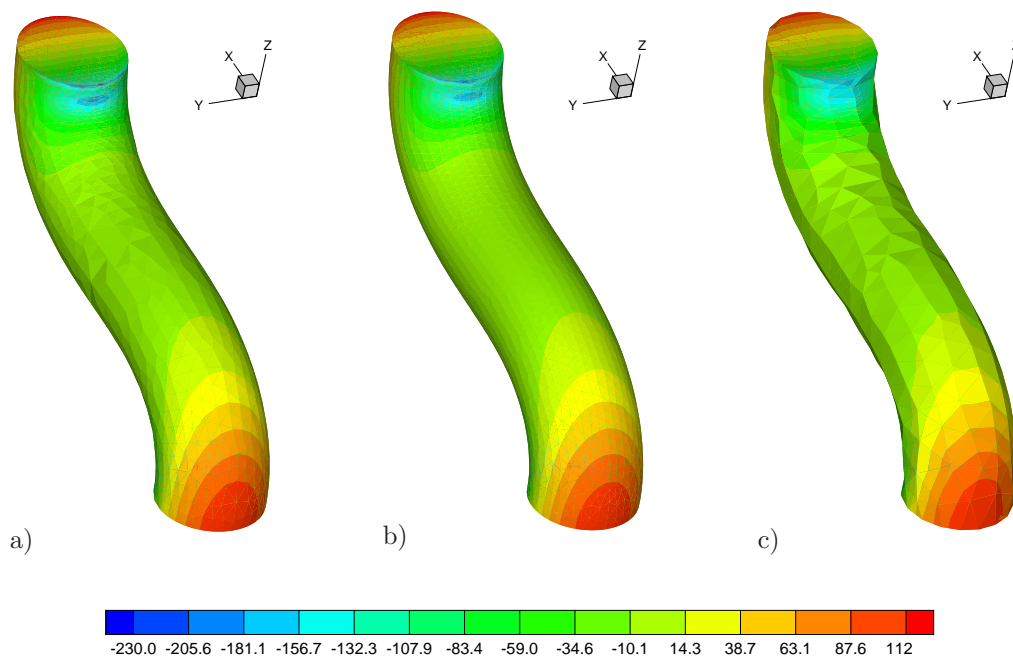


**Figure 6.14:** Contour plot of the distribution of stress-component  $\sigma_{zz}$  for the final deformation step at a vertical top surface displacement of 5.2 mm corresponding to 52%. a) Adaptive mesh, b) fine mesh and c) coarse mesh.

lations are shown in Figure 6.10b), c). The fine mesh contains 39855 elements and 58278 nodes whereas the coarse mesh consists of 2254 elements and 3743 nodes. Figure 6.14 visualizes the distribution of the normal stresses  $\sigma_{zz}$  obtained for the final deformation of 52%. Again, only half of the bar is considered. In the region close to the top surface the negative  $\sigma_{zz}$  stress gained from the coarse mesh solution, Figure 6.14c), significantly differs from the results of the fine mesh simulation shown in Figure 6.14b). Apparently, the coarse mesh is not capable of resolving the critical area. In contrast, the adaptive simulation, Figure 6.14a), deals with a stress distribution that is in very good agreement to the fine mesh as the refined mesh provides an appropriate resolution of the zone under consideration. These characteristics are also highlighted when comparing the overall minimum and maximum stresses  $\sigma_{zz}$  of the three different simulations. In view of the negative range the fine mesh computation ends up with  $\sigma_{zz}^{min} = -228.0$  N/mm<sup>2</sup> while the adaptive solution renders  $\sigma_{zz}^{min} = -240.0$  N/mm<sup>2</sup>. Thus, the difference is about  $\approx 5\%$ . On the contrary, the minimum stress obtained from the coarse mesh simulation is  $\sigma_{zz}^{min} = -203.0$  N/mm<sup>2</sup> and therefore more than 10% lower than the fine mesh benchmark. The same behavior occurs for the maximum values. While the fine mesh and the adaptive solution nearly coincide, i.e.  $\sigma_{zz}^{max} = 123.4 \approx 124.36$  N/mm<sup>2</sup>, the coarse mesh result,  $\sigma_{zz}^{max} = 112.44$  N/mm<sup>2</sup>, deviates by almost 9%. Note that the absolute values of the adaptive solution are higher than those obtained from the fine mesh computation but the coarse mesh results are significantly smaller.

## 6.5. Application to Finite $J_2$ -type Thermo-Plasticity

Within the investigations to follow the configurational-force-based  $h$ -adaptive strategy is applied to quasi-static problems of isothermal and non-isothermal plasticity. After an explanation of some basic aspects of the numerical implementation the adaptive procedure is combined with different constitutive approaches to finite  $J_2$ -type plasticity and utilized for two- and three-dimensional analyses in order to demonstrate its versatility. Within the respective subsections some remarks on the constitutive framework are given whereupon the results of the finite element simulations are discussed in detail. For each example two benchmark computations have been performed which allow for an appraisal of the capability of the proposed method.

**6.5.1. General Remarks.** The basic equations of the material-force-based refinement strategy in the quasi-static context have been introduced at full length in Section 6.2 for the general framework of non-isothermal inelasticity. Hence, they are easily adjusted to the particular model problems which deal with the isothermal setting just by dropping the dependence on the material gradient of the temperature field,  $\theta = const.$ , i.e.  $\nabla_x \theta = \mathbf{0}$ . Nevertheless, one slight modification concerns the relative global criterion (6.6) which is enhanced by an averaging of the global misfit  $\Delta\Pi$  with respect to the number  $n_{int}$  of interior nodes

$$\eta = \frac{\Delta\Pi/n_{int}}{\Pi^{elast}}. \quad (6.22)$$

This averaging has proven to be appropriate due to the following reasoning. For inelastic problems, the evaluation of the discrete material nodal forces induces an additional inaccuracy via the application of the projection algorithm for the internal variable field. In adverse circumstances, this effect can cause an increase of the energetic misfit  $\Delta\Pi$  upon mesh refinement due to an increase of the number of nodal points in turn affecting the

projection procedure. The scaling of the global criterion by the number of interior nodes counteracts this characteristic and ensures convergence of the adaptive refinement procedure as it guarantees a decrease of the global criterion. An additional refinement step is performed irrespective of the value of the global criterion. The process recurs until a global criterion below the permissible value is found that is accompanied by a reduced energetic misfit. In this way, a decrease of the misfit  $\Delta\Pi$  from its primary value obtained from the first discarded mesh up to its magnitude evaluated in terms of the finally accepted mesh is enforced during the simulations. Note furthermore that the influence of the additional inaccuracy originating from the smoothing procedure results in a range of the energetic misfit which is a priori larger compared to that obtained in purely elastic simulations. The scaling brings the range of the global criterion close to that obtained for the elastic case. Finally, the notation  $\Pi^{elast}$  for the reference value of the global criterion is still convenient as solely the elastic part  $\psi^{elast}$  of the free energy function is used for its evaluation.

To set up the global and local refinement criteria (6.22) and (6.7) the evaluation of the discrete configurational nodal forces is required. They depend on the material gradients  $\nabla_{\mathbf{x}}\theta$  of the temperature field and  $\nabla_{\mathbf{x}}\mathcal{I}$  of the internal variable vector. The treatment of the first contribution is readily done as the temperature field  $\theta$  acts as a primary variable of the thermo-mechanically coupled problem. With regard to the internal variable field the methodology is as follows. For the different constitutive models to be introduced below the internal variable vector  $\mathcal{I}$  consists of a second order tensorial object related to a plastic strain measure and a scalar hardening variable. The computation of the respective gradient by means of a global approach appears inappropriate as a full discretization of  $\mathcal{I}$  would be necessary because both the amount and the direction of the evolution of the internal variables are non-constant in general, cf. Section 3.5.1. Hence the local formulation, see Chapter 3.5.2, is adopted which has proven to be sufficiently accurate and numerically much cheaper.

For inelastic problems one further crucial point has to be considered in more detail. In addition to the standard nodal variables, i.e. for the quasi-static case the spatial displacements and the temperature, the history data of the last accepted mesh needs to be transferred to the new mesh. To this end, in a first step the history field is projected from the integration points onto the nodal points. However, this projection has already been performed to evaluate the discrete configurational nodal forces. Consequently, no additional numerical effort arises within the whole procedure. Once the history variables are available at the nodal points they can be mapped in exactly the same manner as the standard nodal fields, see Section 6.3.2. After this transfer the history variables are provided at the nodal points of the new mesh and therefore have to be evaluated at the integration points. This is achieved by application of the standard finite element approach

$$\mathcal{I}_l^e = \sum_{I=1}^{n^e} N_I(\xi_l) \tilde{\mathcal{I}}_I \quad (6.23)$$

at each integration point of every single element. Here,  $\tilde{\mathcal{I}}_I$  denotes the nodal history and  $\mathcal{I}_l^e$  refers to the history field at integration point  $l$  of the current element  $e$ .

**6.5.2. Numerical Example: Plate with a Circular Hole.** Within this section the two-dimensional scenario is highlighted. Some aspects concerning the constitutive model are given. Subsequently, a representative boundary value problem is analyzed in detail.

**6.5.2.1. Material model of finite  $J_2$ -type elasto-plasticity.** The first constitutive model to be combined with the material-force-based adaptive strategy goes back to the work of SIMO & MIEHE [164], see also SIMO [160] and MIEHE [121].

Starting with the geometric setting, the fundamental approach to finite strain plasticity is the multiplicative decomposition of the deformation gradient into an elastic and a plastic part,  $\mathbf{F} = \mathbf{F}^e \mathbf{F}^p$ , cf. (3.95). Based on the metric  $\bar{\mathbf{G}}$  of the intermediate configuration the Eulerian elastic Finger tensor is defined by

$$\mathbf{b}^e := \mathbf{F}^e \bar{\mathbf{G}}^{-1} \mathbf{F}^{eT} = \mathbf{F} \mathbf{C}^{p-1} \mathbf{F}^T \quad \text{with} \quad \mathbf{C}^p = \mathbf{F}^{pT} \bar{\mathbf{G}} \mathbf{F}^p, \quad (6.24)$$

cf. Figure 3.8 in Section 3.6.1. The formulation to follow bases on the alternative representation as the push-forward of the right plastic Cauchy-Green tensor  $\mathbf{C}^{p-1}$  to be used as an internal variable field. The spectral representation of the elastic Finger tensor induces the definition of the logarithmic elastic stretches  $\varepsilon_{i,i=1,2,3}^e$

$$\mathbf{b}^e = \sum_{i=1}^3 \lambda_i^2 \mathbf{n}^i \otimes \mathbf{n}^i \quad \text{and} \quad \varepsilon_i^e := \frac{1}{2} \ln [\lambda_i^2] = \ln [\lambda_i] \quad (6.25)$$

where  $\lambda_{i,i=1,2,3}$  denote the elastic principal stretches and  $\mathbf{n}_{i,i=1,2,3}^i$  the Eulerian eigenvectors. The logarithmic stretches are split up into a volumetric contribution related to the Jacobian  $J^e$  of the elastic part of the deformation gradient and an isochoric part  $\tilde{\varepsilon}_{i,i=1,2,3}^e$

$$\ln J^e := \sum_{j=1}^3 \varepsilon_j^e = \ln [\lambda_1 \lambda_2 \lambda_3], \quad \tilde{\varepsilon}_i^e := \varepsilon_i^e - \frac{1}{3} \ln J^e. \quad (6.26)$$

Enforcing the plastic incompressibility condition, i.e.  $J^p := \det \mathbf{F}^p = 1$ , the volumetric part is governed by the determinant of the deformation gradient,  $\ln J^e = \ln J$ . A Hencky-type free energy function is chosen consisting of an elastic contribution depending in a decoupled volumetric-isochoric fashion on the logarithmic stretches and a non-linear hardening contribution in terms of the scalar hardening variable  $A$

$$\psi = \frac{1}{2} \kappa \ln^2 J + \mu \sum_{i=1}^3 [\tilde{\varepsilon}_i^e]^2 + \frac{1}{2} h A^2 + (y_\infty - y_0) \left( A + \frac{1}{\omega} (\exp[-\omega A] - 1) \right). \quad (6.27)$$

The material parameters are specified in Table 6.1 below. The yield criterion function is defined in terms of the principal stresses  $\sigma_{i,i=1,2,3}$ , i.e. the eigenvalues of the mixed-variant Eulerian stresses  $\mathbf{g}\boldsymbol{\tau} = \mathbf{J}\mathbf{g}\boldsymbol{\sigma}$ . As the von-Mises-type plasticity model assumes incompressible purely isochoric plastic flow, the yield criterion function only depends on the deviatoric principal stresses  $\tilde{\sigma}_{i,i=1,2,3}$

$$\phi = \sqrt{\sum_{i=1}^3 [\tilde{\sigma}_i]^2} - \sqrt{\frac{2}{3}} (y_0 - B) \quad \text{with} \quad B = -\partial_A \psi. \quad (6.28)$$

The specific representation of the constitutive functions based on the logarithmic elastic stretches allows for the application of a return mapping scheme that completely preserves the structures of the infinitesimal theory.

With regard to the evaluation of the discrete configurational nodal forces and the mapping of the history data, the internal variable vector consists of the inverse right plastic Cauchy-Green tensor and the scalar hardening variable, i.e.  $\boldsymbol{\mathcal{I}} = [\mathbf{C}^{p-1}, A]^T$ . Exploiting symmetry, for the two-dimensional case in total four scalar variables have to be accounted for, namely the 11-, 22-, and 12-components of the plastic deformation measure  $\mathbf{C}^{p-1}$  and the hardening variable  $A$ .

**6.5.2.2. Discussion of boundary value problem.** In extension to the analyses in the purely elastic context in Section 6.4.3, the plate with a circular hole is investigated now within the framework of elasto-plasticity. A sketch of the system and boundary conditions has already been provided in Figure 6.5. The material parameters are summarized in Table 6.1. By prescribing incremental displacements  $\bar{u}$  at the top edge the body is deformed

**Table 6.1:** Material parameters of elasto-plastic specimens

bulk modulus	$\kappa$	164.206	kN/mm <sup>2</sup>
shear modulus	$\mu$	80.1938	kN/mm <sup>2</sup>
initial yield stress	$y_0$	0.45	kN/mm <sup>2</sup>
infinite yield stress	$y_\infty$	0.715	kN/mm <sup>2</sup>
hardening modulus	$h$	0.12924	kN/mm <sup>2</sup>
saturation parameter	$\omega$	16.93	–

up to a maximum state of 12% of the original height which coincides with a total displacement of  $\bar{u} = 0.6$  mm. The deformation is applied by 48 increments of  $\Delta\bar{u} = 0.0125$  mm. Due to symmetry only a quarter of the specimen is discretized, cf. Figure 6.15. The  $h$ -

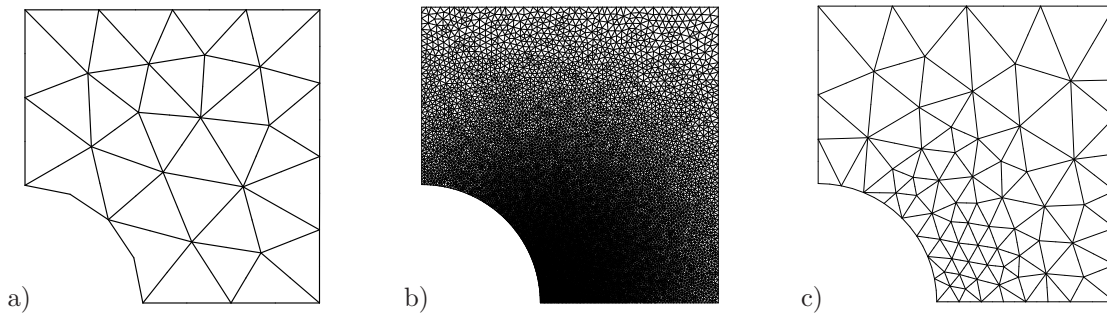


**Figure 6.15:** a) Initial mesh of the adaptive simulation containing 36 elements. b) Fine mesh with 21831 elements and f) coarse mesh with 129 elements.

adaptive simulation starts with a primary mesh with 36 six-noded triangular elements corresponding to 87 nodes or 155 degrees of freedom.

The procedure of adaptive mesh refinement during the deformation process is documented in Figure 6.16. The development of the relative global criterion is plotted versus the deformation of the top edge. The deformation is increased up to that point when the global criterion violates the permitted threshold  $\eta_{perm} = 1.0\%$ . Then, the accuracy of the underlying triangulation is said to be insufficient and refinement is required. After the generation of the new mesh the same deformation step is solved again in order to obtain an equilibrium state. Afterwards the global criterion is evaluated again for the new mesh. For the particular example at hand, in total seven refinement procedures are necessary. After the respective refinement, the global criterion falls below the permitted threshold and the next time step is to be solved. Only in the first refinement process a second refinement step is required.

The evolution of the mesh during the deformation can be observed in Figure 6.17 where the triangulation is depicted for 4%, 8% and 12% deformation with respect to the original height. The mesh is heavily densified along the lower segment of the circle and in addition in a broad band towards the right vertical edge. This characteristic follows the hardening



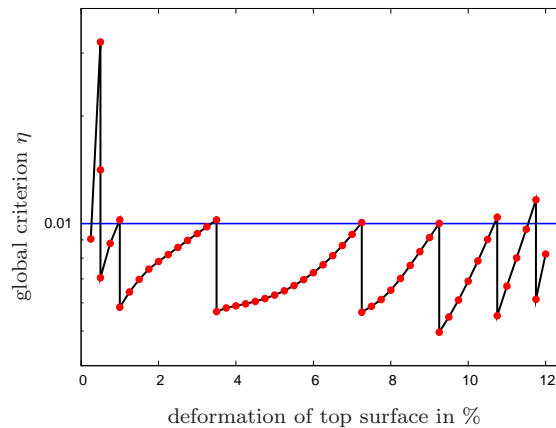


**Figure 6.16:** Disc with circular hole: Evolution of relative global criterion versus deformation. Permitted threshold  $\eta_{perm} = 1\%$  is plotted as straight line.

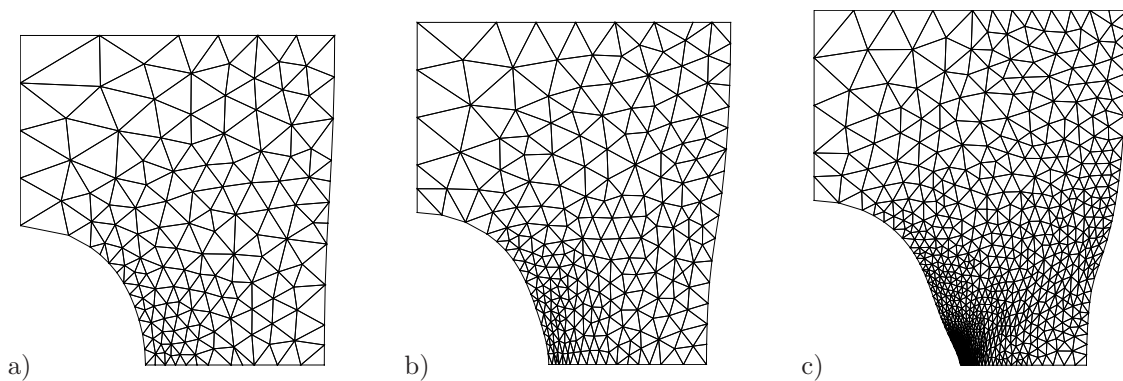


**Figure 6.17:** Deformed meshes at a) 4% b) 8% and c) 12% deformation corresponding to a top edge displacement of  $\bar{u} = 0.2, 0.4, 0.6$  mm. The final mesh consists of 1371 elements.

variable  $A$  which will be discussed below, see Figure 6.19. In contrast the upper left corner remains almost unrefined.

The  $h$ -adaptive refinement process is carried out by remeshing of the entire domain in terms of a density function  $\varphi$ . It is computed from the element criterion  $\xi^e$  which in turn is governed by the non-vanishing numerically caused configurational nodal forces. A three-dimensional contour plot of this density function is visualized in Figure 6.18 for the very last refinement step. The maximum element criterion causes a density function  $\varphi = 0$  whereupon the maximum refinement is applied. On the contrary, for  $\varphi = 1$  no refinement is employed. The resulting mesh is plotted underneath and contains 1371 elements which corresponds to 2852 nodes and 5585 nodal degrees of freedom.

In addition to the adaptive simulation a fine and a coarse mesh solution are presented. By means of a comparison between the results of the different approaches the capability of the proposed adaptive procedure will be demonstrated. The fine mesh contains 21831 elements and 44016 nodes whereas the coarse mesh consists of 129 elements and 288 nodes, see Figure 6.15b), c). In both cases the region around the lower segment of the circle is a priori refined. The distribution of the scalar internal hardening variable  $A$  is illustrated in Figure 6.19. Obviously, the results of the adaptive and fine mesh simulation are very similar. Having a look at the distribution of  $A$ , the maximum value occurs at the lower left corner at the intersection of circle and middle axis. Then, the plastic zone evolves towards the right vertical edge. Comparing the maximum values of  $A$ , the fine mesh solution yields

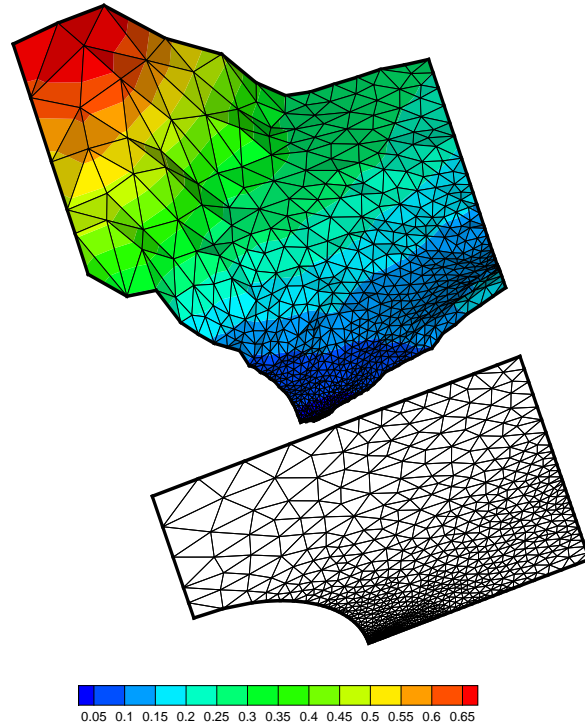


**Figure 6.18:** Density function  $\varphi$  of the last refinement step. For  $\varphi = 1$  no refinement occurs, for  $\varphi = 0$  maximum refinement is applied. The resulting mesh is plotted underneath.

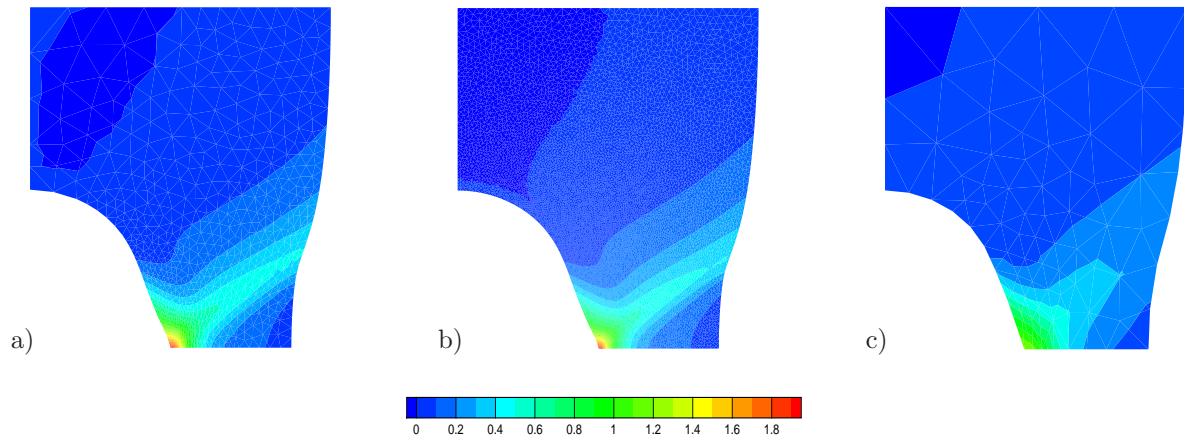


**Figure 6.19:** Distribution of scalar internal hardening variable  $A$  for a) the adaptive approach, b) the fine and c) the coarse mesh solution. Plastic deformation concentrates at the lower segment of the circle and evolves in a band towards the right vertical edge of the body.

$A = 1.8362$  whereas the adaptive strategy ends up with  $A = 1.8126$  corresponding to a deviation of just 1%. In contrast, the coarse mesh is not able to resolve the concentration of plastic deformation at the respective corner. Thus the maximum value  $A = 1.1937$  differs dramatically by more than 30% from the other solutions.

These characteristics also arise when comparing the structural response of the elasto-plastic plate by considering the contraction of the middle axis of the specimen, Figure 6.20a). The contraction is defined by the ratio between current width  $l$  and reference width  $l_0$  of the middle axis of the entire specimen, i.e. the lower edge of the quarter of the plate. Up to a deformation of about 9%, corresponding to a displacement of the top edge of  $\approx 0.45$  mm the response of the plate is almost identical for all the three approaches. After



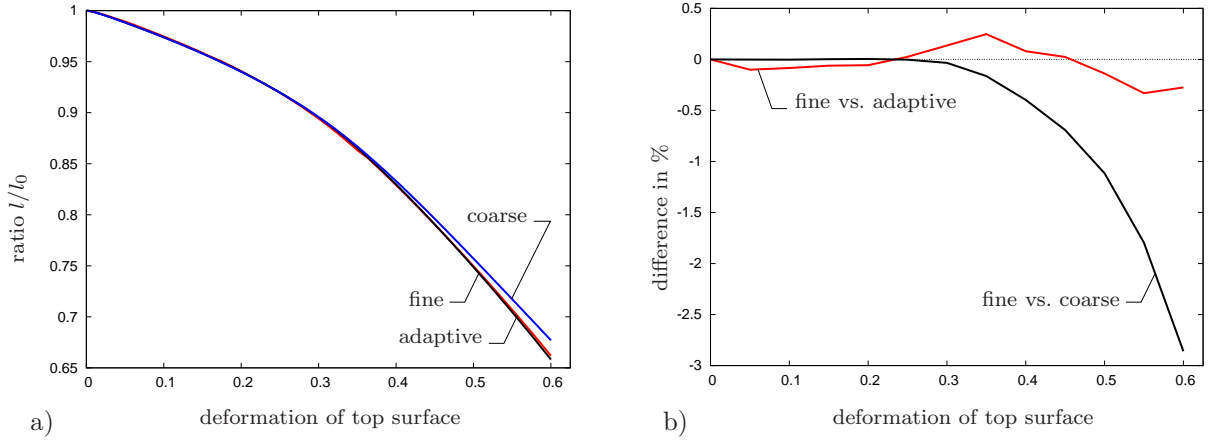


**Figure 6.20:** Disc with circular hole: a) Contraction of middle axis in terms of ratio between current width  $l$  and reference width  $l_0$  versus deformation. b) Deviation between adaptive and fine mesh solution as well as deviation between adaptive and coarse mesh solution.

that, the adaptive and fine mesh solution further on render a similar response whereas the coarse mesh solution deviates. Hereby, the response of the coarse mesh is stiffer which originates from the fact that the plastic deformation does not evolve by the same magnitude as it does for the other two simulations. This observation can be visualized by evaluating the deviation between fine mesh and adaptive solution on the one hand and the fine and coarse mesh solution on the other hand as it is done in Figure 6.20b).

Consequently, also within the framework of inelasticity the results of the adaptive simulation are very close to the fine mesh solution which clearly demonstrates the capability of the proposed procedure.

**6.5.3. Numerical Example: Necking of an Axisymmetric Bar.** The objective of the subsequent treatments is to generalize the investigations to non-isothermal inelasticity. The  $J_2$ -type plasticity model is extended to the non-isothermal case. Afterwards the whole scenario is applied to a boundary value problem.

**6.5.3.1. Extension of material model to thermo-plasticity.** In view of the solution of thermo-mechanically coupled problems the constitutive equations are enhanced by a dependence on the temperature field  $\theta$ . The modified free energy function reads

$$\begin{aligned} \psi = & \frac{1}{2} \kappa \ln^2 J - \kappa \alpha \ln J(\theta - \theta_0) + c(\theta - \theta_0 - \theta \ln \frac{\theta}{\theta_0}) + \mu \sum_{i=1}^3 [\tilde{\varepsilon}_i^e]^2 \\ & + \left[ (y_\infty - y_0) \left( A + \frac{1}{\omega} (\exp(-\omega A) - 1) \right) + \frac{1}{2} h A^2 \right] (1 - w(\theta - \theta_0)). \end{aligned} \quad (6.29)$$

For the denotation of the material parameters see Table 6.2. In addition, the temperature field enters the yield criterion function

$$\phi = \sqrt{\sum_{i=1}^3 [\tilde{\sigma}_i]^2} - \sqrt{\frac{2}{3}} \left[ y_0 (1 - w_0(\theta - \theta_0)) - B \right]. \quad (6.30)$$

The temperature induced softening effects characterized by the factors  $(1 - w_0(\theta - \theta_0))$  and  $(1 - w(\theta - \theta_0))$  are denoted flow stress softening and hardening softening, respectively. The parameters  $w$  and  $w_0$  can be chosen independently from each other.

Obviously, the constitutive model incorporates the same internal variable vector  $\mathcal{I}$  as

the isothermal formulation does. The only modification concerning the evaluation of the discrete configurational forces is such, that the gradient of the temperature field has to be taken into account.

**6.5.3.2. Discussion of boundary value problem.** In this example the necking of a bar is investigated. For the time being the particular symmetry of a bar is exploited which results in an axisymmetric simulation. In Figure 6.21 the system is depicted. The

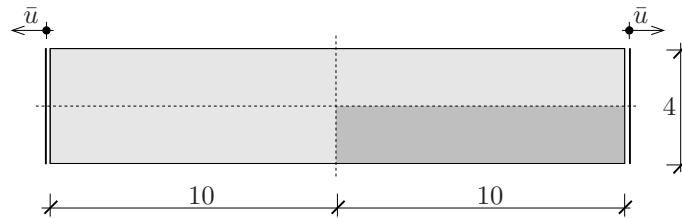


**Figure 6.21:** System and boundary conditions of axisymmetric necking. All dimensions are given in [mm]. Due to symmetry only a quarter of the specimen is discretized.

ratio between length and, say, radius of the entire specimen is  $l/r = 10/1$ . The necking phenomenon is initiated by a reduction of the radius of the middle axis -or plane- of the body to 1.9 mm corresponding to a decrease of 5% compared to the original value. Within a deformation-driven process the bar is elongated up to a total displacement of 2.16 mm which coincides with a deformation of 21.6% of the original height. To be specific, 216 increments  $\Delta\bar{u} = 0.01$  mm are used. In view of the thermal problem, the adiabatic case is assumed. Exploiting symmetry of the two-dimensional geometry, only a quarter of the specimen is investigated, see Figure 6.22a). The system is discretized with six-noded quadratic triangles. In particular, for both subproblems, i.e. the spatial deformation and the temperature evolution, the same interpolation functions have been chosen. The primary mesh used for the adaptive simulation is shown in 6.22b). It contains 138 elements and 317 nodes. For the sake of comparison, two benchmark solutions are performed. Fig-

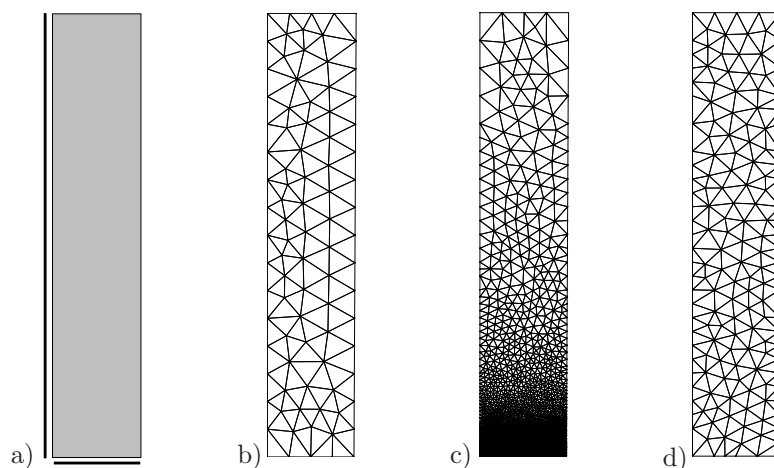


**Figure 6.22:** a) Quarter of the system together with displacement boundary used for the numerical simulation. b) Undeformed bar with primary triangulation of 138 triangular elements. c) Fine mesh with 10964 elements and d) coarse mesh with 251 elements.

ure 6.22c), d) show the respective meshes used for these analyses. The fine mesh holds 10964 elements and 22347 nodes which corresponds to 66362 nodal degrees of freedom

whereas the coarse mesh contains 251 elements and 566 nodes which results in 1621 unknowns. The material parameters are summarized in Table 6.2.

With regard to the progression of the adaptive refinement procedure in Figure 6.23 the

**Table 6.2:** Material parameters of elastoplastic specimens

bulk modulus	$\kappa$	164.206	kN/mm <sup>2</sup>
shear modulus	$\mu$	80.1938	kN/mm <sup>2</sup>
initial yield stress	$y_0$	0.45	kN/mm <sup>2</sup>
infinite yield stress	$y_\infty$	0.715	kN/mm <sup>2</sup>
hardening modulus	$h$	0.12924	kN/mm <sup>2</sup>
saturation parameter	$\omega$	16.93	–
thermal expansion coefficient	$\alpha$	$1 \cdot 10^{-5}$	1/K
conductivity	$k$	0.045	1/K
reference temperature	$\theta_0$	293.0	K
heat capacity	$c$	$3.558 \cdot 10^{-3}$	kN/(s·K)
hardening softening	$w$	0.0002	1/K
flow stress softening	$w_0$	0.0002	1/K

evolution of the relative global criterion  $\eta$  versus the deformation of the top edge is presented. The permitted threshold  $\eta_{perm} = 7.5\%$  is plotted as a straight line. Note that

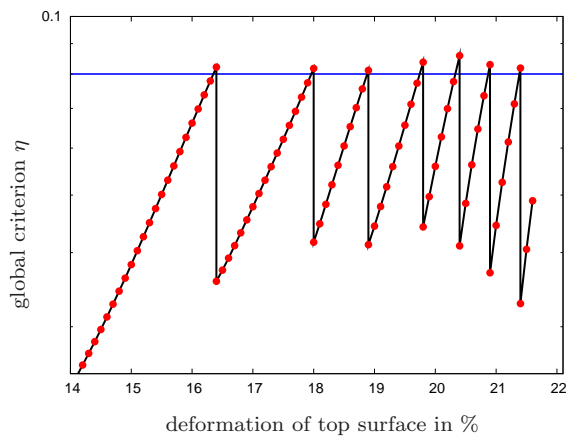


**Figure 6.23:** Necking of an axisymmetric bar: Global criterion versus deformation. Plot starts at  $\approx 14.0\%$  deformation. Permitted criterion  $\eta_{perm} = 7.5\%$  is plotted as straight line.

only the last 7.5% of deformation are depicted because before that state no adaptive step occurs for the particular choice of the permitted criterion. The global criterion and thus the inaccuracy of the mesh is assessed in terms of the numerically caused configurational node point forces at the interior nodes. It increases during ongoing deformation. In case the permitted threshold is violated refinement is required. Afterwards the same time step is computed again in order to achieve equilibrium. In total seven refinement steps have been performed.

In Figure 6.24 different deformation states are shown including the respective triangulation. For a clear visualization of the necking progress the entire domain is plotted. Nevertheless, the following data refer to a quarter of the specimen used for the computation. First, the system at a deformation of 18.6% is depicted. The mesh consists of 306

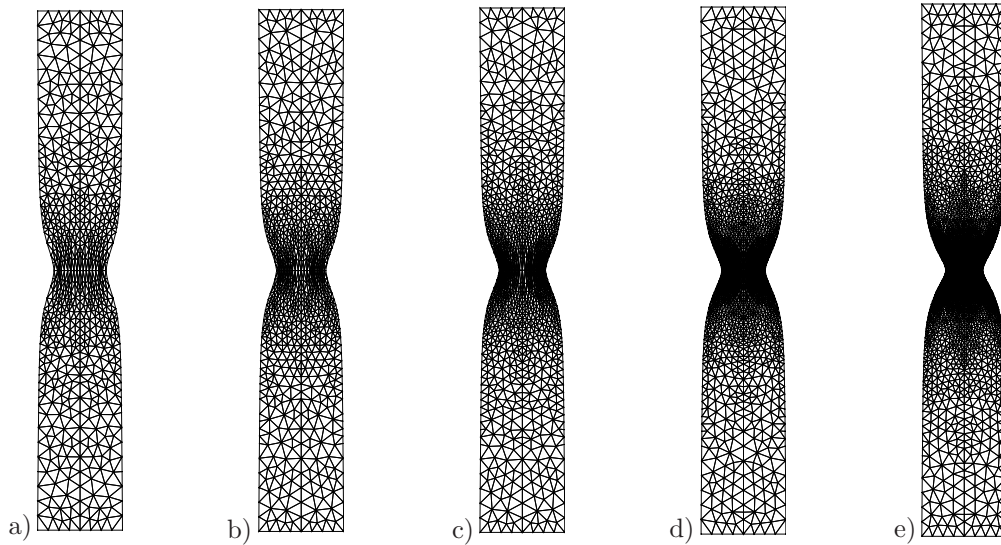


**Figure 6.24:** Visualization of adaptive mesh refinement. Intermediate states at a) 18.6%, b) 19.2%, c) 19.8%, and d) 20.4% deformation. e) Final mesh containing 4x1547 elements at  $\bar{u} = 2.16$  mm corresponding to 21.6% deformation.

elements. In the sequel deformation states of 19.2%, 19.8%, 20.4% and the final state of 21.6% deformation are presented, containing 402, 553, 768 and 1547 elements, respectively. The final triangulation corresponds to 3244 nodes and 9539 degrees of freedom. At the very beginning the mesh refinement takes place in that zone of the system that exhibits the maximum shear stress just a bit above the middle axis. This effect appears in a more distinct manner within the three-dimensional analysis to follow in the next example. For ongoing deformation the plastic deformation concentrates in the necking zone at the middle of the bar and therefore the mesh is densified in this region. In contrast, the element sizes in the upper and lower parts of the body remain almost unchanged. In the last step, the results of the adaptive computation are compared with those obtained from the fine and the coarse meshes, cf. Figure 6.22c), d). To this end, Figure 6.25 displays the distribution of the change  $\Delta\theta$  in the temperature gained from the different analyses. All the results turn out to be similar. In view of the minimum and maximum values the fine mesh, Figure 6.25b), ends up with  $\Delta\theta_{min} = 12.994$  K and  $\Delta\theta_{max} = 40.094$  K whereas the adaptive simulation, Figure 6.25a), yields  $\Delta\theta_{min} = 13.018$  K and  $\Delta\theta_{max} = 41.879$  K. Thus the deviation is less than 4.5%. The results of the coarse mesh simulation, Figure 6.25c), are just in-between.

This characteristic dramatically changes when comparing the distribution of the scalar internal hardening variable  $A$  visualized in Figure 6.26. It is obvious that the coarse mesh solution in Figure 6.26c) is not capable of resolving the concentration of inelastic deformation in the necking zone. By contrast, the adaptive approach, Figure 6.26a), yields a contour plot that is very close to that of the fine mesh solution in Figure 6.25b). To be precise, the maximum value of  $A$  is  $A = 2.0729$  for the adaptive and  $A = 2.0215$  for the fine mesh solution corresponding to a deviation of less than 2.5%. The coarse mesh gives  $A = 1.5998$  and thus differs by almost 20% from the fine mesh benchmark.

Finally the structural response of the three different simulations is investigated. This is achieved by a comparison of the contour plots of the distribution of the  $x$ -component  $u_x$  of the spatial displacement field, Figure 6.27. The plot features a distinct visualization of the necking event as it reflects the concentration of deformation at the lower right corner of

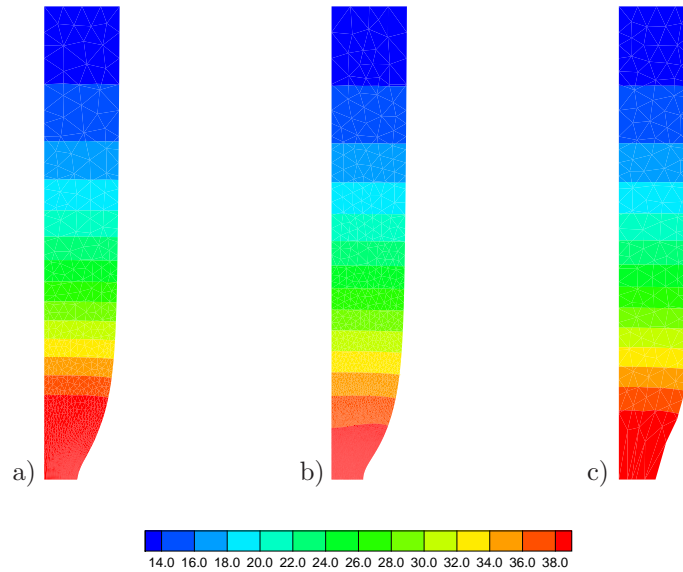


**Figure 6.25:** Change  $\Delta\theta$  in temperature. a) Adaptive, b) fine and c) coarse mesh solutions. Maximum values appear in the necking zone at the bottom of the quarter of the system.

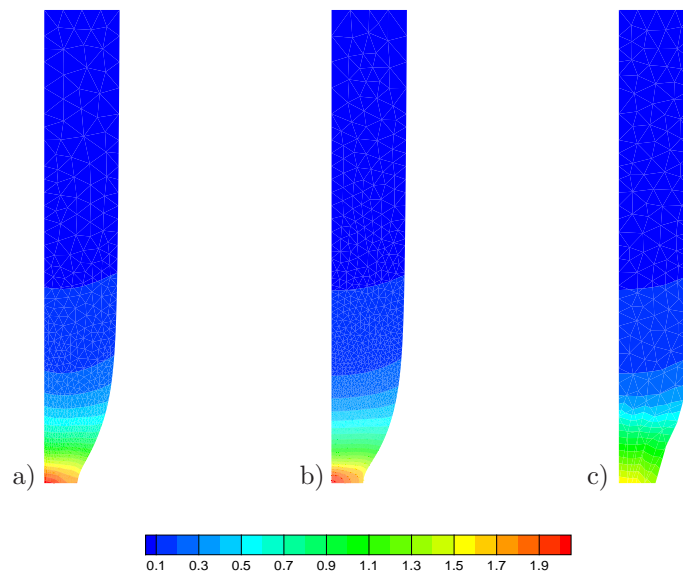


**Figure 6.26:** Distribution of hardening variable  $A$  for a) adaptive, b) fine and c) coarse mesh solution. Concentration of plastic deformation the middle axis of the entire bar.

the system, i.e. the middle plane of the entire bar. It is rather obvious that the coarse mesh solution is not capable to picture this phenomenon. Once more the adaptive simulation turns out to be close to the fine mesh benchmark. This is highlighted when considering the maximum horizontal displacement  $u_x$  which apparently is related to the node located at the lower right corner. The fine mesh and adaptive solutions provide  $u_x = -1.1382$  mm and  $u_x = -1.1065$  mm deviating by just 2.8%. The coarse mesh diverges considerably by more than 11% due to a maximum displacement of  $u_x = -1.0089$  mm.

Hence, also for non-isothermal problems the configurational-force-based adaptive procedure turns out to be a sufficiently accurate approach dealing with results that are very close to a benchmark solution.

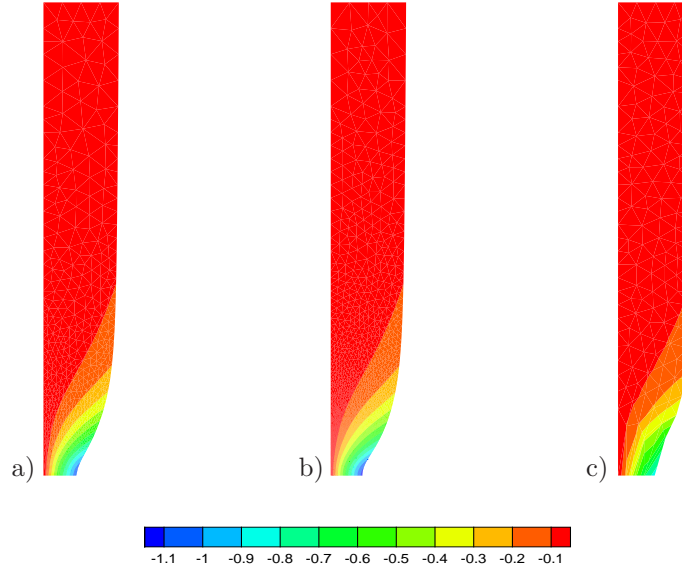


**Figure 6.27:** Contour plot of horizontal displacements  $u_x$ . a) Adaptive simulation, b) fine and c) coarse mesh benchmarks. The plot perspicuously characterizes the necking phenomenon, i.e. a concentration of deformation at the middle axis of the entire bar.

**6.5.4. Numerical Example: Necking of a Metallic Rod.** In the last part the three-dimensional setting is discussed. With the objective of demonstrating the universality of the material-force-based strategy its combination to an alternative constitutive formulation is presented. Afterwards the results of a characteristic boundary value problem are described.

**6.5.4.1. Material model for three-dimensional analyses.** The constitutive approach to be discussed below has been elaborated by MIEHE, APEL & LAMBRECHT [122]. A brief synopsis of the essential properties is given. For more detailed informations the reader is referred to the recent work of APEL [4].

The key ingredient of finite plasticity is the multiplicative decomposition (3.95) of the deformation gradient into elastic and plastic part,  $\mathbf{F} = \mathbf{F}^e \mathbf{F}^p$ . A common approach in finite elasto-plasticity is the multiplicative definition of an elastic strain measure

$$\hat{\mathbf{E}}_m^e := f_m(\mathbf{F}^{P^{-T}} \mathbf{C} \mathbf{F}^{P^{-1}}) \quad (6.31)$$

describing the elastic energy storage of the material. The function  $f_m$  represents the Seth-Hill family of generalized strain measures, cf. equation (2.19) in Section 2.1.4. For some materials it can be shown that the plastic map  $\mathbf{F}^p$  enters the energy storage only through the metric  $\mathbf{G}^p := \mathbf{F}^{pT} \bar{\mathbf{G}} \mathbf{F}^p$  and furthermore that the logarithmic strain measure

$$\mathbf{E}^e = \frac{1}{2} \ln \mathbf{C} - \frac{1}{2} \ln \mathbf{G}^p \quad (6.32)$$

is close to the multiplicative approach (6.31). The logarithmic plastic strain  $\mathbf{E}^p := \frac{1}{2} \ln \mathbf{G}^p$  is considered as the internal variable. In the afore-mentioned contributions it is outlined by means of numerical studies that the additive approach (6.32) yields results close to those obtained from the reference multiplicative split (6.31) for the Hencky-type strain measures,  $m = 0$ . The additive split of the total strains into elastic and plastic parts is a typical feature of the geometrically linear theory of plasticity. Based on this arguments



MIEHE, APEL & LAMBRECHT [122] proposed a modular structure defining a class of finite strain plasticity models consistent with (6.32). It acts in three different steps:

- 
1. *Geometric Preprocessing*: evaluate logarithmic strain measure

$$\mathbf{E}^e = \frac{1}{2} \ln \mathbf{C} - \mathbf{E}^P$$

2. *Constitutive model*: perform stress update in the logarithmic strain space

$$\{\mathbf{E}, \mathcal{I}\} \Rightarrow \text{model} \Rightarrow \{\mathbf{T}, \mathbb{E}^{ep}\} \quad (6.33)$$

3. *Geometric Postprocessing*: get nominal stresses and moduli via chain rule

$$\mathbf{P} = \mathbf{T} : \mathbb{P} \quad \text{and} \quad \mathbb{C} = \mathbb{P}^T : \mathbb{E}^{ep} : \mathbb{P} + \mathbf{T} : \mathbb{L}$$


---

Within the geometric postprocessing the total logarithmic strain measure  $\mathbf{E} = \frac{1}{2} \ln \mathbf{C}$  is computed in terms of the right Cauchy Green tensor  $\mathbf{C} = \mathbf{F}^T \mathbf{g} \mathbf{F}$ . The plastic strains  $\mathbf{E}^P$  are introduced as an internal variable. Based on these objects the elastic strain measure  $\mathbf{E}^e$  is evaluated whereupon its spectral decomposition can be performed

$$\mathbf{E}^e = \frac{1}{2} \ln \mathbf{C} - \mathbf{E}^P \quad \text{and} \quad \mathbf{E}^e = \sum_{i=1}^3 \varepsilon_i^e \mathbf{n}_i \otimes \mathbf{n}_i \quad (6.34)$$

in what  $\varepsilon_{i,i=1,2,3}^e$  denote the elastic principal stretches and  $\mathbf{n}_{i,i=1,2,3}^e$  the respective eigenvectors. Observe that the spectral representation of the elastic strain measure is not required in general by the modular structure but is adopted here in order to use the specific form of the constitutive equations given in Section 6.5.2.1.

The constitutive modeling in the logarithmic strain space is identical to the geometrically linear theory. The input are the total strains  $\mathbf{E}$  and the generalized internal variable vector  $\mathcal{I}$  containing the plastic strains  $\mathbf{E}^P$  and a scalar hardening variable  $A$ . These variables define the storage mechanism of the material. The free energy function is given by (6.27),

$$\psi = \frac{1}{2} \kappa \left[ \sum_{i=1}^3 \varepsilon_i^e \right]^2 + \mu \sum_{i=1}^3 [\tilde{\varepsilon}_i^e]^2 + \frac{1}{2} h A^2 + (y_\infty - y_0) \left( A + \frac{1}{\omega} (\exp[-\omega A] - 1) \right) \quad (6.35)$$

whereas the yield criterion is defined by (6.28),

$$\phi = \sqrt{\sum_{i=1}^3 [\tilde{\sigma}_i]^2} - \sqrt{\frac{2}{3}} (y_0 - B) \quad (6.36)$$

The deviatoric principal stresses  $\tilde{\sigma}_{i,i=1,2,3}$  are obtained by a spectral representation of the logarithmic stress tensor  $\mathbf{T}$ . The output gained from the constitutive model are the logarithmic stresses  $\mathbf{T}$  and the respective moduli  $\mathbb{E}^{ep}$ .

Within the geometric postprocessing the stresses  $\mathbf{T}$  and moduli  $\mathbb{E}^{ep}$  are transformed to the physical space. Attention is focused on a two-point representation referring to the nominal stresses  $\mathbf{P}$  and moduli  $\mathbb{C}$ . Application of chain rule results in

$$\mathbf{P} = \partial_{\mathbf{F}} \psi = \mathbf{T} : \mathbb{P} \quad \text{and} \quad \mathbb{C} = \partial_{\mathbf{F}} \mathbf{P} = \mathbb{P}^T : \mathbb{E}^{ep} : \mathbb{P} + \mathbf{T} : \mathbb{L} \quad (6.37)$$

with the fourth- and six-order transformation tensors  $\mathbb{P} := \partial_{\mathbf{F}} \mathbf{E}$  and  $\mathbb{L} := \partial_{\mathbf{F} \mathbf{F}}^2 \mathbf{E}$ . Algorithms for the evaluation of these objects are provided by MIEHE & LAMBRECHT [125].



For the evaluation of the discrete configurational nodal forces within the general three-dimensional setting all components of the internal variable vector have to be taken into account. Due to symmetry of the plastic strain measure  $\mathbf{E}^p$  a total of seven scalar fields has to be considered.

**6.5.4.2. Discussion of boundary value problem.** The last boundary value problem is devoted to the tension of a circular metallic rod. The material parameters coincide with those used for the plastic plate with a circular hole and are provided in Table 6.1 in Section 6.5.2.2. The geometry and the boundary conditions are shown in Figure 6.28. The notion

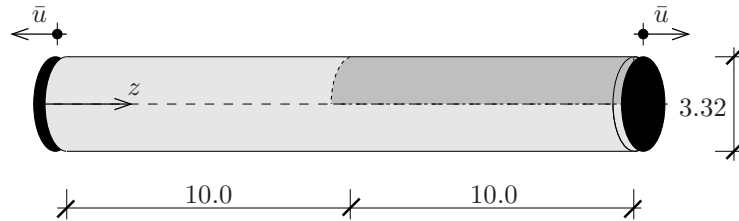


**Figure 6.28:** Necking of a metallic rod: System and boundary conditions. All dimensions are given in [mm]. Due to symmetry only an eighth of the rod is analyzed.

necking describes the decrease of the area of the cross section at the middle of the bar under tensile loading. To achieve this behavior a geometric imperfection has to be applied in the form of a slightly smaller radius at that location. The radius decreases linearly from the ends with a value of 1.66 mm to the middle with 1.6 mm. The length of the body is 20.0 mm. The specimen is subjected to a maximum prescribed displacement of 2.0 mm at the ends corresponding to 20% deformation with respect to the original length. The symmetry of the specimen is exploited by analyzing only an eighth of the entire body. For the triangulation ten-noded quadratic tetrahedrons have been used. The primary mesh for the adaptive simulation contains 360 elements, 738 nodes and is depicted in Figure 6.29a). Regarding the outer shape of the elements the shortcoming of the visualization software

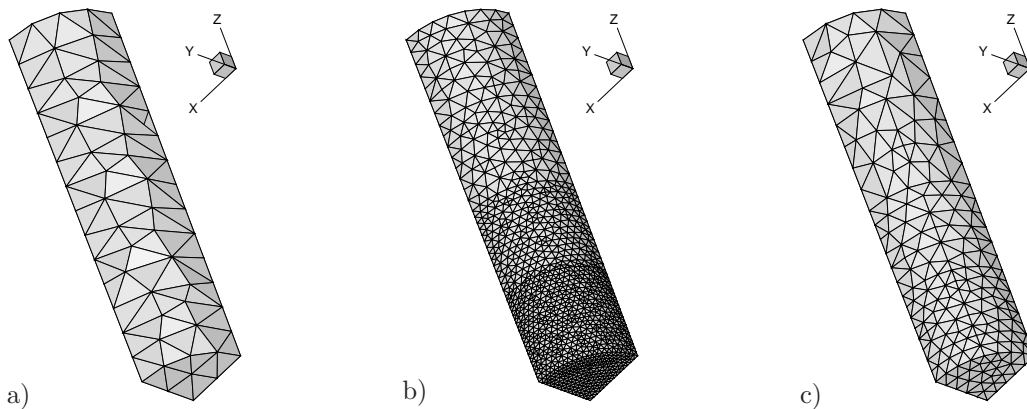


**Figure 6.29:** a) Primary triangulation for the adaptive analysis holding 360 elements. b) Fine mesh with 34922 elements and c) coarse mesh with 2289 elements.

has to be mentioned which is only capable to display linear elements, see also Remark 6.2. In addition once again two benchmark analyses have been investigated which later on allow for the assessment of the adaptive solution. The respective meshes are shown in Figure 6.29b), c).

During the analysis the global criterion  $\eta$  develops as depicted in Figure 6.30. Observe

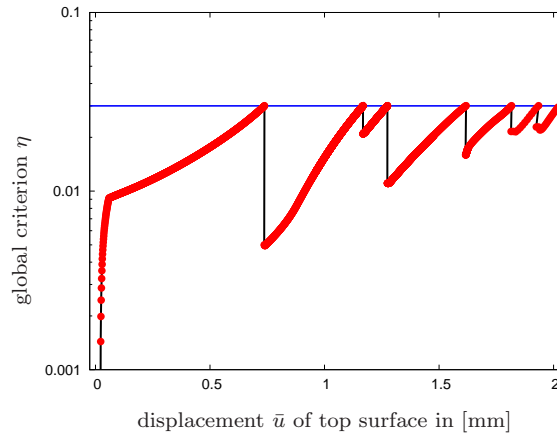


**Figure 6.30:** Necking of a metallic rod: Global criterion versus displacement of top surface. Admissible value  $\eta_{perm} = 3\%$  is plotted as straight line. The plot starts at a top surface displacement of 0.023 mm. Subsequent to mesh refinement the displacement increment is reduced for just one deformation step in order to ensure convergence to an equilibrium state.

that the axis of the global criterion starts at 0.001 or 0.1%. The very first deformation steps up to a deformation of 0.22% exhibit a global criterion beyond this value. The permitted criterion is set to  $\eta_{perm} = 3\%$ . It is readily identifiable that the initial mesh is sufficiently accurate until a prescribed displacement of 0.74 mm is achieved. Then, the solution of that deformation step performed on the initial mesh is discarded and the first remeshing event takes place. The number of nodes increases from 738 to 2542 resulting in a decrease of the global criterion down to  $\eta = 0.5\%$  for the improved mesh. In the sequel remeshing is required more frequently. In total five more meshes are created during the analysis. With regard to the remeshing one crucial point has to be explained in detail. For the case a triangulation is said to be insufficient the current deformation step is discarded and a locally refined mesh is generated. The solution of the last accepted deformation state is mapped onto the new mesh. This state does not necessarily pose a spatial equilibrium state with respect to the new mesh. Hence the same deformation step is computed once again until equilibrium is achieved. Thereby, and this is contrast to the procedure in the previous examples, in order to guarantee convergence of that deformation step an incremental displacement is applied that is only a tenth of that employed prior to remeshing. Afterwards, when the system is equilibrated, the magnitude of the incremental displacement is adjusted to the old value used before. It has to be mentioned, that the deformation steps finally used in the simulation are very small. Thus, in Figure 6.30 the discrete points uniquely indicating one single deformation step almost appear as a continuous line.

In Figure 6.31 the six different meshes generated during the analysis are shown. Recall that the initial triangulation is presented in Figure 6.29a). With the objective of providing a proper visualization of the deformed structure for now the whole system is depicted. Figure 6.31a) deals with the second mesh featuring 1490 elements and 2542 nodes at 10% deformation. Obviously the top and bottom regions as well as the middle zone of the body are unaffected until that point but an area a little bit above the middle plane is considerably refined. The same scenario, even though less distinct, is detectable for the third and fourth triangulation shown in 6.29b), c) including 2207 and 5285 elements at 12% and 14.8% deformation, respectively. The mesh refinement in this area originate from the concentration of the shear stress in this region which is a typical characteristic of the

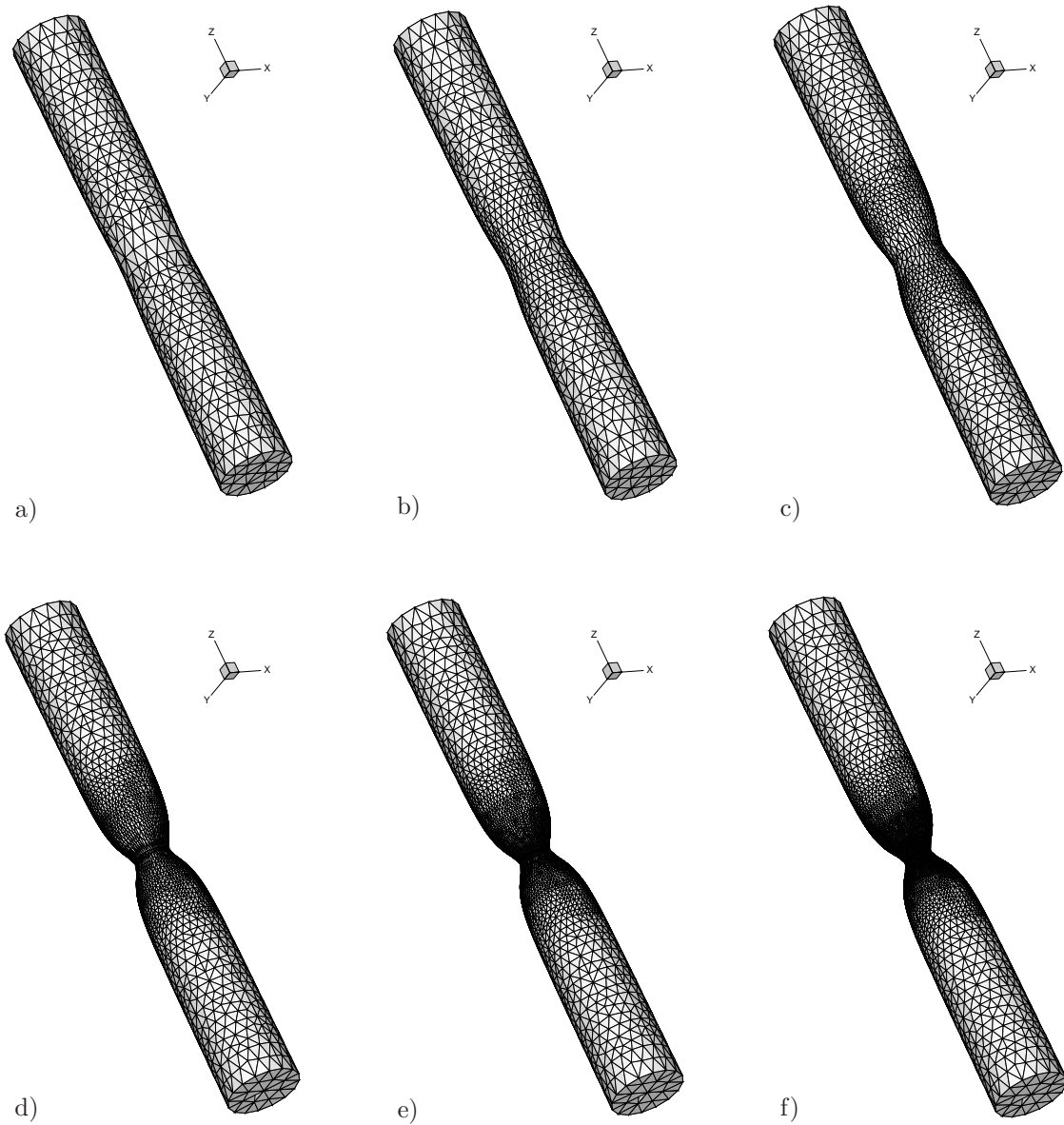


**Figure 6.31:** Adaptively refined meshes during deformation. a) 1490 elements at  $\bar{u} = 1.0$  mm. b) 2207 elements at 1.2 mm, c) 5285 elements at 1.48 mm, d) 9162 elements at 1.81 mm, e) 14054 elements at 1.9 mm. f) Final mesh with 22031 elements or 32354 nodes at maximum displacement of 2.0 mm.

necking process. Upon ongoing deformation this effect is overlaid by the concentration of plastic deformation within the necking zone. Consequently, the remaining meshes reveal massive refinement of this region. Passing deformation states of 18% and 19% Figure 6.29f) visualizes the system at 2.0 mm displacement of the top surface, i.e. 20% deformation of the original height. The final mesh consists of 22031 elements or 32354 nodes which corresponds to 92986 unknowns. Note that the mesh at the top and bottom surfaces of the entire bar remains completely unchanged during the simulation. The cross section of the middle plane of the bar is significantly reduced, the necking phenomenon is very well observable. Hence, the configurational-force-based adaptive strategy deals with a combination of two different effects. At first, the dominating effect arises from the shear-stress distribution within the system which affect internal nodal contribution  $\mathbf{F}_I$  in terms of the Eshelby tensor  $\Sigma$ . Then, for ongoing deformation due to the onset of huge plastic defor-

mations the influence of the internal part decreases and the configurational nodal force  $\mathbf{P}_I$  driven by the gradient of the internal variable vector becomes more important. Carefully note that the sum of both quantities needs to vanish at the interior nodes of the discrete domain from the theoretical viewpoint. Apparently, this condition is not satisfied exactly which results in the occurrence of numerically caused remaining nodal forces. These forces originate from the violation of the material nodal equilibrium, i.e.  $\mathbf{F}_I + \mathbf{P}_I \neq \mathbf{0}$ , which allows for the afore-mentioned reasoning.

The effect of local mesh refinement on these spurious configurational nodal forces is illustrated in Figure 6.32. Both pictures display a state of 11.68% deformation. The plots only

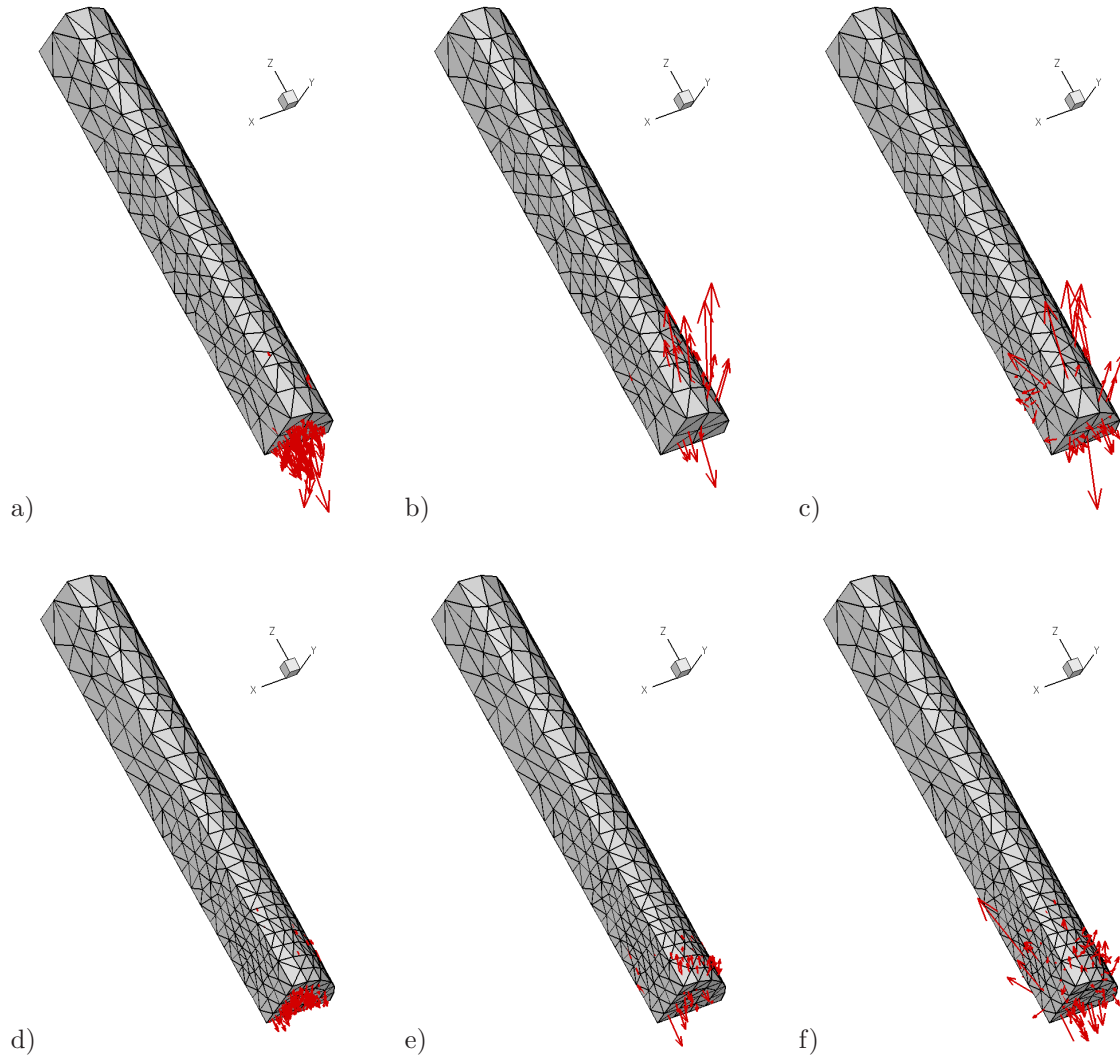


**Figure 6.32:** Change of out of balance forces upon mesh refinement. a), d) Internal part  $\mathbf{F}_I$ , b), e) discrete configurational nodal forces  $\mathbf{P}_I$ , and c), f) resulting forces, scaled by 3.0, prior to and after refinement. Second line is scaled by 2.0 compared to first line. Boundary forces are omitted. Discarded mesh possessed 2542 nodes, new triangulation holds 3680 nodes. The sum of the magnitude of the nodal forces decreases from  $\Delta\Pi = 0.5435$  N to  $\Delta\Pi = 0.4372$  N corresponding to  $\eta = 0.030084$  and  $\eta = 0.0209$  and a reduction of about 25%.

show the vectors related to the interior nodes because the true boundary nodes are not taken into account. In addition, the visualization of the structure is shaded for the sake of clarity. Therefore, however, only those vectors are visible which penetrate the outer shape of the body whereas the smaller vectors are suppressed. Furthermore it has to be

mentioned that the particular deformation state has been chosen on purpose as it features a comparatively coarse triangulation which allows for a precise visualization of the crucial effects. In the first line the old mesh successfully employed for the previous deformation states is shown containing 1490 elements and 2542 nodes. After having performed the spatial computation the discrete material nodal forces are evaluated. Figure 6.32a) and b) deal with the internal contribution  $\mathbf{F}_I$  and the configurational nodal force  $\mathbf{P}_I$ . The sum of both parts is depicted in Figure 6.32c) using a scaling factor of 3.0 compared to the previous plots. Obviously the material equilibrium condition is violated in the discrete setting. The norm of all non-vanishing nodal forces sums up to  $\Delta\Pi = 0.5435$  N resulting in a relative global criterion  $\eta = 3.01\%$  which breaches the admissible threshold  $\eta_{perm} = 3\%$ . Hence, mesh refinement is required. The new mesh is generated taking into account the element criterion  $\xi^e$  in terms of the spurious nodal forces. The new mesh is refined in that regions which exhibit large non-vanishing nodal forces. It contains 2207 elements and 3680 nodes. In order to achieve spatial equilibrium with respect to the mapped solution data the old deformation step is solved for the second time. In the postprocessing step the global criterion is evaluated once again. In Figure 6.32d) and e) the internal part and the configurational nodal forces are presented whereas in Figure 6.32f) the remaining nodal forces ( $\mathbf{F}_I + \mathbf{P}_I$ ) are shown again scaled by 3.0. It is clearly observable that for all three cases the forces are smaller compared to those appearing at the nodes of the old mesh. This holds all the more as the scaling factor of the forces related to the new mesh is twice the factor of the old mesh. The success of the refinement procedure is manifested by the fact that the sum of numerically caused resultant interior forces is now  $\Delta\Pi = 0.4372$  N which coincides with a decrease of the inaccuracy of almost 25% upon mesh refinement. The respective relative global criterion is  $\eta = 2.09\%$  and falls below the permitted value. The triangulation is said to be sufficient and the next deformation step is applied. In the last step the results of the adaptive simulation are compared to those obtained

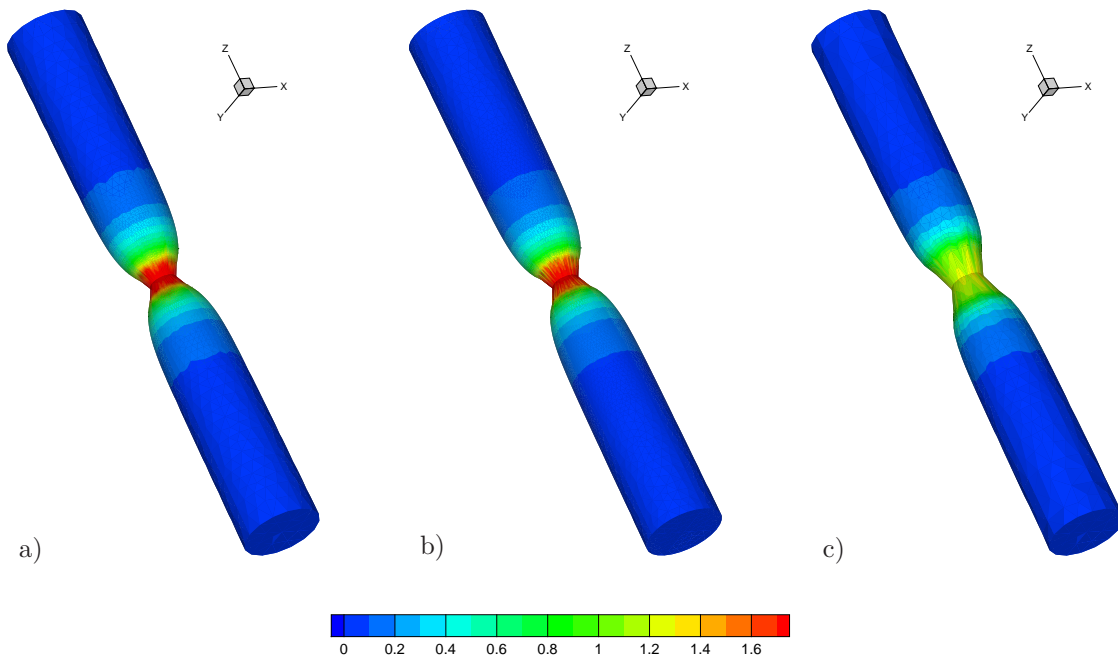


**Figure 6.33:** Distribution of scalar hardening variable  $A$ . a) Adaptive, b) fine and c) coarse mesh solutions at a final deformation of 20%. Plastic deformation concentrates in the necking zone, or vice versa, accumulation of plastic deformation initiates necking of the bar.



from two benchmark analyses. The triangulation of the fine and coarse mesh computations has been introduced in Figure 6.29b), c) above. The fine mesh consists of 34922 elements and 51034 nodes or 147231 degrees of freedom. On the other hand, the coarse mesh features 2289 elements and 3773 nodes or 10387 nodal degrees. It is well observable that in both triangulations the element sizes or rather element edge length  $h$  decrease from the top to the middle, i.e. the zone where the neck occurs. The contour plots in Figure 6.33 display the distribution of the hardening variable  $A$  at the final deformation state of 20%. The adaptive solution, Figure 6.33a), turns out to be almost identical to the fine mesh benchmark depicted in Figure 6.33b). In contrast the coarse triangulation is not able to provide an appropriate resolution of the necking zone, cf. Figure 6.33c). The maximum values  $A_{max}$  prove this observation. The fine mesh and the adaptive solution end up with  $A_{max} = 2.18275 \approx 2.21617$  whereas the coarse solution differs significantly by  $A_{max} = 1.71673$  or more than 20%.

The same behavior arises for a comparison of the structural response of the three analyses. To this end, Figure 6.34a) deals with a diagram where the area of the cross section at the middle of the bar is plotted versus the maximum vertical displacement. The deviation

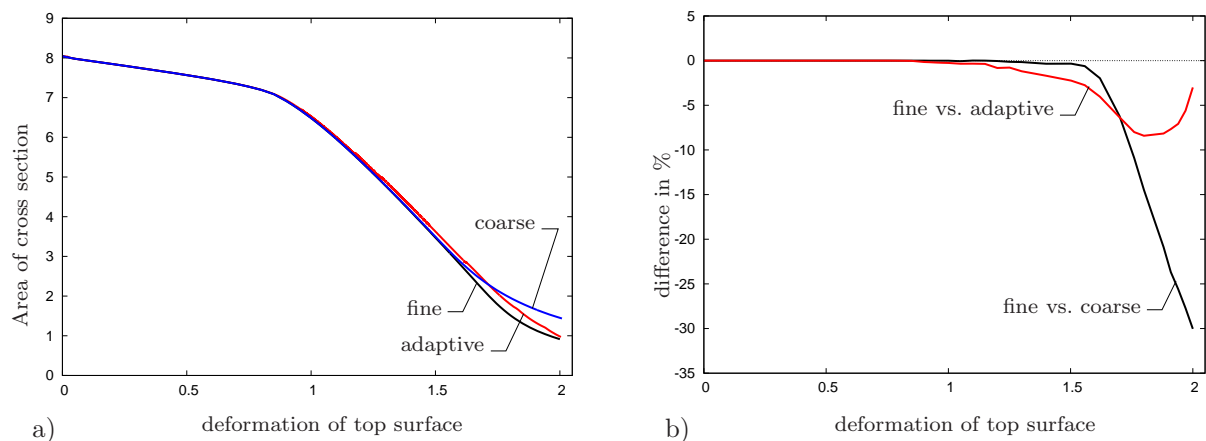


**Figure 6.34:** Necking of a metallic rod: a) Area, in  $[\text{mm}^2]$ , of the cross section at the middle of the bar versus displacement of the top surface in  $[\text{mm}]$ . b) Deviation between adaptive and fine mesh solutions as well as between adaptive and coarse mesh solutions.

of the adaptive and coarse mesh solutions from the fine mesh benchmark is highlighted in Figure 6.34b). Up to a displacement of 1.15 mm no differences between the three approaches is detectable. Then, the adaptive simulation provides a slightly stiffer response up to a maximum deviation of 7% at a top surface displacement of 1.8 mm. At that time, the next remeshing event occurs and the final mesh is generated whereupon the response of the adaptive simulation tends to the benchmark solution. At the final deformation state of 2.0 mm or 20% the deviation between both approaches is negligible. The coarse mesh solution remains close to the fine mesh simulation up to a deformation state of 1.6 mm or 16%. Then the solution starts to diverge. Of course, no mesh improvement is adopted and therefore the deviation from the fine mesh benchmark increases rapidly which finally results in a dramatic difference of about 30%.

Within the above numerical studies the proposed configurational-force-based  $h$ -adaptive strategy has been successfully applied to a variety of model problems in the quasi-static context. The capability of the method has been demonstrated by means of comparisons to benchmark solutions. The adaptive approach renders results very close to fine mesh

solutions while the numerical effort of the computation is decreased dramatically. Consequently, the configurational-force-based procedure turns out to be a very powerful and appropriate tool for an efficient simulation of problems of finite elasticity and inelasticity.

## 6.6. Application to Finite Elastodynamics

The investigations of the previous subsections are extended to the more general dynamical framework. However, attention is restricted to purely elastic material behavior. The treatment of dynamical problems demands some modifications concerning the numerical implementation which are commented on in the first step. Subsequently, a descriptive boundary value is discussed.

**6.6.1. Remarks on Particular Numerical Treatment.** Up to now, the essential equations of the material-force-based adaptive strategy have been formulated in view of the solution of quasi-static problems. Turning now to dynamical problems the basic ideas remain unchanged. Instead of the material equilibrium condition (6.14) from now on the equation of material motion governs the change of Lagrangian coordinates

$$\text{Div}\boldsymbol{\Sigma} + \bar{\boldsymbol{\Gamma}}_0 = \frac{\partial}{\partial t}\boldsymbol{\mathcal{P}}. \quad (6.38)$$

Remember that not only the pseudomomentum  $\boldsymbol{\mathcal{P}}$  enters the material balance law but also the other two quantities are affected. To be precise, the kinetic energy per unit reference volume enters Eshelby's energy-momentum tensor,  $\boldsymbol{\Sigma} = (\psi - \frac{1}{2}\rho_0\mathbf{v} \cdot \mathbf{v})\mathbf{1} - \mathbf{F}^T\mathbf{P}$ , and the configurational force depends on the material gradient  $\nabla_X\rho_0$  of the reference density. Neglecting once again spatial volume forces and assuming a homogeneous material body the configurational force disappears,  $\bar{\boldsymbol{\Gamma}}_0 = \mathbf{0}$ . Upon discretization the remaining strict conservation law,  $\text{Div}\boldsymbol{\Sigma} = \partial\boldsymbol{\mathcal{P}}/\partial t$ , results in the discrete nodal balance

$$\mathbf{F}_I - \mathbf{A}_I = \mathbf{0} \quad (6.39)$$

with the internal and dynamical -material- nodal forces  $\mathbf{F}_I$  and  $\mathbf{A}_I$ . The overall energetic misfit  $\Delta\Pi$ , (6.4), and the element misfit  $\Delta\pi^e$  specified in (6.8) are readily adjusted by replacing the true configurational force  $\mathbf{P}_I$  with the dynamical contribution  $-\mathbf{A}_I$ .

With all these quantities at hand, the local criterion (6.7) is evaluated without any modification. On the contrary, the global process of the adaptive simulation cannot be controlled in the same manner as it has been done for the quasi-static case. The global criterion was defined by the ratio of the energetic misfit with respect to the elastically stored energy of the system. For problems of elastodynamics this argumentation is no longer appropriate in particular with regard to undamped oscillations investigated here. For such a system the total energy, i.e. the sum of the potential and kinetic energies, remains always constant while a continual change between both contributions proceeds including the case that one of the contributions even vanishes.

It has proven to be convenient to control the simulation in the following way. As it has been exemplarily elaborated for the boundary value problem in Section 4.5.2 the non-vanishing out of balance forces indicate the, say, critical region within the discrete body. Consequently, based on the local criterion which in fact represents these numerically caused forces a new mesh is generated after a prescribed number of time steps. This allows for a controlled motion of the refined zones of the mesh. An alternative possibility compares the distributions of the values of the local criterion obtained for the current and the previous



time steps. In case that these comparison reveals significant changes a remeshing in terms of the current criterion has to be performed. Apparently, both procedures do not incorporate a global criterion in the sense of the one employed within the quasi-static setting but the decision on mesh refinement is made in a rather intuitive fashion. Nevertheless, they allow for a self-controlled adaptive simulation. Anticipating the key conclusion of the next subsection, the first approach turns out to give very reasonable results.

**6.6.2. Numerical Example: Oscillation of a Two-dimensional Strip.** The investigations to follow directly resume the analysis of the free oscillation of a two-dimensional strip presented in Chapter 4.5 where also a description of the boundary value problem is given in detail. The only difference concerns the triangulation of the strip. In contrast to the bilinear quadrilaterals in the sequel six-noded quadratic triangular elements are employed due to simplicity of the mesh generation. Recall that the spatial motion problem is characterized by two interacting phenomena. On the one hand, the oscillation of the specimen starts from a pre-stretched position at  $H = 6$  mm passes maximum compression at  $H \approx 4$  mm and finally again reaches the initial pre-stretched state. On the other hand, this oscillation is accompanied by the movement of a jump in the axial velocity which characterizes the wave front.

At first, a non-adaptive solution has been performed. The mesh consists of 534 triangular elements. Referring to Figure 4.6 in Section 4.5 the internal and dynamical material nodal forces arise in the region of the wave front. Although the equation of material motion (6.38) or rather its discrete version (6.39) expects the sum of these forces to vanish, numerically caused forces appear induced by an insufficient triangulation. To use these out of balance forces within the proposed adaptive strategy their norm  $|(\mathbf{F}_I - \mathbf{A}_I)|$  has to be evaluated. A contour plot of the distribution of this scalar measure is provided in Figure 6.35 for some selected time steps. Note that the original values are scaled with respect to the interval  $[0; 1]$  for the sake of visualization. Apparently, the occurrence of non-vanishing nodal forces concentrates in one region of the strip. Furthermore, it is well observable that the change of the position of this crucial region coincides with the movement of the wave front through the strip. Consequently, the configurational-force-based indicator demands a higher resolution of the region around the wave front.

Turning next to the adaptive simulation, the overall control of the analysis is such that a new mesh is generated after ten time steps. The initial mesh which also has been used for the non-adaptive simulation holds 534 elements. The refinement process is performed by remeshing of the body in terms of a density function  $\varphi$  which in turn is constituted by the local element criterion  $\xi^e$  obtained from the material out of balance forces. The topology of this density function is displayed in Figure 6.36 by means of a three-dimensional contour plot for one typical time step associated with the same state of the oscillation as shown in the second picture in the first line of Figure 6.35. Carefully note that these previous results are obtained from a non-adaptive computation but as a matter of course the characteristic remains unchanged within the adaptive simulation. The contour of the density function mirrors the distribution of the norm of the non-vanishing nodal forces. The resulting mesh which is plotted underneath with respect to the undeformed geometry incorporates massive refinement of the crucial region.

Finally, in Figure 6.37 the evolution of the adaptively refined meshes is depicted with the profile of the axial velocity plotted alongside. The number of elements of the refined meshes varies from about 1500 elements up to  $\approx 3400$  elements. The motion of the evolving mesh exactly matches the movement of the wave front. The range of the jump of the

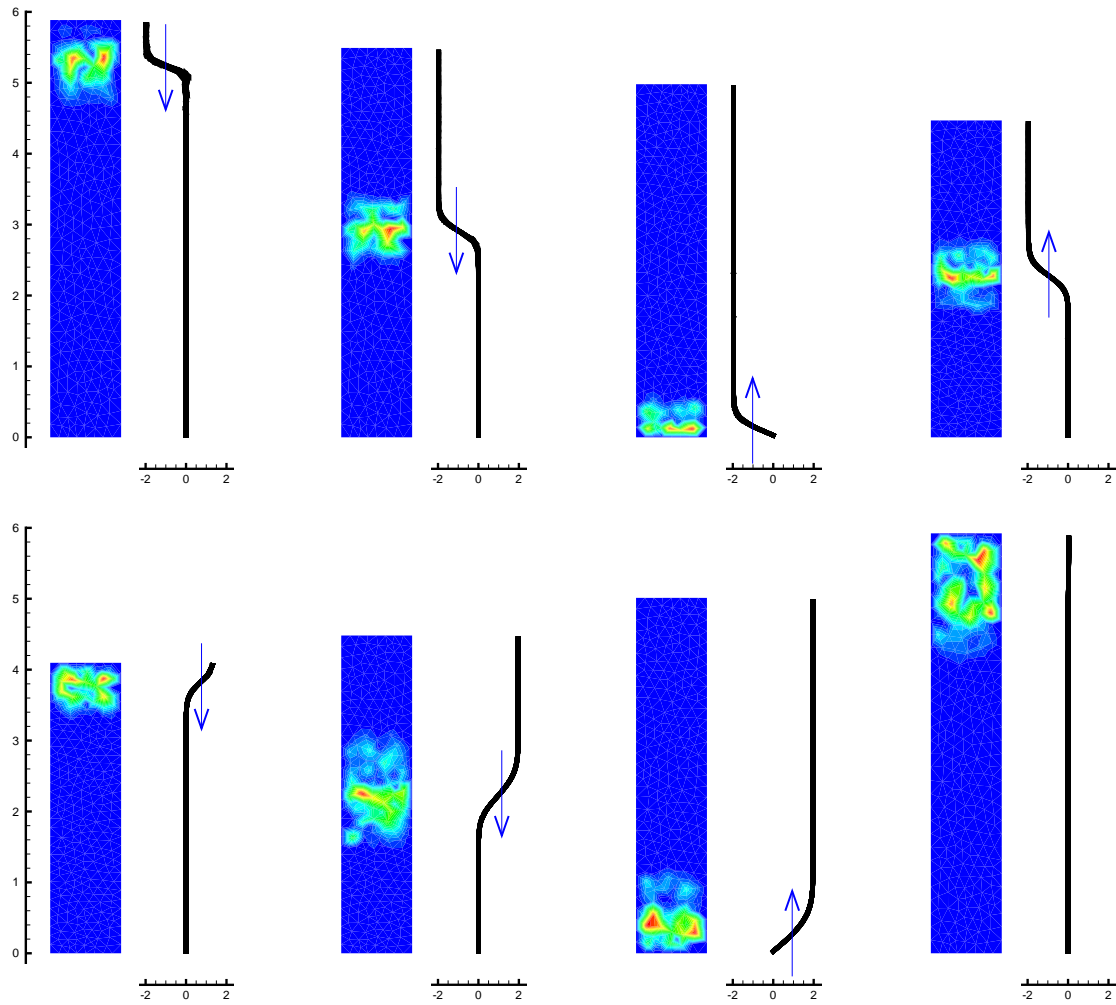


**Figure 6.35:** Contour plot of the norm of non-vanishing nodal forces. The range is scaled to the interval  $[0; 1]$ . The out of balance forces concentrate in a certain region that corresponds to the position of the wave front indicated by the profile of the axial velocity.

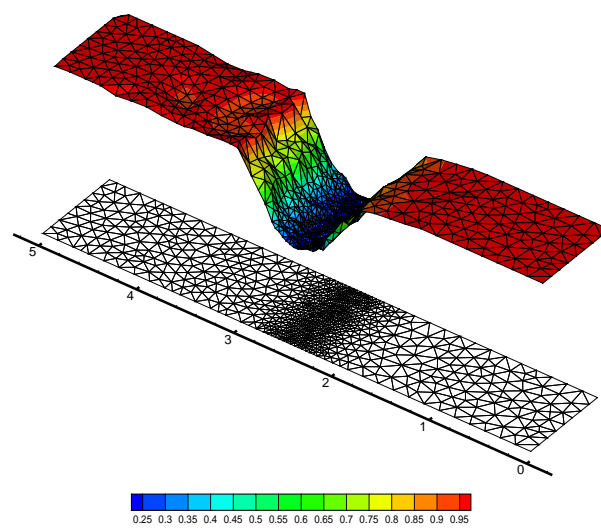


**Figure 6.36:** Density function  $\varphi$  of a typical refinement step. For  $\varphi = 1$  no refinement, for  $\varphi = 0$  maximum refinement is employed. The resulting mesh is plotted underneath.

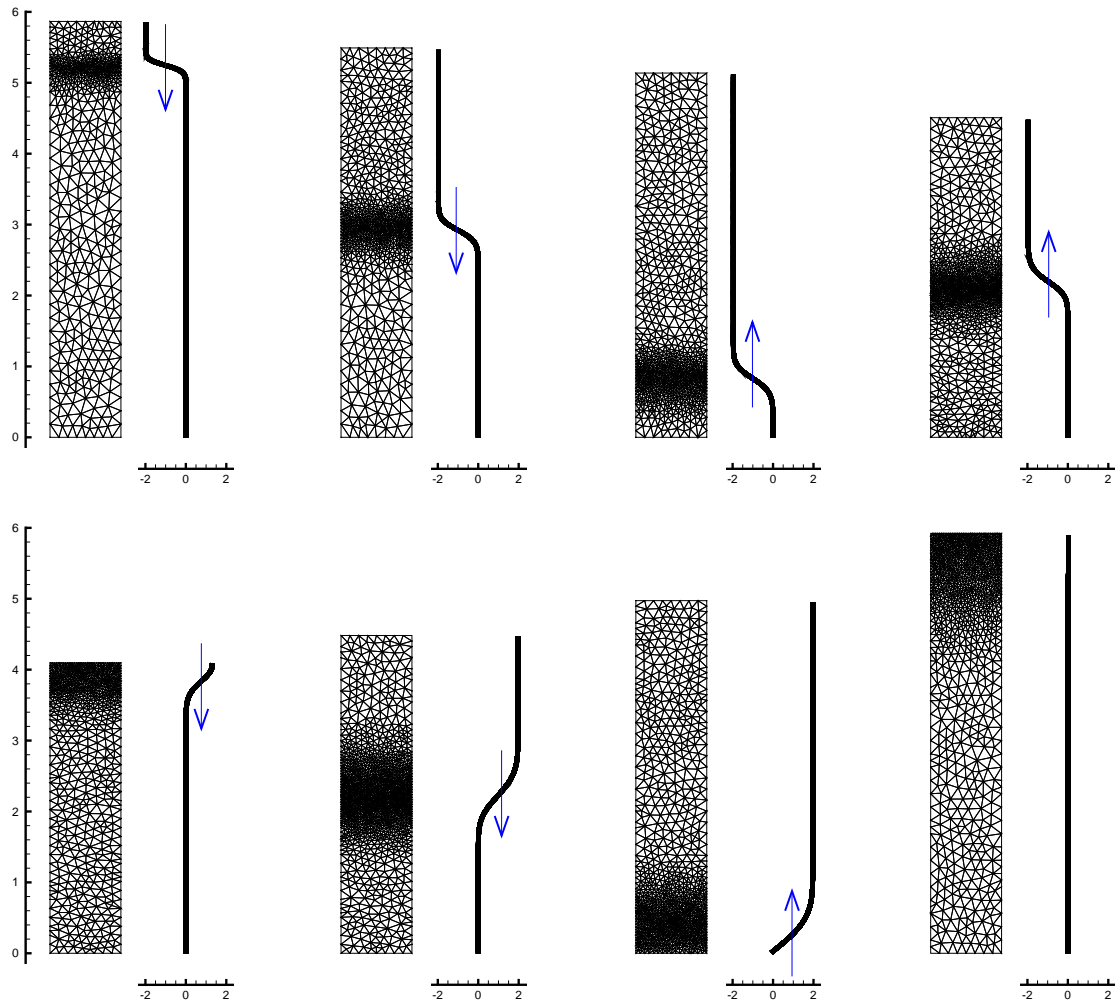


**Figure 6.37:** Mesh refinement during oscillation of the strip controlled by the local criterion. Movement of the refined region coincides with the motion of the jump in the axial velocity.

axial velocity is fitted by a highly refined zone within the mesh whereas the edge lengths within the other regions of the mesh remain unaffected.

To conclude, the above example demonstrates that the configurational-force-based adaptive procedure is applicable even to the simulation of dynamical problems. This once more confirms the versatility and universality of the proposed method.



## 7. Material-Force-Based Simulation of Crack Propagation

The investigations of this section are devoted to brittle fracture mechanics. A staggered solution strategy is elaborated capturing the crack propagation process accompanied by a local mesh refinement of the crack tip zone. As a crack characterizes an inhomogeneity within the material structure of a solid, the study of fracture processes appears as an intrinsic feature of configurational mechanics. The crack tip driving force, i.e. the configurational force acting on the inhomogeneity, or rather singularity at the tip, is used to set up a global criterion for the decision on crack propagation and to determine the direction of crack evolution. This scenario is combined with  $h$ -adaptive mesh refinement controlled by a configurational-force-based remeshing algorithm. Subsequent to some introductory remarks including a brief synopsis on existing literature the theoretical framework is presented. It bases on the reformulation of the global dissipation postulate introduced in Section 3.2 in view of dissipative mechanisms in non-linear elasticity and renders a variational formulation of brittle fracture. The crack evolution problem is described by an evolution equation locally at the crack tip. Upon spatial and temporal discretization the field equations appear as discrete nodal expressions. The crack evolution is recast into a discrete crack extension algorithm. The solution scheme relies on the separation of the geometry and the triangulation. The crack propagation is carried out on the geometry model and the generation of the new finite element mesh incorporates adaptive refinement. In the last part, the procedure is applied to representative boundary value problems.

### 7.1. Introductory Aspects

The classical theory of brittle fracture dates back to the seminal works of GRIFFITH [54, 55], IRWIN [72] and BARENBLATT [10]. The description of the crack evolution problem of brittle fracture by means of variational formulations has been elaborated by STUMPF & LE [177] and MAUGIN & TRIMARCO [110]. An extension to finite inelastic problems is suggested by the first authors as well, STUMPF & LE [178]. These local variational formulations exploit Eshelby's idea on a driving force acting on the crack tip singularity and are in line with the trendsetting work of RICE [152], see also GURTIN [59]. Later on, GURTIN & PODIO-GUIDUGLI [62, 63] used configurational forces in fracture mechanics in a non-variational setting where these forces are assumed to be independent primitive objects governed by their own balance law. Configurational forces in dynamical fracture have been studied by MAUGIN [102] and GURTIN & SHVARTSMAN [64] whereas MAUGIN, EPSTEIN & TRIMARCO [109] discuss the application to electromagnetic materials. In the theoretical part in a series of two papers STEINMANN [171] elaborated the notion of material forces in hyperelastostatic fracture mechanics. Further theoretical aspects are presented by AGIASOFITOU & KALPAKIDES [2] while OLEAGA [141, 142] deal with the variational setting of dynamic crack propagation in two and three dimensions.

With regard to the numerical treatment, STEINMANN, ACKERMANN & BARTH [175] and DENZER, BARTH & STEINMANN [35] considered the evaluation of configurational forces in elastic solids at frozen crack state, see also MÜLLER, KOLLING & GROSS [133]. An attempt including adaptive refinement strategies can be found in HEINTZ, LARSSON, HANSBO & RUNESSON [68]. The interaction of cracks and embedded inclusions is shown by KOLLING, BAASER & GROSS [80]. The use of configurational forces in inelastic fracture mechanics has been investigated by NGUYEN, GOVINDJEE, KLEIN & GAO [138] at small strains and NÄSER, KALISKE & MÜLLER [136] in the finite strain context.

The numerical implementation of configurational forces in view of the simulation of crack

propagation was first performed by MÜLLER & MAUGIN [134] and later on, KOLLING & MÜLLER [81], extended to the dynamical setting. Recently, MIEHE & GÜRSES [123] proposed a configurational-force-based algorithm incorporating  $r$ -adaptive mesh alignment. This approach has also been successfully applied in the small strain context, cf. MIEHE, GÜRSES & BIRKLE [124]. In the works of LARSSON & FAGERSTROEM [87] and FAGERSTROEM & LARSSON [45] the simulation of configurational-force-driven crack propagation is based on the extended finite element method (XFEM) while HEINTZ [67] employs a discontinuous Galerkin scheme.

The simulation of crack propagation accompanied by adaptive remeshing is discussed by BITTENCOURT ET AL. [16], BOUCHARD ET AL. [19], BOUCHARD, BAY & CHASTEL [18] and PHONGTHANAPANICH & DECHAUMPHAI [147]. In a series of papers, MEDIAVILLA, PEERLINGS & GEERS [112, 113, 114] elaborated the setting of ductile fracture and combined continuum damage models as well as damage enhanced constitutive models for softening plasticity with the discrete crack modeling using adaptive remeshing.

The theoretical formulation of brittle fracture used in the following bases on a global dissipation analysis as proposed by MIEHE & GÜRSES [123]. The conceptual treatment follows the recent contribution of MIEHE & ZIMMERMANN [128] who suggested a staggered solution scheme for the  $h$ -adaptive modeling of brittle crack propagation with both the crack propagation and the adaptive remeshing being controlled by configurational forces.

## 7.2. Variational Setting of Brittle Fracture

This section provides the theoretical basis for the present investigations. The formulation to follow appears as a modification of the fundamental approach based on the global dissipation postulate evoked in Section 3.2. The geometric setting is adjusted to the description of a cracked body and the global dissipation postulate is exploited in view of the formulation of a crack propagation criterion for brittle fracture.

**7.2.1. Basic Geometry of a Cracked Solid.** Let  $\mathcal{B} \subset \mathbb{E}^3$  be the reference configuration of a material body containing a crack. The crack is assumed to be a smooth surface  $\Gamma$ , its boundary  $\partial\Gamma$  is denoted the crack tip. The set of material points in the Euclidean space is the region

$$\mathcal{B}_\Gamma := \mathcal{B} \setminus \{\Gamma \cup \partial\Gamma\} \subset \mathbb{E}^3 \quad (7.1)$$

referred to as the bulk material. Its boundary decomposes into an exterior part  $\partial\mathcal{B}$  and an interior part formed by the crack. As usual, the exterior boundary splits up into a part  $\partial\mathcal{B}_\varphi$  with prescribed spatial deformation and a part  $\partial\mathcal{B}_\bar{\mathbf{i}}$  subjected to given tractions by von Neumann-type boundary conditions with  $\partial\mathcal{B} = \partial\mathcal{B}_\varphi \cup \partial\mathcal{B}_\bar{\mathbf{i}}$  and  $\partial\mathcal{B}_\varphi \cap \partial\mathcal{B}_\bar{\mathbf{i}} = \emptyset$  being obvious. The interior part consists of the crack surfaces  $\Gamma^+$ ,  $\Gamma^-$  and a torus-like tube surface  $C \cup \partial\Gamma$  with outward normal  $\mathbf{N}$

$$\partial\mathcal{B}_\Gamma := \partial\mathcal{B} \cup \Gamma^- \cup \Gamma^+ \cup \{C \cup \partial\Gamma\}. \quad (7.2)$$

The curve  $C$  encircles the crack tip and is denoted the process zone. A sketch of the present situation is depicted in Figure 7.1. Observe that in the two-dimensional setting the crack surfaces are curves and the crack tip is just a point. The subsequent analyses consider the limits

$$\Gamma^- \rightarrow \Gamma, \quad \Gamma^+ \rightarrow \Gamma \quad \text{and} \quad |C| \rightarrow 0. \quad (7.3)$$

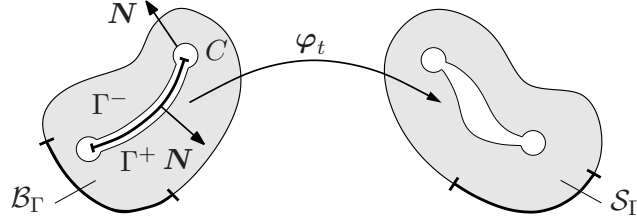


**Figure 7.1:** Deformation of a cracked solid. The limits  $\Gamma^-, \Gamma^+ \rightarrow \Gamma$  and  $|C| \rightarrow 0$  give the crack surface  $\Gamma$  with the crack tip  $\partial\Gamma$ . The spatial deformation of the bulk material  $\mathcal{B}_\Gamma := \mathcal{B} \setminus \{\Gamma \cup \partial\Gamma\}$  is described by the non-linear point map  $\varphi_t$ .

Turning next to the spatial deformation, the material coordinates  $\mathbf{X} \in \mathcal{B}_\Gamma$  are mapped onto their spatial counterparts  $\mathbf{x} \in \mathcal{S}_\Gamma$  by the non-linear point map at time  $t \in \mathcal{R}_+$

$$\varphi_t : \begin{cases} \mathcal{B}_\Gamma \rightarrow \mathcal{S}_\Gamma \\ \mathbf{X} \mapsto \mathbf{x} = \varphi_t(\mathbf{X}) \end{cases} \quad (7.4)$$

where  $\mathcal{S}_\Gamma \subset \mathbb{E}^3$  is the current configuration of the cracked solid. On the part  $\partial\mathcal{B}_\varphi$  of the exterior boundary the deformation is prescribed by the Dirichlet conditions (3.2), i.e.

$$\varphi_t(\mathbf{X}) = \mathbf{X} + t\bar{\mathbf{v}}(\mathbf{X}) \quad \text{on} \quad \partial\mathcal{B}_\varphi. \quad (7.5)$$

Note that the non-linear point map is exclusively defined on the bulk material  $\mathcal{B}_\Gamma$  but not at positions  $\mathbf{X} \in \{\Gamma \cup \partial\Gamma\}$ . Typically, the deformation across the surfaces of the crack is characterized by a jump in the deformation field

$$\llbracket \varphi_t \rrbracket := \varphi_t(\mathbf{X}^+) - \varphi_t(\mathbf{X}^-) \quad \text{with} \quad \mathbf{X}^\pm \in \Gamma^\pm. \quad (7.6)$$

Recalling the geometric framework introduced in Section 3.2.1, the kinematics of a body  $\mathcal{B}$  including material inhomogeneities is governed by the dual material and spatial coordinate maps (3.3). The non-linear deformation map appears as their composition

$$\varphi_t(\mathbf{X}) = \boldsymbol{\xi}_t(\boldsymbol{\theta}) \circ \boldsymbol{\Xi}_t^{-1}(\mathbf{X}) \quad \text{with} \quad \boldsymbol{\Xi}_t : \begin{cases} \Omega_\Gamma \rightarrow \mathcal{B}_\Gamma \\ \boldsymbol{\theta} \mapsto \mathbf{X} = \boldsymbol{\Xi}_t \end{cases}, \quad \boldsymbol{\xi}_t : \begin{cases} \Omega_\Gamma \rightarrow \mathcal{S}_\Gamma \\ \boldsymbol{\theta} \mapsto \mathbf{x} = \boldsymbol{\xi}_t \end{cases}. \quad (7.7)$$

The material configurational map  $\boldsymbol{\Xi}_t$  describes the movement of the crack tip with respect to the ambient material in the sense of a change of the material structure. The spatial coordinate map  $\boldsymbol{\xi}_t$  includes the motion of the crack tip as well as the opening of the crack due to physical loading. Both objects are parameterized by the coordinates  $\boldsymbol{\theta}$  of the time-independent parameter space  $\Omega_\Gamma \subset \mathbb{E}^3$ . Figure 7.2 visualizes this geometric scenario. The deformation gradient is the composition  $\mathbf{F} = \mathbf{j}\mathbf{J}^{-1}$  of the gradients  $\mathbf{j} = \nabla_{\boldsymbol{\theta}}\boldsymbol{\xi}_t$  and  $\mathbf{J} = \nabla_{\boldsymbol{\theta}}\boldsymbol{\Xi}_t$  of the spatial and material coordinate maps with respect to the parameter coordinates  $\boldsymbol{\theta}$ . The time derivatives of the basic kinematic quantities are given by (3.8), see also Appendix B for more details. They use the time derivatives (3.9) of the spatial and material configurational maps,  $\dot{\boldsymbol{\xi}} = \partial\boldsymbol{\xi}/\partial t \circ \boldsymbol{\Xi}_t^{-1}(\mathbf{X})$  and  $\dot{\boldsymbol{\Xi}} = \partial\boldsymbol{\Xi}/\partial t \circ \boldsymbol{\Xi}_t^{-1}(\mathbf{X})$ . These fields are constrained by Dirichlet boundary conditions defining the admissible velocities. While the spatial velocity is still governed by (3.10), the admissible material velocity takes into account the particular situation at the crack front

$$\dot{\boldsymbol{\Xi}} \in \{ \dot{\boldsymbol{\Xi}} \mid \dot{\boldsymbol{\Xi}} = \mathbf{0} \text{ on } \partial\mathcal{B} \cup \Gamma \text{ and } \dot{\boldsymbol{\Xi}} = \dot{\mathbf{a}} \text{ on } \partial\Gamma \}. \quad (7.8)$$

Here,  $\dot{\mathbf{a}}$  describes the rate of extension of the crack surface  $\Gamma$  at the crack tip  $\partial\Gamma$ . The determination of this quantity constitutes the goal of the forthcoming treatments.



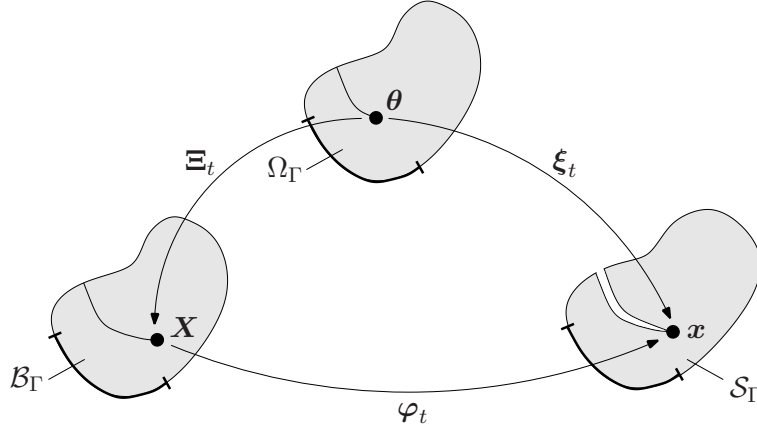


**Figure 7.2:** Kinematics of a cracked solid. The *material coordinate map*  $\Xi_t$  describes the movement of the crack tip with respect to the ambient material. The *spatial coordinate map*  $\xi_t$  includes the motion of the crack tip as well as the crack opening. The deformation of the solid is governed by the *non-linear point map*  $\varphi_t(\mathbf{X}) = \xi_t(\boldsymbol{\theta}) \circ \Xi_t^{-1}(\mathbf{X})$ .

**7.2.2. Global Response of a Cracked Solid.** Based on the above kinematic relationships, the exploitation of the global dissipation postulate renders a constitutive formulation for the crack evolution.

**7.2.2.1. Formulation of a global dissipation postulate.** The global dissipation postulate (3.21) elaborated in Section 3.2.2 within the context of non-isothermal inelasticity is reformulated with regard to dissipative processes in finite isothermal elasticity. It states that the difference between the external stress power  $\mathcal{P}$  and the change of the bulk energy storage  $\Pi_{int}$  is always greater than or equal to zero

$$\mathcal{D} = \mathcal{P} - \frac{d}{dt} \Pi_{int} = \int_{\partial \mathcal{B}_t} \mathbf{v} \cdot \bar{\mathbf{t}} \, dA - \frac{d}{dt} \int_{\mathcal{B}_t} \psi \, dV \geq 0. \quad (7.9)$$

For simplicity, spatial volume forces have been omitted,  $\bar{\gamma}_0 = \mathbf{0}$ , and the bulk material is assumed to be homogeneous,  $\partial_{\mathbf{X}} \psi^{\text{expl}} = \mathbf{0}$ .

**7.2.2.2. Global elastic response.** By substitution of the kinematic relations, equation (3.31) for the global dissipation boils down to

$$\mathcal{D} = \int_{\mathcal{B}_t} \{ -\mathbf{P} : \nabla_{\mathbf{X}} \dot{\boldsymbol{\xi}} - \boldsymbol{\Sigma} : \nabla_{\mathbf{X}} \dot{\boldsymbol{\Xi}} \} \, dV + \int_{\partial \mathcal{B}_t} \bar{\mathbf{t}} \cdot \dot{\boldsymbol{\xi}} \, dA \geq 0. \quad (7.10)$$

with the well-known constitutive expressions for the first Piola-Kirchhoff stresses  $\mathbf{P} = \partial_{\mathbf{F}} \psi$  and the Eshelby stress tensor  $\boldsymbol{\Sigma} = \psi \mathbf{1} - \mathbf{F}^T \mathbf{P}$ . For the surface integral, the first part of the material boundary condition (7.8) has been inserted. Application of integration by parts and a generalized version of Gauss integration theorem, cf. e.g. MAUGIN & TRIMARCO [110], for cracked solids

$$\int_{\mathcal{B}_t} \text{Div}(\bullet) \, dV = \int_{\partial \mathcal{B}} (\bullet) \cdot \mathbf{N} \, dA - \int_{\Gamma} [(\bullet)] \cdot \mathbf{N} \, dA - \int_{\partial \Gamma} \left\{ \lim_{|C| \rightarrow 0} \int_C (\bullet) \cdot \mathbf{N} \, dS \right\} \, d\Gamma, \quad (7.11)$$

yields the alternative representation of the global dissipation

$$\begin{aligned} \mathcal{D} = & \int_{\mathcal{B}_t} \text{Div} \mathbf{P} \cdot \dot{\boldsymbol{\xi}} + \text{Div} \boldsymbol{\Sigma} \cdot \dot{\boldsymbol{\Xi}} \, dV + \int_{\partial \mathcal{B}_t} \bar{\mathbf{t}} \cdot \dot{\boldsymbol{\xi}} \, dA \\ & + \int_{\Gamma} [[\dot{\boldsymbol{\xi}} \mathbf{P}]] \cdot \mathbf{N} + [[\dot{\boldsymbol{\Xi}} \boldsymbol{\Sigma}]] \cdot \mathbf{N} \, dA + \int_{\partial \Gamma} \mathbf{f}_{\partial \Gamma} \cdot \dot{\boldsymbol{\xi}} + \mathbf{F}_{\partial \Gamma} \cdot \dot{\boldsymbol{\Xi}} \, d\Gamma \geq 0. \end{aligned} \quad (7.12)$$

This inequality has to be satisfied for arbitrary admissible spatial and material configurational changes. The integral around the crack tip bases on the definitions of the limits

$$\mathbf{f}_{\partial\Gamma} := \lim_{|C| \rightarrow 0} \int_C \mathbf{P}\mathbf{N} \, dS \quad \text{and} \quad \mathbf{F}_{\partial\Gamma} := \lim_{|C| \rightarrow 0} \int_C \boldsymbol{\Sigma}\mathbf{N} \, dS. \quad (7.13)$$

Apparently, the integral in the second expression is the global inhomogeneity force, cf. (A.6) for its derivation based on Eshelby's thought experiment or (4.49) and the following for the formulation of global material forces. For the limit  $|C| \rightarrow 0$  the vector  $\mathbf{F}_{\partial\Gamma}$  represents the configurational force at the crack tip. Proceeding in the sense of a Coleman-type exploitation, (7.12) induces for admissible spatial velocities the local equations

$$\text{Div}\mathbf{P} = \mathbf{0} \quad \text{in } \mathcal{B}_\Gamma, \quad \mathbf{P}\mathbf{N} = \bar{\mathbf{t}} \quad \text{on } \partial\mathcal{B}_\Gamma, \quad \mathbf{P}\mathbf{N} = \mathbf{0} \quad \text{on } \Gamma^\pm \quad \text{and} \quad \mathbf{f}_{\partial\Gamma} = \mathbf{0} \quad \text{on } \partial\Gamma. \quad (7.14)$$

The first two equations display the spatial equilibrium condition for the bulk material and the traction boundary condition. The third identity demands traction free crack surfaces  $\Gamma^\pm$  while the fourth contribution enforces the limit (7.13)<sub>1</sub> to vanish at the crack tip. For admissible material velocity fields the volume integral renders the dual material equilibrium condition for the bulk material

$$\text{Div}\boldsymbol{\Sigma} = \mathbf{0} \quad \text{in } \mathcal{B}_\Gamma \quad (7.15)$$

whereas the contribution in the integral over the crack surfaces  $\Gamma$  vanishes due to the first part of the material boundary condition (7.8). The second part of this condition concerns the final integral associated with the crack tip and causes the ensuing developments.

**7.2.2.3. Crack evolution obtained from principle of maximum dissipation.** Upon Coleman-type exploitation the global dissipation postulate degenerates to the reduced dissipation inequality

$$\mathcal{D} = \int_{\partial\Gamma} \delta_{\partial\Gamma} \, d\Gamma \geq 0 \quad \text{with} \quad \delta_{\partial\Gamma} := \mathbf{F}_{\partial\Gamma} \cdot \dot{\mathbf{a}}. \quad (7.16)$$

Here,  $\delta_{\partial\Gamma}$  characterizes the dissipation per unit length of the crack tip being the inner product of the driving force  $\mathbf{F}_{\partial\Gamma}$  and the rate  $\dot{\mathbf{a}}$  of crack propagation at  $\mathbf{X} \in \partial\Gamma$  which remains unspecified up to now. The crucial idea is to formulate an evolution equation for  $\dot{\mathbf{a}}$  in formally the same way as it has been done for the internal variable field in Section 3.2.2.4. In this sense, an isotropic Griffith-type crack criterion function is introduced

$$\phi(\mathbf{F}_{\partial\Gamma}) = f(\mathbf{F}_{\partial\Gamma}) - g_c = |\mathbf{F}_{\partial\Gamma}| - g_c \leq 0 \quad (7.17)$$

with the level set function  $f$  being identified as the absolute value of the driving force  $\mathbf{F}_{\partial\Gamma}$ . The material parameter  $g_c$  is a threshold for the critical energy release per unit crack length. The crack criterion defines an elastic domain bounding the configurational force at the tip. Using the principle of maximum dissipation for the rate-independent limit the procedure results in a normality rule analogous to (3.49)

$$\dot{\mathbf{a}} = \lambda \partial_{\mathbf{F}_{\partial\Gamma}} \phi(\mathbf{F}_{\partial\Gamma}) = \lambda \frac{\mathbf{F}_{\partial\Gamma}}{|\mathbf{F}_{\partial\Gamma}|} \quad (7.18)$$

governing the evolution of crack propagation locally at the crack tip  $\partial\Gamma$ . The crack propagation is characterized by an amount  $\lambda$  into the direction of the configurational driving

force  $\mathbf{F}_{\partial\Gamma}$  according to (7.13)<sub>2</sub>. This evolution equation is valid along with the Karush-Kuhn-Tucker loading-unloading conditions

$$\phi \leq 0, \quad \lambda \geq 0 \quad \text{and} \quad \phi\lambda = 0. \quad (7.19)$$

The normality rule provides the direction of crack propagation and the loading-unloading conditions govern its discontinuous evolution but the amount  $\lambda$  remains still unspecified.

### 7.3. Space-Time-Discrete Setting of Brittle Fracture

The constitutive formulation of configurational-force-driven crack propagation is rewritten in the discrete setting including both the spatial discretization of cracked solid as well as the algorithmic integration of the crack evolution equation.

**7.3.1. Global Response of the Spatially Discretized Cracked Solid.** The spatial discretization of the cracked solid is performed in the same way as in Section 3.3.1. The cracked body is subdivided into a set of  $n_{ele}$  finite elements, see Figure 7.3 for a schematic visualization. The spatial and material coordinate maps are approximated via

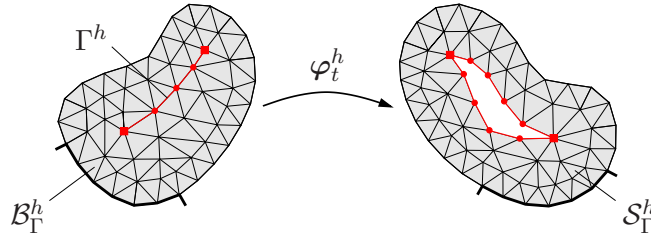


**Figure 7.3:** Discretization of the cracked solid. Spatial discretization of the configurational maps  $\xi_t$  and  $\Xi_t$  by typical finite elements.

the standard finite element approach (3.52) in terms of global vector fields  $\mathbf{d}_t \in \mathcal{R}^{\mathcal{N}_t}$  and  $\mathbf{D}_t \in \mathcal{R}^{\mathcal{N}_t}$  containing the discrete spatial and material positions at every node  $I \in \mathcal{N}_t$  of the finite element mesh. The same procedure is applied for the spatial and material velocity fields  $\dot{\xi}$ ,  $\dot{\Xi}$ , cf. (3.55). With these approximations at hand, the global dissipation postulate is rewritten in its discrete representation (3.57), i.e.

$$\mathcal{D}^h = \sum_{I=1}^{\mathcal{N}_t} \{ [\mathbf{p}_I + \mathbf{f}_I] \cdot \dot{\mathbf{d}}_I + \mathbf{F}_I \cdot \dot{\mathbf{D}}_I \} \geq 0. \quad (7.20)$$

The spatial external and internal nodal forces  $\mathbf{p}_I$  and  $\mathbf{f}_I$  are specified in (3.58) and (3.59), the first one obviously without spatial volume forces due to  $\bar{\gamma}_0 = \mathbf{0}$ . The internal material nodal contribution  $\mathbf{F}_I$  is given by (3.61)

$$\mathbf{F}_I := - \mathbf{A} \int_{\mathcal{B}_I^e} \mathbf{B}_I^T \Sigma \, dV \quad (7.21)$$

and, on account of Remark 5.1, can also be denoted the – negative – discrete configurational node point force. Due to discretization, the admissible spatial and material velocities (3.10) and (7.8) are transferred into conditions for the discrete nodal velocities. For the spatial part (3.62)<sub>1</sub> still holds whereas the admissible material nodal velocities are

$$\dot{\mathbf{D}}_I := \{ \dot{\mathbf{D}}_I \mid \dot{\mathbf{D}}_I = \mathbf{0} \text{ on } \partial\mathcal{B}^h \cup \Gamma^h \text{ and } \dot{\mathbf{D}}_I = \dot{\mathbf{a}}_I \text{ on } \partial\Gamma^h \}. \quad (7.22)$$

Exploitation of the discrete version of the global dissipation postulate renders for arbitrary admissible spatial configurational changes the spatial nodal equilibrium conditions

$$\mathbf{f}_I = \mathbf{0} \text{ in } \mathcal{B}_\Gamma^h, \quad \mathbf{f}_I = \mathbf{p}_I \text{ on } \partial\mathcal{B}_\Gamma^h \quad \text{and} \quad \mathbf{f}_I = \mathbf{0} \text{ on } \Gamma^h. \quad (7.23)$$

The last expression demands vanishing spatial nodal forces on the discrete crack surfaces  $\Gamma^h$ . On the other hand, for arbitrary material nodal velocities the discrete material equilibrium condition is obtained

$$\mathbf{F}_I = \mathbf{0} \text{ in } \mathcal{B}_\Gamma^h. \quad (7.24)$$

It has proven to be a suitable basis for the setting up of an adaptive refinement indicator, cf. Section 5 and Section 6, and consequently states a condition for an optimal mesh.

**7.3.2. Time Discretization of Crack Evolution Problem.** With the spatial and material nodal conditions (7.23) and (7.24) at hand and on account of the second part of condition (7.22) for admissible material velocities, the dissipation postulate reduces to

$$\mathcal{D}^h = \sum_{I \in \partial\Gamma^h} \mathbf{F}_I \cdot \dot{\mathbf{a}}_I \geq 0. \quad (7.25)$$

Hence, the discrete version of the reduced dissipation inequality is governed by the product of the configurational nodal forces  $\mathbf{F}_I$  at node  $I$  of the crack tip and the rate of crack propagation  $\dot{\mathbf{a}}_I$  of the respective node. In view of the formulation of an evolution equation for the rate  $\dot{\mathbf{a}}_I$  it is appropriate to describe the movement of node  $I$  of the crack tip by means of the normality rule (7.18)

$$\dot{\mathbf{a}}_I = \lambda_I \frac{\mathbf{F}_I}{|\mathbf{F}_I|} \text{ at } I \in \partial\Gamma^h \quad (7.26)$$

in combination with the loading-unloading conditions

$$(|\mathbf{F}_I| - g_c) \leq 0, \quad \lambda_I \geq 0 \quad \text{and} \quad (|\mathbf{F}_I| - g_c)\lambda_I = 0. \quad (7.27)$$

The time integration of the evolution equation within the time interval  $[t_n; t_{n+1}]$  defines the incremental dissipation

$$\Delta\mathcal{D}_{n+1}^h := \int_{t_n}^{t_{n+1}} \mathcal{D}^h dt \approx \sum_{I \in \partial\Gamma_{n+1}^h} \mathbf{F}_I \cdot \Delta\mathbf{a}_I \geq 0. \quad (7.28)$$

By assumption, the amount  $\Delta\gamma$  of the increment  $\Delta\mathbf{a}_I$  of the crack surface is constant and will be related to the maximum edge length  $h_{max}$  of the finite element mesh. Note the association  $\gamma = \lambda\Delta t$ . Consequently, the discretization reads

$$\Delta\mathbf{a}_I = \Delta\gamma_I \frac{\mathbf{F}_I}{|\mathbf{F}_I|} \text{ at } I \in \partial\Gamma_{n+1}^h \quad \text{with} \quad \Delta\gamma_I = \begin{cases} \alpha h_{max} & \text{for } |\mathbf{F}_I| > g_c \\ 0 & \text{otherwise} \end{cases} \quad (7.29)$$

in terms of a scaling factor  $\alpha$  to be commented on below.

**Remark 7.1:** As already mentioned in the context of equation (7.21) the internal material nodal contribution  $\mathbf{F}_I$  can be denoted the discrete configurational nodal force. Using the discrete material nodal balance, e.g. equation (5.25), the sign of these objects differs from each other, i.e.  $\mathbf{F}_I = -\mathbf{P}_I$ . For this reason, the material crack tip force, which in the present context is the internal force, points in the opposite direction of the true configurational force and consequently in the direction of an energy *decrease*, or rather *release* upon movement of the material node point position.

## 7.4. Solution Procedure for Adaptive Fracture Simulation

In this section an adaptive solution procedure for the simulation of crack propagation in brittle materials is proposed. The whole algorithm is driven by configurational forces. The key feature is the *separation of finite element mesh and geometry model*. Basically, the approach consists of three major parts as visualized in Figure 7.4. At first, the discrete

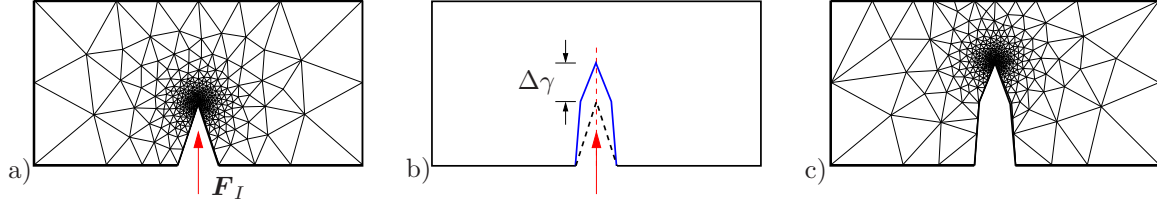


**Figure 7.4:** Separation between finite element triangulation and geometry model. a) Primary mesh used for the evaluation of the material force at the crack tip. b) The mesh has been discarded and crack propagation is performed on the geometry model. c) Remeshing of the geometry using configurational-force-based refinement indicator.

configurational nodal forces belonging to the primary triangulation are computed. For the case that crack propagation takes effect, its process is carried out by an update of the geometry model. Finally, a new mesh is generated incorporating  $h$ -adaptive refinement of the crack tip zone. The algorithmic treatment of these essential aspects is discussed in detail within the following subsections. In the end, an overall strategy is developed in the sense of a staggered solution scheme.

**7.4.1. Material-Force-Based Geometry Update.** The implementation of the crack propagation process is subdivided into three parts. A schematic sketch of this scenario is depicted in Figure 7.5 and the fundamental steps are summarized in Box 7.1.

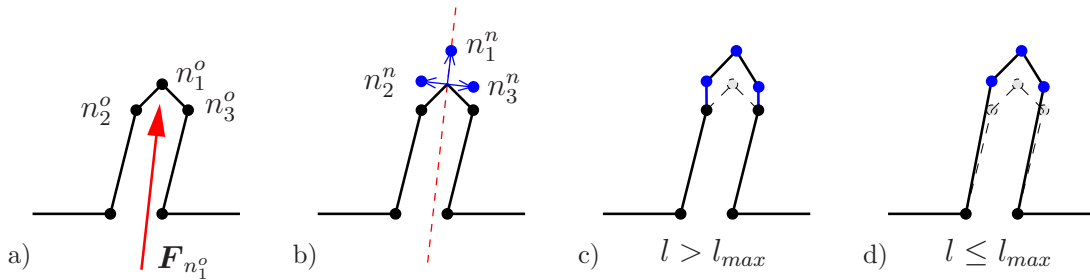


**Figure 7.5:** Structural update of geometry model. a) Discrete material crack tip force at node  $n_1^o$ . b) Insertion of new crack tip node  $n_1^n$  and doubling of old crack tip node into  $n_2^n$  and  $n_3^n$ . c) Erasure of old crack tip node and introduction of new border segments or d) erasure of all old contour nodes keeping the number of border segments constant.

First of all the configurational force at the crack tip has to be evaluated in a postprocessing step subsequent to the solution of the spatial problem. Following the idea of DENZER, BARTH & STEINMANN [35], not only the crack tip force itself is used but all material forces within a certain radius  $r_c$  around the crack tip are summed up defining the driving force at the crack tip node  $n_1^o$

$$\mathbf{F}_{n_1^o} = \sum_{I=1}^{n_R} \mathbf{F}_I \quad \text{with} \quad n_R = \{ I \mid |\mathbf{X}_I - \mathbf{X}_{n_1^o}| \leq r_c \}. \quad (7.30)$$

**Box 7.1:** Material-force-driven geometry update for crack propagation1. *Compute material force at the crack tip*

Sum up all material nodal forces within a certain radius  $r_c$  around the tip

$$\mathbf{F}_{n_1^o} = \sum_{I=1}^{n_R} \mathbf{F}_I \quad \text{with} \quad n_R = \{I \mid |\mathbf{X}_I - \mathbf{X}_{n_1^o}| \leq r_c\}.$$

2. *Check global criterion*

IF  $|\mathbf{F}_{n_1^o}| > g_c$  crack propagates

ELSE increase load step  $t \leftarrow t + \Delta t$ . EXIT

3. *Insert new contour nodes*

- Crack propagation into the direction of the crack tip force defines new crack tip node  $n_1^n$

$$\Delta \mathbf{a} = \Delta \gamma \mathbf{F}_{n_1^o} / |\mathbf{F}_{n_1^o}| \quad \text{with} \quad \Delta \gamma = \alpha h_{max}$$

- Doubling of old crack tip node  $n_1^o$  into  $n_2^n$  and  $n_3^n$
- Crack opening by moving  $n_2^n$  and  $n_3^n$  according to

$$\Delta \mathbf{p} = \pm \frac{1}{2} \Delta \gamma \mathbf{n} / |\mathbf{n}| \quad \text{with} \quad \mathbf{n} \cdot \mathbf{F}_{n_1^o} = 0$$

4. *Generate geometry model*

Update length of current border segment

$$l \leftarrow l + \Delta \gamma$$

IF  $l > l_{max}$  delete old crack tip node  $n_1^o$   
introduce additional border segments

ELSE delete old contour nodes  $n_1^o$ ,  $n_2^o$ , and  $n_3^o$   
keep number of border segments constant

5. *Generate new finite element mesh*

Based on the amount of this quantity the global decision on crack propagation is made. In case a given critical value  $g_c$  is violated, i.e.  $|\mathbf{F}_{n_1^o}| > g_c$ , the crack propagates. Otherwise,  $|\mathbf{F}_{n_1^o}| \leq g_c$ , no crack propagation occurs.

The crack propagation process is modeled by an update of the underlying geometry model. In this scenario, new contour nodes are introduced in the following way, see Figure 7.5b). According to (7.29) the position of the new crack tip node  $n_1^n$  is defined by

$$\Delta \mathbf{a} = \Delta \gamma \frac{\mathbf{F}_{n_1^o}}{|\mathbf{F}_{n_1^o}|} \quad (7.31)$$

displaying a movement of the crack tip in the direction of the driving force, i.e. opposite to the true material force. To enforce an opening of the crack, the old crack tip node  $n_1^o$  is doubled into the nodes  $n_2^n$  and  $n_3^n$ . Their positions are obtained by the vector shift

$$\Delta \mathbf{p} = \pm \left( \frac{1}{2} \Delta \gamma \right) \frac{\mathbf{n}}{|\mathbf{n}|} \quad (7.32)$$

where  $\mathbf{n}$  is perpendicular to the direction of crack propagation, i.e.  $\mathbf{n} \cdot \mathbf{F}_{n_1^o} = 0$ . By assumption, the amount of crack extension  $\Delta \gamma$  is evaluated by a certain fraction  $\alpha$  of the maximum edge length  $h_{max}$  used in the context of the mesh generation, e.g.  $\Delta \gamma = 0.05 h_{max}$  has proven to be reasonable. It has to be emphasized that the specific choice of the amount  $\Delta \gamma$  is critical for the accuracy of the algorithm in view of a realistic simulation of crack propagation. In particular, if the incremental crack extension is chosen too big, the configurational-force-driven procedure will fail to predict the crack path observed in experiments.

The modified geometry model is generated by linking the contour nodes via border segments. The length of the current segment is updated by  $l \leftarrow l + \Delta \gamma$ . This length is compared to a prescribed value  $l_{max}$  for the maximum segment length depending on the maximum edge length  $h_{max}$  as well. For  $l > l_{max}$  only the old crack tip node  $n_1^o$  is deleted and additional border segments are introduced, Figure 7.5c). Otherwise,  $l \leq l_{max}$ , the old contour nodes  $n_1^o$ ,  $n_2^o$  and  $n_3^o$  are deleted and the number of border segments is kept constant, Figure 7.5d). The reason for this algorithmic check arises from two counteracting arguments. On the one hand, as the border segments constitute a piecewise linear traverse, an appropriate number of segments is required to be able to model curved crack paths. On the other hand, every contour node has to be matched by a nodal point of the new finite element mesh to be generated in the next step. By deleting the old contour nodes in case that they are not needed any more, e.g. for straight crack propagation, this constraint is avoided which in turn allows for coarsening upon remeshing in regions far from the crack tip.

Subsequent to the update of the geometry model a new finite element mesh is generated. To obtain a reasonably accurate resolution of the crack tip region, the remeshing procedure incorporates the local refinement criterion evaluated in terms of the configurational nodal forces belonging to the discarded mesh, see below for more details. The solution data is mapped onto the new mesh using the algorithms proposed in Section 6.3.2.

It is a remarkable circumstance that the crack propagation process, i.e. the update of the geometry model, appears as a *structural update of the material configuration*. Consequently, the motion of the crack tip basically displays the action of the material configurational map. This motion is accompanied by a change in the energetic state, namely an energy release, of the system. It includes in a straightforward manner the definition of the – negative – configurational force as the change of energy with respect to the structural change of the reference configuration, i.e. the change of the material position.

**7.4.2. Material-Force-Based Adaptive Refinement Procedure.** The second ingredient of the proposed procedure bases on the exploitation of the material balance equation (7.15) or rather its discrete counterpart (7.24). Due to an insufficient triangulation numerically caused material forces occur in the discrete bulk domain  $\mathcal{B}_\Gamma$ . The application of these out of balance forces to set up a  $h$ -adaptive refinement strategy has been discussed at full length within Section 6, particularly within Section 6.4 in view of elastic problems. A short summary of the basic features is presented in Box 7.2. The method relies on the



**Box 7.2:** Material-force-based  $h$ -adaptive refinement procedure

1. *Compute global criterion  $\eta$*

Out of balance material forces violating the material nodal balance (7.24) indicate an energetic misfit of the current triangulation

$$\Delta\Pi = \left(1 + \frac{n_{bnd}}{n_{int}}\right) \sum_{I=1}^{n_{int}} |\mathbf{F}_I|$$

Global criterion: ratio of misfit with respect to elastically stored energy

$$\eta = \Delta\Pi / \Pi \quad \text{with} \quad \Pi = \int_{\mathcal{B}} \psi \, dV$$

2. *Check global criterion*

IF  $\eta > \eta_{perm}$  mesh refinement is required

ELSE check for crack propagation. EXIT

3. *Compute element criterion  $\xi^e$*

Energetic misfit on the element level

$$\Delta\pi^e = \left(1 + \frac{n_{bnd}^e}{n_{int}^e}\right) \sum_{I=1}^{n_{int}^e} |(\mathbf{F}_I + \mathbf{P}_I)^e|.$$

Local criterion: ratio of misfit with respect to an averaged element value

$$\xi^e = [\Delta\pi^e / \pi_m]^{1/p} \quad \text{with} \quad \pi_m = \eta_{perm} f_S \Delta\Pi / n_{ele}$$

4. *Adaptive refinement procedure*

Mesh generation with local refinement based on element criterion  $\xi^e$ .

definition of global and local criteria used for the global decision on mesh refinement and the control of the local refinement process, respectively.

**7.4.3. Staggered Solution Algorithm.** In the final step, the two algorithms introduced above are linked to a staggered solution scheme for the simulation of crack propagation. A flowchart of the proposed solution procedure is given in Figure 7.6.

The algorithm starts with a standard spatial computation for the current load or time step  $t$ . Within a postprocessing step the discrete material nodal forces are evaluated. Based on these quantities the global criterion  $\eta$  is computed and the decision on mesh refinement is made. If mesh refinement is required, i.e. for  $\eta > \eta_{perm}$ , a new mesh has to be generated. The local mesh refinement is controlled by the element criterion  $\xi^e$  also determined in terms of the material nodal forces. The  $h$ -adaptive mesh refinement guarantees an appropriate resolution of the process zone. In case the triangulation is said to be sufficiently

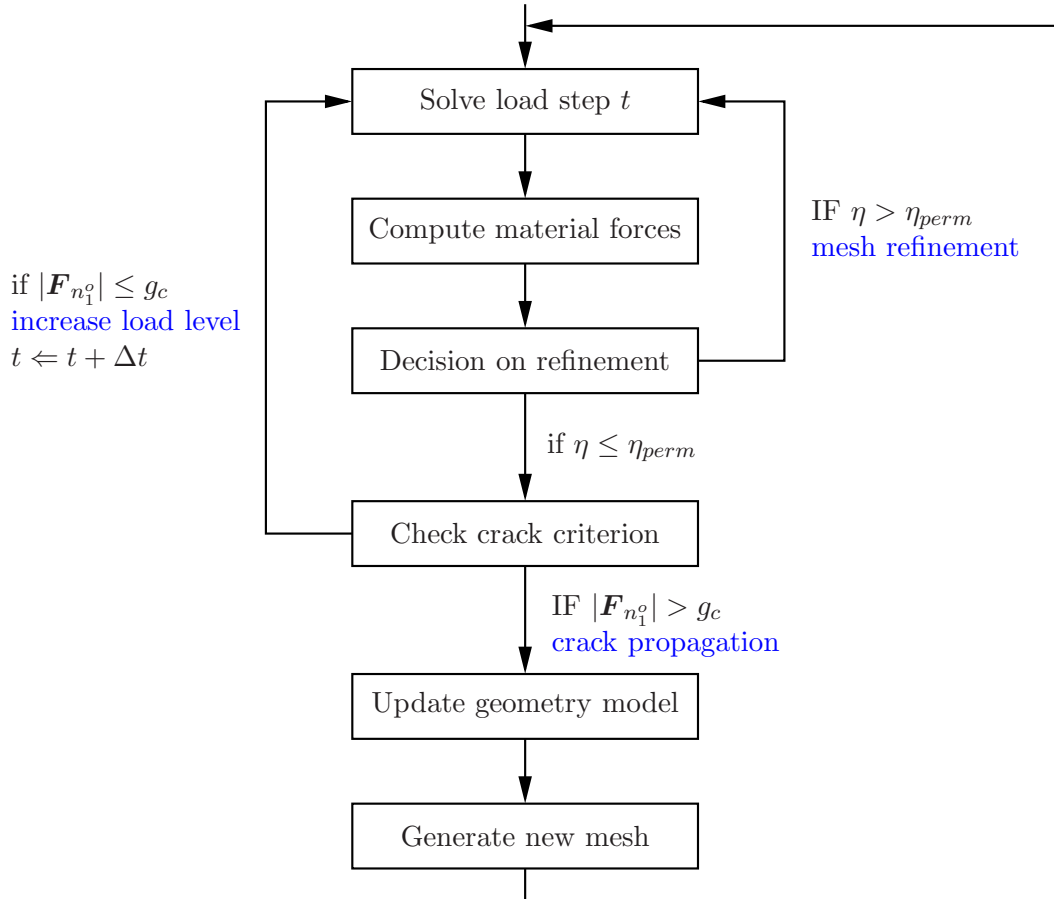


**Figure 7.6:** Staggered solution scheme for  $h$ -adaptive fracture simulation. At first, the current triangulation is checked via a global refinement criterion  $\eta$ . Thus a sufficiently accurate mesh is guaranteed for the decision on crack propagation to be made in the second step.

accurate, i.e.  $\eta \leq \eta_{perm}$ , the decision on crack propagation is made. To this end, the discrete configurational forces at all nodes within a certain radius surrounding the crack tip are summed up and the critical crack tip force, i.e. the energy release rate, is evaluated according to (7.30). For  $|\mathbf{F}_{n_1^o}| \leq g_c$  the crack does not propagate. Hence, the load level is increased,  $t \leftarrow t + \Delta t$ , and the spatial solution of the next load step is performed. Otherwise,  $|\mathbf{F}_{n_1^o}| > g_c$ , crack propagation takes effect. The underlying geometry model is modified by the structural update and a new mesh is generated. The meshing procedure is governed by the element value  $\xi^e$  and thus a priori provides a better resolution of the process zone. However, as the element criterion stems from the discarded mesh belonging to the old geometry model, the refined zone may not necessarily match the crack tip of the new geometry. This will be achieved at the latest by an additional refinement step. Subsequent to remeshing, the same time step  $t$  is computed one more time and the whole procedure recurs until a maximum number of time step is reached.

It has to be emphasized that the key parts of the proposed algorithm, i.e. the crack propagation process, the mesh generation and the refinement procedure, are driven by material nodal forces. These quantities are evaluated in a postprocessing step by just one more element loop and then are capable to control the whole procedure. From the numerical point of view, the algorithm presented here allows for an extremely efficient and robust  $h$ -adaptive simulation of crack propagation.

## 7.5. Numerical Examples

The capability of the staggered solution procedure is demonstrated by means of numerical examples. The constitutive model of finite elasticity relies on the particular representation (4.82) of the free energy function for a compressible Neo-Hookean-type material, see Section 4.5.1. The material parameters are the shear modulus  $\mu = 8.0 \text{ kN/mm}^2$  and Poisson's ratio  $\nu = 0.3$  corresponding to  $\beta = 1.5$ . The critical energy release rate is set to  $g_c = 1 \cdot 10^{-6} \text{ kN}$  referring to unit depth of the specimen in the two-dimensional case. For the spatial discretization six-noded quadratic triangular elements have been used. The admissible threshold for the global refinement criterion is  $\eta_{perm} = 5\%$  in the first, but  $\eta_{perm} = 3.5\%$  in the other examples.

**7.5.1. Tension Test of a Notched Specimen.** In the first example the tension test of a notched specimen is investigated. The system together with the boundary conditions is depicted in Figure 7.7. Despite symmetry the full body is discretized in order to demon-

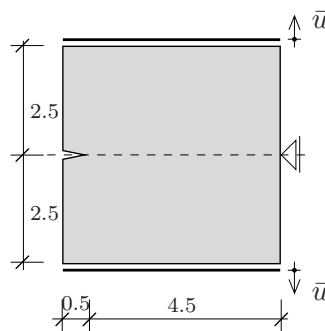


**Figure 7.7:** System and boundary conditions of notched specimen in tension. All dimensions are given in [mm]. Despite symmetry the whole specimen is analyzed.

strate the capability of the proposed method to simulate straight crack propagation. The body is deformed within a displacement-driven process by prescribed incremental displacements  $\Delta \bar{u} = 0.00025 \text{ mm}$  at both the bottom and the top edges. The crack is initiated by the given notch at the left hand side of the specimen.

In Figure 7.8 the evolution crack propagation together with the adaptively evolving meshes is visualized. Starting from an uniform and very coarse primary triangulation with 212 elements, mesh refinement is required twice in the very first deformation step until the global refinement indicator falls below the admissible value  $\eta_{perm} = 3.5\%$  for a mesh holding 762 triangles. After the second displacement increment has been applied, i.e. at a deformation of 0.1% of the original heights of the body, the admissible crack criterion  $g_c$  is violated and the crack starts propagating. The crack path develops as a straight line strictly along the horizontal symmetry axis of the body. Enforcing the global adaptive criterion, the mesh evolves according to the progress of crack propagation. The mesh is heavily refined in the crack tip region and moves together with the crack tip. This movement ensures a sufficient resolution of the process zone surrounding the tip. During the simulation the number of elements increases up to 8430 elements for the final mesh when the crack tip almost reaches the right edge of the specimen and the simulation terminates.

Figure 7.9 shows the distribution of the  $P_{yy}$ -component of the first Piola-Kirchhoff stress tensor for four states of the crack evolution with  $y$  referring to the vertical direction. Due to the geometric singularity the maximum tensile stress occurs directly at the crack tip and the stress level decreases rapidly for an increasing distance from the tip.

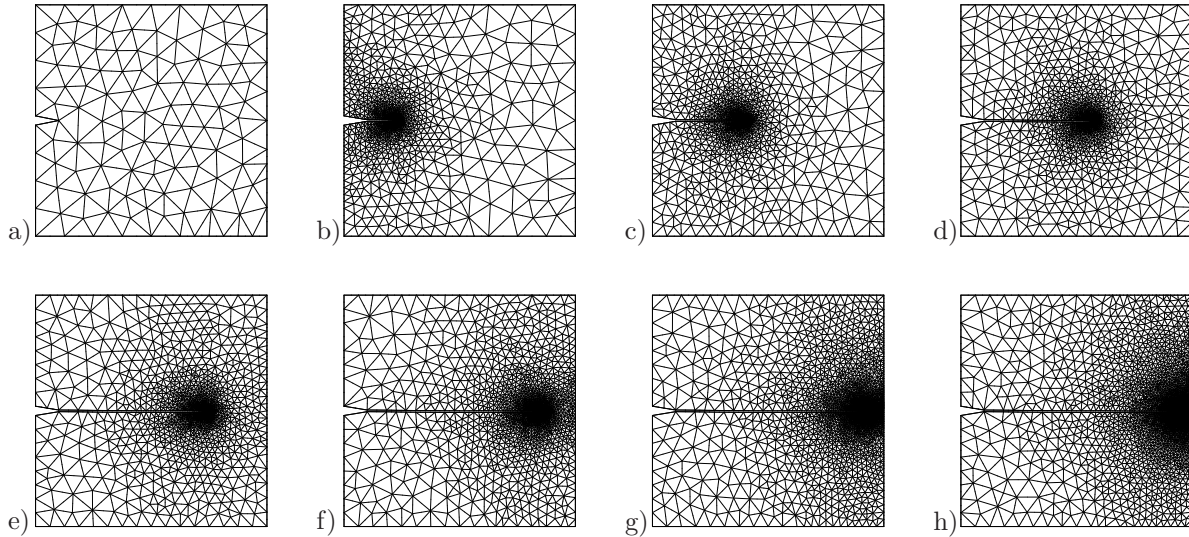


**Figure 7.8:** Progress of crack propagation and evolution of adaptively refined meshes. a) Primary triangulation with 212 elements. Different crack states containing b) 2271, c) 2615, d) 2363, e) 2732, f) 3554, g) 5919 and h) 8430 elements.

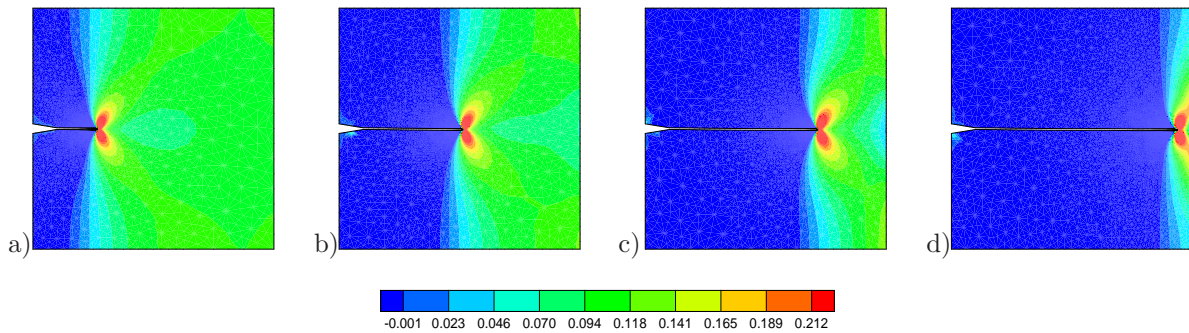


**Figure 7.9:** Distribution of  $P_{yy}$ -component of first Piola-Kirchhoff stresses during crack propagation. The crack tip singularity induces a stress concentration around the tip accompanied by a steep decrease for an increasing distance from the tip.

**7.5.2. Three Point Bending Test.** The second example is concerned with a non-symmetric three point bending test. This example has been studied experimentally and numerically by BITTENCOURT ET AL. [16] and, more recently, by PHONGTHANAPANICH & DECHAUMPHAI [147]. The system with boundary conditions is visualized in Figure 7.10. The diameter of the holes is  $d = 0.4$  mm. The specimen is subjected to a displacement-driven deformation by prescribed incremental displacements  $\Delta \bar{u} = 0.0001$  mm at the midpoint of the upper edge. The crack propagation is initiated by a notch at the lower left edge of the specimen. Two different geometries of this notch have been investigated. In the first setting, the notch is in a distance of  $a = 5.0$  mm from the middle axis of the specimen and has a length of  $b = 1.5$  mm. For the second geometry the values are  $a = 6.0$  mm and  $b = 1.0$  mm.

The primary uniform meshes consist of 397 and 415 triangular elements for geometry I and II, respectively. For the first notch geometry, this triangulation is said to be insufficient right after the first displacement increment has been applied. After two refinement steps the improved mesh holds 702 elements and is successfully used for the next 29 load steps. Applying the subsequent displacement increment, the global adaptive criterion again is violated. Subsequent to two more adaptive refinement steps, the triangulation turns out



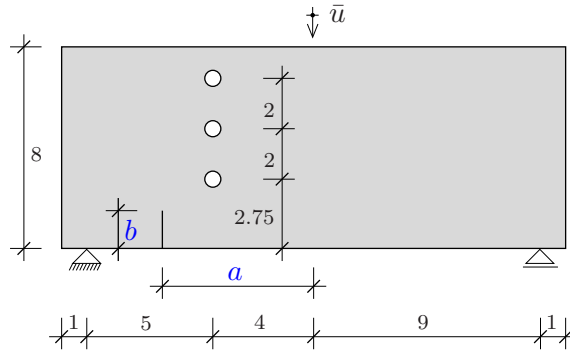


**Figure 7.10:** System and boundary conditions of three point bending test. Two different notch geometries are discussed, namely (i)  $a = 5$ ,  $b = 1.5$  and (ii)  $a = 6$ ,  $b = 1$ . All dimensions are given in [mm].

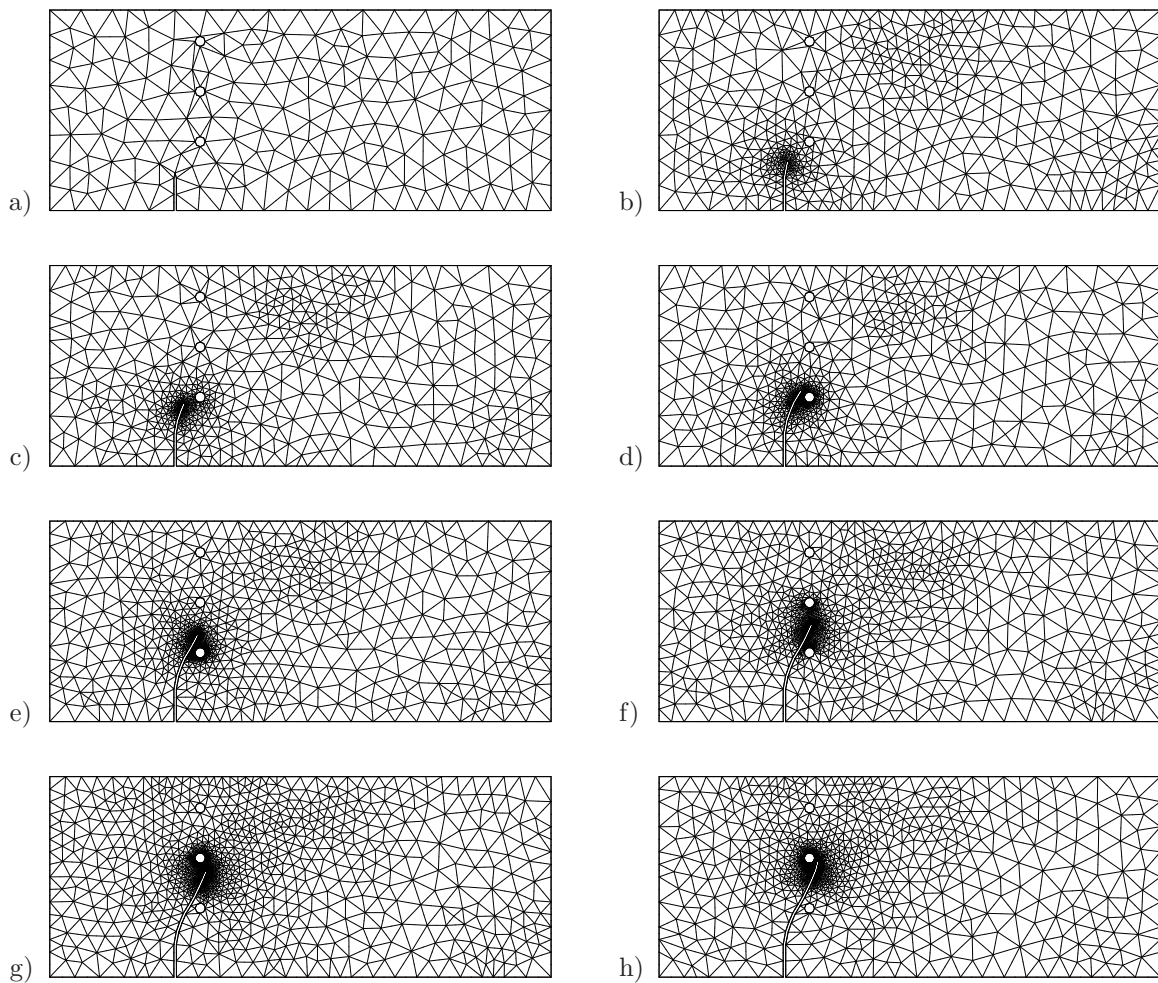


**Figure 7.11:** Crack propagation and development of refined meshes for notch geometry I. a) Primary triangulation with 397 elements. Different states of crack propagation. Meshes contain b) 967, c) 1083, d) 1247, e) 1679, f) 1933, g) 2532, and h) 2171 triangular elements.

to be sufficiently accurate and the crack criterion is checked. The norm of the crack tip force exceeds the critical value  $g_c$ . The crack tip node is moved in the direction of the driving force by the amount  $\Delta\gamma = 0.05h_{max}$  in terms of the prescribed maximum edge length  $h_{max} = 1.3$  mm. For the updated geometry model a new mesh is generated containing 934 elements and the current deformation step is recomputed. In the following,

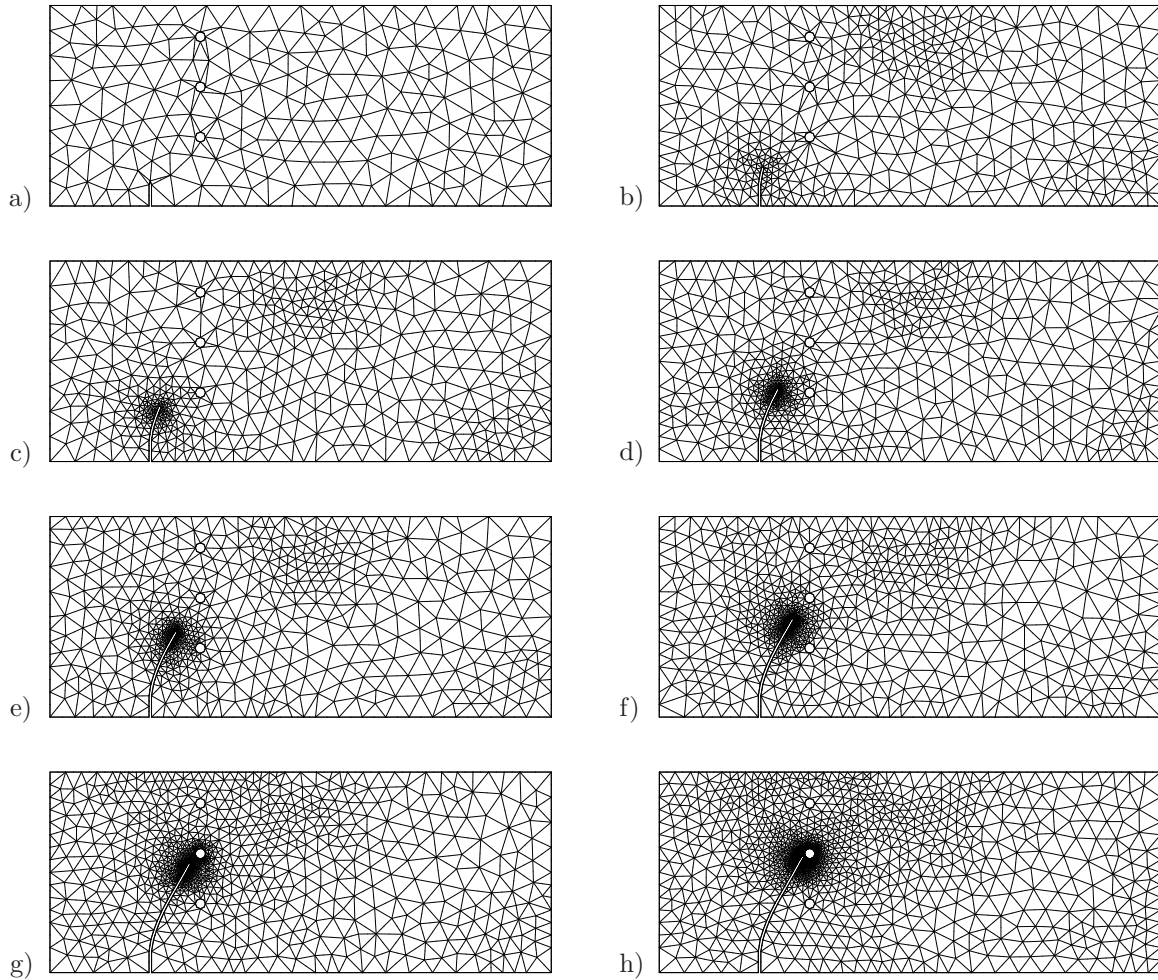


**Figure 7.12:** Crack propagation and development of refined meshes for notch geometry II. a) Primary triangulation with 415 elements. Different states of crack propagation. Meshes contain b) 847, c) 968, d) 1235, e) 1226, f) 1637, g) 2104, and h) 3005 triangular elements.

no further displacement increment can be applied as the norm of the crack tip force does not fall below the critical threshold  $g_c$  any more. The crack propagates accompanied by adaptive remeshing until the simulation terminates. The simulation based on the second notch geometry deals with the same characteristics, however, the onset of crack propagation does not occur until a total displacement of  $\bar{u} = 0.0042$  mm is applied. The progress of crack propagation and the evolution of the adaptively refined meshes are depicted for both geometries in Figure 7.11 and Figure 7.12, respectively. The mesh is heavily densified around the crack tip and evolves together with the movement of the crack tip. The final meshes consist of 2171 and 3005 elements for geometry I and II. Carefully note that in the present example the influences of both the three holes as well as the Dirichlet boundary conditions on the mesh refinement have been neglected. Per definition, the holes represent an inhomogeneity within the material structure of the body while the boundary constraints being prescribed at single points of the finite element mesh cause singularities in the current triangulation. Both effects demand for mesh refinement. In present studies, these influences are suppressed by skipping the material forces in the respective regions in order to focus attention on the refinement at the crack tip and to allow for a precise visualization of the crack propagation process. As a matter of course, in case the crack tip zone intersects with these critical regions, the material forces do contribute to the

global and local adaptive criteria and therefore are not ignored. It is emphasized that this treatment does not pose any restriction to the staggered solution procedure as these inhomogeneities and singularities would only induce an *additional* refinement but would not effect the refinement around the crack tip. The evolution of the adaptively generated meshes renders a very good agreement with the results shown in [147].

The capability of the proposed procedure to predict curvilinear crack geometries is highlighted in Figure 7.13 by a comparison of the crack paths obtained by the numerical simulations to those gained from experiments, cf. [16]. Apparently, the results of the finite

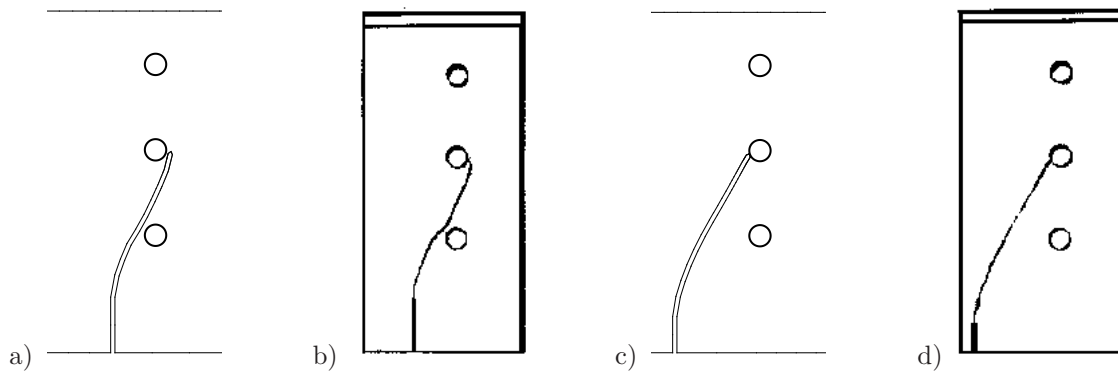


**Figure 7.13:** Comparison of crack trajectories obtained from the numerical simulation, a) and c), to those observed in experiments, b) and d), for both initial notch geometries. The pictures showing the experimental results are taken from BITTENCOURT ET AL. [16].

element analyses are in very good agreement with the experimental observations. For the first notch geometry, the crack trajectory intersects the axis of the three holes and reaches the middle hole from the right hand side. In contrast, for the second geometry the crack directly moves towards the left hand side of the hole.

Finally, the distribution of the  $P_{xx}$ -component of the first Piola-Kirchhoff stress tensor is visualized in Figure 7.14 and Figure 7.15 for different states of the crack propagation process. The subscript  $x$  denotes the horizontal axis. The sharp geometric singularity at

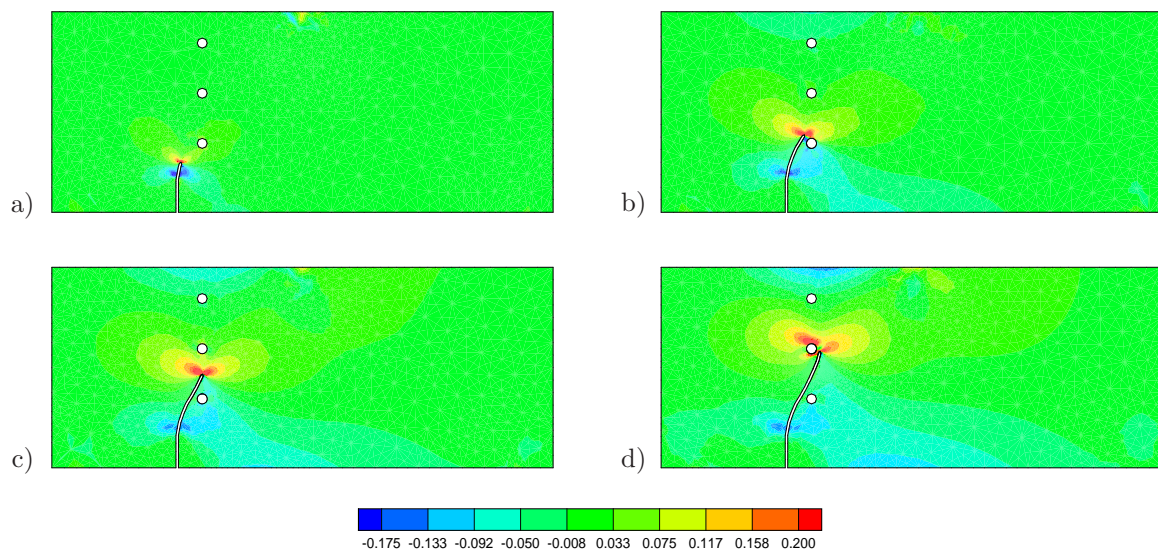


**Figure 7.14:** Notch geometry I: Evolution of first Piola-Kirchhoff stresses  $P_{xx}$  during crack propagation. The crack tip singularity induces a concentration of the stress field.



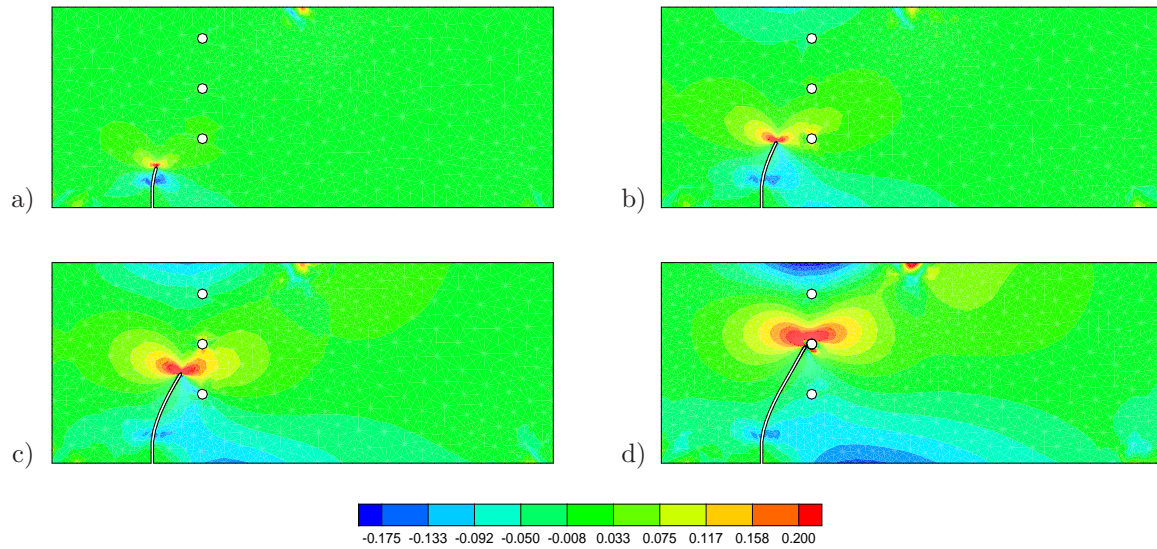


**Figure 7.15:** Notch geometry II: Distribution of first Piola-Kirchhoff stresses  $P_{xx}$  for different crack states. The stress concentration is caused by the crack tip singularity.

the crack tip induces a concentration of the tensile stresses in the region around the tip with the maximum value occurring directly at the tip.

**7.5.3. Tension Test of Planar Sheet with Two Holes.** In the last example, the tension test of a plane sheet including two holes is discussed, see Figure 7.16 for a sketch of the system. This boundary value problem has been studied by BOUCHARD ET AL. [19]

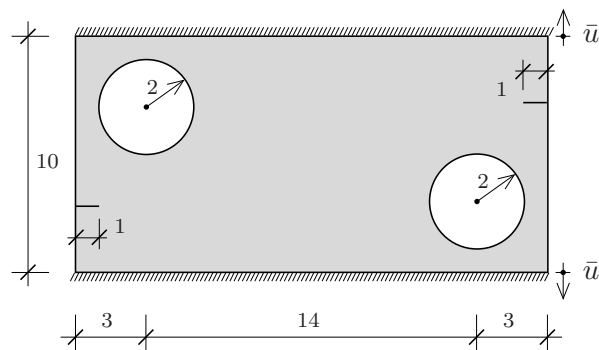


**Figure 7.16:** System and boundary conditions of a tension test of planar sheet with two holes. All dimensions are given in [mm].

and BOUCHARD, BAY & CHASTEL [18] investigating adaptive remeshing strategies and different criteria for crack propagation. The radius of the holes is one fifth of the heights of the specimen. The upper and lower edges are clamped with the vertical direction being subjected to prescribed displacement increments  $\Delta\bar{u} = 0.0001$  mm. The goal of the subsequent analyses is to show the ability of the staggered solution procedure to capture the evolution of multiple cracks. To be precise, two cracks are initiated by two notches at the vertical boundary edges of the body. In the algorithmic implementation, this situation is handled by an independent successive treatment of both crack tips according to the update algorithm given in Box 7.1 above.

The primary triangulation holds 429 elements. After the first deformation step adaptive refinement has to be done yielding an improved mesh with 683 elements. This triangulation is said to be sufficiently accurate up to a deformation of  $\bar{u} = 0.0014$  mm. By

application of the next displacement increment at first the global adaptive criterion is violated and two further refinement steps are needed until the global crack criterion can be enforced for a mesh with 796 elements. At both notches the crack starts propagating. The crack propagation process along with the development of the refined meshes is depicted in Figure 7.17. It is well observable that each crack tip has its own refinement.

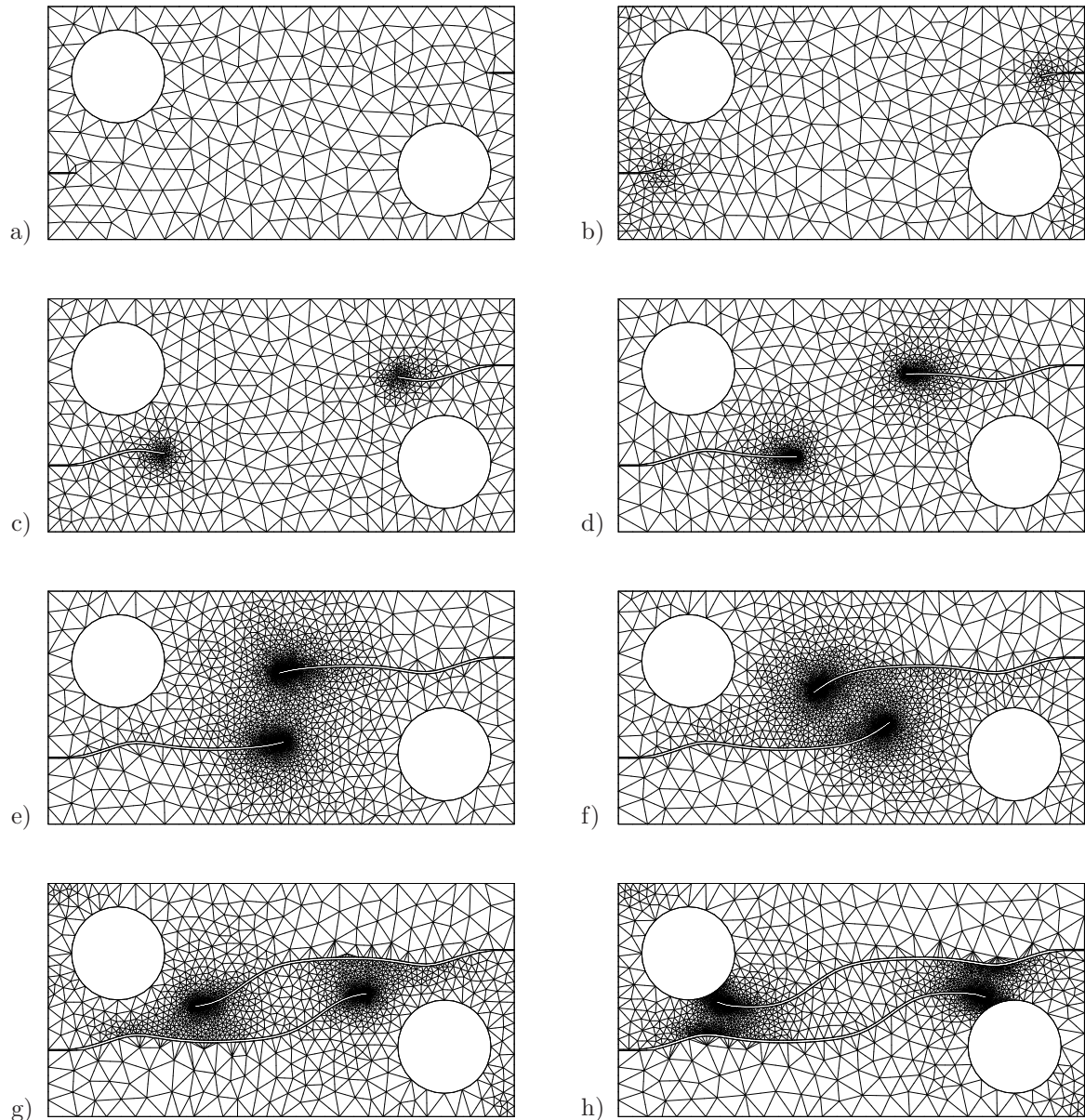


**Figure 7.17:** Evolution of adaptively refined meshes during crack propagation. Each crack tip possesses its own refinement. a) Primary triangulation with 429 elements, b)–g) intermediate states, and h) final mesh containing 4302 elements.

evolve in a symmetric fashion and undergo multiple changes in their direction. At first, the densified areas of the mesh concentrate in a small radius around the tips containing about 1000 elements, Figure 7.17b)–d). When the crack fronts reach the vertical middle axis of the specimen, Figure 7.17e), f), these zones intersect and the number of elements rapidly increases to a total number of approximately 4000 elements. This characteristic still holds for further crack propagation as the crack tips approach the profile of the other crack, Figure 7.17g), and finally, again showing a distinct change in their orientation, move towards

the holes, Figure 7.17h). The final mesh consists of 4302 elements. However, during this period of the simulation the crack does not propagate at a constant external deformation but further displacement increments are applied in between up to a final deformation of  $\bar{u} = 0.0096$  mm. The crack patterns gained from the computation show a good agreement with the results presented in [19, 18].

The change in the distribution of the first Piola-Kirchhoff stresses  $P_{yy}$  with  $y$  denoting the vertical axis is highlighted in Figure 7.18. As already known from the previous exam-

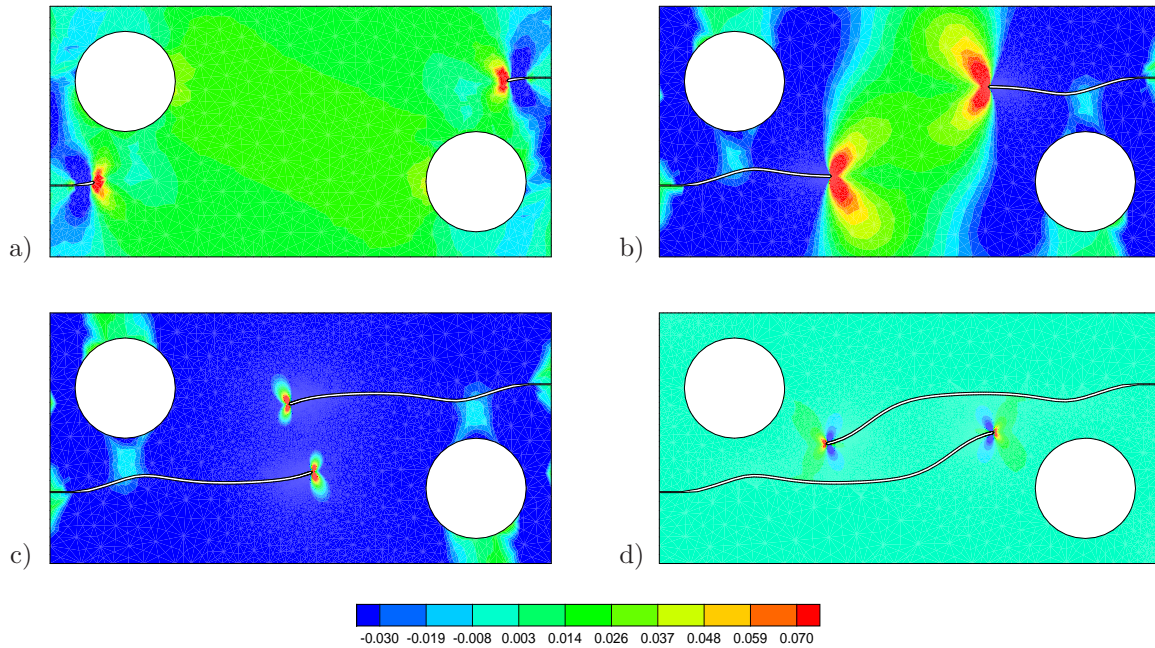


**Figure 7.18:** Distribution of  $P_{yy}$ -component of first Piola-Kirchhoff stress tensor during the crack propagation process. The crack tip singularity induces a stress concentration around the tip. Due to an increase of the externally applied deformation, the contour plot d) showing the final period of the simulation, is characterized by a different stress level.

ples, the maximum tensile stress localizes in the process zone surrounding the crack tip caused by the geometric singularity. Due to the afore-mentioned further increase of the prescribed deformation, the stress distribution or rather the stress level obtained for the final part of the computation, Figure 7.18d), significantly differs from that of the initial steps. However it still shows the same characteristic in view of the concentration of the stress field surrounding the moving crack front.

In summary, the configurational-force-based staggered solution procedure has been successfully used for the  $h$ -adaptive simulation of brittle crack propagation. The movement of the crack tip zone is accompanied by the evolution of the finite element mesh. The adaptive refinement at the tip ensures a sufficient accuracy in view of the computation of the mechanical fields, in particular the configurational nodal forces and the crack tip driving force. From the numerical point of view, the algorithmic setting turns out to be extremely efficient and robust. The method proves to be capable of the prediction of straight and curvilinear crack profiles even in case of multiple cracks.



## 8. Conclusion

The thesis provides a discussion about several aspects of configurational mechanics. To be precise, various theoretical approaches, algorithmic treatments and a broad spectrum of numerical applications are investigated.

From the theoretical point of view, two different approaches are presented. With regard to problems of thermo-inelasticity and dissipative processes in elasticity, namely fracture mechanics, the introduction of a global dissipation postulate turns out to be a powerful and straightforward procedure. This postulate is established by means of a comparison between the external and the internal power produced during the thermo-mechanical deformation of an inelastic solid subjected to the restrictions arising from the second law of thermodynamics in order to guarantee thermodynamical consistency. The exploitation of this postulate in the sense of a Coleman-type procedure results in the dual material and spatial field equations. The remaining reduced dissipation inequality is used for the formulation of either a set of evolution equations for the inelastic state variables or an algorithm for the crack evolution problem. For thermo-mechanically coupled problems under consideration, an evolution equation for the temperature field is obtained starting from the balance of internal energy.

In view of problems of structural dynamics, a true variational formulation based on Hamilton's principle is elaborated. The principle states the action functional to be stationary and thus demands a vanishing first variation of the action functional. The variation is performed with respect to the spatial and material coordinates as well as the time. The corresponding Euler-Lagrange equations of the variational framework are the equations of spatial and material motion and the balance of kinetic energy. The global counterparts of the dual equations of motion represent the balance of linear momentum with respect to the Eulerian setting in terms of physical Newtonian forces and the balance of pseudomomentum with respect to the Lagrangian framework in terms of material Eshelbian forces. The whole scenario is related to a variational approach in terms of Noether's theorem including a brief discussion about conservation laws.

The numerical treatment is carried out by means of the finite element method. In this sense, the dual spatial-material balance equations and, in case of thermo-mechanical coupling, the temperature evolution equation are recast into discrete nodal balances. For the solution of this set of coupled equations, a staggered solution procedure is adopted with the material subproblem being implemented as a mere postprocessing procedure subsequent to the solution of the spatial problem. The strategy is applied to the analyses of descriptive boundary value problems, namely the thermo-mechanical deformation of Cook's membrane and the free oscillation of a strip.

The second main part of the thesis is devoted to the use of configurational forces in various fields of computational mechanics. At first, the application in the context of topology optimization is investigated. Using the terminology of optimization, the objective function is the potential energy of the system while the spatial and material coordinates constitute the designvariables. In contrast to the just-mentioned staggered strategy, a simultaneous solution of the dual spatial-material problem is performed. This procedure is denoted a variational arbitrary Lagrangian-Eulerian (ALE) formulation and results in a simultaneous equilibration of physical and configurational forces. Two different solution algorithms are discussed, namely a conjugate gradient method and a Newton-Raphson iteration scheme including a viscous-type damping technique. The variational setting is

specified to  $r$ -adaptive mesh improvement and to structural optimization of truss structures. Representative model problems are analyzed with the coupled simulation displaying a superior solution with respect to the energetic state of the system compared to a purely spatial simulation.

In the next section, a configurational-force-based  $h$ -adaptive strategy is proposed. In contrast to the continuous setting, where the spatial and material balance equations are completely equivalent, the discretization, or rather triangulation in terms of a finite element mesh of an otherwise homogeneous body induces an artificial inhomogeneity in the system. This results in the occurrence of numerically caused discrete configurational nodal forces breaking the equivalence of the continuous setting. Adopting the afore-mentioned staggered solution procedure, these out of balance forces are used in a postprocessing step to set up a global criterion used for the decision on mesh refinement and an element criterion governing the local refinement algorithm. The outline of the numerical treatment incorporates the adaptive mesh generation and the mapping of the state variables. The procedure is applied to problems of finite elasticity and (thermo-)plasticity including the quasi-static and the dynamical framework. Representative boundary value problems are investigated dealing with both the two- and the three-dimensional case. To appraise their quality, the results of the adaptive simulations are compared to those obtained from benchmark analyses. To this end, for the two-dimensional elastic case an alternative error estimator is used, whereas for the other cases coarse and fine mesh simulations are performed. The material-force-based adaptive strategy provides results very close to the benchmark simulations. The advantages of the adaptive strategy with respect to the computing time due to a significant reduction of the nodal degrees of freedom are emphasized.

In the final chapter a material-force-based algorithm for crack propagation in brittle materials is elaborated. Starting from the global dissipation postulate, the Coleman-type exploitation procedure ends up with the reduced dissipation inequality. An algorithm for the crack evolution problem is derived by application of the principle of maximum dissipation. The numerical implementation again uses the staggered solution scheme. Subsequent to the spatial computation, the discrete material nodal forces are evaluated. The decision on crack propagation is made by means of a Griffith-type criterion comparing the amount of the material driving force at the crack tip with a given critical energy release rate. In case of crack propagation, the finite element mesh is discarded and the crack propagation process is performed exclusively on the geometry model. The new mesh is generated in terms of a element refinement criterion evaluated from the numerically caused nodal forces of the discarded mesh. The process of crack propagation is accompanied by  $h$ -adaptive remeshing based on the refinement strategy introduced in the previous section guaranteeing a suitable resolution of the crack tip region. Finally, different boundary problems are discussed. Thereby, the proposed method proves to be capable of the prediction of curved crack paths and of handling the propagation of multiple cracks.

## A. A Reminder of Eshelby's Reasoning

### A.1. Eshelby's Concept of a Force on a Singularity

In his pioneering work, ESHELBY [42] showed that the value of a path-independent integral surrounding a defect included in an elastic continuum can be interpreted as the change in the total energy associated with an unit defect translation. The subsequent treatments follow the physical interpretation given by ESHELBY [44]. He suggested the following thought experiment. Figure A.1a) shows an elastic body  $\mathcal{B}$  containing a singularity enclosed by an arbitrary surface  $S$ . The body is subjected to mechanical loading, e.g. by the traction field  $\mathbf{t}$ . This body is called the *original system*. Figure A.1b) represents

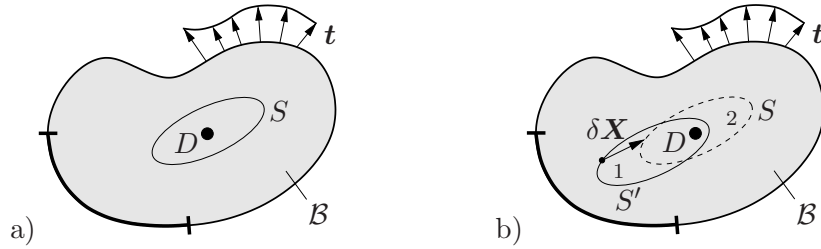


**Figure A.1:** Eshelby's thought experiment. a) Original system with defect  $D$  surrounded by a surface  $S$ . b) Replica with surrounding surface  $S'$  shifted by  $-\delta \mathbf{X}$ . Cutting out the material inside of  $S$  in the original system and replacing it by the suitably deformed material inside of  $S'$  of the replica models a *shift of the defect* by  $\delta \mathbf{X}$ . The change of energy at fixed spatial position defines the energy release rate associated with the translation of the defect.

an *exact replica* of the original body with surfaces  $S$  and  $S'$  marked out. The surface  $S'$  is the surface  $S$  that has suffered a shift  $-\delta \mathbf{X}$  in the *undeformed* state. If the material inside  $S$  of the original body is replaced by the material inside  $S'$  of the replica in the *deformed* state, a configuration arises that differs from the original one by a vector shift  $\delta \mathbf{X}$  of the defect. To compute the change in energy within this scenario, the following steps are performed:

*Step 1:* After both bodies, Figure A.1a) and Figure A.1b), have come to an equilibrium state under the mechanical loading, the material inside  $S$  in the original system is cut out and thrown away. Equivalent surface tractions on the resulting hole are applied to prevent the rest of the original system from relaxing.

*Step 2:* The material inside of  $S'$  from the replica is cut out and surface tractions are applied to prevent relaxation. The stored energies inside of  $S$  and  $S'$  are given by  $\Pi_{int,S} := \int_{vol(S)} \psi dV$  and  $\Pi_{int,S'} := \int_{vol(S')} \psi dV$ . Thereby,  $\psi = \rho_0 \Psi$  denotes the stored free Helmholtz energy per unit volume of the reference configuration. The energies differ by addition of energy in region 1 and subtraction of energy in region 2. For an infinitesimal amount of  $|\delta \mathbf{X}|$ , this difference is evaluated by integrating the flux of  $\psi$  over the surface  $S$

$$\delta \Pi_{int,1} := \Pi_{int,S'} - \Pi_{int,S} = \int_S \psi(-\delta \mathbf{X}) \mathbf{N} dA. \quad (\text{A.1})$$

Here,  $\mathbf{N}$  is the outward normal on  $S$ . At this stage there is no change in the energy in the material outside the hole in the original system, or in the energy of its loading mechanism.

*Step 3:* The material inside of  $S'$  is tried to be fitted into the hole of  $S$  of the original system. But since, by construction,  $S$  and  $S'$  can be made to coincide by a simple translation in the undeformed state they will not do so after deformation. In fact, for a suitable



translation to move it from the replica to the original system, the displacement on  $S'$  will differ from that on  $S$  for an infinitesimal amount of  $|\delta\mathbf{X}|$  by

$$\delta\mathbf{x} := \mathbf{x}_{S'} - \mathbf{x}_S = \mathbf{F}(-\delta\mathbf{X}) \quad (\text{A.2})$$

in terms of the deformation gradient  $\mathbf{F}$ . To fit  $S'$  into the hole of the original system, a displacement of an amount (A.2) has to be supplied on the surface of the hole. This requires work done at the negative traction  $(-\mathbf{t})$  on the hole, i.e.

$$\delta\Pi_{int,2} := \int_S \delta\mathbf{x}(-\mathbf{t})dA \quad (\text{A.3})$$

raising the energy in the material outside  $S$ . The surface tractions are computed via the Cauchy-type theorem  $\mathbf{t} = \mathbf{P}\mathbf{N}$  in terms of the first Piola-Kirchhoff stress tensor  $\mathbf{P}$ .

*Step 4:* Now  $S'$  can be fitted into  $S$  and welded across the interface. Though the displacements are continuous across the interface, the stresses differ by an order of  $\delta\mathbf{X}$ . As they are relaxed, the displacements would be of the order  $\delta\mathbf{X}$  and an amount of energy of the order  $(\delta\mathbf{X})^2$  is extracted but is ignored in comparison to (A.1), (A.3). Now, the defect in the original body has moved by  $\delta\mathbf{X}$ . The total energy change during this procedure is

$$\delta\Pi_{int} = \delta\Pi_{int,1} + \delta\Pi_{int,2} = -\delta\mathbf{X} \int_S [\psi\mathbf{1} - \mathbf{F}^T\mathbf{P}] \mathbf{N}dA. \quad (\text{A.4})$$

*Step 5:* The *configurational* or *material force* acting on the defect is defined by the negative gradient of the total energy of the body with respect to the change of position of the defect

$$\mathbf{J} := -\left(\frac{\partial\Pi_{int}}{\partial\mathbf{X}}\right)^{\text{expl}}. \quad (\text{A.5})$$

The abbreviation  $\left(\frac{\partial(\bullet)}{\partial\mathbf{X}}\right)^{\text{expl}}$  – the expressions  $\frac{\partial}{\partial\mathbf{X}}(\bullet)^{\text{expl}}$  and  $\partial_{\mathbf{X}}(\bullet)^{\text{expl}}$  will also be used – denotes the *explicit* derivative of the quantity  $(\bullet)$  with respect to the material coordinate  $\mathbf{X}$  due to the *explicit* dependence of  $(\bullet)$  on  $\mathbf{X}$ . Comparing (A.4) and (A.5), the configurational force can be expressed by the integral

$$\mathbf{J} = \int_S \boldsymbol{\Sigma}\mathbf{N} dA \quad \text{with} \quad \boldsymbol{\Sigma} := \psi\mathbf{1} - \mathbf{F}^T\mathbf{P}. \quad (\text{A.6})$$

The purely material second order tensor  $\boldsymbol{\Sigma}$  is referred to as the *Maxwell tensor of elasticity*, ESHELBY [42], the *energy-momentum tensor*, ESHELBY [43, 44], or nowadays the *Eshelby (stress) tensor*. In the sense of the above idea, the material force, i.e. the path-independent integral  $\mathbf{J}$  over a surface  $S$  surrounding the defect, represents the energy release rate.

## A.2. Eshelby's Concept of a Force on an Inhomogeneity

The subsequent developments directly refer to ESHELBY [42]. The goal is to compute the configurational force acting on an inhomogeneity, i.e. a region of a body  $\mathcal{B}$  where material properties such as elasticity coefficients vary pointwise with respect to the material. Consider the particular case of small strain kinematics and assume that the elastic constants, and hence the fourth order elasticity moduli  $\mathbb{E}$ , depend on three parameters  $\boldsymbol{\xi} = \xi_{a=1,2,3}$

$$\mathbb{E} = \mathbb{E}_{ijkl} = \mathbb{E}_{ijkl}(x_a - \xi_a) = \mathbb{E}(\mathbf{x} - \boldsymbol{\xi}). \quad (\text{A.7})$$

On the surface  $\partial\mathcal{B}$  of the body  $\mathcal{B}$  fixed tractions  $\mathbf{t}$  are applied. Using Cauchy's theorem,  $\mathbf{t} = \boldsymbol{\sigma}\mathbf{n}$ , with  $\boldsymbol{\sigma}$  denoting the Cauchy stress tensor, this condition reads

$$\frac{\partial}{\partial \boldsymbol{\xi}} \mathbf{t} = \frac{\partial}{\partial \boldsymbol{\xi}} (\boldsymbol{\sigma}\mathbf{n}) = \mathbf{0} \quad \text{on } \partial\mathcal{B}. \quad (\text{A.8})$$

The external potential energy  $\Pi_{ext}$  of the system, i.e. the potential of the external physical loading, is computed in terms of the displacement field  $\mathbf{u}$  and the surface tractions  $\mathbf{t}$  based on the assumption that physical volume forces are neglected,  $\bar{\boldsymbol{\gamma}}_0 = \mathbf{0}$ . The change of the external potential energy with respect to a change  $\delta\boldsymbol{\xi}$  of the parameters  $\boldsymbol{\xi}$  is

$$-\frac{\partial}{\partial \boldsymbol{\xi}} \Pi_{ext} = \frac{\partial}{\partial \boldsymbol{\xi}} \int_{\partial\mathcal{B}} \mathbf{u} \cdot \mathbf{t} \, dA = \int_{\partial\mathcal{B}} \frac{\partial}{\partial \boldsymbol{\xi}} \mathbf{u} \cdot (\boldsymbol{\sigma}\mathbf{n}) \, dA = \frac{\partial}{\partial \boldsymbol{\xi}} \int_{\mathcal{B}} \boldsymbol{\sigma} : \boldsymbol{\varepsilon} \, dV \quad (\text{A.9})$$

where  $\boldsymbol{\varepsilon} := \text{sym}[\nabla\mathbf{u}]$  is the strain tensor of the infinitesimal theory. The last manipulation bases on the static equilibrium condition,  $\text{div } \boldsymbol{\sigma} = \mathbf{0}$ , and Gauss integration theorem. Using Hooke's law  $\boldsymbol{\sigma} = \mathbb{E} : \boldsymbol{\varepsilon}$ , the stored energy of a linear elastic body reads

$$\Pi_{int} = \int_{\mathcal{B}} \frac{1}{2} \boldsymbol{\varepsilon} : \mathbb{E} : \boldsymbol{\varepsilon} \, dV = \int_{\mathcal{B}} \frac{1}{2} \boldsymbol{\sigma} : \boldsymbol{\varepsilon} \, dV. \quad (\text{A.10})$$

Hence, the change (A.9) of the external potential with respect to the parameters  $\boldsymbol{\xi}$  coincides with twice the change of the stored energy  $\Pi_{int}$ , i.e.  $-\partial\Pi_{ext}/\partial\boldsymbol{\xi} = 2\partial\Pi_{int}/\partial\boldsymbol{\xi}$ . The *configurational* or *material force* acting on the inhomogeneity is defined by

$$\mathbf{J} := \frac{\partial\Pi_{int}}{\partial\boldsymbol{\xi}} = -\frac{1}{2} \int_{\mathcal{B}} \boldsymbol{\varepsilon} : \left( \frac{\partial}{\partial\boldsymbol{\xi}} \mathbb{E} \right) : \boldsymbol{\varepsilon} \, dV. \quad (\text{A.11})$$

In order to proof that this representation fits the above definition (A.6), consider two material bodies of the same size and shape with different elastic constants including an inhomogeneity as indicated in (A.7). Both bodies are loaded by the same surface traction  $\mathbf{t}$  on the boundary  $\partial\mathcal{B}$ . The difference between the stored energies of both systems is

$$\Delta\Pi_{int} = \frac{1}{2} \int_{\mathcal{B}} \bar{\boldsymbol{\varepsilon}} : \bar{\mathbb{E}} : \bar{\boldsymbol{\varepsilon}} - \boldsymbol{\varepsilon} : \mathbb{E} : \boldsymbol{\varepsilon} \, dV = \frac{1}{2} \int_{\mathcal{B}} \bar{\boldsymbol{\sigma}} : \bar{\boldsymbol{\varepsilon}} - \boldsymbol{\sigma} : \boldsymbol{\varepsilon} \, dV. \quad (\text{A.12})$$

As for both bodies the same surface tractions are applied, the boundary conditions  $\boldsymbol{\sigma}\mathbf{n} = \bar{\boldsymbol{\sigma}}\mathbf{n} = \mathbf{t}$  on  $\partial\mathcal{B}$  result in a vanishing difference in the external potentials  $\Delta\Pi_{ext} = 0$ . By substitution of the spatial equilibrium condition,  $\text{div } \boldsymbol{\sigma} = \text{div } \bar{\boldsymbol{\sigma}} = \mathbf{0}$ , this identity yields

$$\Delta\Pi_{ext} = \int_{\partial\mathcal{B}} \mathbf{u} \cdot (\bar{\boldsymbol{\sigma}} - \boldsymbol{\sigma})\mathbf{n} \, dA = \int_{\mathcal{B}} (\bar{\boldsymbol{\sigma}} - \boldsymbol{\sigma}) : \boldsymbol{\varepsilon} \, dV = 0. \quad (\text{A.13})$$

By combination of (A.12) and (A.13), in fact being valid in terms of either  $\boldsymbol{\varepsilon}$  or  $\bar{\boldsymbol{\varepsilon}}$ , and again substitution of Hooke's law of linear elasticity the energy difference appears as

$$\Delta\Pi_{int} = \frac{1}{2} \int_{\mathcal{B}} \boldsymbol{\sigma} : \bar{\boldsymbol{\varepsilon}} - \bar{\boldsymbol{\sigma}} : \boldsymbol{\varepsilon} \, dV = \frac{1}{2} \int_{\mathcal{B}} \bar{\boldsymbol{\varepsilon}} : (\mathbb{E} - \bar{\mathbb{E}}) : \boldsymbol{\varepsilon} \, dV. \quad (\text{A.14})$$

For the assumption of small changes  $|\Delta\xi|$ , the limit of the ratio of the energy change  $\Delta\Pi_{int}$  with respect to a change  $\Delta\xi$  of the parameters  $\xi$  results in the derivative

$$\frac{\partial\Pi_{int}}{\partial\xi} = -\frac{1}{2} \int_{\mathcal{B}} \varepsilon : \left( \frac{\partial}{\partial\xi} \mathbb{E} \right) : \varepsilon \, dV. \quad (\text{A.15})$$

This expression equals definition (A.11) of the configurational force acting on the inhomogeneity. This intermediate result can be transformed as follows

$$\begin{aligned} \mathbf{J} &= -\frac{1}{2} \int_{\mathcal{B}} \varepsilon : \left( \frac{\partial}{\partial\xi} \mathbb{E} \right) : \varepsilon \, dV \stackrel{(\text{A.7})}{=} \frac{1}{2} \int_{\mathcal{B}} \varepsilon : \left( \frac{\partial}{\partial\mathbf{x}} \mathbb{E} \right) : \varepsilon \, dV \\ &= \frac{1}{2} \int_{\mathcal{B}} \frac{\partial}{\partial\mathbf{x}} (\varepsilon : \mathbb{E} : \varepsilon) - 2(\varepsilon : \mathbb{E}) : \left( \frac{\partial}{\partial\mathbf{x}} \varepsilon \right) \, dV \\ &= \int_{\mathcal{B}} \left( \frac{1}{2} \varepsilon_{ij} \mathbb{E}_{ijkl} \varepsilon_{kl} \right)_{,m} - \sigma_{kl} \varepsilon_{kl,m} \, dV = \int_{\mathcal{B}} \psi_{,m} - \sigma_{kl} u_{kl,m} \, dV \\ &= \int_{\mathcal{B}} (\psi \delta_{ml})_{,l} - (\sigma_{kl} u_{km})_{,l} + (\sigma_{kl,l} u_{km}) \, dV = \int_{\mathcal{B}} (\psi \delta_{ml} - \sigma_{kl} u_{km})_{,l} \, dV \end{aligned} \quad (\text{A.16})$$

where the compatibility of the displacement gradient,  $u_{i,jk} = u_{i,kj}$ , the definition of the linear elastic free energy,  $\psi = \psi(\varepsilon) = \frac{1}{2} \varepsilon : \mathbb{E} : \varepsilon$ , and the spatial equilibrium condition  $\text{div } \boldsymbol{\sigma} = \sigma_{kl,l} = \mathbf{0}$  have been employed. By application of Gauss integration theorem it is readily shown that (A.16) coincides with representation (A.6) of the configurational force

$$\mathbf{J} = \int_{\partial\mathcal{B}} \boldsymbol{\Sigma} \mathbf{n} \, dA \quad \text{with} \quad \boldsymbol{\Sigma} := \psi \mathbf{1} - \nabla^T \mathbf{u} \boldsymbol{\sigma} \quad (\text{A.17})$$

in terms of the small strain Eshelby tensor  $\boldsymbol{\Sigma}$  (or Maxwell tensor of elasticity or energy-momentum tensor) and the outward normal  $\mathbf{n}$  of the surface  $\partial\mathcal{B}$  of the body  $\mathcal{B}$ .

**Remark A.1:** Note that a one-dimensional formulation of the path-independent integral, or rather material force  $\mathbf{J}$  renders the so-called  $J$ -integral of fracture mechanics introduced by RICE [152].

**Remark A.2:** As, in the author's opinion, memorable aspect has been emphasized by MAUGIN [99]: When he introduced material forces acting on singularities and inhomogeneities, ESHELBY [44] remarked that *this kind of force, in a sense fictitious, is introduced to give a picturesque description of energy changes (author's emphasis), and they must not be confused with the ordinary surface or body forces acting on the material.* MAUGIN links this statement with a citation taken from JAMMER [73] (a new edition is quoted here), who pointed out, that *to introduce the term 'force' as an explanatory element in the theory of physical sciences means to develop a misleading vocabulary.*

Consequently, when using the expression configurational or material force, one should carefully remember the afore-mentioned origin of this quantity as a measure of the change in energy of an elastic continuum upon movement of a defect or an inhomogeneity within the material configuration of the body.

## B. Time Derivatives of Fundamental Kinematic Objects

The rate expressions of the fundamental kinematic quantities required for the exploitation of the global dissipation postulate are derived. Recall definition (3.4) of the non-linear deformation map

$$\varphi_t(\mathbf{X}) = \boldsymbol{\xi}_t(\boldsymbol{\theta}) \circ \boldsymbol{\Xi}_t^{-1}(\mathbf{X}) \quad (\text{B.1})$$

in terms of the spatial and material configurational maps  $\boldsymbol{\xi}_t(\boldsymbol{\theta}) = \boldsymbol{\xi}(\boldsymbol{\theta}, t)$  and  $\boldsymbol{\Xi}_t(\boldsymbol{\theta}) = \boldsymbol{\Xi}(\boldsymbol{\theta}, t)$ , cf. (3.3).  $\boldsymbol{\theta}$  are the time-independent coordinates of the parameter space  $\Omega$ . (B.1) can be solved for the spatial configurational map

$$\boldsymbol{\xi}_t(\boldsymbol{\theta}) = \varphi_t(\mathbf{X}) \circ \boldsymbol{\Xi}_t(\boldsymbol{\theta}) = \varphi(\mathbf{X}, t) \circ \boldsymbol{\Xi}(\boldsymbol{\theta}, t) = \varphi(\boldsymbol{\Xi}(\boldsymbol{\theta}, t), t) = \boldsymbol{\xi}(\boldsymbol{\theta}, t) \quad (\text{B.2})$$

allowing for the evaluation of the time derivative by means of Leibniz' formula

$$\frac{\partial}{\partial t} \boldsymbol{\xi}(\boldsymbol{\theta}, t) = \frac{\partial}{\partial t} \varphi(\mathbf{X}, t) + \frac{\partial}{\partial \mathbf{X}} \varphi(\mathbf{X}, t) \frac{\partial}{\partial t} \boldsymbol{\Xi}(\boldsymbol{\theta}, t) \quad (\text{B.3})$$

with the typical split into local and convective part. As  $\boldsymbol{\theta} = \text{const.}$ , partial and total time derivatives of the configurational maps commute. In this equation the dual partial derivatives of the non-linear deformation map with respect to the Lagrangian space-time  $(\mathbf{X}, t)$  are identified, namely the deformation gradient and the spatial velocity

$$\mathbf{F} = \frac{\partial}{\partial \mathbf{X}} \varphi(\mathbf{X}, t) = \nabla_{\mathbf{X}} \varphi_t(\mathbf{X}) \quad \text{and} \quad \mathbf{v} = \frac{\partial}{\partial t} \varphi(\mathbf{X}, t). \quad (\text{B.4})$$

Upon introduction of the abbreviations for the time derivatives  $\dot{\boldsymbol{\xi}} = \partial \boldsymbol{\xi}(\boldsymbol{\theta}, t) / \partial t$  and  $\dot{\boldsymbol{\Xi}} = \partial \boldsymbol{\Xi}(\boldsymbol{\theta}, t) / \partial t$  the velocity  $\mathbf{v}$  can finally be expressed by

$$\mathbf{v} = \dot{\boldsymbol{\xi}} - \mathbf{F} \dot{\boldsymbol{\Xi}}. \quad (\text{B.5})$$

In the next step consider the partial derivative of the spatial configurational map with respect to the parameter coordinates  $\boldsymbol{\theta}$

$$\frac{\partial}{\partial \boldsymbol{\theta}} \boldsymbol{\xi}(\boldsymbol{\theta}, t) = \frac{\partial}{\partial \mathbf{X}} \varphi(\mathbf{X}, t) \frac{\partial}{\partial \boldsymbol{\theta}} \boldsymbol{\Xi}(\boldsymbol{\theta}, t) \Leftrightarrow \mathbf{j} = \mathbf{F} \mathbf{J} \quad (\text{B.6})$$

using the gradients  $\mathbf{j}$ ,  $\mathbf{J}$  of the material and spatial configurational maps introduced in (3.6). This relationship states the alternative representation of the deformation gradient  $\mathbf{F} = \mathbf{j} \mathbf{J}^{-1}$ . Next, the time derivative of (B.6) is computed by means of the product rule

$$\frac{\partial}{\partial t} \left( \frac{\partial}{\partial \boldsymbol{\theta}} \boldsymbol{\xi} \right) = \frac{d}{dt} \left( \frac{\partial}{\partial \mathbf{X}} \varphi \right) \frac{\partial}{\partial \boldsymbol{\theta}} \boldsymbol{\Xi} + \frac{\partial}{\partial \mathbf{X}} \varphi \frac{\partial}{\partial t} \left( \frac{\partial}{\partial \boldsymbol{\theta}} \boldsymbol{\Xi} \right) \quad (\text{B.7})$$

where the functional dependencies have been dropped for the sake of clarity. The crucial point of this derivative is that for the material gradient of the non-linear point map, i.e. the deformation gradient, the total time derivative has to be applied as the temporal change of the reference coordinates  $\mathbf{X}$  has to be taken into account as well. The derivatives of the spatial and material configurational map  $\boldsymbol{\xi}$  and  $\boldsymbol{\Xi}$  with respect to the coordinates  $\boldsymbol{\theta}$  and time  $t$  commute as the parameter coordinates  $\boldsymbol{\theta}$  are time-independent

$$\frac{\partial}{\partial \boldsymbol{\theta}} \dot{\boldsymbol{\xi}} = \frac{d}{dt} \mathbf{F} \frac{\partial}{\partial \boldsymbol{\theta}} \boldsymbol{\Xi} + \mathbf{F} \frac{\partial}{\partial \boldsymbol{\theta}} \dot{\boldsymbol{\Xi}}. \quad (\text{B.8})$$

By multiplication with the inverse of the gradient of the material configurational map this equation can directly be solved for the total time derivative of the deformation gradient

$$\frac{d}{dt}\mathbf{F} = \nabla_{\mathbf{X}}\dot{\boldsymbol{\xi}} - \mathbf{F}\nabla_{\mathbf{X}}\dot{\boldsymbol{\Xi}}. \quad (\text{B.9})$$

This multiplication coincides with a re-parameterization of the equation by the material coordinates  $\mathbf{X}$  which is also adopted by representation (B.5) of the velocity. Therefore, the time derivatives of the spatial and material configurational map

$$\dot{\boldsymbol{\xi}} = \frac{\partial}{\partial t}\boldsymbol{\xi} \circ \boldsymbol{\Xi}_t^{-1}(\mathbf{X}) \quad \text{and} \quad \dot{\boldsymbol{\Xi}} = \frac{\partial}{\partial t}\boldsymbol{\Xi} \circ \boldsymbol{\Xi}_t^{-1}(\mathbf{X}) \quad (\text{B.10})$$

in fact depend on the Lagrangian space-time  $(\mathbf{X}, t)$ , cf. (3.9). At last, consider the total temporal change of the material volume element

$$\frac{d}{dt}dV = \frac{d}{dt}[\det \mathbf{J} d\Omega] = \frac{d}{dt}[\det \mathbf{J}] d\Omega. \quad (\text{B.11})$$

The time derivative of  $d\Omega$  vanishes because the configuration  $\Omega$  is time-independent. The rate of the determinant of the gradient of the material configurational map is evaluated

$$\frac{d}{dt}[\det \mathbf{J}] = \det \mathbf{J} \mathbf{J}^{-T} : \frac{d}{dt}\mathbf{J} = \det \mathbf{J} (\mathbf{1} : (\frac{d}{dt}\mathbf{J})\mathbf{J}^{-1}). \quad (\text{B.12})$$

The total time derivative of the gradient of the material configurational map can be replaced by the partial one as the coordinates  $\boldsymbol{\theta}$  of the parameter space are time-independent. The contraction of the derivative and the inverse of  $\mathbf{J}$  can be reformulated

$$(\frac{d}{dt}\mathbf{J})\mathbf{J}^{-1} = (\frac{d}{dt}(\frac{\partial}{\partial \boldsymbol{\theta}}\boldsymbol{\Xi}))\mathbf{J}^{-1} = (\frac{\partial}{\partial \boldsymbol{\theta}}(\frac{\partial}{\partial t}\boldsymbol{\Xi}))\mathbf{J}^{-1} = \nabla_{\mathbf{X}}\dot{\boldsymbol{\Xi}} \quad (\text{B.13})$$

again inducing the re-parameterization of  $\dot{\boldsymbol{\Xi}}$ . At the end, the total time derivative of the volume element  $dV$  of the reference configuration is given by

$$\frac{d}{dt}dV = \frac{d}{dt}dV = (\mathbf{1} : \nabla_{\mathbf{X}}\dot{\boldsymbol{\Xi}}) dV. \quad (\text{B.14})$$

Apparently, this development matches the derivation of the temporal change of the Eulerian volume element outlined in the context of equation (2.23) in Section 2.1.5.

### C. Enhanced Strain Formulation

The global formulation introduced in Section 3.5.1 is combined with an enhanced strain formulation as proposed in Section 3.6.2. The enhanced strain formulation bases on the method of incompatible modes which dates back to the works of WILSON, TAYLOR, DOHERTY & GHABOUSSI [188] and TAYLOR, BERESFORD & WILSON [181]. A variational formulation starting from the Euler-Lagrange equations associated with the principle of Hu-Washizu has been proposed by SIMO & RIFAI [165]. The extension to the geometrically non-linear setting is due to SIMO & ARMERO [161] and SIMO, ARMERO & TAYLOR [162]. The investigations to follow are conceptually in line with MIEHE [117].

In the subsequent treatments the temperature problem is neglected for the sake of simplicity. This does not pose any restriction as in the sense of the thermo-mechanical operator split no coupling matrices occur within the stiffness matrix of the governing system of linear equations. The formulation is readily adjusted to the local approach by skipping the contributions arising from the supplementary constitutive subproblem.

Central to this particular finite element formulation is the enhancement of the deformation gradient by an incompatible part  $\nabla_X \varphi_E$  in addition to the standard compatible part, i.e. the gradient  $\nabla_X \varphi_C$  of the non-linear deformation map,

$$\mathbf{F} = \mathbf{F}_C + \mathbf{F}_E = \nabla_X \varphi_C + \nabla_X \varphi_E. \quad (\text{C.1})$$

The formulation to be elaborated refers to the current configuration. The representations outlined in Section 3.5, which actually were performed in the two-point setting, are reformulated in the purely Eulerian framework. To this end, the fundamental kinematic relationship (C.1) is rewritten in the spatial format

$$\nabla_x \varphi = \nabla_x \varphi_C + \nabla_x \varphi_E. \quad (\text{C.2})$$

The strong form equations can be summarized by

spatial equilibrium condition	$\operatorname{div} [J^{-1} \bar{\mathbf{s}}] + J^{-1} \bar{\boldsymbol{\gamma}}_0 = \mathbf{0}$	
stresses	$\bar{\mathbf{s}} = \boldsymbol{\tau}$	
loading-unloading	$\phi \leq 0, \quad \dot{\gamma} \geq 0$	(C.3)
kinematics	$\nabla_x \varphi = \nabla_x \varphi_C + \nabla_x \varphi_E$	
enhanced strain part	$\nabla_x \varphi_E = \mathbf{0}$	

with the Jacobian  $J = \det \mathbf{F}$  and the Kirchhoff stress tensor  $\boldsymbol{\tau} = J \boldsymbol{\sigma}$ . The strong form is valid in combination with the essential and natural boundary conditions (3.81)<sub>1</sub> and the decomposition (3.82) of the entire domain into active and non-active parts. Within the strong form the enhanced part of the deformation is set to zero. However, in the discrete finite element setting this equation is no longer satisfied identically resulting in the desired enhancement of the deformation gradient. To obtain the weak counterpart the strong form equations are multiplied by some arbitrary test functions and are integrated over the domain. For the equilibrium condition (C.3)<sub>1</sub> it follows

$$G_{\varphi_c} = \int_B \bar{\mathbf{s}} : \nabla_x \delta \varphi_C \, dV - G_{ext} = 0 \quad (\text{C.4})$$



in which the external part represents the influence of the physical forces, i.e. the surface tractions and the volume forces. The stress equation (C.3)<sub>2</sub> is, on the one hand, multiplied by the variation  $\nabla_x \delta \varphi_C$  of the compatible part and, on the other hand, by the variation  $\nabla_x \delta \varphi_E$  of the incompatible part of the spatial deformation gradient

$$\begin{aligned} G_{\tau_C} &= \int_{\mathcal{B}} \bar{\mathbf{s}} : \nabla_x \delta \varphi_C \, dV - \int_{\mathcal{B}} \boldsymbol{\tau} : \nabla_x \delta \varphi_C \, dV = 0 \\ G_{\tau_E} &= \int_{\mathcal{B}} \bar{\mathbf{s}} : \nabla_x \delta \varphi_E \, dV - \int_{\mathcal{B}} \boldsymbol{\tau} : \nabla_x \delta \varphi_E \, dV = 0. \end{aligned} \quad (\text{C.5})$$

With regard to the loading-unloading conditions (C.3)<sub>3</sub> the yield criterion is multiplied by a virtual scalar field  $\delta \dot{\gamma}$  whereas  $\dot{\gamma}$  is tested by a virtual yield criterion  $\delta \phi$

$$G_\phi = \int_{\mathcal{B}} \delta \dot{\gamma} \phi \, dV \leq 0 \quad \text{and} \quad G_\gamma = \int_{\mathcal{B}} \delta \phi \dot{\gamma} \, dV \geq 0. \quad (\text{C.6})$$

Finally, equation (C.3)<sub>5</sub> for the enhanced part of the deformation gradient is multiplied by a virtual stress field  $\delta \bar{\mathbf{s}}$

$$G_\tau = \int_{\mathcal{B}} \nabla_x \varphi_E : \delta \bar{\mathbf{s}} \, dV = 0. \quad (\text{C.7})$$

In the next step the  $L_2$ -orthogonality for the stresses  $\bar{\mathbf{s}} = \boldsymbol{\tau}$  and the enhanced strain part is adopted. This condition states that the spaces of the stresses and the enhanced strain field are perpendicular to each other. Consequently, (C.7) can be rewritten as

$$\int_{\mathcal{B}} \nabla_x \varphi_E : \bar{\mathbf{s}} \, dV = 0 \quad \Rightarrow \quad \int_{\mathcal{B}} \nabla_x \varphi_E : \delta \bar{\mathbf{s}} \, dV = \int_{\mathcal{B}} \nabla_x \delta \varphi_E : \bar{\mathbf{s}} \, dV = 0. \quad (\text{C.8})$$

Substitution of this intermediate result into (C.5)<sub>2</sub> as well as substitution of (C.5)<sub>1</sub> into (C.4) yield the weak form expressions

$$\begin{aligned} G_{\varphi_c} &= \int_{\mathcal{B}} \nabla_x \delta \varphi_C : \boldsymbol{\tau} \, dV - G_{ext} = 0, & G_\tau &= \int_{\mathcal{B}} \nabla_x \delta \varphi_E : \boldsymbol{\tau} \, dV = 0 \\ G_\phi &= \int_{\mathcal{B}} \delta \dot{\gamma} \phi \, dV \leq 0, & G_\gamma &= \int_{\mathcal{B}} \delta \phi \dot{\gamma} \, dV \geq 0 \end{aligned} \quad (\text{C.9})$$

valid in combination with the essential boundary conditions for the spatial deformation and the decomposition (3.82) of the entire domain into active and non-active parts. (C.9) represents a set of non-linear equations to be solved by a Newton-Raphson iteration scheme. In contrast to the order used in Section 3.5, the weak form equations are linearized prior to discretization. Anticipating the fact that the expression  $G_\gamma$  will appear in an incremental format after temporal discretization, only the first three weak forms are linearized, each with respect to the total deformation  $\varphi$  and the scalar parameter  $\gamma$ . The non-linearity in the deformation measures has to be taken into account resulting in the typical split of the stiffness matrix into a material tangent term and a geometric part.

The linearized expressions read

$$\begin{aligned}
\text{Lin } G_{\varphi_c} &= G_{\varphi_c} + \int_{\mathcal{B}} \nabla_x \delta \varphi_C : \Delta_\varphi \boldsymbol{\tau} \, dV + \int_{\mathcal{B}} \nabla_x \delta \varphi_C : \Delta_\gamma \boldsymbol{\tau} \, dV = 0 \\
&\quad + \int_{\mathcal{B}} \Delta_\varphi (\nabla_x \delta \varphi_C) : \boldsymbol{\tau} \, dV \\
\text{Lin } G_\tau &= G_\tau + \int_{\mathcal{B}} \nabla_x \delta \varphi_E : \Delta_\varphi \boldsymbol{\tau} \, dV + \int_{\mathcal{B}} \nabla_x \delta \varphi_E : \Delta_\gamma \boldsymbol{\tau} \, dV = 0 \quad (\text{C.10}) \\
&\quad + \int_{\mathcal{B}} \Delta_\varphi (\nabla_x \delta \varphi_E) : \boldsymbol{\tau} \, dV \\
\text{Lin } G_\phi &= G_\phi + \int_{\mathcal{B}} \delta \dot{\gamma} \Delta_\varphi \phi \, dV + \int_{\mathcal{B}} \delta \dot{\gamma} \Delta_\gamma \phi \, dV = 0.
\end{aligned}$$

The increments of the virtual compatible and enhanced spatial deformation gradients are evaluated according to

$$\Delta_\varphi (\nabla_x \delta \varphi_{C/E}) = \Delta (\nabla_X \delta \varphi_{C/E} \mathbf{F}^{-1}) = \nabla_X \delta \varphi_{C/E} \Delta \mathbf{F}^{-1} = -\nabla_x \delta \varphi_{C/E} \nabla_x \Delta \boldsymbol{\varphi} \quad (\text{C.11})$$

due to  $\Delta \mathbf{F}^{-1} = -\mathbf{F}^{-1} \nabla_x \Delta \boldsymbol{\varphi}$ . The increments of the Kirchhoff stress tensor with respect to  $\boldsymbol{\varphi}$  and  $\gamma$  are given by

$$\Delta_\varphi \boldsymbol{\tau} = \boldsymbol{\mathfrak{c}} : \nabla_x \Delta \boldsymbol{\varphi} + \nabla_x \Delta \boldsymbol{\varphi} \boldsymbol{\tau} + \boldsymbol{\tau} \nabla_x^T \Delta \boldsymbol{\varphi} \quad \text{and} \quad \Delta_\gamma \boldsymbol{\tau} = \partial_\gamma \boldsymbol{\tau} \Delta \gamma \quad (\text{C.12})$$

where  $\boldsymbol{\mathfrak{c}}$  denote the fourth order Eulerian moduli. To compute the increment  $\Delta_\varphi \phi$  of the yield criterion with respect to  $\boldsymbol{\varphi}$  consider the time derivative of  $\phi$

$$\dot{\phi} = \partial_{\mathbf{g}} \phi : \mathcal{L}_{\mathbf{v}} \mathbf{g} = 2 \partial_{\mathbf{g}} \phi : \frac{1}{2} (\mathbf{g} \mathbf{l} + \mathbf{l}^T \mathbf{g}) = 2 \partial_{\mathbf{g}} \phi : \mathbf{g} \mathbf{l} \quad (\text{C.13})$$

in terms of the Lie-derivative  $\mathcal{L}_{\mathbf{v}} \mathbf{g}$  of the current metric or the spatial velocity gradient  $\mathbf{l} = \nabla_x \mathbf{v} = \nabla_x \dot{\boldsymbol{\varphi}}$ , cf. (2.26). The time derivative ( $\dot{\bullet}$ ) can be identified with the increment  $\Delta(\bullet)$  per time increment  $\Delta t$ . Then, the increments of the yield criterion function  $\phi$  are

$$\Delta_\varphi \phi = 2 \partial_{\mathbf{g}} \phi : \nabla_x \Delta \boldsymbol{\varphi} \quad \text{and} \quad \Delta_\gamma \phi = \partial_\gamma \phi \Delta \gamma. \quad (\text{C.14})$$

The spatial gradient of the increment of  $\boldsymbol{\varphi}$  is given in analogy to (C.2)

$$\nabla_x \Delta \boldsymbol{\varphi} = \nabla_x \Delta \boldsymbol{\varphi}_C + \nabla_x \Delta \boldsymbol{\varphi}_E. \quad (\text{C.15})$$

The spatial discretization of the linearized set of equations is performed by a three-field interpolation. The compatible spatial deformation, the enhanced strain field and the temporal change  $\dot{\gamma}$  of the scalar field  $\gamma$  are approximated independently. Compared to Section 3.3, a formally alternative representation of the finite element interpolation is used which circumvents the introduction of global matrices but is directly related to the element level

$$\begin{aligned}
\boldsymbol{\varphi} &\approx \sum_I^{n^e} \mathbf{N}_I \mathbf{d}_I, \quad \delta \boldsymbol{\varphi} \approx \sum_I^{n^e} \mathbf{N}_I \delta \mathbf{d}_I, \quad \Delta \boldsymbol{\varphi} \approx \sum_I^{n^e} \mathbf{N}_I \Delta \mathbf{d}_I \\
\dot{\gamma} &\approx \sum_I^{n^e} \mathbf{N}_I^T \tilde{\gamma}_I, \quad \delta \dot{\gamma} \approx \sum_I^{n^e} \mathbf{N}_I^T \delta \tilde{\gamma}_I, \quad \Delta \gamma \approx \sum_I^{n^e} \mathbf{N}_I^T \Delta \tilde{\gamma}_I.
\end{aligned} \quad (\text{C.16})$$

The matrices  $\mathbf{N}_I$ ,  $\mathbf{N}_I^T$  denote the shape functions associated with node  $I$  while  $\delta\mathbf{d}_I$ ,  $\Delta\mathbf{d}_I$  as well as  $\delta\tilde{\gamma}_I$ ,  $\Delta\tilde{\gamma}_I$  represent the virtual and incremental vector fields containing the nodal variations or increments of the primary variables at all  $n^e$  nodes of each element. The virtual yield criterion is approximated by  $\delta\phi \approx \sum_I^{n^e} \mathbf{N}_I^T \delta\tilde{\phi}_I$  with the nodal variations  $\delta\tilde{\phi}_I$ . The reason to use this alternative scenario becomes clear when considering the approximation of the incompatible field. For this field no interelement continuity is demanded but it is governed by internal degrees exclusively defined on each element domain

$$\varphi_E \approx \sum_e^n M_e \mathbf{w}_e, \quad \delta\varphi_E \approx \sum_e^n M_e \delta\mathbf{w}_e \quad \text{and} \quad \Delta\varphi_E \approx \sum_e^n M_e \Delta\mathbf{w}_e. \quad (\text{C.17})$$

Here,  $\mathbf{w}_e$  represents the internal element degrees and  $\delta\mathbf{w}_e$  and  $\Delta\mathbf{w}_e$  their virtual and incremental counterparts. The structure of the interpolation functions  $M_e$  depends on the incompatible modes to be generated. For the particular case of four internal degrees, the interpolation functions read  $M_e = \frac{1}{2}(\xi_e^2 - 1)$ ,  $e = 1, 2$  where  $\boldsymbol{\xi} = [\xi_1, \xi_2]^T = [\xi, \eta]^T$  refers to the coordinates of the finite element parameter space  $\Omega^e$ . The material gradient of these interpolation functions is evaluated according to

$$\nabla_X M_e := \frac{\det \mathbf{J}}{\det \mathbf{J}_0} \mathbf{J}_0^{-T} \nabla_\xi M_e. \quad (\text{C.18})$$

The matrix  $\mathbf{J}$  denotes the gradient  $\nabla_\xi \hat{\mathbf{X}}$  of the isoparametric map  $\hat{\mathbf{X}}$  between the coordinates  $\boldsymbol{\xi}$  of the parameter space and the material coordinates  $\mathbf{X}$ . The subscript 0 indicates that the gradient and its determinant have to be evaluated at the element center  $\boldsymbol{\xi} = \mathbf{0}$ . The spatial compatible and incompatible gradients are computed by

$$\begin{aligned} \nabla_x \delta\varphi_C &= \sum_I^{n^e} \delta\mathbf{d}_I \otimes \nabla_x N_I & \text{with} & \quad \nabla_x N_I = \mathbf{F}^{-T} \nabla_X N_I \\ \nabla_x \delta\varphi_E &= \sum_e^n \delta\mathbf{w}_e \otimes \nabla_x M_e & \text{with} & \quad \nabla_x M_e = \mathbf{F}^{-T} \nabla_X M_e \end{aligned} \quad (\text{C.19})$$

applying in the same manner for their incremental counterparts. It is convenient to introduce the element matrices  $\mathbf{B}_I$  and  $\mathbf{G}_e$  containing the gradients  $\nabla_x N_I$  and  $\nabla_x M_e$ . The derivative of the interpolation functions with respect to the current coordinates  $\mathbf{x}$  is computed by the contraction of their derivative with respect to the reference coordinates  $\mathbf{X}$  and the transpose inverse of the approximated deformation gradient. This quantity is finally given by the sum of the compatible and incompatible contributions

$$\mathbf{F} = \mathbf{1} + \sum_I^{n^e} \mathbf{d}_I \otimes \nabla_X N_I + \sum_e^n \mathbf{w}_e \otimes \nabla_X M_e. \quad (\text{C.20})$$

Substitution of the finite element approximation into the linearized expressions (C.10) and application of the lemma of variational calculus result in the following system of linear equations on the element level

$$\begin{bmatrix} \mathbf{k}_{\varphi_c \varphi_c}^e & \mathbf{k}_{\varphi_c \gamma}^e & \mathbf{k}_{\varphi_c w}^e \\ \mathbf{k}_{\phi \varphi_c}^e & \mathbf{k}_{\phi \gamma}^e & \mathbf{k}_{\phi w}^e \\ \mathbf{k}_{w \varphi_c}^e & \mathbf{k}_{w \gamma}^e & \mathbf{k}_{w w}^e \end{bmatrix} \begin{bmatrix} \Delta \mathbf{d} \\ \Delta \tilde{\gamma} \\ \Delta \mathbf{w} \end{bmatrix} = \begin{bmatrix} -\mathbf{f}_{\varphi_c}^{e,int} + \mathbf{f}_{\varphi_c}^{e,ext} \\ -\mathbf{f}_{\phi}^{e,int} \\ -\mathbf{f}_w^{e,int} \end{bmatrix}. \quad (\text{C.21})$$

It bases on the definitions of the element stiffness matrices

$$\begin{aligned}
\mathbf{k}_{\varphi_c \varphi_c}^e &= \int_{\mathcal{B}^e} \mathbf{B}_I^T [\mathfrak{c} \mathbf{B}_J + \boldsymbol{\tau} \mathbf{B}_J \circ \mathbf{1}] dV \\
\mathbf{k}_{\phi \gamma}^e &= \int_{\mathcal{B}^e} \mathbf{N}_K^{\mathcal{I}T} \partial_\gamma \phi \mathbf{N}_L^{\mathcal{I}} dV \\
\mathbf{k}_{ww}^e &= \int_{\mathcal{B}^e} \mathbf{G}_e^T [\mathfrak{c} \mathbf{G}_f + \boldsymbol{\tau} \mathbf{G}_f \circ \mathbf{1}] dV \\
\mathbf{k}_{\varphi_c \gamma}^e &= \int_{\mathcal{B}^e} \mathbf{B}_I^T \partial_\gamma \boldsymbol{\tau} \mathbf{N}_L^{\mathcal{I}} dV, & \mathbf{k}_{\phi \varphi_c}^e &= \int_{\mathcal{B}^e} \mathbf{N}_K^{\mathcal{I}T} 2\partial_g \phi \mathbf{B}_J dV \\
\mathbf{k}_{\varphi_c w}^e &= \int_{\mathcal{B}^e} \mathbf{B}_I^T [\mathfrak{c} \mathbf{G}_f + \boldsymbol{\tau} \mathbf{G}_f \circ \mathbf{1}] dV, & \mathbf{k}_{w \varphi_c}^e &= \int_{\mathcal{B}^e} \mathbf{G}_e^T [\mathfrak{c} \mathbf{B}_J + \boldsymbol{\tau} \mathbf{B}_J \circ \mathbf{1}] dV \\
\mathbf{k}_{\phi w}^e &= \int_{\mathcal{B}^e} \mathbf{N}_K^{\mathcal{I}T} 2\partial_g \phi \mathbf{G}_f dV, & \mathbf{k}_{w \gamma}^e &= \int_{\mathcal{B}^e} \mathbf{G}_e^T \partial_\gamma \boldsymbol{\tau} \mathbf{N}_L^{\mathcal{I}T} dV
\end{aligned} \tag{C.22}$$

and the element residuals

$$\begin{aligned}
\mathbf{f}_{\varphi_c}^{e,int} &= \int_{\mathcal{B}^e} \mathbf{B}_I^T \boldsymbol{\tau} dV, & \mathbf{f}_{\varphi_c}^{e,ext} &= \int_{\mathcal{B}^e} \mathbf{N}_I^T \boldsymbol{\gamma} dV + \int_{\partial \mathcal{B}_t^e} \mathbf{N}_I^T \bar{\mathbf{t}} dA \\
\mathbf{f}_{\phi}^{e,int} &= \int_{\mathcal{B}^e} \mathbf{N}_K^{\mathcal{I}T} \phi dV, & \mathbf{f}_w^{e,int} &= \int_{\mathcal{B}^e} \mathbf{G}_e^T \boldsymbol{\tau} dV.
\end{aligned} \tag{C.23}$$

The pairs  $(I, J)$ ,  $(K, L)$  and  $(e, f)$  indicate a sum over the nodes corresponding to the spatial deformation, the accompanying subproblem and the internal element parameters, respectively. The stiffness matrices related to the compatible and incompatible part of the deformation split up into a material tangent term arising from the linearization of the stresses and a geometric contribution due to the non-linear deformation measure. The expressions for the spatial deformation problem and the constitutive subproblem can be symmetrized by multiplication of the second equation of (C.21) by  $-1$ .

Upon assembly the residual expressions can alternatively be written as a sum of discrete nodal contributions in strict analogy to (3.84). In this sense, the weak form expressions associated with the loading-unloading conditions are recast into the nodal residuals

$$r_K^\phi := \mathbf{A} \int_{e=1}^{n_{ele}} \mathbf{N}_K^{\mathcal{I}T} \phi dV \quad \text{and} \quad \Delta r_K^\gamma := \mathbf{A} \int_{e=1}^{n_{ele}} \mathbf{N}_K^{\mathcal{I}T} (\gamma_{n+1} - \gamma_n) dV. \tag{C.24}$$

In addition to the spatial discretization the time discretization of the second part has been performed within a discrete time step  $[t_n; t_{n+1}]$ . With these nodal values at hand, the discrete counterpart of the decomposition (3.82) of the material body reads

$$\begin{aligned}
\text{non-active part} \quad \mathcal{B}_{el}^h &= \{ K \in \mathcal{B}^h \mid r_K^\phi \leq 0 \wedge \Delta r_K^\gamma = 0 \} \\
\text{active part} \quad \mathcal{B}_{inel}^h &= \{ K \in \mathcal{B}^h \mid r_K^\phi = 0 \wedge \Delta r_K^\gamma > 0 \}.
\end{aligned} \tag{C.25}$$

By means of this decomposition of the discrete domain the decision on inelastic loading is no longer made at the integration points, as it is done in standard local formulations, cf. Section 3.5.2, but from now on is performed on the node point level of the mesh.

As already mentioned, no interelement continuity of the internal degrees is required. Thus, they do not need to be assembled to a global array but are eliminated on the element level by static condensation. To this end, the linear system of equations (C.21) is solved for the increments  $\Delta \mathbf{w}$  of the internal degrees and the result is re-substituted into the system of equations. The resulting system has to be treated in a global manner. All the element contributions are assembled yielding a governing system of linear equations

$$\mathbf{A}_{e=1}^{n_{ele}} \hat{\mathbf{k}}^e \mathbf{A}_{e=1}^{n_{ele}} \begin{bmatrix} \Delta \mathbf{d} \\ \Delta \tilde{\gamma} \end{bmatrix} = \mathbf{A}_{e=1}^{n_{ele}} \hat{\mathbf{f}}^e \quad (\text{C.26})$$

in terms of the condensed versions of the element stiffness and the element residual

$$\begin{aligned} \hat{\mathbf{k}}^e &= \begin{bmatrix} \mathbf{k}_{\varphi_c \varphi_c}^e & \mathbf{k}_{\varphi_c \gamma}^e \\ \mathbf{k}_{\phi \varphi_c}^e & \mathbf{k}_{\phi \gamma}^e \end{bmatrix} - \begin{bmatrix} \mathbf{k}_{\varphi_c w}^e \\ \mathbf{k}_{\phi w}^e \end{bmatrix} \mathbf{k}_{ww}^{e-1} \begin{bmatrix} \mathbf{k}_{w \varphi_c}^e & \mathbf{k}_{w \gamma}^e \end{bmatrix} \\ \hat{\mathbf{f}}^e &= \begin{bmatrix} -\mathbf{f}_{\varphi_c}^{e,int} + \mathbf{f}_{\varphi_c}^{e,ext} \\ -\mathbf{f}_{\phi}^{e,int} \end{bmatrix} - \begin{bmatrix} \mathbf{k}_{\varphi_c w}^e \\ \mathbf{k}_{\phi w}^e \end{bmatrix} \mathbf{k}_{ww}^{e-1} \begin{bmatrix} -\mathbf{f}_w^{e,int} \end{bmatrix}. \end{aligned} \quad (\text{C.27})$$

The overall system (C.26) is solved for the increments  $\Delta \mathbf{d}$  of the spatial nodal displacements and  $\Delta \tilde{\gamma}$  of the nodal values of  $\gamma$ . Afterwards the current nodal solutions are obtained via the Newton-update

$$\mathbf{d} \leftarrow \mathbf{d} + \Delta \mathbf{d} \quad \text{and} \quad \tilde{\gamma} \leftarrow \tilde{\gamma} + \Delta \tilde{\gamma}. \quad (\text{C.28})$$

Both contributions, the spatial balance law and the loading-unloading conditions, are solved by a monolithic solution strategy. The constitutive subproblem only needs to be treated if the considered nodal point is active in the sense of (C.25). Otherwise purely elastic response occurs and only the spatial equilibrium problem has to be accounted for. Within this procedure the current dimension of the governing system of equations changes during the computation according to the development of inelastic deformation which apparently demands a non-standard finite element data environment. For given solutions of the spatial deformation  $\Delta \mathbf{d}$  and the scalar nodal variable  $\Delta \tilde{\gamma}$  the increments  $\Delta \mathbf{w}$  of the internal degrees are computed on the element level

$$\Delta \mathbf{w} = \mathbf{k}_{ww}^{e-1} \left( -\mathbf{f}_w^{e,int} - \begin{bmatrix} \mathbf{k}_{w \varphi_c}^e & \mathbf{k}_{w \gamma}^e \end{bmatrix} \begin{bmatrix} \Delta \mathbf{d} \\ \Delta \tilde{\gamma} \end{bmatrix} \right). \quad (\text{C.29})$$

Having a closer look at equation (C.27)<sub>1</sub>, it is obvious that the element stiffness of the formulation without internal degrees is reduced by subtraction of a contribution arising from the enhanced strain approach. This results in the elimination of locking-phenomena which occur in standard displacement formulations. Despite the fact that an explicit inversion of the matrix  $\mathbf{k}_{ww}^e$  is required for each element the numerical effort is significantly reduced as the method avoids the introduction of higher order shape functions but the use of bilinear shapes turns out to be sufficient.

## D. Noether's Theorem

A formally alternative approach to derive the fundamental field equations of configurational solid dynamics is presented using Noether's reasoning, cf. NOETHER [139]. The formalism follows the conceptual framework outlined by KIENZLER & HERRMANN [76]. Basic idea is the simultaneous variation of both the dependent and independent variables, respectively referred to as variables and field. In the current investigations the independent variables are given by the Lagrangian space-time coordinates  $(\mathbf{X}, t)$  whereas the field is represented by the non-linear point map  $\varphi$ . Consider now infinitesimal changes of these quantities

$$t \rightarrow t + \delta t, \quad \mathbf{X} \rightarrow \mathbf{X} + \delta \mathbf{X}, \quad \varphi \rightarrow \varphi + \delta \varphi \quad (\text{D.1})$$

in which  $\delta t$ ,  $\delta \mathbf{X}$  and  $\delta \varphi$  denote the variations of the respective objects. This transformations can be reformulated in terms of an  $\epsilon$ -perturbation and some arbitrary functions  $\zeta$ ,  $\xi$  and  $\eta$  in the following way

$$\begin{aligned} t &\rightarrow t^* = t + \epsilon \zeta \\ \mathbf{X} &\rightarrow \mathbf{X}^* = \mathbf{X} + \epsilon \xi \\ \varphi &\rightarrow \varphi^* = \varphi + \epsilon \eta. \end{aligned} \quad (\text{D.2})$$

Upon transformation of the dependent field  $\varphi$ , its derivatives with respect to the independent variables  $(\mathbf{X}, t)$ , namely the deformation gradient and the spatial velocity field, transform according to

$$\begin{aligned} \mathbf{F} &\rightarrow \mathbf{F}^* = \mathbf{F} + \epsilon \left( \frac{\partial \eta}{\partial \mathbf{X}} - \mathbf{F} \frac{\partial \xi}{\partial \mathbf{X}} \right) \\ \mathbf{v} &\rightarrow \mathbf{v}^* = \mathbf{v} + \epsilon \left( \frac{\partial \eta}{\partial t} - \mathbf{F} \frac{\partial \xi}{\partial t} - \mathbf{v} \frac{\partial \zeta}{\partial t} \right). \end{aligned} \quad (\text{D.3})$$

Finally, the transformations of the material volume element and the infinitesimal time increment are obtained by

$$\begin{aligned} dV &\rightarrow dV^* = \left( 1 + \epsilon \mathbf{1} : \frac{\partial \xi}{\partial \mathbf{X}} \right) dV \\ dt &\rightarrow dt^* = \left( 1 + \epsilon \frac{\partial \zeta}{\partial t} \right) dt. \end{aligned} \quad (\text{D.4})$$

Consider now the variation of the action functional  $H$  introduced in (4.12) in terms of the Lagrangian density  $\mathcal{L}$  per unit volume of the reference configuration. For the sake of simplicity, the surface contribution related to the material boundary  $\partial \mathcal{B}$  is neglected,  $\bar{\mathcal{L}} = 0$ . On account of the transformations of the above objects, the transformed action functional reads

$$H^* = \int_{t_1}^{t_2} \int_{\mathcal{B}} \mathcal{L}(t^*, \mathbf{X}^*, \varphi^*, \mathbf{v}^*, \mathbf{F}^*) \left( 1 + \epsilon \mathbf{1} : \frac{\partial \xi}{\partial \mathbf{X}} \right) dV \left( 1 + \epsilon \frac{\partial \zeta}{\partial t} \right) dt. \quad (\text{D.5})$$



Expansion of this identity in a Taylor series and truncation after the linear terms results in the expression

$$\begin{aligned}
H^* = H + \epsilon \int_{t_1}^{t_2} \int_{\mathcal{B}} & \zeta \frac{\partial \mathcal{L}}{\partial t} + \boldsymbol{\xi} \cdot \frac{\partial \mathcal{L}}{\partial \mathbf{X}} + \boldsymbol{\eta} \cdot \frac{\partial \mathcal{L}}{\partial \boldsymbol{\varphi}} \\
& + \left( \frac{\partial \boldsymbol{\eta}}{\partial \mathbf{X}} - \mathbf{F} \frac{\partial \boldsymbol{\xi}}{\partial \mathbf{X}} \right) : \frac{\partial \mathcal{L}}{\partial \mathbf{F}} + (\mathbf{1} : \frac{\partial \boldsymbol{\xi}}{\partial \mathbf{X}}) \mathcal{L} \\
& + \left( \frac{\partial \boldsymbol{\eta}}{\partial t} - \mathbf{F} \frac{\partial \boldsymbol{\xi}}{\partial t} - \mathbf{v} \frac{\partial \zeta}{\partial t} \right) \cdot \frac{\partial \mathcal{L}}{\partial \mathbf{v}} + \frac{\partial \zeta}{\partial t} \mathcal{L} \quad dV \quad dt.
\end{aligned} \tag{D.6}$$

This equation can be manipulated as follows. At first, the second line is reformulated by means of integration by parts with respect to the material coordinates

$$\begin{aligned}
\left( \frac{\partial \boldsymbol{\eta}}{\partial \mathbf{X}} - \mathbf{F} \frac{\partial \boldsymbol{\xi}}{\partial \mathbf{X}} \right) : \frac{\partial \mathcal{L}}{\partial \mathbf{F}} &= \text{Div} \left[ \boldsymbol{\eta} \frac{\partial \mathcal{L}}{\partial \mathbf{F}} \right] - \boldsymbol{\eta} \cdot \text{Div} \left[ \frac{\partial \mathcal{L}}{\partial \mathbf{F}} \right] \\
& - \text{Div} \left[ \boldsymbol{\xi} \mathbf{F}^T \frac{\partial \mathcal{L}}{\partial \mathbf{F}} \right] + \underbrace{\boldsymbol{\xi} \nabla_{\mathbf{X}} \mathbf{F} : \frac{\partial \mathcal{L}}{\partial \mathbf{F}}}_{(i)} + \boldsymbol{\xi} \mathbf{F}^T \cdot \text{Div} \left[ \frac{\partial \mathcal{L}}{\partial \mathbf{F}} \right]
\end{aligned} \tag{D.7}$$

$$\begin{aligned}
(\mathbf{1} : \frac{\partial \boldsymbol{\xi}}{\partial \mathbf{X}}) \mathcal{L} &= \text{Div} \left[ \boldsymbol{\xi} \mathcal{L} \mathbf{1} \right] - \boldsymbol{\xi} \cdot \nabla_{\mathbf{X}} \mathcal{L} \\
&= \text{Div} \left[ \boldsymbol{\xi} \mathcal{L} \mathbf{1} \right] - \boldsymbol{\xi} \cdot \left\{ \frac{\partial \mathcal{L}}{\partial \mathbf{X}} + \frac{\partial \mathcal{L}}{\partial \boldsymbol{\varphi}} \mathbf{F} + \underbrace{\frac{\partial \mathcal{L}}{\partial \mathbf{v}} \nabla_{\mathbf{X}} \mathbf{v}}_{(ii)} + \underbrace{\frac{\partial \mathcal{L}}{\partial \mathbf{F}} : \nabla_{\mathbf{X}} \mathbf{F}}_{(i)} \right\}.
\end{aligned} \tag{D.8}$$

Due to compatibility, which induces the following relation for the material gradient of the deformation gradient,  $\nabla_{\mathbf{X}} \mathbf{F} = F^a_{A,B} = F^a_{B,A}$ , the terms indicated by (i) are eliminated. Turning now to the third line of (D.6), recall that the partial time derivative of the function  $\zeta$  coincides with its total time derivative at fixed material position,  $\partial \zeta / \partial t = \partial \zeta / t|_{X \text{ fixed}}$ . Then, integration by parts with respect to time provides

$$\begin{aligned}
\left( \frac{\partial \boldsymbol{\eta}}{\partial t} - \mathbf{F} \frac{\partial \boldsymbol{\xi}}{\partial t} - \mathbf{v} \frac{\partial \zeta}{\partial t} \right) \cdot \frac{\partial \mathcal{L}}{\partial \mathbf{v}} &= \frac{\partial}{\partial t} \left( \boldsymbol{\eta} \cdot \frac{\partial \mathcal{L}}{\partial \mathbf{v}} \right) - \boldsymbol{\eta} \cdot \frac{\partial}{\partial t} \left[ \frac{\partial \mathcal{L}}{\partial \mathbf{v}} \right] \\
& - \frac{\partial}{\partial t} \left( \boldsymbol{\xi} \cdot \mathbf{F}^T \frac{\partial \mathcal{L}}{\partial \mathbf{v}} \right) + \underbrace{\boldsymbol{\xi} \cdot \frac{\partial}{\partial t} \mathbf{F}^T \frac{\partial \mathcal{L}}{\partial \mathbf{v}}}_{(ii)} + \boldsymbol{\xi} \mathbf{F}^T \cdot \frac{\partial}{\partial t} \left( \frac{\partial \mathcal{L}}{\partial \mathbf{v}} \right) \\
& - \frac{\partial}{\partial t} \left( \zeta \mathbf{v} \cdot \frac{\partial \mathcal{L}}{\partial \mathbf{v}} \right) + \zeta \frac{\partial}{\partial t} \mathbf{v} \cdot \frac{\partial \mathcal{L}}{\partial \mathbf{v}} + \zeta \mathbf{v} \cdot \frac{\partial}{\partial t} \left( \frac{\partial \mathcal{L}}{\partial \mathbf{v}} \right)
\end{aligned} \tag{D.9}$$

$$\begin{aligned}
\frac{\partial \zeta}{\partial t} \mathcal{L} &= \frac{\partial}{\partial t} (\zeta \mathcal{L}) - \zeta \frac{\partial}{\partial t} \mathcal{L} = \frac{d}{dt} \Big|_{X \text{ fixed}} (\zeta \mathcal{L}) - \zeta \frac{d}{dt} \Big|_{X \text{ fixed}} \mathcal{L} \\
&= \frac{\partial}{\partial t} (\zeta \mathcal{L}) - \zeta \left\{ \frac{\partial \mathcal{L}}{\partial t} + \frac{\partial \mathcal{L}}{\partial \boldsymbol{\varphi}} \cdot \mathbf{v} + \frac{\partial \mathcal{L}}{\partial \mathbf{v}} \cdot \frac{\partial}{\partial t} \mathbf{v} + \frac{\partial \mathcal{L}}{\partial \mathbf{F}} : \frac{\partial}{\partial t} \mathbf{F} \right\}.
\end{aligned} \tag{D.10}$$

The components labeled by (ii) cancel out due to the compatibility-like identity (4.2),  $\nabla_{\mathbf{X}} \mathbf{v} = \partial \mathbf{v} / \partial \mathbf{X} = \partial \mathbf{F} / \partial t$ . Using the same reasoning, the final addend of (D.10)<sub>2</sub> can be expressed by

$$\frac{\partial \mathcal{L}}{\partial \mathbf{F}} : \frac{\partial}{\partial t} \mathbf{F} = \frac{\partial \mathcal{L}}{\partial \mathbf{F}} : \frac{\partial}{\partial \mathbf{X}} \mathbf{v} = \text{Div} \left[ \zeta \left( -\mathbf{v} \frac{\partial \mathcal{L}}{\partial \mathbf{F}} \right) \right] - \zeta \mathbf{v} \cdot \left( -\text{Div} \left[ \frac{\partial \mathcal{L}}{\partial \mathbf{F}} \right] \right). \quad (\text{D.11})$$

Rearranging all the terms, the variation  $H^*$  of the action functional can be written in the compact format

$$\begin{aligned} H^* = H + \epsilon \int_{t_1}^{t_2} \int_{\mathcal{B}} & \left[ \boldsymbol{\eta} - \boldsymbol{\xi} \mathbf{F}^T - \zeta \mathbf{v} \right] \cdot \left\{ \frac{\partial \mathcal{L}}{\partial \boldsymbol{\varphi}} - \text{Div} \left[ \frac{\partial \mathcal{L}}{\partial \mathbf{F}} \right] - \frac{\partial}{\partial t} \left( \frac{\partial \mathcal{L}}{\partial \mathbf{v}} \right) \right\} \\ & + \left\{ \text{Div} \left[ \boldsymbol{\eta} \frac{\partial \mathcal{L}}{\partial \mathbf{F}} \right] + \frac{\partial}{\partial t} \left( \boldsymbol{\eta} \cdot \frac{\partial \mathcal{L}}{\partial \mathbf{v}} \right) \right\} \\ & + \left\{ \text{Div} \left[ \boldsymbol{\xi} \left( \mathcal{L} \mathbf{1} - \mathbf{F}^T \frac{\partial \mathcal{L}}{\partial \mathbf{F}} \right) \right] + \frac{\partial}{\partial t} \left( \boldsymbol{\xi} \cdot \left( -\mathbf{F}^T \frac{\partial \mathcal{L}}{\partial \mathbf{v}} \right) \right) \right\} \\ & + \left\{ \text{Div} \left[ \zeta \left( -\mathbf{v} \frac{\partial \mathcal{L}}{\partial \mathbf{F}} \right) \right] + \frac{\partial}{\partial t} \left( \zeta \left( \mathcal{L} - \mathbf{v} \cdot \frac{\partial \mathcal{L}}{\partial \mathbf{v}} \right) \right) \right\} dV dt. \end{aligned} \quad (\text{D.12})$$

This equation in turn is expressed in the short cut notation

$$H^* = H + \epsilon \int_{t_1}^{t_2} \int_{\mathcal{B}} \boldsymbol{\mathcal{Q}} \cdot EL_{\boldsymbol{\varphi}} + \frac{\partial}{\partial (\mathbf{X}, t)} \boldsymbol{\mathcal{E}} dV dt \quad (\text{D.13})$$

in terms of the characteristic  $\boldsymbol{\mathcal{Q}}$  and the spatial Euler-Lagrange equation  $EL_{\boldsymbol{\varphi}}$

$$\boldsymbol{\mathcal{Q}} = \left[ \boldsymbol{\eta} - \boldsymbol{\xi} \mathbf{F}^T - \zeta \mathbf{v} \right] \quad \text{and} \quad EL_{\boldsymbol{\varphi}} = \frac{\partial \mathcal{L}}{\partial \boldsymbol{\varphi}} - \text{Div} \left[ \frac{\partial \mathcal{L}}{\partial \mathbf{F}} \right] - \frac{\partial}{\partial t} \left( \frac{\partial \mathcal{L}}{\partial \mathbf{v}} \right) \quad (\text{D.14})$$

as well as the current or flux  $\boldsymbol{\mathcal{E}}$  with space-time derivative

$$\begin{aligned} \frac{\partial}{\partial (\mathbf{X}, t)} \boldsymbol{\mathcal{E}} = & \text{Div} \left[ \boldsymbol{\eta} \frac{\partial \mathcal{L}}{\partial \mathbf{F}} \right] + \text{Div} \left[ \boldsymbol{\xi} \left( \mathcal{L} \mathbf{1} - \mathbf{F}^T \frac{\partial \mathcal{L}}{\partial \mathbf{F}} \right) \right] + \text{Div} \left[ \zeta \left( -\mathbf{v} \frac{\partial \mathcal{L}}{\partial \mathbf{F}} \right) \right] \\ & + \frac{\partial}{\partial t} \left( \boldsymbol{\eta} \cdot \frac{\partial \mathcal{L}}{\partial \mathbf{v}} \right) + \frac{\partial}{\partial t} \left( \boldsymbol{\xi} \cdot \left( -\mathbf{F}^T \frac{\partial \mathcal{L}}{\partial \mathbf{v}} \right) \right) + \frac{\partial}{\partial t} \left( \zeta \left( \mathcal{L} - \mathbf{v} \cdot \frac{\partial \mathcal{L}}{\partial \mathbf{v}} \right) \right) \end{aligned} \quad (\text{D.15})$$

which basically establishes the last three lines of equation (D.12). From the current  $\boldsymbol{\mathcal{E}}$  an additional quantity  $\boldsymbol{\mathcal{C}}$  can be extracted denoted the space-time energy-momentum tensor, see e.g. MAUGIN [99], ZIELONKA [191],

$$\boldsymbol{\mathcal{C}} = \begin{bmatrix} \left( \mathcal{L} \mathbf{1} - \mathbf{F}^T \frac{\partial \mathcal{L}}{\partial \mathbf{F}} \right) & \left( -\mathbf{v} \frac{\partial \mathcal{L}}{\partial \mathbf{F}} \right) \\ \left( -\mathbf{F}^T \frac{\partial \mathcal{L}}{\partial \mathbf{v}} \right) & \left( \mathcal{L} - \mathbf{v} \cdot \frac{\partial \mathcal{L}}{\partial \mathbf{v}} \right) \end{bmatrix}. \quad (\text{D.16})$$

Based on equation (D.12) it is now straightforward to adopt Noether's reasoning. Her first theorem states that if the action functional  $H$  is invariant with respect to the given transformations, i.e.  $H = H^*$ , then there exists a strict conservation law. The invariance

condition implies that the integrand on the right hand side of (D.12) has to vanish identically. Since the system is assumed to be balanced in the sense, that the Euler-Lagrange equation is satisfied,  $EL_\varphi = \mathbf{0}$ , the space-time derivative of the current  $\boldsymbol{\mathcal{E}}$  has to be equal to zero as well inducing the strict conservation laws

$$\frac{\partial}{\partial(\mathbf{X}, t)} \boldsymbol{\mathcal{E}} = \mathbf{0}. \quad (\text{D.17})$$

Hence, the current  $\boldsymbol{\mathcal{E}}$  itself has to be constant. Condition (D.17) governs three cases:

- (i)  $\boldsymbol{\xi} = \mathbf{0}$ ,  $\zeta = 0$  and  $\boldsymbol{\eta} = \text{const.}$

As  $\boldsymbol{\eta}$  is constant, it is not affected by the respective derivatives and can be factored out. The remaining equation is the spatial Euler-Lagrange equation (4.19) or, by substitution of the Lagrangian density  $\mathcal{L}$ , (4.21),

$$-\text{Div} \left[ \frac{\partial \mathcal{L}}{\partial \mathbf{F}} \right] = \frac{\partial}{\partial t} \left( \frac{\partial \mathcal{L}}{\partial \mathbf{v}} \right) \quad \text{or} \quad \text{Div} \mathbf{P} = \rho_0 \frac{\partial}{\partial t} \mathbf{v} \quad (\text{D.18})$$

without source term which in the former representations has been established by the physical volume forces  $\bar{\gamma}_0$ .

- (ii)  $\boldsymbol{\eta} = \mathbf{0}$ ,  $\zeta = 0$  and  $\boldsymbol{\xi} = \text{const.}$

Since  $\boldsymbol{\xi}$  is constant, it can be factored out of the derivatives. This scenario results in the material Euler-Lagrange equation (4.28) or, by substitution of the Lagrangian density  $\mathcal{L}$ , (4.31),

$$\text{Div} \left[ -\mathcal{L} \mathbf{1} + \mathbf{F}^T \frac{\partial \mathcal{L}}{\partial \mathbf{F}} \right] = \frac{\partial}{\partial t} \left( -\mathbf{F}^T \frac{\partial \mathcal{L}}{\partial \mathbf{v}} \right) \quad \text{or} \quad \text{Div} \boldsymbol{\Sigma} = \frac{\partial}{\partial t} \mathcal{P}. \quad (\text{D.19})$$

Again, the resulting balance is a strict conservation law without source term as the configurational or inhomogeneity force  $\bar{\Gamma}_0$  does not enter the equation.

- (iii)  $\boldsymbol{\eta} = \mathbf{0}$ ,  $\boldsymbol{\xi} = \mathbf{0}$  and  $\zeta = \text{const.}$

Finally, for constant values of  $\zeta$ , the procedure ends up with the temporal Euler-Lagrange equation (4.42) or, by substitution of the Lagrangian density  $\mathcal{L}$  and some straightforward manipulations, (4.44),

$$\text{Div} \left[ \mathbf{v} \frac{\partial \mathcal{L}}{\partial \mathbf{F}} \right] = \frac{\partial}{\partial t} \left( \mathcal{L} - \frac{\partial \mathcal{L}}{\partial \mathbf{v}} \cdot \mathbf{v} \right) \quad \text{or} \quad \mathbf{v} \cdot \text{Div} \mathbf{P} = \rho_0 \mathbf{v} \cdot \frac{\partial}{\partial t} \mathbf{v} \quad (\text{D.20})$$

with  $\partial \mathcal{L} / \partial t = d\mathcal{L} / dt|_{X \text{ fixed}}$  being obvious. Observe that this balance equation a priori does not contain any source term as the phenomena of growth and resorption as well as ageing have been excluded, cf. Section 4.2.5 for further comments.

## E. Dual Variational Formulation of Truss Structures

Recall equation (5.50) for the variation of the energy functional

$$\delta\Pi = 0 \iff \sum_{e=1}^{n_b} \left[ (P \dot{l} + \Sigma \dot{L}) A \right] = 0. \quad (\text{E.1})$$

Substitution of the rates (5.48), i.e.  $\dot{L} = \mathbf{N}(\dot{\Xi}_2 - \dot{\Xi}_1)$  and  $\dot{l} = \mathbf{n}(\dot{\xi}_2 - \dot{\xi}_1)$ , yields

$$\mathbf{A}_{e=1}^{n_b} \left\{ \begin{bmatrix} \dot{\xi}_1 \\ \dot{\xi}_2 \end{bmatrix}^T \begin{bmatrix} -\mathbf{n} \\ \mathbf{n} \end{bmatrix} P A + \begin{bmatrix} \dot{\Xi}_1 \\ \dot{\Xi}_2 \end{bmatrix}^T \begin{bmatrix} -\mathbf{N} \\ \mathbf{N} \end{bmatrix} \Sigma A \right\} = 0 \quad (\text{E.2})$$

with the assembly operator  $\mathbf{A}$  accounting for the connectivity of the truss structure.

With the objective of applying a Newton-Raphson iteration scheme, the consistent linearization of (5.51) needs to be evaluated. Based on (E.2) the linear increment reads

$$\Delta(\delta\Pi) = \mathbf{A}_{e=1}^{n_b} \left[ (\dot{\xi}_2 - \dot{\xi}_1)^T \{ \Delta P \mathbf{n} + P \Delta \mathbf{n} \} A + (\dot{\Xi}_2 - \dot{\Xi}_1)^T \{ \Delta \Sigma \mathbf{N} + \Sigma \Delta \mathbf{N} \} A \right] \quad (\text{E.3})$$

displaying the typical split into a material and geometric part. The material tangent term is governed by the increments of the stress measures  $P$  and  $\Sigma$

$$\begin{aligned} \Delta P &= P_{,F} \Delta F = P_{,F} (L^{-1} \Delta l - F L^{-1} \Delta L) \\ &= P_{,F} L^{-1} \left[ \mathbf{n}^T (\Delta \mathbf{x}_2 - \Delta \mathbf{x}_1) - F \mathbf{N}^T (\Delta \mathbf{X}_2 - \Delta \mathbf{X}_1) \right] \\ \Delta \Sigma &= \Sigma_{,F} \Delta F = \Sigma_{,F} (L^{-1} \Delta l - F L^{-1} \Delta L) \\ &= \Sigma_{,F} L^{-1} \left[ \mathbf{n}^T (\Delta \mathbf{x}_2 - \Delta \mathbf{x}_1) - F \mathbf{N}^T (\Delta \mathbf{X}_2 - \Delta \mathbf{X}_1) \right]. \end{aligned} \quad (\text{E.4})$$

The increments of the deformation gradient and the spatial and material lengths are defined in analogy to the rates (5.47) and (5.48).  $\Delta \mathbf{X}_i$ ,  $\Delta \mathbf{x}_i$  denote the increments of the material and spatial coordinates of the truss joints. The geometric parts arise from the non-linear geometry of the structure. The increments of the direction vectors are

$$\begin{aligned} \Delta \mathbf{n} &= \Delta \frac{\mathbf{x}_2 - \mathbf{x}_1}{l} = \Delta \frac{\mathbf{x}_2 - \mathbf{x}_1}{|\mathbf{x}_2 - \mathbf{x}_1|} = \frac{1}{l} (\mathbf{1} - \mathbf{n} \mathbf{n}^T) (\Delta \mathbf{x}_2 - \Delta \mathbf{x}_1) \\ \Delta \mathbf{N} &= \Delta \frac{\mathbf{X}_2 - \mathbf{X}_1}{L} = \Delta \frac{\mathbf{X}_2 - \mathbf{X}_1}{|\mathbf{X}_2 - \mathbf{X}_1|} = \frac{1}{L} (\mathbf{1} - \mathbf{N} \mathbf{N}^T) (\Delta \mathbf{X}_2 - \Delta \mathbf{X}_1). \end{aligned} \quad (\text{E.5})$$

Substitution of these intermediate results into the linearization (E.3) yields

$$\begin{aligned} \Delta(\delta\Pi) &= \mathbf{A}_{e=1}^{n_b} \left\{ (\dot{\xi}_2 - \dot{\xi}_1)^T \left[ \frac{P_{,F} A}{L} \mathbf{n} \mathbf{n}^T + \frac{P A}{l} \mathbf{g} \right] (\Delta \mathbf{x}_2 - \Delta \mathbf{x}_1) \right. \\ &\quad + (\dot{\xi}_2 - \dot{\xi}_1)^T \left[ -\frac{P_{,F} A}{L} F \mathbf{n} \mathbf{N}^T \right] (\Delta \mathbf{X}_2 - \Delta \mathbf{X}_1) \\ &\quad + (\dot{\Xi}_2 - \dot{\Xi}_1)^T \left[ \frac{\Sigma_{,F} A}{L} \mathbf{N} \mathbf{n}^T \right] (\Delta \mathbf{x}_2 - \Delta \mathbf{x}_1) \\ &\quad \left. + (\dot{\Xi}_2 - \dot{\Xi}_1)^T \left[ -\frac{\Sigma_{,F} A}{L} F \mathbf{N} \mathbf{N}^T + \frac{\Sigma A}{L} \mathbf{G} \right] (\Delta \mathbf{X}_2 - \Delta \mathbf{X}_1) \right\} \end{aligned} \quad (\text{E.6})$$

where the abbreviations  $\mathbf{g} = (\mathbf{1} - \mathbf{nn}^T)$  and  $\mathbf{G} = (\mathbf{1} - \mathbf{NN}^T)$  have been introduced. Rearranging the terms and using the relation  $F = l/L$ , one ends up with the expression

$$\begin{aligned} \Delta(\delta\Pi) = & \mathbf{A}_{e=1}^{n_b} \left\{ \begin{bmatrix} \dot{\xi}_1 \\ \dot{\xi}_2 \end{bmatrix}^T \left( \frac{P_{,F} A}{L} \begin{bmatrix} \mathbf{nn}^T & -\mathbf{nn}^T \\ -\mathbf{nn}^T & \mathbf{nn}^T \end{bmatrix} + \frac{PA}{l} \begin{bmatrix} \mathbf{g} & -\mathbf{g} \\ -\mathbf{g} & \mathbf{g} \end{bmatrix} \right) \begin{bmatrix} \Delta\mathbf{x}_1 \\ \Delta\mathbf{x}_2 \end{bmatrix} \right. \\ & + \begin{bmatrix} \dot{\xi}_1 \\ \dot{\xi}_2 \end{bmatrix}^T \frac{P_{,F} Al}{L^2} \begin{bmatrix} -\mathbf{nN}^T & \mathbf{nN}^T \\ \mathbf{nN}^T & -\mathbf{nN}^T \end{bmatrix} \begin{bmatrix} \Delta\mathbf{X}_1 \\ \Delta\mathbf{X}_2 \end{bmatrix} \\ & + \begin{bmatrix} \dot{\Xi}_1 \\ \dot{\Xi}_2 \end{bmatrix}^T \frac{\Sigma_{,F} A}{L} \begin{bmatrix} \mathbf{Nn}^T & -\mathbf{Nn}^T \\ -\mathbf{Nn}^T & \mathbf{Nn}^T \end{bmatrix} \begin{bmatrix} \Delta\mathbf{x}_1 \\ \Delta\mathbf{x}_2 \end{bmatrix} \\ & \left. + \begin{bmatrix} \dot{\Xi}_1 \\ \dot{\Xi}_2 \end{bmatrix}^T \left( \frac{\Sigma_{,F} Al}{L^2} \begin{bmatrix} -\mathbf{NN}^T & \mathbf{NN}^T \\ \mathbf{NN}^T & -\mathbf{NN}^T \end{bmatrix} + \frac{PA}{l} \begin{bmatrix} \mathbf{G} & -\mathbf{G} \\ -\mathbf{G} & \mathbf{G} \end{bmatrix} \right) \begin{bmatrix} \Delta\mathbf{X}_1 \\ \Delta\mathbf{X}_2 \end{bmatrix} \right\}. \end{aligned} \quad (\text{E.7})$$

From this equation the element stiffness matrices are obtained with the split into the material tangent terms

$$\begin{aligned} \mathbf{k}_{ss}^{e,mat} &= \frac{P_{,F} A}{L} \begin{bmatrix} \mathbf{nn}^T & -\mathbf{nn}^T \\ -\mathbf{nn}^T & \mathbf{nn}^T \end{bmatrix}, & \mathbf{k}_{sm}^{e,mat} &= \frac{P_{,F} Al}{L^2} \begin{bmatrix} -\mathbf{nN}^T & \mathbf{nN}^T \\ \mathbf{nN}^T & -\mathbf{nN}^T \end{bmatrix} \\ \mathbf{k}_{ms}^{e,mat} &= \frac{\Sigma_{,F} A}{L} \begin{bmatrix} \mathbf{Nn}^T & -\mathbf{Nn}^T \\ -\mathbf{Nn}^T & \mathbf{Nn}^T \end{bmatrix}, & \mathbf{k}_{mm}^{e,mat} &= \frac{\Sigma_{,F} Al}{L^2} \begin{bmatrix} -\mathbf{NN}^T & \mathbf{NN}^T \\ \mathbf{NN}^T & -\mathbf{NN}^T \end{bmatrix} \end{aligned} \quad (\text{E.8})$$

and the geometric contributions

$$\mathbf{k}_{ss}^{e,geo} = \frac{\Sigma A}{L} \begin{bmatrix} \mathbf{g} & -\mathbf{g} \\ -\mathbf{g} & \mathbf{g} \end{bmatrix}, \quad \mathbf{k}_{mm}^{e,geo} = \frac{\Sigma A}{L} \begin{bmatrix} \mathbf{G} & -\mathbf{G} \\ -\mathbf{G} & \mathbf{G} \end{bmatrix}. \quad (\text{E.9})$$

The geometric terms only appear for the purely spatial and material subproblems. Upon assembly, the stiffness matrix of the whole truss structure is given by

$$\mathbf{K} = \mathbf{A}_{e=1}^{n_b} \begin{bmatrix} \mathbf{k}_{ss}^{e,mat} + \mathbf{k}_{ss}^{e,geo} & \mathbf{k}_{sm}^{e,mat} \\ \mathbf{k}_{ms}^{e,mat} & \mathbf{k}_{mm}^{e,mat} + \mathbf{k}_{mm}^{e,geo} \end{bmatrix}. \quad (\text{E.10})$$

Due to the variational structure of the formulation, the tangent operator is symmetric. This can easily be proven via

$$\frac{\Sigma_{,F} A}{L} = \frac{(\psi - FP)_{,F} A}{L} = \frac{(\psi_{,F} - P - FP_{,F}) A}{L} = -\frac{P_{,F} Al}{L^2}. \quad (\text{E.11})$$

With relations (5.51) for the residual and (E.11) for the stiffness matrix at hand, the overall system of linear equations can be written in the standard format (5.52).

## References

- [1] ABAQUS, VERSION 6.6: *Documentation*. <http://www.hlrs.de/organization/aw/services/cae/app/abaqus/Documentation/docs/v6.6/>.
- [2] AGIASOFITOU, E. K.; KALPAKIDES, V. K. [2006]: *The concept of a balance law for a cracked elastic body and the configurational force and moment at the crack tip*. International Journal of Engineering Science, 44: 127–139.
- [3] AINSWORTH, M.; ZHU, J. Z.; CRAIG, A. W.; ZIENKIEWICZ, O. C. [1989]: *Analysis of the Zienkiewicz-Zhu A-Posteriori Error Estimator in the Finite Element Method*. International Journal for Numerical Methods in Engineering, 28: 2161–2174.
- [4] APEL, N. [2004]: *Approaches to the description of anisotropic material behavior at finite elastic and plastic deformations. Theory and numerics*. No. I-12, Institut für Mechanik (Bauwesen), Universität Stuttgart.
- [5] ARMERO, F.; PETÖCZ, E. [1998]: *Formulation and analysis of conserving algorithms for frictionless dynamic contact/impact problems*. Computer Methods in Applied Mechanics and Engineering, 158: 269–300.
- [6] ARMERO, F.; SIMO, J. [1992]: *A new unconditionally stable fractional step method for non-linear coupled thermomechanical problems*. International Journal for Numerical Methods in Engineering, 35: 737–766.
- [7] ASKES, H.; BARGMANN, S.; KUHL, E.; STEINMANN, P. [2005]: *Structural optimisation by simultaneous equilibration of spatial and material forces*. Communications in Numerical Methods in Engineering, 21: 433–442.
- [8] ASKES, H.; KUHL, E.; STEINMANN, P. [2004]: *An ALE formulation based on spatial and material settings of continuum mechanics. Part 2: Classification and applications*. Computer Methods in Applied Mechanics and Engineering, 193: 4223–4245.
- [9] BABUŠKA, I.; RHEINBOLDT, W. C. [1978]: *A-Posteriori Error Estimates for the Finite Element Method*. International Journal for Numerical Methods in Engineering, 12: 1597–1615.
- [10] BARENBLATT, G. I. [1962]: *The mathematical theory of equilibrium cracks in brittle fracture*. Advances in Applied Mechanics, 7: 55–129.
- [11] BAŞAR, Y.; WEICHERT, D. [2000]: *Nonlinear continuum mechanics of solids*. Springer-Verlag, Berlin, Heidelberg.
- [12] BATRA, R. C. [1987]: *The force on a lattice defect in an elastic body*. Journal of Elasticity, 17: 3–8.
- [13] BECKER, M. [2006]: *Incompatibility and instability based size effects in crystals and composites at finite elastoplastic strains*. No. I-18, Institut für Mechanik (Bauwesen), Universität Stuttgart.
- [14] BELYTSCHKO, T.; LIU, W. K.; MORAN, B. [2000]: *Nonlinear Finite Elements for Continua and Structures*. John Wiley & Sons.
- [15] BENDSØE, M.P.; SIGMUND, O. [2003]: *Topology Optimization*. Springer, Berlin, Heidelberg, 2 Edition.



- [16] BITTENCOURT, T. N.; WAWRZYNEK, P. A.; INGRAFFEA, A. R.; L., J. [1996]: *Quasi-automatic simulation of crack propagation for 2D LFEM problems*. Engineering Fracture Mechanics, 55: 321–334.
- [17] BROOMAND, B.; ZIENKIEWICZ, O. C. [1999]: *Recovery procedures in error estimation and adaptivity. Part II: Adaptivity in nonlinear problems of elasto–plasticity behaviour*. Computer Methods in Applied Mechanics and Engineering, 176: 127–146.
- [18] BOUCHARD, P.O.; BAY, F.; CHASTEL, Y. [2003]: *Numerical modelling of crack propagation: automatic remeshing and comparison of different criteria*. Computer Methods in Applied Mechanics and Engineering, 192: 3887–3908.
- [19] BOUCHARD, P.O.; BAY, F.; CHASTEL, Y.; TOVENA, I. [2000]: *Crack propagation modelling using an advanced remeshing technique*. Computer Methods in Applied Mechanics and Engineering, 189: 723–742.
- [20] BRAESS, D. [1997]: *Finite Elemente*. Springer–Verlag.
- [21] BRAUN, M. [1997]: *Configurational forces induced by finite-element discretization*. Proceedings of the Estonian Academy of Sciences, Physics, Mathematics, 46: 24–31.
- [22] BRENNER, S. C.; CARSTENSEN, C. [2004]: *Finite element methods*. In STEIN, E.; DEBORST, R.; HUGHES, J. R. (Editors): *Encyclopedia of Computational Mechanics. Volume 1: Fundamentals*, pp. 73–118. John Wiley & Sons.
- [23] BRUSS, I. [2005]: *Anwendung des Konzepts materieller Kräfte in der Strukturoptimierung*. Technical Report 05-I-08, Institut für Mechanik (Bauwesen), Universität Stuttgart.
- [24] BUDIANSKY, B.; RICE, J. R. [1973]: *Conservation laws and energy-release rates*. Journal of Applied Mechanics, 40: 201–203.
- [25] BUGGISCH, H.; GROSS, D.; KRÜEGER, K.-H. [1981]: *Einige Erhaltungssätze der Kontinuumsmechanik vom J-Integral-Typ*. Ingenieur-Archiv, 50: 103–111.
- [26] CAPRIZ [1989]: *Continua with microstructure*. Springer.
- [27] CARSTENSEN, C.; FUNKEN, S. [2001]: *Averaging technique for FE–a posteriori error control in elasticity. Part I: Conforming FEM*. Computer Methods in Applied Mechanics and Engineering, 190: 2483–2498.
- [28] CARSTENSEN, C.; FUNKEN, S. [2001]: *Averaging technique for FE–a posteriori error control in elasticity. Part II:  $\lambda$ –independent estimates*. Computer Methods in Applied Mechanics and Engineering, 190: 4663–4675.
- [29] CARSTENSEN, C.; FUNKEN, S. [2001]: *Averaging technique for FE–a posteriori error control in elasticity. Part III: Locking–free nonconforming FEM*. Computer Methods in Applied Mechanics and Engineering, 191: 861–877.
- [30] CHADWICK, P. [1975]: *Applications of an energy–momentum tensor in non–linear elastostatics*. Journal of Elasticity, 5: 249–258.
- [31] CHUNG, J.; HULBERT, G. [1993]: *A Time Intergration Algorithm for Structural Dynamics With Improved Numerical Dissipation: The Generalized-alpha Method*. Journal of Applied Mechanics, 60: 371–375.
- [32] CLEJA-TIGOIU, S.; MAUGIN, G. A. [2000]: *Eshelby’s tensor in finite elastoplasticity*. Acta Mechanica, 139: 231–249.

- [33] DASCALU, C.; MAUGIN, G. A. [1993]: *Material forces and energy-release rates in homogeneous elastic bodies with defects*. Comptes Rendus de l'Académie des Sciences/2, 317: 1135–1140.
- [34] DASCALU, C.; MAUGIN, G. A. [1995]: *The thermoelastic material-momentum equation*. Journal of Elasticity, 39: 201–212.
- [35] DENZER, R.; BARTH, F. J.; STEINMANN, P. [2003]: *Studies in elastic fracture mechanics based on the material force method*. International Journal for Numerical Methods in Engineering, 58: 1817–1835.
- [36] EPSTEIN, M. [2002]: *The Eshelby tensor and the theory of distributions of inhomogeneities*. Mechanics Research Communications, 29: 501–506.
- [37] EPSTEIN, M.; MAUGIN, G. A. [1990]: *The energy-momentum tensor and material uniformity in finite elasticity*. Acta Mechanica, 83: 127–133.
- [38] EPSTEIN, M.; MAUGIN, G. A. [1995]: *Thermoelastic material forces: definition and geometric aspects*. Comptes Rendus de l'Académie des Sciences Paris, 320(IIb): 63–68.
- [39] EPSTEIN, M.; MAUGIN, G. A. [1996]: *Geometric material structure of finite-strain elasticity and anelasticity*. Zeitschrift für Angewandte Mathematik und Mechanik, 76(S4): 125–128.
- [40] EPSTEIN, M.; MAUGIN, G. A. [1996]: *On the geometrical material structure of anelasticity*. Acta Mechanica, 115: 119–131.
- [41] ERICKSEN, J. L. [1998]: *On nonlinear elasticity theory for crystal defects*. International Journal of Plasticity, 14: 9–24.
- [42] ESHELBY, J. D. [1951]: *The force on an elastic singularity*. Philosophical Transactions of the Royal Society London A, 224: 87–112.
- [43] ESHELBY, J. D. [1970]: *Energy relations and the energy-momentum tensor in continuum mechanics*. Inelastic Behavior of Solids, pp. 77–115.
- [44] ESHELBY, J. D. [1975]: *The elastic energy-momentum tensor*. Journal of Elasticity, 5: 321–335.
- [45] FAGERSTOEM, M.; LARSSON, R. [2006]: *Theory and numerics for finite deformation fracture modelling using strong discontinuities*. International Journal for Numerical Methods in Engineering, 66: 911–948.
- [46] FLETCHER, D. C. [1976]: *Conservation laws in linear elastodynamics*. Archive for Rational Mechanics and Analysis, 60: 329–353.
- [47] FLOREZ-LOPEZ, J.; BENALLAL, A.; GEYMONAT, G.; BILLARDON, R. [1994]: *A two-field finite element formulation for elasticity coupled to damage*. Computer Methods in Applied Mechanics and Engineering, 114: 193–212.
- [48] FRANCFORT, G.; GOLEBIEWSKA HERRMANN, A. [1982]: *Conservation laws and material momentum in thermoelasticity*. Journal of Applied Mechanics, 49: 710–714.
- [49] FRANKENREITER, I. [2007]: *Configurational mechanics of nonlocal higher-order continua with microstructures*. Technical Report 07-I-05, Institut für Mechanik (Bauwesen), Universität Stuttgart.

- [50] FÜRLE, F. [2007]: *Coupling of efficient software tools in material-force-based h-adaptive strategies for three-dimensional analyses at finite inelastic deformations*. Technical Report 07-I-01, Institut für Mechanik (Bauwesen), Universität Stuttgart.
- [51] GANGADHARAN, R.; RAJAGOPAL, A.; SIVAKUMAR, S. M. [2004]: *An r-h-adaptive strategy based on material forces and error assessment*. *Computers, Materials & Continua*, 1: 229–243.
- [52] GOLEBIEWSKA HERRMANN, A. [1981]: *On conservation of continuum mechanics*. *International Journal of Solids and Structures*, 17: 1–9.
- [53] GOLEBIEWSKA HERRMANN, A. [1982]: *Material momentum tensor and path-independent integrals of fracture mechanics*. *International Journal of Solids and Structures*, 18: 319–326.
- [54] GRIFFITH, A. A. [1921]: *The phenomena of rupture and flow in solids*. *Philosophical Transactions of the Royal Society London A*, 221: 163–198.
- [55] GRIFFITH, A. A. [1924]: *The theory of rupture*. In BIEZENO, C. B.; BURGERS, J. M. (Editors): *Proceedings of the First International Congress for Applied Mechanics, Delft*, pp. 55–63.
- [56] GROSS, D.; KOLLING, S.; MÜLLER, R.; SCHMIDT, I. [2003]: *Configurational forces and their application in solid mechanics*. *European Journal of Mechanics*, 22: 669–692.
- [57] GÜNTHER, W. [1962]: *Über einige Randintgrale der Elastomechanik*. *Abhandlungen der Braunschweigischen Wissenschaftlichen Gesellschaft*, 14: 53–72.
- [58] GUPTA, A. [2004]: *Noether's theorem and its application in configurational mechanics*. University of California, Berkeley, CE 299 Report, 52: 52.
- [59] GURTIN, M. E. [1979]: *On the energy release rate in quasi-static elastic crack propagation*. *Journal of Elasticity*, 9: 187–195.
- [60] GURTIN, M. E. [1995]: *The nature of configurational forces*. *Archive for Rational Mechanics and Analysis*, 131: 67–100.
- [61] GURTIN, M. E. [2000]: *Configurational forces as basic concepts of continuum physics*. Springer-Verlag, New York.
- [62] GURTIN, M. E.; PODIO-GUIDUGLI, P. [1996]: *Configurational forces and the basic laws for crack propagation*. *Journal of the Mechanics and Physics of Solids*, 44: 905–927.
- [63] GURTIN, M. E.; PODIO-GUIDUGLI, P. [1998]: *Configurational forces and a constitutive theory for crack propagation that allows for kinking and curving*. *Journal of the Mechanics and Physics of Solids*, 46: 1343–1378.
- [64] GURTIN, M. E.; SHVARTSMAN, M. M. [1997]: *Configurational forces and the dynamics of planar cracks in three-dimensional bodies*. *Journal of Elasticity*, 48: 167–191.
- [65] HAFTKA, R.T.; GURDAL, Z.; KAMAT, M. [1990]: *Elements of Structural Optimization*. Kluwer Academic Publishers, Boston, 2 Edition.
- [66] HAUPT, P. [2000]: *Continuum mechanics and theory of materials*. Springer Verlag, Berlin.

- [67] HEINTZ, P. [2006]: *On the numerical modelling of quasi-static crack growth in linear elastic fracture mechanics*. International Journal for numerical methods in Engineering, 65: 174–189.
- [68] HEINTZ, P.; LARSSON, F.; HANSBO, P.; RUNESSON, K. [2004]: *Adaptive strategies and error control for computing material forces in fracture mechanics*. International Journal for numerical methods in Engineering, 60: 1287–1299.
- [69] HILL, R. [1986]: *Energy–momentum tensors in elastostatics: Some reflections on the general theory*. Journal of the Mechanics and Physics of Solids, 34: 305–317.
- [70] HOFACKER, M. [2007]: *A variational approach to configurational solid dynamics. Theoretical treatment and numerical implementation*. Technical Report 07-I-03, Institut für Mechanik (Bauwesen), Universität Stuttgart.
- [71] HOLZAPFEL, G. A. [2000]: *Nonlinear solid mechanics. A continuum approach for engineering*. John Wiley & Sons, 1 Edition.
- [72] IRWIN, G. R. [1958]: *Fracture*. In FLÜGGE, S. (Editor): *Encyclopedia of Physics*, Vol. 6, Elasticity and Plasticity, pp. 551–590. Springer.
- [73] JAMMER, M. [1999]: *Concepts of force*. Dover Publications Inc., New York.
- [74] KALPAKIDES, V. K.; DASCALU, C. [2002]: *On the configurational force balance in thermomechanics*. Proceedings of the Royal Society London A, 458: 3023–3039.
- [75] KHAREVYCH, L.; WEIWEI; TONG, Y.; KANSO, E.; MARSDEN, J.; SCHROEDER, P.; DESBRUN, M. [2006]: *Geometric, Variational Integrators for Computer Animation*. In CANI, M.-P.; O’BRIEN, J. (Editors): *Eurographics/ ACM SIGGRAPH Symposium on Computer Animation*. www.geometry.caltech.edu.
- [76] KIENZLER, R.; HERRMANN, G. [2000]: *Mechanics in material space with applications to defect and fracture mechanics*. Springer–Verlag, Berlin, Heidelberg.
- [77] KIRSCH, U. [1989]: *Optimal Topologies of Structures*. Applied Mechanics Review, 42: 223–239.
- [78] KNOWLES, J. K.; STERNBERG, E. [1972]: *On a class of conservation laws in linearized and finite elastostatics*. Archive for Rational Mechanics and Analysis, 44: 187–211.
- [79] KOCH, A. [2003]: *Adaptive Finite-Element-Berechnungen der nichtlinearen Festkörpermechanik bei kleinen und großen Verzerrungen*. No. I-10, Universität Stuttgart, Institut für Mechanik (Bauwesen), Lehrstuhl 1.
- [80] KOLLING, S.; BAASER, H.; GROSS, D. [2002]: *Material forces due to crack-inclusion interaction*. International Journal of Fracture, 118: 229–238.
- [81] KOLLING, S.; MUELLER, R. [2005]: *On configuartional forces in short-time dynamics and their computation with an explicit solver*. Computational Mechanics, 35: 392–399.
- [82] KUHL, D.; CRISFIELD, M. A. [1999]: *Energy-conserving and decaying algorithms in non-linear structural dynamics*. International Journal for Numerical Methods in Engineering, 45: 569–599.
- [83] KUHL, E.; ASKES, H.; STEINMANN, P. [2004]: *An ALE formulation based on spatial and material settings of continuum mechanics. Part 1: Generic hyperelastic formulation*. Computer Methods in Applied Mechanics and Engineering, 193: 4207–4222.

- [84] KUHL, E.; DENZER, R.; BARTH, F. J.; STEINMANN, P. [2004]: *Application of the material force method to thermo-hyperelasticity*. Computer Methods in Applied Mechanics and Engineering, 193: 3303–3325.
- [85] KUHL, E.; STEINMANN, P. [2005]: *A hyperelastodynamic ALE formulation based on referential, spatial and material settings of continuum mechanics*. Acta Mechanica, 174: 201–222.
- [86] LANCZOS, C. [1986]: *The variational principles of mechanics*. Dover Publications Inc., New York, 4 Edition.
- [87] LARSSON, R.; FAGERSTOEM, M. [2005]: *A framework for fracture modelling based on material forces concept with XFEM kinematics*. International Journal for Numerical Methods in Engineering, 62: 1763–1788.
- [88] LIEBE, T.; DENZER, R.; STEINMANN, P. [2003]: *Application of the material force method to isotropic continuum damage*. Computational Mechanics, 30: 171–184.
- [89] LIEBE, T.; MENZEL, A.; STEINMANN, P. [2003]: *Theory and numerics of geometrically non-linear gradient plasticity*. International Journal of Engineering Science, 41: 1603–1629.
- [90] LIEBE, T.; STEINMANN, P. [2001]: *Theory and numerics of a thermodynamically consistent framework for geometrically linear gradient plasticity*. International Journal for Numerical Methods in Engineering, 51: 1437–1467.
- [91] LIEBE, T.; STEINMANN, P.; BENALLAL, A. [2001]: *Theoretical and computational aspects of a thermodynamically consistent framework for geometrically linear gradient damage*. Computer Methods in Applied Mechanics and Engineering, 190: 6555–6576.
- [92] LI, L.-Y.; BETTESS, P. [1997]: *Error Estimates and Adaptive Remeshing Techniques in Elasto-Plasticity*. Communications in Numerical Methods in Engineering, 13: 285–299.
- [93] LI, S.; GUPTA, A. [2006]: *On dual configurational forces*. Journal of Elasticity, 84: 13–31.
- [94] LI, X. [1988]: *Dual conservation laws in elastostatics*. Engineering Fracture Mechanics, 29: 233–241.
- [95] MALVERN, L. E. [1969]: *Introduction to the mechanics of a continuous medium*. Prentice-Hall Inc., New Jersey.
- [96] MARIANO, P. M. [2000]: *Configurational forces in continua with microstructure*. Zeitschrift für angewandte Mathematik und Physik, 51: 752–791.
- [97] MARIANO, P. M. [2001]: *Multifield theories in mechanics of solids*. Advances in Applied Mechanics, 38: 1–93.
- [98] MARSDEN, J. E.; HUGHES, T. J. R. [1983]: *Mathematical foundation of elasticity*. Dover Publications Inc., New Jersey.
- [99] MAUGIN, G. A. [1993]: *Material inhomogeneities in elasticity*. Chapman & Hall, London.
- [100] MAUGIN, G. A. [1993]: *The role of material forces in inhomogeneous elastic and inelastic solids*. ASME Applied Mechanics Division, 158: 39–49.



- [101] MAUGIN, G. A. [1994]: *Eshelby stress in elastoplasticity and ductile fracture*. International Journal of Plasticity, 10: 393–408.
- [102] MAUGIN, G. A. [1994]: *On the  $J$ -integral and energy-release rates in dynamical fracture*. Acta Mechanica, 105: 33–47.
- [103] MAUGIN, G. A. [1995]: *Material forces: Concepts and applications*. Applied mechanics reviews, 48: 213–245.
- [104] MAUGIN, G. A. [2000]: *On the universality of the thermomechanics of forces driving singular sets*. Archive of Applied Mechanics, 70: 31–45.
- [105] MAUGIN, G. A. [2002]: *Remarks on eshelbian thermomechanics of materials*. Mechanics Research Communications, 29: 537–542.
- [106] MAUGIN, G. A. [2003]: *Pseudo-plasticity and pseudo-inhomogeneity effects in materials mechanics*. Journal of Elasticity, 71: 81–103.
- [107] MAUGIN, G. A. [2006]: *On canonical equations of continuum thermomechanics*. Mechanics Research Communications, 33: 705–710.
- [108] MAUGIN, G. A.; BEREZOVSKI, A. [1999]: *Material formulation of finite-strain thermoelasticity and applications*. Journal of Thermal Stresses, 22: 421–449.
- [109] MAUGIN, G. A.; EPSTEIN, M.; TRIMARCO, C. [1992]: *Pseudomomentum and material forces in inhomogeneous materials*. International Journal of Solids and Structures, 29: 1889–1900.
- [110] MAUGIN, G. A.; TRIMARCO, C. [1992]: *Pseudomomentum and material forces in nonlinear elasticity: variational formulations and application to brittle fracture*. Acta Mechanica, 94: 1–28.
- [111] MAUTE, K.; SCHWARZ, S.; RAMM, E. [1999]: *Structural Optimization - The Interaction between Form and Mechanics*. Zeitschrift für Angewandte Mathematik und Mechanik, 79 (10): 651–673.
- [112] MEDIAVILLA, J.; PEERLINGS, R. H. J.; GEERS, M. G. D. [2006]: *Discrete modelling of ductile fracture driven by non-local softening plasticity*. International Journal for Numerical Methods in Engineering, 66: 661–688.
- [113] MEDIAVILLA, J.; PEERLINGS, R. H. J.; GEERS, M. G. D. [2006]: *An integrated continuous-discontinuous approach towards damage engineering in sheet metal forming processes*. Engineering Fracture Mechanics, 73: 895–916.
- [114] MEDIAVILLA, J.; PEERLINGS, R. H. J.; GEERS, M. G. D. [2006]: *A robust and consistent remeshing-transfer operator for ductile fracture simulations*. Computers and Structures, 84: 604–623.
- [115] MENZEL, A.; DENZER, R.; STEINMANN, P. [2004]: *On the comparison of two approaches to compute material forces for inelastic materials. Application to single-slip crystal-plasticity*. Computer Methods in Applied Mechanics and Engineering, 193: 5411–5428.
- [116] MENZEL, A.; STEINMANN, P. [2007]: *On configurational forces in multiplicative elastoplasticity*. International Journal of Solids and Structures, 44: 4442–4471.
- [117] MIEHE, C. [1994]: *Aspects of the formulation and finite element implementation of large strain isotropic elasticity*. International Journal of Numerical Methods in Engineering, 37: 1981–2004.



- [118] MIEHE, C. [1995]: *Entropic thermo-elasticity at finite strains: Aspects of the formulation and numerical implementation*. Computer Methods in Applied Mechanics and Engineering, 120: 243–269.
- [119] MIEHE, C. [1996]: *Exponential Map Algorithm for Stress Updates in Anisotropic Elastoplasticity at Large Strains for Single Crystals*. International Journal Numerical Methods in Engineering, 39: 3367–3390.
- [120] MIEHE, C. [1996]: *Multisurface thermoplasticity for single crystals at large strains in terms of Eulerian vector updates*. International Journal of Solids and Structures, 33: 3103–3130.
- [121] MIEHE, C. [1998]: *A constitutive frame of elastoplasticity at large strains based on the notion of a plastic metric*. International Journal of Solids and Structures, 35: 3859–3897.
- [122] MIEHE, C.; APEL, N.; LAMBRECHT, M. [2002]: *Anisotropic additive plasticity in the logarithmic strain space. Modular kinematic formulation and implementation based on incremental minimization principles for standard materials*. Computer Methods in Applied Mechanics and Engineering, 191: 5383–5425.
- [123] MIEHE, C.; GÜRSES, E. [2007]: *A robust algorithm for configurational-force-driven brittle crack propagation with  $r$ -adaptive mesh alignment*. International Journal for Numerical Methods in Engineering, 72: 127–155.
- [124] MIEHE, C.; GÜRSES, E.; BIRKLE, M. [2007]: *Configurational-force-driven brittle crack propagation based on incremental energy minimization*. International Journal of Fracture, accepted for publication.
- [125] MIEHE, C.; LAMBRECHT, M. [2001]: *Algorithms for computation of stresses and elasticity moduli in terms of Seth-Hill's family of generalized strain tensors*. Communications in Numerical Methods in Engineering, 17: 337–353.
- [126] MIEHE, C.; SCHRÖDER, J. [2001]: *A Comparative Study of Stress Update Algorithms for Rate-Independent and Rate-Dependent Crystal Plasticity*. International Journal for Numerical Methods in Engineering, 50: 273–298.
- [127] MIEHE, C.; ZIMMERMANN, D. [2007]: *Configurational-force-based  $h$ -adaptive remeshing procedures in finite inelasticity*. Computer Methods in Applied Mechanics and Engineering, to appear.
- [128] MIEHE, C.; ZIMMERMANN, D. [2007]: *Configurational-force-based structural updates for brittle crack propagation coupled with  $h$ -adaptive mesh refinement*. International Journal for Numerical Methods in Engineering, to appear.
- [129] MOLINARI, J. F.; ORTIZ, M. [2002]: *Three-dimensional adaptive meshing by subdivision and edge-collapse in finite-deformation dynamic-plasticity problems with application to adiabatic shear banding*. International Journal for Numerical Methods in Engineering, 53: 1101–1126.
- [130] MOSLER, J.; ORTIZ, M. [2006]: *On the numerical implementation of variational arbitrary Lagrangian-Eulerian (VALE) formulations*. International Journal for Numerical Methods in Engineering, 67: 1272–1289.
- [131] MOSLER, J.; ORTIZ, M. [2007]: *Variational  $h$ -adaptation in finite elasticity and plasticity*. International Journal for Numerical Methods in Engineering, in press.

- [132] MÜLLER, R.; GROSS, D.; MAUGIN, G. A. [2004]: *Use of material forces in adaptive finite element methods*. Computational Mechanics, 33: 421–434.
- [133] MÜLLER, R.; KOLLING, S.; GROSS, D. [2001]: *On configurational forces in the context of the finite element method*. International Journal for Numerical Methods in Engineering, 53: 1557–1574.
- [134] MÜLLER, R.; MAUGIN, G. A. [2002]: *On material forces and finite element discretizations*. Computational Mechanics, 29: 52–60.
- [135] NÄSER, B.; KALISKE, M. [2004]: *Formulierung materieller Kräfte für elastische und inelastische Materialien*. Leipzig Annual Civil Engineering Report, 9.
- [136] NÄSER, B.; KALISKE, M.; MÜLLER, R. [2007]: *Material forces for inelastic models at large strains: application to fracture mechanics*. Computational Mechanics, 40: 1005–1013.
- [137] NEWMARK, N. M. [1959]: *A method of computation for structural dynamics*. ASCE Journal of Engineering Mechanics Division, 85: 67–94.
- [138] NGUYEN, T. D.; GOVINDJEE, S.; KLEIN, P. A.; GAO, H. [2005]: *A material force method for inelastic fracture mechanics*. Journal of Mechanics and Physics of Solids, 53: 91–121.
- [139] NOETHER, E. [1918]: *Invariante Variationsprobleme*. Nachrichten von der Königlichen Gesellschaft der Wissenschaften zu Göttingen, Mathematisch-Physikalische Klasse, 2: 235–257.
- [140] OGDEN, R. W. [1975]: *A note on duality in finite elasticity*. Journal of Elasticity, 5: 83–88.
- [141] OLEAGA, G. E. [2001]: *Remarks on a Basic Law for Dynamic Crack Propagation*. Journal of the Mechanics and Physics of Solids, 49: 2273–2306.
- [142] OLEAGA, G. E. [2003]: *On the Dynamics of Cracks in Three Dimension*. Journal of the Mechanics and Physics of Solids, 51: 169–185.
- [143] OLVER, P. J. [1984]: *Conservation laws in elasticity. I. General results*. Archive for Rational Mechanics and Analysis, 85: 111–129.
- [144] OLVER, P. J. [1984]: *Conservation laws in elasticity. II. Linear homogeneous isotropic elastostatics*. Archive for Rational Mechanics and Analysis, 85: 131–160.
- [145] ORTIZ, M.; QUIGLEY, J. J. [1991]: *Adaptive Mesh Refinement in Strain Localization Problems*. Computer Methods in Applied Mechanics and Engineering, 90: 781–804.
- [146] PERIĆ, D.; YU, J.; OWEN, D. R. J. [1994]: *On Error Estimates and Adaptivity in Elastoplastic Solids: Applications to the Numerical Simulation of Strain Localization in Classical and Cosserat Continua*. International Journal for Numerical Methods in Engineering, 37: 1351–1379.
- [147] PHONGTHANAPANICH, S.; DECHAUMPHAI, P. [2004]: *Adaptive Delaunay triangulation with object-oriented programming for crack propagation analysis*. Finite Elements in Analysis and Design, 40: 1753–1771.
- [148] PINSKY, P.M. [1987]: *A finite element formulation for elastoplasticity based on a three-field variational equation*. Computer Methods in Applied Mechanics and Engineering, 61: 41–60.

- [149] PRESS, W.H.; TEUKOLSKY, S.; VETTERLING, W.; FLANNERY, B. [1992]: *Numerical Recipes in Fortran*. Cambridge University Press, 2 Edition.
- [150] RADOVITZKY, R.; ORTIZ, M. [1999]: *Error estimation and adaptive meshing in strongly nonlinear dynamic problems*. Computer Methods in Applied Mechanics and Engineering, 172: 203–240.
- [151] RHEINBOLDT, W. C. [1985]: *Error Estimates for Nonlinear Finite Element Computations*. Computers & Structures, 20: 91–98.
- [152] RICE, J. R. [1968]: *A path independent integral and the approximate analysis of strain concentration by notches and cracks*. Journal of Applied Mechanics, 35: 379–386.
- [153] ROGULA, D. [1977]: *Forces in material space*. Archives of Mechanics, 29: 705–713.
- [154] ROZVANY, G.I.N.; BENDSØE, M.; KIRSCH, U. [1995]: *Layout Optimization of Structures*. Applied Mechanics Review, 48: 41–119.
- [155] ROZVANY, G.I.N.; ZHOU, M.; SIGMUND, O. [1994]: *Optimization of Topology*. In ADELI, H. (Editor): *Advances in design optimization*, pp. 340–399. Chapman & Hall, London, Weinheim.
- [156] RUPPERT, J. [1994]: *A Delaunay Refinement Algorithm for Quality 2-Dimensional Mesh Generation*. Technical report, NASA Ames Research Center, Submission to Journal of Algorithms.
- [157] SHEWCHUK, J. R.: *Triangle: Engineering a 2D Quality Mesh Generator and Delaunay Triangulator*. Technical report, School of Computer Science Carnegie Mellon University Pittsburgh, Pennsylvania 15213.
- [158] SHEWCHUK, J.R. [1994]: *An Introduction to the Conjugate Gradient Method Without the Agonizing Pain*. Technical Report, University of California, Berkeley.
- [159] SHIELD, R. T. [1967]: *Inverse deformation results in finite elasticity*. Zeitschrift für Angewandte Mathematik und Physik, 18: 490–500.
- [160] SIMO, J.C. [1992]: *Algorithms for static and dynamic multiplicative plasticity that preserve the classical return mapping schemes of the infinitesimal theory*. Computer Methods in Applied Mechanics and Engineering, 99: 61–112.
- [161] SIMO, J. C.; ARMERO, F. [1992]: *Geometrically non-linear enhanced strain mixed methods and the method of incompatible modes*. International Journal for Numerical Methods in Engineering, 33: 1413–1449.
- [162] SIMO, J. C.; ARMERO, F.; TAYLOR, R. L. [1993]: *Improved versions of assumed enhanced strain tri-linear elements for 3D finite deformation problems*. Computer Methods in Applied Mechanics and Engineering, 110: 359–386.
- [163] SIMO, J.C.; KENNEDY, J.; TAYLOR, R. [1989]: *Complementary mixed finite element formulation for elastoplasticity*. Computer Methods in Applied Mechanics and Engineering, 74: 177–206.
- [164] SIMO, J. C.; MIEHE, C. [1992]: *Associative coupled thermoplasticity at finite strains: Formulation, numerical analysis and implementation*. Computer Methods in Applied Mechanics and Engineering, 98: 41–104.

- [165] SIMO, J. C.; RIFAI, M. S. [1990]: *A class of mixed assumed strain methods and the method of incompatible modes*. International Journal for Numerical Methods in Engineering, 29: 1595–1638.
- [166] SIMO, J. C.; TARNOW, N. [1992]: *The discrete energy momentum method. Conserving algorithms for nonlinear elastodynamics*. Zeitschrift für angewandte Mathematik und Physik, 43: 757–792.
- [167] SIMO, J. C.; TARNOW, N. [1994]: *A new energy and momentum conserving algorithm for the nonlinear dynamics of shells*. International Journal for Numerical Methods in Engineering, 37: 2527–2549.
- [168] SLOAN, S. W. [1987]: *A Fast Algorithm for Constructing Delaunay Triangulations in the Plane*. Advanced Engineering Software, 9, No.1: 34–55.
- [169] SLOAN, S. W. [1991]: *A Fast Algorithm for Generating Constrained Delaunay Triangulations*. Technical Report 065.07.1991, Department of Civil Engineering and Surveying, The University of Newcastle, New South Wales, Australia 2308.
- [170] STEIN, E.; SEIFERT, B.; OHNIMUS, S.; CARSTENSEN, C. [1994]: *Adaptive Finite Element Analysis of Geometrically Non-linear Plates and Shells, Especially Buckling*. International Journal for Numerical Methods in Engineering, 37: 2631–2655.
- [171] STEINMANN, P. [2000]: *Application of material forces to hyperelastostatic fracture mechanics I. Continuum mechanical setting*. International Journal of Solids and Structures, 37: 7371–7391.
- [172] STEINMANN, P. [2001]: *On spatial and material settings of hyperelastodynamics*. Acta Mechanica, 156: 193–218.
- [173] STEINMANN, P. [2002]: *On spatial and material settings of hyperelastostatic crystal defects*. Journal of the Mechanics and Physics of Solids, 50: 1743–1766.
- [174] STEINMANN, P. [2002]: *On spatial and material settings of thermo-hyperelastodynamics*. Journal of Elasticity, 66: 109–157.
- [175] STEINMANN, P.; ACKERMANN, D.; BARTH, F. J. [2000]: *Application of material forces to hyperelastostatic fracture mechanics II. Computational setting*. International Journal of Solids and Structures, 38: 5509–5526.
- [176] STEINMANN, P.; MAUGIN, G. A. [2005]: *Mechanics of material forces*. Springer.
- [177] STUMPF, H.; LE, K. C. [1990]: *Variational principles of nonlinear fracture mechanics*. Acta Mechanica, 83: 25–37.
- [178] STUMPF, H.; LE, K. C. [1992]: *Variational formulation of the crack problem for an elastoplastic body at finite strain*. Zeitschrift für angewandte Mathematik und Mechanik, 9: 387–396.
- [179] SVENDSEN, B. [1992]: *Formulation of balance relations and configurational fields for continua with microstructure and moving point defects via invariance*. International Journal of Solids and Structures, 9: 387–396.
- [180] SZABO, B.; BABUŠKA, I. [1991]: *Finite Element Analysis*. John Wiley & Sons Inc., New York.
- [181] TAYLOR, R. L.; BERESFORD, P. J.; WILSON, E. L. [1976]: *A non-conforming element for stress analysis*. International Journal for Numerical Methods in Engineering, 10: 1211–1219.

- [182] THOURTIREDDY, P.; ORTIZ, M. [2004]: *A variational  $r$ -adaption and shape-optimization method for finite-deformation elasticity*. International Journal for Numerical Methods in Engineering, 61: 1–21.
- [183] THOUTIREDDY, P. [2003]: *Variational Arbitrary Lagrangian-Eulerian method*. PhD Thesis. Pasadena CA.
- [184] TIMMEL, M.; KALISKE, M.; KOLLING, S.; MÜLLER, R. [2004]: *Materielle Kräfte in dynamisch beanspruchten Strukturen*. Leipzig Annual Civil Engineering Report, 9.
- [185] TRUESDELL, C. A.; NOLL, W. [1965]: *The non-linear field theories of mechanics*. In FLÜGGE, S. (Editor): *Handbuch der Physik, Vol. III (3)*. Springer Verlag, Berlin.
- [186] TRUESDELL, C. A.; TOUPIN, R. A. [1960]: *The classical field theories*. In FLÜGGE, S. (Editor): *Handbuch der Physik, Vol. III (1)*. Springer Verlag, Berlin.
- [187] WELSCHINGER, F. [2005]: *Fehlerindikatoren in  $h$ -adaptiven FE-Strategien. Ein alternativer Zugang auf Basis materieller Kräfte*. Technical Report 05-I-07, Institut für Mechanik (Bauwesen), Universität Stuttgart.
- [188] WILSON, E. L.; TAYLOR, R. L.; DOHERTY, W. P.; GHABOUSSI, J. [1973]: *Incompatible displacement models*. In FENVES, S. J. ET AL. (Editor): *Numerical and Computer Methods in Structural Mechanics*, pp. 43–57. Academic Press: New York and London.
- [189] YALÇINKAYA, T. [2005]: *Theory and numerics of material forces in thermo-elastic-plastic materials*. Technical Report 05-I-05, Institut für Mechanik (Bauwesen), Universität Stuttgart.
- [190] ZHU, J. Z.; ZIENKIEWICZ, O. C. [1990]: *Superconvergence recovery technique and a posteriori error estimates*. International Journal for Numerical Methods in Engineering, 30: 1321–1339.
- [191] ZIELONKA, M. G. [2006]: *Configurational forces and variational mesh adaption in solid dynamics*. Ph.D. Thesis, California institute of Technology.
- [192] ZIENKIEWICZ, O. C.; TAYLOR, R. L. [2000]: *The Finite Element Method. Vol. 1, The basis*. Butterworth–Heinemann, Oxford.
- [193] ZIENKIEWICZ, O. C.; ZHU, J. Z. [1987]: *A Simple Error Estimator and Adaptive Procedure for Practical Engineering Analysis*. International Journal for Numerical Methods in Engineering, 24: 337–357.
- [194] ZIENKIEWICZ, O. C.; ZHU, J. Z. [1992]: *The superconvergent patch recovery (SPR) and a posteriori error estimators. Part I: The recovery technique*. International Journal for Numerical Methods in Engineering, 33: 1331–1364.
- [195] ZIENKIEWICZ, O. C.; ZHU, J. Z. [1992]: *The superconvergent patch recovery (SPR) and adaptive finite element refinement*. Computer Methods in Applied Mechanics and Engineering, 101: 207–224.
- [196] ZIMMERMANN, D.; MIEHE, C. [2005]: *Computation of material forces in thermo-plasticity based on alternative smoothing algorithms*. Proceedings in Applied Mathematics and Mechanics, 5: 323–324.



# Curriculum Vitae

## Personal Data

Name: Dominik Zimmermann  
Date of Birth: April 21, 1977  
Place of Birth: Koblenz, Germany  
Parents: Dr. Joachim Zimmermann and Rita Zimmermann  
Siblings: Benedikt Zimmermann

## School Education/Military Service

1983 – 1987 Elementary School: Koblenz-Pfaffendorf  
1987 – 1996 Secondary School: Johannes-Gymnasium, Lahnstein  
May 1996 University Entrance Certificate (Abitur)  
1996 – 1998 Military Service: Pionier-Bataillon 320, Lahnstein

## University Education

1998 – 2003 Studies of Civil Engineering, Universität Stuttgart  
2002 – 2003 Scholarship of the Studienstiftung des deutschen Volkes  
March 2003 Graduation as Diplom-Ingenieur

## Professional Occupation

Since 2003 Research Associate and Lecturer, Institute of Applied Mechanics (Civil Engineering), Universität Stuttgart





**In dieser Schriftenreihe bisher erschienene Berichte:**

- I-1(1996) *Theoretische und algorithmische Konzepte zur phänomenologischen Beschreibung anisotropen Materialverhaltens*, J. Schröder, Dissertation, 1996.
- I-2(1996) *Zur Theorie und Numerik finiter elastoplastischer Deformationen von Schalentragwerken*, B. Seifert, Dissertation, 1996.
- I-3(1996) *Zur Modellierung des künstlichen Infrarot-Dichroismus in Polymerfolien bei großen Verformungen*, J. Buhler, Dissertation, 1996.
- I-4(1998) *Verfahren zur Ermittlung der Erdbebenlasten mit Berücksichtigung des stochastischen Charakters des Bebens*, S. Zhang, Dissertation, 1998.
- I-5(1998) *Zur Beschreibung finiter Deformationen von Polymeren: Experimente, Modellbildung, Parameteridentifikation und Finite-Elemente-Formulierung*, J. Keck, Dissertation, 1998.
- I-6(1999) *Berechnungsverfahren instationär erregter Systeme im Frequenzbereich*, A. Jaworek, Dissertation, 1999.
- I-7(2000) *Homogenisierungsmethoden der nichtlinearen Kontinuumsmechanik unter Beachtung von Stabilitätsproblemen*, J. Schröder, Habilitation, 2000.
- I-8(2002) *Theorie und Numerik von Materialinstabilitäten elastoplastischer Festkörper auf der Grundlage inkrementeller Variationsformulierungen*, M. Lambrecht, Dissertation, 2002.
- I-9(2002) *Mikromechanisch motivierte Modelle zur Beschreibung finiter Deformationen gummiartiger Polymere: physikalische Modellbildung und numerische Simulation*, F. Lulei, Dissertation, 2002.
- I-10(2003) *Adaptive Finite-Elemente-Berechnungen der nichtlinearen Festkörpermechanik bei kleinen und großen Verzerrungen*, A. Koch, Dissertation, 2003.
- I-11(2003) *Theorie und Numerik der Parameteridentifikation von Materialmodellen der finiten Elastizität und Inelastizität auf der Grundlage optischer Feldmeßmethoden*, G. Scheday, Dissertation, 2003.
- I-12(2004) *Approaches to the Description of Anisotropic Material Behaviour at Finite Elastic and Plastic Deformations, Theory and Numerics*, N. Apel, Dissertation, 2004.
- I-13(2004) *Temperaturabhängige Beschreibung visko-elasto-plastischer Deformationen kurzglasfaserverstärkter Thermoplaste: Modellbildung, Numerik und Experimente*, S. Rieger, Dissertation, 2004.
- I-14(2005) *Zur Parameteridentifikation komplexer Materialmodelle auf der Basis realer und virtueller Testdaten*, A. Rieger, Dissertation, 2005.
- I-15(2005) *Viskoelastisches Verhalten von Elastomeren bei finiten Verzerrungen: Experimente, Modellierung und Simulationen*, H. Zecha, Dissertation, 2005.

- I-16(2005) *Mehrskalenmodelle in der Festkörpermechanik und Kopplung von Mehrgittermethoden mit Homogenisierungsverfahren*, C.G. Bayreuther, Dissertation, 2005.
- I-17(2005) *Static and Dynamic Homogenization Analyses of Discrete Granular and Atomistic Structures on Different Time and Length Scales*, J. Dettmar, Dissertation, 2005.
- I-18(2006) *Incompatibility and Instability Based Size Effects in Crystals and Composites at Finite Elastoplastic Strains*, M. Becker, Dissertation, 2006.
- I-19(2007) *Aspects of Energy Minimization in Solid Mechanics: Evolution of Inelastic Microstructures and Crack Propagation*, E. Gürses, Dissertation, 2007.
- I-20(2007) *Micro-Macro Approaches to Rubbery and Glassy Polymers: Predictive Micromechanically-Based Models and Simulations*, S. Göktepe, Dissertation, 2007.
- I-21(2008) *Material Forces in Finite Inelasticity and Structural Dynamics: Topology Optimization, Mesh Refinement and Fracture*, D. Zimmermann, Dissertation, 2008.